LBL-15254

Lawrence Berkeley Laboratory

UNIVERSITY OF CALIFORNIA

Materials & Chemical Sciences Division

Computer Studies of Multiple-Quantum Spin Dynamics

J.B. Murdoch
(Ph.D. Thesis)

November 1982

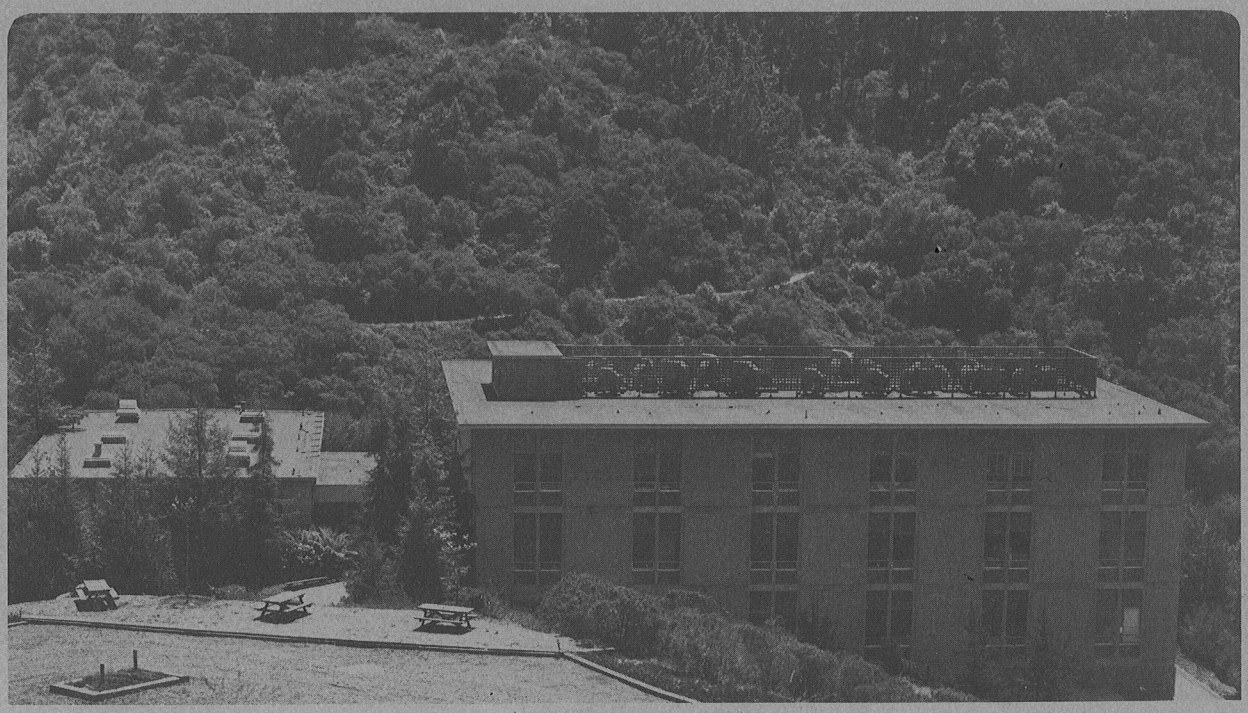

Prepared for the U.S. Department of Energy under Contract DE-AC03-76SF00098

DISCLAIMER

This document was prepared as an account of work sponsored by the United States Government. Neither the United States Government nor any agency thereof, nor The Regents of the University of California, nor any of their employees, makes any warranty, express or implied, or assumes any legal liability or responsibility for the accuracy, completeness, or usefulness of any information, apparatus, product, or process disclosed, or represents that its use would not infringe privately owned rights. Reference herein to any specific commercial products process, or service by its trade name, trademark, manufacturer, or otherwise, does not necessarily constitute or imply its endorsement, recommendation, or favoring by the United States Government or any agency thereof, or The Regents of the University of California. The views and opinions of authors expressed herein do not necessarily state or reflect those of the United States Government or any agency thereof or The Regents of the University of California and shall not be used for advertising or product endorsement purposes.

Lawrence Berkeley Laboratory is an equal opportunity employer.

LBL 15254

COMPUTER STUDIES OF MULTIPLE-QUANTUM SPIN DYNAMICS

James Bryce Murdoch

Ph.D. Thesis

November 1982

Materials and Molecular Research Division
Lawrence Berkeley Laboratory
University of California
Berkeley, CA 94720

This work was supported by the Director, Office of Energy Research, Office of Basic Energy Sciences, Materials Sciences Division of the U. S. Department of Energy under Contract Number DE-AC03-76SF00098.

COMPUTER STUDIES OF MULTIPLE-QUANTUM SPIN DYNAMICS

JAMES BRYCE MURDOCH

ABSTRACT

The excitation and detection of multiple-quantum (MQ) transitions in Fourier transform NMR spectroscopy is an interesting problem in the quantum mechanical dynamics of spin systems as well as an important new technique for investigation of molecular structure. In particular, multiple-quantum spectroscopy can be used to simplify overly complex spectra or to separate the various interactions between a nucleus and its environment. The emphasis of this work is on computer simulation of spin-system evolution to better relate theory and experiment.

The first example to be considered is the three-level system of a spin-one nucleus, specifically deuterium in solids. Using an operator formalism and a physical model for coherence, the evolution of the density matrix during a variety of pulse sequences is analyzed in detail. Optimized pulse sequences are developed for the generation of chemical shielding powder lineshapes via the double-quantum transition. The phenomenon of double-quantum spin locking is investigated and used to measure spin-lattice relaxation times in the rotating frame.

The dipolar-coupled protons of molecules dissolved in liquid crystal solvents comprise the second type of spin system to be examined here. For these systems, MQ spectroscopy offers better resolution than the conventional single-quantum approach, simplifying the determination of dipolar couplings that in turn can be related

to the averaged molecular conformation. The work reported here focuses on the MQ intensities expected from the basic three-pulse sequence. At the most concrete level, specific values for the preparation and detection times are used to simulate six- and eight-spin experimental spectra. The concept of time-independent MQ intensities is then introduced, an algorithm for efficient computation of these quantities is described, and several representative spectra are presented. A correlation between the relative standard deviation of dipolar couplings and the intensity of high-quantum lines is discussed at length; in many cases, these intensities are predicted to be considerably larger than a simple statistical argument would suggest. The effect of varying the preparation and detection times independently is analyzed as a random-walk problem.

ACKNOWLEDGMENTS

One advantage of my rather lengthy stay in Berkeley has been the opportunity to meet a large number of terrific people. As a result, these acknowledgments must be somewhat more voluminous than the norm. However, this entire thesis has a weight problem, so a little excess verbiage here is certainly appropriate.

First, of course, I'd like to thank my research director, Alex Pines, for his energy, enthusiasm, wit, and generosity. He has been a continual source of intellectual cross-polarization, recharging my mental spin vectors regularly with a wealth of suggestions and physical insights. Moreover, his success in combining first-rate science with panache and style is a role model most worthy of emulating.

Second on my list of acknowledgments must be Shimon Vega, for welcoming me into his nine-dimensional world of spin-one operators. Chapters II and III are a direct outgrowth of our work together. In addition to having elegant formalism, he's one heck of a nice guy.

Saying anything concise about my other fellow Pines group members is difficult. It would be fun to ramble on about our joint experiences that transcend spin space--blowgun fights, post-midnight treks to Biffs or IHOP, a shared appreciation of the literary merits of The Executioner: Chicago Wipeout and Fear and Loathing in Las Vegas, etc. --but the urge to exit thesis mode far outweighs my taste for nostalgia right now. With an emphasis on scientific interactions, then, let me briefly thank ... Dan Weitekamp, for first alerting me to the strange and wondrous things afoot in the

Pines lab and for n years ($n \to \infty$) of ideas, insights, and basketball since ... Tom Shattuck, for getting me started on the old α-spectrometer ... Dave Ruben, for imparting some of his vast knowledge of computer systems, spectrometer design, and Star Trek trivia ... Dave Wemmer, for introducing me to the β-spectrometer (and to racquetball) and for blazing the trail in both double- and multiple-quantum NMR ... Larry Sterna and Jau Tang, for correlated conversations ... Gary Drobny and Steve Sinton, for helping me relate my computer simulations to the real world of experiments and for doing their best to keep me "living large and staying hard" ... Dick Eckman, for much insight regarding NMR of solids and magic-angle spinning ... Warren Warren, for providing applications and analysis of my calculations ... Yu-Sze Yen, for many multiple-quantum (second) moments to remember ... Joel Garbow, for his consistent interest in exploring MQ NMR ... and Luciano Mueller, for a transfer of coherence regarding coherence transfer. Finally, although they arrived on the scene too late to impinge much on the work detailed herein, my nouvelle vague colleagues deserve mention as well. John Millar, Rob Tycko, Jean Baum, and Dave Zax, plus the even newer wave of Tony, Erika, Baek, and Herman, have already demonstrated that the twisted brilliance and cultural perversity of the Pines ensemble will be maintained for years to come.

But back to science. My experimental forays were made possible by our resident alchemists: Herbert Zimmermann, who prepared a treasure trove of isotopically labeled compounds, and Sid Wolfe, of Dr. Stu's Deutering Clinic, who continued the magic as visiting scientist from the University of the Absurd.

In turn, my large-scale calculations were made possible by Mel Klein of the Laboratory for Chemical Biodynamics, who kindly provided access to the LCB VAX. In addition, Mel and his students have always been most helpful and enjoyable to talk with. Particularly satisfying have been explorations of "Vega space" with Tom Pratum.

Whom else should I mention? Certainly Bob Palmer--without his efforts in the Low Temperature Plant, our superconducting magnets would be just so much decorative sculpture. The group secretaries--Carol Hacker, Kathy Altes, Terri Judson, and Dione Carmichael--deserve praise for doing their part to maintain order in the midst of chaos. In the Chemistry Department office, Dot Crane has always been exceptionally helpful.

As for the preparation of this tome, my sincere thanks go to Carol Hacker for her superb typing and to Nancy Monroe and Gloria Pelatowski for their artful drafting. My Earth Science colleagues, Ellory Schempp, Stan Klainer, and Ian Carmichael, have shown remarkable and much appreciated forbearance while this labor of logorrhea has lingered on ... and on.

Naturally, the graduate school experience encompasses more than hanging around in lab, massaging a terminal, or staring impotently at a half-written chapter. As such, I would also like to toast my compadres from the G.S.O. Social Committee, from the Chem Pistols softball and football teams, and from the various incarnations of our basketball squad (Gauss Encounters of the Second Rank, the Revolutionary Spectroscopist Youth Brigade, the League of Evil Mutants, and the Pinenuts). I don't want to be guilty of excessive name-dropping,

but Tony Gallo, Steve "Roland" Winkle, Carl Hayden, Tom Tufano, Mike Berman, Steve Hansen, my Christmas co-conspirator Henry Luftman, Sue Sherrow, John Winn, Vicky Shannon, Tony O'Keefe, my fellow Moo U alumni Ann Hriciga and Jim Weisshaar, and many more have added a lot of fun to my Berkeley years.

I'd like to close on a personal note. Without the love and support of my parents, my sisters, and my wife Eileen, none of this would have been possible. Their faith in me has kept me going through the occasional pits of grad school despair, and their patience during the protracted gestation of this literary monstrosity has been super-human. Eileen especially deserves thanks for proofreading and for enduring a most unnatural menage à trois with my thesis and me.

This work was supported by a National Science Foundation Graduate Fellowship (much appreciated) and by the Materials and Molecular Research Division of Lawrence Berkeley Laboratory.

Simulated Thoughts

(may be sung, if desired, to "Oh Little Town of Bethlehem")

Down in the depths of Hildebrand
Where sunlight never goes,
I sit and stare--I'm happy where
My terminal faintly glows.
My fingers stroke the keyboard
In near-orgasmic bliss;
I've often heard that nerd's the word
That fits a case like this.

I have no use for chemicals,
I haven't touched one yet;
They slosh and spill and make one ill,
That's not my basis set.
I'd rather be computing
The world's most perfect psi;
Just let me solve how states evolve,
And I'm a happy guy.

That little screen in Hildebrand
Holds all I want to know;
If things compile then life's worthwhile,
Just let those numbers flow.
My lab-mates try to tell me
The real world's overhead;
Who needs that life of toil and strife?
I'll simulate instead.

I. Back to Basics

1.1 Introduction 1

1.2 A Note on Units 3

1.3 The Fundamental Interaction 4

1.4 Gauss Encounters of the Second Rank 6

1.5 Hamiltonians on Parade 11

1.5.1 Zeeman Hamiltonian 12

1.5.2 Radio Frequency Hamiltonian 13

1.5.3 Chemical Shielding Hamiltonian 16

1.5.4 Quadrupole Hamiltonian 18

1.5.5 Direct Dipole-Dipole Hamiltonian 20

1.5.6 Indirect Dipole-Dipole Hamiltonian 22

1.5.7 Other Terms 24

1.6 The Density Matrix 24

1.7 The Basic Computational Approach 29

1.8 Assorted Thoughts 31

II. Deuterium Double-Quantum NMR in Solids

2.1 Introduction 33

2.2 An Outline of Previous Work 36

2.3 An Actual, Although Tenuous, Link to Chemistry 38

2.3.1 We Gaze Upon the Deuteron: Two-Quantum Yielding the Chemical Shielding 38

2.3.2 Single Crystals vs. Powders 40

2.4 Operator Assistance for Studying Spin-System Evolution 42

2.4.1 Starting Small: A Look Back at Two Levels 44

2.4.2 The Three-Level Circus 47

2.4.3 The World According to $I_{p,i}$ Operators 50

2.4.4 Additional Models for the Three-Level System 66

2.5 Expressions for the Effects of Various Hamiltonians . . 73

2.5.1 $\mathcal{H}_{off} \neq 0$, $\mathcal{H}_{rf} \neq 0$, $\mathcal{H}_Q = 0$ 74

2.5.2 $\mathcal{H}_{off} \neq 0$, $\mathcal{H}_{rf} = 0$, $\mathcal{H}_Q \neq 0$ 74

2.5.3 $\mathcal{H}_{off} = 0$, $\mathcal{H}_{rf} \neq 0$, $\mathcal{H}_Q \neq 0$ 75

2.5.4 The General Hamiltonian 86

2.6 Pulse Sequences for Creation and Detection of Double-Quantum Coherence 87

2.7 On the Nature of Powders 92

2.8 Preparing Double-Quantum Coherence: An In-Depth Report 94

2.8.1 Results for a Fixed Value of ν_Q 95

2.8.2 Preparing Double-Quantum Coherence in Powders 106

2.9 Analysis of the Quadrupole Echo Sequence 118

2.10 At Long Last Lineshapes 129

2.10.1 Aligned and Axially Symmetric EFG and Chemical Shielding Tensors 129

2.10.2 Comparison with Experiments 133

2.10.3 Non-axial But Aligned Tensors: A Simulated Lineshape for $Ba(ClO_3)_2 \cdot HDO$ 135

2.11 Lineshapes for General Tensor Orientations 140

2.12 Effect of the Second-Order Quadrupole Shift 148

2.13 Double-Quantum Spin-Locking 153

III. Continuous-Wave NMR with Phase-Cycled Pulses

3.1 Introduction 159

3.2 The Frequency Spectrum of a Phase-Cycled Sequence . . 163

3.3 Calculation of Conventional cw NMR Spectra for a Three-Level System 174

3.4 Calculating the Steady-State Response to Phase-Cycled rf Irradiation 181

3.5 Phase-Cycled cw Spectra for a Three-Level System . . . 187

IV. Beyond the Three-Level System: Fundamentals of Multiple-Quantum NMR

4.1 Introduction 198

4.2 NMR in Liquid Crystal Solvents 200

4.2.1 The Order Tensor 201

4.2.2 The Basics of NMR in Nematic Phase 207

4.2.3 Effects of Molecular Motion on the Hamiltonian 207

4.2.4 The Case for Multiple-Quantum NMR 212

4.3 Up Close and Personal with the Multiple-Quantum Hamiltonian 215

4.4 The Effect of Symmetry 219

4.5 Your Basic Multiple-Quantum Pulse Sequence 223

4.6 Properties of the Prepared Density Matrix 226

4.6.1 Even-Odd Selection 228

4.6.2 Rotation about I_z: The Ways of Phase 232

4.6.3 Spin-Inversion States 233

4.6.4 A Note on Degeneracy 239

4.7 Separation of Multiple-Quantum Orders 240

4.7.1 A Frequency Offset 241

4.7.2 Phase Fourier Transforms 242

4.7.3 Frequency Adjustment to Separate Orders . . . 243

4.7.4 Time-Proportional Phase Incrementation 246

4.7.5 Coherence Transfer Echoes 247

4.8 Meet the Molecules 248

4.8.1 Benzene 249

4.8.2 4-cyano-4'-n-pentyl-d_{11}-biphenyl 254

4.8.3 Acetaldehyde 258

4.9 Gerade-Ungerade Selectivity 259

4.10 Summary 265

V. Computer Simulation of Multiple-Quantum Intensities

5.1 Introduction 269

5.2 An Expression for Multiple-Quantum Intensity 270

5.3 Coherence Magnitude as a Function of Preparation Time 276

5.4 τ-Independent Spectra 287

5.4.1 The Statistical Limit Model 287

5.4.2 Symmetry-Adjusted Statistical-Limit Intensities 290

5.4.3 Ultimate τ Average Intensities 295

5.4.3.1 Simplifying the Calculation 298

5.4.3.2 Some Ultimate τ Averate Spectra . . . 300

5.5 Higher-Quantum Selectivity in the Ultimate τ Average 301

5.5.1 Equivalent-Spin Systems 304

5.5.2 General Spin Systems 306

5.5.3 Residual Symmetry Effects When $\bar{D}$ is Zero . . 313

5.5.4 A Comparison of Two Eight-Spin Systems . . . 314

5.6 The Autocorrelation Function of Prepared Coherence . 320

5.7 Average Intensities in Isotropic Systems 322

5.8 Total Spectral Intensity When τ Does Not Equal t_2 325

5.9 Further Tinkering with the Pulse Sequence 337

5.9.1 Flip-Angle Frolics 337

5.9.2 Effects of a Pi Pulse in Evolution 341

5.10 Conclusions 347

Appendix A. Some Properties of Exponential Operators 350

Appendix B. Vanishing B_1 Transitions in Benzene 353

B.1 Introduction 353

B.2 Symmetry-Adapted Functions 353

B.3 Analyzing the Hamiltonian for M=0 355

B.4 Constructing the Wayward Eigenstate 356

Appendix C. An Analysis of Dipolar-Coupled Four-Spin Systems 358

C.1 Introduction 358

C.2 A Look at the M=0 Eigenstates of $\mathcal{H}_D$ 358

C.3 The Wayward State 359

C.4 Four-Quantum Intensity for D_4 Symmetry . . . 362

C.5 Four-Quantum Intensity for C_{3v} Symmetry . . 367

Appendix D. A Look at Three-Pulse Multiple-Quantum Programs . . . 371

Appendix E. Program Notes 376

Appendix F. Postscript 383

References 384

I. BACK TO BASICS

1.1 Introduction

From its humble beginnings at Harvard and Stanford in 1946 [1,2], the field of nuclear magnetic resonance spectroscopy has grown prodigiously, and today, a robust and mature technique, it looms Colossus-like over many areas of physical and biological science. This dissertation will focus on one new wrinkle on the aforementioned Colossus, namely Fourier transform multiple-quantum NMR as applied to solids and liquid crystals.

The "normal" spectroscopic transition involves the absorption or emission of a single photon. Multiple-quantum transitions, those involving more than one photon, were first postulated by Goeppert-Mayer in 1931 [3]. They made their appearance in magnetic resonance in 1956, when Anderson [4] and Kaplan and Meiboom [5] independently discovered that when they turned up the radio frequency irradiation power in their continuous-wave (cw) NMR spectrometers, sharp lines sprouted up between the featureless blobs of saturation-broadened single-quantum transitions. The use of these new lines to assign transitions and to determine the sign of J-couplings enjoyed a brief heyday in the ensuing years [6-9], but the impossibility of separating lines corresponding to different numbers of quanta limited the applicability of the technique (see Chapter III).

The development in recent years of pulsed magnetic resonance methods has made possible the investigation of a much wider range of multiple-quantum phenomena, summarized in a new review article

by Bodenhausen [10]. This multiple-quantum renaissance is not due so much to the practical advantages of Fourier transform spectroscopy [11,12]--improved signal-to-noise and signal-averaging capabilities--but rather to the very nature of time-domain spectroscopy, as will be discussed in the pages to come.

Multiple-quantum NMR is characterized by a number of valuable properties that motivate its study. For instance, MQ techniques can be used to isolate a small but interesting term in the magnetic resonance Hamiltonian, one that would be masked in a normal single-quantum experiment. An example, to be discussed in Chapter II, is the determination of deuterium chemical shielding tensors via the double-quantum transition; in the single-quantum spectrum, the deuterium quadrupolar splitting usually dominates any chemical shielding effect. Alternately, MQ NMR can be used to simplify an overly complex spectrum, yet retain the structural and conformational information it can provide. Chapters IV and V describe the virtues of this simplification in the proton spectra of small molecules dissolved in liquid crystal solvents. A third useful feature is the accessibility of additional spectral density parameters and information on relaxation correlation from multiple-quantum relaxation or lineshape measurements [13-18]. The number of lines in an MQ spectrum can also be used to determine the degree to which intramolecular motion is correlated [18,19].

The investigation of multiple-quantum spectroscopy is motivated by more than mere practicality, however. It is, in fact, an elegant example of "quantum mechanics in action", and

one for which theoretical predictions, computer simulations, and experimental results can be carefully compared.

In the next several sections, a few important concepts in magnetic resonance are briefly discussed: the basic nature of the interaction, the forces at work and the Hamiltonians that describe them, the density matrix formalism, and the properties of spherical tensors. This information can of course be found elsewhere in more profuse and useful detail [20-25]; it is included here as a fleeting glimpse of "normal" NMR before we wander off down the path to forbidden transitions. The chapter ends with a few musings on the nature of simulated magnetic resonance.

The remainder of the thesis addresses a variety of multiple-quantum phenomena. Chapter II provides an in-depth analysis of the simple three-level system of an isolated deuteron. A phase-shifted cw technique for MQ spectroscopy and its application to deuterium NMR are investigated in Chapter III. Pulsed multiple-quantum NMR in multi-level systems is introduced in Chapter IV, and the resulting spectral intensities are explored at length as a function of pulse sequence parameters and dipolar coupling distributions in Chapter V.

1.2 A Note on Units

"2π or not 2π, that is the question." In any discussion of Hamiltonians, coupling constants, etc., one is faced with a choice of units: frequency (Hz) or angular frequency (radians/sec).

There are advantages and disadvantages, of course, to each. Normal frequency units ("ν's") find practical application but drag along a distracting and inelegant factor of 2π when used in any $\nu \cdot$time expression. Angular frequency units ("ω's") are the traditional choice for NMR formalism, but one never hears of a 200 megaradian-per-second spectrometer or a 1.5 kiloradian-per-second linewidth. A complete duplicate set of symbols becomes awkward, so it is probably best to sacrifice consistency on the well-worn altar of convenience. In definitions and formulas, therefore, each D_{jk}, $\Delta\omega$, σ_j, or the like will be assumed, unless stated otherwise, to be in radians/sec; when assigned a value, however, the <u>same</u> symbol will be expressed in hertz. (Example; $U = e^{-iD_{jk}t}$ with $D_{jk} = 1200$ Hz.) The exception is in the analysis of the three-level deuterium system--there the distinction between ω's and ν's will be carefully maintained.

1.3 The Fundamental Interaction

Nuclear magnetic resonance involves the interaction of the magnetic dipole moment of a nucleus with static and oscillating magnetic fields. This magnetic moment $\underset{\sim}{\mu}$ is proportional to the nuclear spin vector $\underset{\sim}{I}$:

$$\underset{\sim}{\mu} = \gamma\hbar\underset{\sim}{I} \tag{I.1}$$

where γ is the magnetogyric ratio. The energy of interaction with a field $\underset{\sim}{H}$ is given by $-\underset{\sim}{\mu}\cdot\underset{\sim}{H}$ [26]. $\underset{\sim}{I}$ is an angular momentum vector

operator, and the usual relations hold [27]:

$$\underset{\sim}{I}^2|\psi\rangle = (I)(I+1)|\psi\rangle \tag{I.2a}$$

$$I_z|\psi\rangle = m|\psi\rangle \qquad m=-I,-I+1,\ldots,I-1,I \tag{I.2b}$$

$$[I_p,I_q] = I_pI_q-I_qI_p = i\ I_r$$

$$p,q,r\equiv x,y,z;\ y,z,x;\ z,x,y \quad . \tag{I.2c}$$

As far as we chemists are concerned, the nuclei themselves are "black boxes"; we are simply grateful that some of them possess a non-zero spin and thus can be used as sensitive probes of their magnetic and electronic environment. The two types of nuclei of interest in this work are normal hydrogen (^1H, I=1/2, $\gamma/2\pi$ = 4.2575 MHz/kilogauss) and deuterium (^2H, I=1, $\gamma/2\pi$ = 0.6536 MHz/kilogauss). A nucleus of spin I has 2I+1 eigenstates, each labeled by m, the eigenvalue of I_z. For I=1/2, m=±1/2; for I=1, m=-1,0, and 1.

If N of the same type of nuclei interact, we must deal with $(2I+1)^N$ states. In the absence of relaxation mechanisms (coupling to additional distant nuclei, fluctuating electric or magnetic fields, phonons, etc.), the spin system of interest can thus be described fully in terms of a <u>finite</u> number of eigenstates--unlike, say, the hydrogen atom or a harmonic oscillator. When N is not unduely large, a computer can be used to solve for the exact spin dynamics--no perturbation treatment is necessary.

1.4 Gauss Encounters of the Second Rank

The interaction of a spin with its neighbors and with external forces is described mathematically in terms of a Hermitian operator $\mathcal{H}$, the Hamiltonian. ("Hermitian" implies that $\mathcal{H}_{ij} = \mathcal{H}_{ji}^{*}$.) However, before the grand unveiling of these all-important operators for the systems that interest us, an introduction to their form and properties would be useful. Each individual term of the total Hamiltonian that we will consider can be written as follows [28,29]:

$$\mathcal{H} = c\ \underset{\sim}{X} \cdot \underset{\approx}{A} \cdot \underset{\sim}{I}_n = c \sum_{a=1}^{3} \sum_{b=1}^{3} X_a\ A_{ab}\ (I_n)_b \quad , \qquad (I.3)$$

where c is a constant, $\underset{\sim}{I}_n$ is the spin vector (I_x, I_y, I_z) for nucleus n, and $\underset{\sim}{X}$ can be, depending on the type of interaction being formulated, a magnetic field vector, the spin vector of another nucleus, or $\underset{\sim}{I}_n$ itself. $\underset{\approx}{A}$ is a symmetric second-rank Cartesian tensor [28-32] (or 3x3 matrix) which describes some physical quantity--field gradients, internuclear distances, etc. $\mathcal{H}$ is thus a product of real-space and spin-space terms; we will be exploring and manipulating both. Let us tarry first in real space and examine $\underset{\approx}{A}$.

As a symmetric 3x3 matrix, $\underset{\approx}{A}$ has at most six unique elements: A_{11}, A_{22}, A_{33}, $A_{12}=A_{21}$, $A_{13}=A_{31}$, and $A_{23}=A_{32}$. The value of these elements depends on the reference frame chosen. In particular, $\underset{\approx}{A}$ is diagonal in one frame--its principal axis system (PAS). The diagonal elements of $\underset{\approx}{A}$ in this frame are called its principal values and are labeled A_{XX}, A_{YY}, and A_{ZZ}. The elements of $\underset{\approx}{A}$ in another reference frame (the laboratory axis system, for example)

are related to the principal values by an orthogonal transformation $\underset{\approx}{R}$ [29-31]:

$$\underset{\approx}{A}\,(\mathrm{LAB}) = \underset{\approx}{R}\,\underset{\approx}{A}\,(\mathrm{PAS})\,\underset{\approx}{R}^{\dagger}$$

$$= \underset{\approx}{R}\begin{bmatrix} A_{XX} & 0 & 0 \\ 0 & A_{YY} & 0 \\ 0 & 0 & A_{ZZ} \end{bmatrix}\underset{\approx}{R}^{\dagger} \quad , \qquad \text{(I.4)}$$

where each element R_{ij} equals the cosine of the angle between the i-axis of the lab frame and the j-axis of the PAS. The elements of $\underset{\approx}{R}$ also characterize the Euler angles of rotation α, β, and γ necessary to rotate the principal axis system into coincidence with the lab frame* [31,32]:

---

*The Euler prescription for transformation from an x,y,z axis system to an x''', y''', z''' axis system is as follows: 1. rotate about the z axis by an angle α and transform to an intermediate frame x',y',z' (z'≡z), 2. rotate about the y' axis by an angle β to transform to a second intermediate frame x",y",z" (y"≡ y'), 3. rotate about the z" axis to complete the transformation to x''',y''',z''' (z'''≡z").

$$\underset{\approx}{R} = \begin{pmatrix} \cos\alpha\cos\beta\cos\gamma-\sin\alpha\sin\gamma & \sin\alpha\cos\beta\cos\gamma+\cos\alpha\sin\gamma & -\sin\beta\cos\gamma \\ -\cos\alpha\cos\beta\sin\gamma-\sin\alpha\cos\gamma & -\sin\alpha\cos\beta\sin\gamma+\cos\alpha\cos\gamma & \sin\beta\sin\gamma \\ \cos\alpha\sin\beta & \sin\alpha\sin\beta & \cos\beta \end{pmatrix} . \tag{I.5}$$

In a general axis system, $\underset{\approx}{A}$ can thus be determined by knowing its three principal values and the three angles that specify the orientation of the PAS relative to that axis system--six pieces of information to match its six unique elements.

It is convenient to replace the principal values of $\underset{\approx}{A}$ with new quantities. Define $\bar{A}$, the isotropic component of $\underset{\approx}{A}$, as 1/3 Tr $\underset{\approx}{A} = 1/3(A_{XX}+A_{YY}+A_{ZZ})$. Assume that the axes are labeled such that

$$|A_{ZZ}-\bar{A}| \geq |A_{XX}-\bar{A}| \geq |A_{YY}-\bar{A}| \quad .$$

Two useful quantities are then the anisotropy of $\underset{\approx}{A}$, given by $\delta = A_{ZZ}-\bar{A}$, and the asymmetry parameter, given by

$$\eta = \frac{|A_{XX}-A_{YY}|}{\delta} \quad . \tag{I.6}$$

η is unitless and varies between 0 and 1.

And what of $\underset{\sim}{X}$ and $\underset{\sim}{I}_n$? They are combined into another second-rank tensor, the dyadic $\underset{\approx}{T}$ [28,29]:

$$\mathcal{H} = c \sum_{a=1}^{3} \sum_{b=1}^{3} X_a A_{ab} (I_n)_b \equiv c \sum_{a=1}^{3} \sum_{b=1}^{3} A_{ab} T_{ba} \quad .$$

The effect of rotations on the form of $\mathcal{H}$ is most easily analyzed if $\underset{\approx}{A}$ and $\underset{\approx}{T}$ are rewritten in terms of spherical tensors $A_{\ell m}$ and $T_{\ell m}$ [31,32]. Spherical tensors of a given rank ℓ transform among themselves under a rotation in a manner analogous to the spherical harmonic functions. If $\underset{\approx}{A}$ is assumed to be symmetric, then only tensors of rank zero and rank two need be considered in the calculation of $\mathcal{H}$:

$$\mathcal{H} = c\{A_{00}T_{00} + \sum_{m=-2}^{2} (-1)^m A_{2-m}T_{2m}\} \quad . \tag{I.7}$$

$T_{\ell m}$ tensors are usually expressed in the lab reference frame, the appropriate choice not only for applied magnetic fields but also for operators in spin space [29]. (The parallel between magnetization in real space and a "state vector" in spin space will be discussed in Chapter II.) Expressions for the $T_{\ell m}$ tensors used in Hamiltonians of interest here are on display in Table I.1.

$\underset{\approx}{A}$ in the lab frame is related to its spherical tensor components in the principal axis system by Wigner rotation matrix elements $\mathcal{D}^{\ell}_{m'm}$ (the spherical tensor alternate to the transformation matrix $\underset{\approx}{R}$) [31,32]:

Table I.1

Spherical Tensor Operators for NMR Hamiltonians[a]

(those needed in the high-field approximation)

Hamiltonian	T_{00}	T_{20}
Chemical Shielding	$H_0\ I_z$	$\sqrt{2/3}\ H_0\ I_z$
Quadrupole	$\underset{\sim}{I}^2$	$1/\sqrt{6}\ [3\ I_z^2 - \underset{\sim}{I}^2]$
Dipole-Dipole J-Coupling	$\underset{\sim}{I}_j \cdot \underset{\sim}{I}_k$	$1/\sqrt{6}\ [3\ I_{zj} I_{zk} - \underset{\sim}{I}_j \cdot \underset{\sim}{I}_k]$

[a]Adapted from Ref. 24.

Table I.2

Three Relevant Wigner Rotation Matrix Elements[a]

$\mathcal{D}^2_{20}\ (\alpha,\beta,\gamma)$	$\sqrt{3/8}\ \sin^2\beta\ e^{2i\gamma}$
$\mathcal{D}^2_{00}\ (\alpha,\beta,\gamma)$	$1/2\ (3\ \cos^2\beta - 1)$
$\mathcal{D}^2_{-20}\ (\alpha,\beta,\gamma)$	$\sqrt{3/8}\ \sin^2\beta\ e^{-2i\gamma}$

[a]Condensed from Ref. 24.

$$A_{00}\ (\mathrm{LAB}) = A_{00}\ (\mathrm{PAS}) = \bar{A} \tag{I.8a}$$

$$A_{2m}\ (\mathrm{LAB}) = \sum_{m'} \mathcal{D}^2_{m',m}\ (\Omega)\ A_{2m'}\ (\mathrm{PAS}) \quad , \tag{I.8b}$$

where Ω is shorthand for α, β, and γ, the Euler angles by which the lab frame is superimposed onto the PAS.* (The same sort of transformation connects <u>any</u> two axis systems. A partial list of $\mathcal{D}^2_{m',m}$ values can be found in Table I.2.) It so happens that in the principal axis system, only A_{20} and $A_{2\pm2}$ are non-zero, with values $\frac{\sqrt{6}}{2}\ \delta$ and $\frac{1}{2}\ \eta\delta$ respectively [29]. Thus

$$A_{2m}(\mathrm{LAB}) = \frac{\sqrt{6}}{2}\ \delta\ \mathcal{D}^2_{0m}(\Omega) + \frac{1}{2}\ \eta\delta\ [\mathcal{D}^2_{2m}(\Omega) + \mathcal{D}^2_{-2m}(\Omega)]\ . \tag{I.9}$$

Equations I.7 and I.9 will prove quite useful in the struggle ahead.

1.5 Hamiltonians on Parade

In accord with Pines group tradition, a Hamiltonian operator will now be proudly and prominently displayed. This Hamiltonian is comprised of a number of different terms, corresponding to the various interactions experienced by the nuclei of interest, In general, we can write these as follows;

---

*Unfortunately, the opposite transformation path was used for $\underset{\approx}{R}$. Convenience triumphs again over consistency.

$$\mathcal{H} = \mathcal{H}_z + \mathcal{H}_{rf} + \mathcal{H}_{cs} + \mathcal{H}_Q + \mathcal{H}_D + \mathcal{H}_J \quad . \tag{I.10}$$

Each of these terms will be showcased in the remainder of this section.

1.5.1 Zeeman Hamiltonian

In the 42 kilogauss field of our superconducting magnets, the largest Hamiltonian term by far is that describing the direct coupling of the nuclear magnetic dipoles to the static field. Assuming this field lies along the z-axis, the so-called Zeeman Hamiltonian is, in angular frequency units [26],

$$\mathcal{H}_z = -\gamma \, \underset{\sim}{H}_0 \cdot \underset{\sim}{I} = -\gamma \, H_0 \, I_z = -\omega_0 \, I_z \quad . \tag{I.11}$$

In our magnets, ω_0 (the Larmor frequency) is roughly 180 MHz for protons and 27.5 MHz for deuterons. This frequency describes not only the splitting between eigenstates but also the precession frequency of the nuclear magnetic moment about the applied field.

Although the largest term in the nuclear spin Hamiltonian, the Zeeman interaction is miniscule in comparison to typical vibrational or electronic energies. As a result, NMR spectroscopy is fundamentally different in several respects from infrared or optical spectroscopy. To begin with, the Boltzmann distribution for nuclear magnetic systems at temperatures greater than roughly 1°K is such that all Zeeman energy levels are very nearly equally populated. For a proton with a resonance frequency of 180 MHz in

a sample at 25°C, the ratio of the "ground" state $m=\frac{1}{2}$ population to the "excited" state $m=-\frac{1}{2}$ population is only 1.000029 (a far cry from the usual situation in vibrational or electronic systems of a populated ground state and essentially empty excited states). Since the magnetization to be detected is proportional to this population difference, effectively less than two nuclei in 10^5 contribute to the NMR signal.

A second difference between NMR and its higher-energy spectroscopic cousins is the relative rate of spontaneous and stimulated emission, most simply described by the Einstein coefficients A_{mn} and B_{mn} respectively [33,34]. The ratio A_{mn}/B_{mn} equals $8\pi h\nu^3/c^3$; the ν^3 factor implies that spontaneous emission is a vastly more important phenomenon in optical transitions than in NMR transitions. (If $\nu_{optical} = 6 \times 10^{14}$ Hz and $\nu_{NMR} = 200 \times 10^6$ Hz, then the ratio of the frequencies cubed is 2.7×10^{19}.) In fact, the effects of spontaneous emission in NMR can be essentially ignored. Absorption and stimulated emission are treated semiclassically with no explicit mention of photons.

1.5.2 Radio Frequency Hamiltonian

The static magnetic field in an NMR experiment merely lifts the degeneracy of spin eigenstates with different values of m. As in other forms of spectroscopy, a source of electromagnetic radiation is needed to induce transitions between levels. In NMR, the resonant radio-frequency (rf) irradiation is applied perpendicular to the static field and can be described semiclassically by the following time-dependent Hamiltonian [35,36]:

$$\mathcal{H}_{rf} = -2\gamma H_1 \cos\omega t \; I_x \tag{I.12a}$$

$$= -2\omega_1 \cos\omega t \; I_x \tag{I.12b}$$

$$= -\omega_1 \left(e^{i\omega t}+e^{-i\omega t}\right) I_x \quad . \tag{I.12c}$$

Here ω is the rf frequency, H_1 is the strength of the oscillating magnetic field, and ω_1 is the corresponding spin precession frequency. Typical values for ω_1 in a pulsed spectrometer are 30-120 kHz.

Mathematically and conceptually, it is easier to deal with a time-independent Hamiltonian. The standard technique is to switch from the laboratory frame of reference to one rotating about the z-axis at the rf frequency ω. In this rotating frame, one of the counter-rotating $e^{\pm i\omega t}$ components of $\mathcal{H}_{rf}$ will appear to stand still; the other will rotate with frequency 2ω and can almost always be ignored. Thus the rf Hamiltonian in the rotating frame is given simply by the following [35,36]:

$$\mathcal{H}^*_{rf} = -\omega_1 I_x \quad , \tag{I.13}$$

where the asterisk denotes the rotating frame.

The Zeeman Hamiltonian is also affected by the change in reference system. In the rotating frame, the transverse magnetization is seen to precess not at the Larmor frequency ω_0 but rather at frequency $\Delta\omega = \omega_0-\omega$. (For all experiments to be described here, we will be close to resonance with $\Delta\omega \ll \omega_0,\omega$.) The Zeeman

Hamiltonian in the rotating frame becomes

$$\mathcal{H}_z^* = -\Delta\omega\, I_z \quad .$$

Henceforth, we shall remain firmly rooted in that frame and so will discontinue the asterisk notation. Additionally, since the Larmor frequency has been replaced by a frequency offset, the expression "offset Hamiltonian" and $\mathcal{H}_{off}$ will be used interchangeably with Zeeman Hamiltonian and $\mathcal{H}_z$.

The rotating frame transformation is an example of a more general technique: rewriting a Hamiltonian in the so-called interaction representation [37] to eliminate large terms which give rise to simple but uninteresting time development. Such a transformation will usually modify other terms in the overall Hamiltonian. The general approach for $\mathcal{H} = \mathcal{H}_a + \mathcal{H}_b$ with $\|\mathcal{H}_a\| >> \|\mathcal{H}_b\|$ ($\|\ldots\|$ can be thought of simply as "the size of ...,"; more rigorously, $\|\mathcal{H}\| = [\mathrm{Tr}(\mathcal{H}^2)/N]^{\frac{1}{2}}$.) is to compute $\mathcal{H}_b' = e^{-i\mathcal{H}_a t}\, \mathcal{H}_b\, e^{i\mathcal{H}_a t}$. The time-independent or "secular" portion of $\mathcal{H}_b'$ is retained in the interaction representation [28]. The time-dependent, "non-secular" part of $\mathcal{H}_b'$ will not perturb energy levels to first order and can be ignored. This exclusion of time-dependent terms when $\mathcal{H}_a$ is the Zeeman Hamiltonian is known as the high-field approximation.

$\mathcal{H}_z$ and $\mathcal{H}_{rf}$ both describe the effect of external magnetic fields and both are under the control of the (competent) experimenter through his choice of magnet and rf parameters. The remaining terms describe forces at the molecular level and together comprise

what is called the internal Hamiltonian. To better understand $\mathcal{H}_{internal}$ is the motivation for most of NMR spectroscopy.

1.5.3 Chemical Shielding Hamiltonian

A nucleus in an atom or molecule is never exposed to the full force of the external static magnetic field. Instead, it is shielded to varying degrees by compensating magnetic fields which result from the motion of surrounding electrons. The degree of shielding depends on the orientation of the molecule with respect to the external field. As such, the chemical shielding (or chemical shift) for a given nucleus can be expressed in terms of the external field vector, the nuclear spin, and a Cartesian shielding tensor $\underset{\approx}{S}$ [28,29]:

$$\mathcal{H}_{cs} = -\gamma \, \underset{\sim}{H}_0 \cdot \underset{\approx}{S} \cdot \underset{\sim}{I} \quad . \tag{I.14}$$

With the static field along the z-axis and the high-field approximation, this simplifies to the following:

$$\mathcal{H}_{cs} = -\gamma \, H_0 \, S_{zz} \, I_z \equiv -\sigma_{zz} \, I_z \quad , \tag{I.15}$$

where $\underset{\approx}{\sigma} = \gamma \, H_0 \, \underset{\approx}{S}$. With a number of different nuclear sites,

$$\mathcal{H}_{cs} = -\sum_i \sigma_{zzi} \, I_{zi} \quad . \tag{I.16}$$

Note the similarity to the Zeeman offset Hamiltonian:

$$\mathcal{H}_{off} = -\Delta\omega\ I_z = -\sum_i \Delta\omega\ I_{zi} \quad . \tag{I.17}$$

The division into offset and chemical shielding terms of that portion of the total Hamiltonian proportional to an operator I_{zi} is arbitrary. Experimentally, the chemical shielding is measured relative to a reference compound (usually tetramethylsilane, TMS, for proton work). For computational purposes, it is often convenient to write $\mathcal{H}_{off}$ and $\mathcal{H}_{cs}$ such that the chemical shifts σ_{zzi} sum to zero.

The directional aspects of chemical shielding are most clearly understood when spherical tensors are used. The high-field approximation requiring $[\mathcal{H}_{cs}, I_z] = 0$ limits the sum of spherical tensor operators in Eq. I. to those terms with m=0. For a single nucleus,

$$\mathcal{H}_{cs} = c\{A_{00}\ T_{00} + A_{20}\ T_{20}\} \tag{I.18a}$$

$$= c\{\bar{A}\ T_{00} + [\ \frac{\sqrt{6}}{2}\ \delta\ \mathcal{D}^2_{00} + (\frac{1}{2}\ \eta\ \delta)(\mathcal{D}^2_{20} + \mathcal{D}^2_{-20})]T_{20}\} \ . \tag{I.18b}$$

With the substitutions $c = -\gamma$ and $\underset{\approx}{A} \equiv \underset{\approx}{S}$, plus the tensor and rotation matrix values from Table I.1 and I.2,

$$\mathcal{H}_{cs} = -\gamma\ H_0\{\bar{S} + \delta[\frac{3\cos^2\beta - 1}{2} + \frac{1}{2}\ \eta\ \sin^2\beta\ \cos 2\gamma]\}I_z \quad . \tag{I.19}$$

Replacing angles β and γ with the more familiar polar angles θ and ϕ (describing the orientation of the external field vector in the principal axis system of the chemical shielding tensor) and

substituting a few more variables, this becomes

$$\mathcal{H}_{cs} = - \{\bar{\sigma} + \sigma_o \, [(3 \cos^2\theta - 1) + \eta \sin^2\theta \cos 2\phi]\} I_z \quad . \qquad (I.20)$$

$\bar{\sigma}$ is the isotropic chemical shift, the quantity measured from a liquid sample (in which rapid molecular motion averages the angle-dependent terms to zero). For hydrogen in organic compounds, $\bar{\sigma}$ varies over a range of roughly 15 ppm of the resonance frequency [38]. In a magnet with proton resonance at 180 MHz, this translates to 2.7 kHz for protons and 420 Hz for deuterons. σ_o will be called the characteristic chemical shielding anisotropy; typical values are on the order of 0-10 ppm [39,40].

When the spin system of interest consists of nuclei with different shielding environments, then the overall chemical shielding Hamiltonian is composed of a sum of terms like Eq. I.20.

1.5.4 Quadrupole Hamiltonian

A nucleus with $I > 1/2$ is non-spherical and as such, its energy depends on its orientation relative to local electric field gradients. This interaction is described by the quadrupole Hamiltonian [29,41]:

$$\mathcal{H}_Q = \frac{eQ}{2\hbar I(2I-1)} \sum_{\alpha,\beta=1}^{3} V_{\alpha\beta} \, [\tfrac{3}{2} (I_\alpha I_\beta + I_\beta I_\alpha) - \delta_{\alpha\beta} \, \underset{\sim}{I}^2] \quad . \qquad (I.21a)$$

$$= \frac{eQ}{2\hbar I(2I-1)} \, \underset{\sim}{I} \cdot \underset{\approx}{V} \cdot \underset{\sim}{I} \quad . \qquad (I.21b)$$

where $\underset{\approx}{V}$, a traceless, symmetric second-rank tensor, characterizes the electric field gradients at the nucleus. (If the electric potential is ϕ, then $V_{xx} = \frac{\partial^2\phi}{\partial x^2}$, $V_{xy} = \frac{\partial^2\phi}{\partial x \partial y}$, etc.) e is the charge of the electron, and Q is the nuclear quadrupole moment, an intrinsic property of each type of nucleus. A positive value of Q indicates a prolate (football-like) shape; a negative value corresponds to an oblate (Frisbee-like) nucleus. Q for deuterium is 2.8×10^{-3} in units of 10^{-24} cm^2 (1 "barn"), rather small as such things go. (In comparison, the Q's for chlorine-35 and bromine-79 are -7.89×10^{-2} barn and 0.33 barn respectively.)

As with chemical shielding, it will be useful to rewrite $\mathcal{H}_Q$ in terms of spherical tensors. Because $\underset{\approx}{V}$ is traceless, V_{00} is zero; hence there is no isotropic component of the quadrupole interaction. Furthermore, in the high-field approximation (which is often not completely valid with regard to $\mathcal{H}_Q$--see section 2.12), we again limit the sum in Eq. I.7 to terms with m=0. With the conventional choice of writing "eq" for δ or $|V_{zz}|$ and once more replacing angles and γ with θ and ϕ, the quadrupole Hamiltonian becomes β

$$\mathcal{H}_Q = \frac{e^2qQ}{2\hbar I(2I-1)} \left[\frac{\sqrt{6}}{2} \mathcal{D}^2_{00} + \frac{1}{2}\eta \left(\mathcal{D}^2_{20}+\mathcal{D}^2_{-20}\right)\right] T_{20} \qquad \text{(I.22a)}$$

$$= \frac{e^2qQ}{8\hbar I(2I-1)} \left[(3\cos^2\theta-1) + \eta \sin^2\theta\cos 2\phi\right](3 I_z^2-\underset{\sim}{I}^2) \quad . \qquad \text{(I.22b)}$$

I=1 for deuterium and $\mathcal{H}_Q$ simplifies to

$$\mathcal{H}_Q = \frac{3e^2qQ}{8\hbar}\,[(3\cos^2\theta - 1) + \eta\sin^2\theta\cos 2\phi](I_z^2 - \tfrac{2}{3}) \tag{I.23a}$$

$$\equiv \omega_Q\,(I_z^2 - \tfrac{2}{3}) \quad , \tag{I.23b}$$

where

$$\omega_Q = \frac{3}{8}\,\frac{e^2qQ}{\hbar}\,[(3\cos^2\theta - 1) + \eta\sin^2\theta\cos 2\phi] \quad . \tag{I.24}$$

As a final variable, we will define (in Hz) the characteristic quadrupole frequency ν_{Qc}:

$$\nu_{Qc} = \frac{3}{8}\,\frac{e^2qQ}{h} \quad . \tag{I.25}$$

Values for ν_{Qc} are typically 5-70 kHz for deuterium in organic solids [40,42].

1.5.5 Direct Dipole-Dipole Hamiltonian

This term is the first of those we've considered that is not a single-spin Hamiltonian; rather it describes the direct magnetic dipole-magnetic dipole interaction between pairs of nuclei (one little magnet responding to the field of another). Written in terms of Cartesian tensors [28,29,43],

$$\mathcal{H}_D = \sum_{j}^{N} \sum_{<k}^{N} \hbar\gamma_j\gamma_k\, \underset{\sim}{I}_j \cdot \underset{\approx}{D}^{jk} \cdot \underset{\sim}{I}_k \quad . \tag{I.26}$$

For each pair of nuclei, the strength of the coupling (expressed

as elements of $\underset{\approx}{D}^{jk}$) is inversely proportional to the cube of r_{jk}, the distance between the nuclei, and depends also on the orientation of the internuclear vector relative to the magnetic field.

The transition to spherical tensors is uncomplicated, as $\underset{\approx}{D}^{jk}$ is traceless and the interaction is axially symmetric (η=0). Setting $\delta_{jk} = -2/r_{jk}^3$ and invoking yet again the high-field (m=0) approximation, $\mathcal{H}_D$ for a homonuclear collection of spins is given by the following [29,44]:

$$\mathcal{H}_D = \sum_{j<}^{N} \sum_{k}^{N} \hbar\gamma_j\gamma_k \frac{\sqrt{6}}{2} \delta_{jk} \mathcal{D}_{00}^2 (\Omega_{jk}) T_{20} \tag{I.27a}$$

$$= \sum_{j<}^{N} \sum_{k}^{N} \frac{1}{2} \frac{\hbar\gamma_j\gamma_k}{r_{jk}^3} (1-3\cos^2\theta_{jk})(3 I_{zj}I_{zk} - \underset{\sim}{I}_j \cdot \underset{\sim}{I}_k) \tag{I.27b}$$

$$= \sum_{j<}^{N} \sum_{k}^{N} \frac{\hbar\gamma_j\gamma_k}{r_{jk}^3} (1-3\cos^2\theta_{jk})[I_{zj}I_{zk} - \frac{1}{2}(I_{xj}I_{xk}+I_{yj}I_{yk})] \tag{I.27c}$$

$$\equiv \sum_{j<}^{N} \sum_{k}^{N} D_{jk} [I_{zj}I_{zk} - \frac{1}{2}(I_{xj}I_{xk}+I_{yj}I_{yk})] \tag{I.28}$$

$$= \sum_{j<}^{N} \sum_{k}^{N} D_{jk} [I_{zj}I_{zk} - \frac{1}{4}(I_{+j}I_{-k}+I_{-j}I_{+k})] \quad , \tag{I.29}$$

where θ_{jk} is the angle between the internuclear vector jk and the static field and $I_\pm = I_x \pm i\, I_y$. The definition here of D_{jk}, the dipolar coupling constant for spins j and k, is consistent with Meiboom and Snyder's usage [45], but unfortunately differs from

Diehl's definition [46]:

$$\text{this } D_{jk} = 2 \times \text{Diehl's } D_{jk} \quad . \tag{I.30}$$

For heteronuclear spins I and S, flip-flop terms such as $I_{+j}S_{-k}$ and $I_{-j}S_{+k}$ do not conserve energy in high field, so $\mathcal{H}_D$ must be further truncated:

$$\mathcal{H}_{D(\text{heteronuclear})} = \sum_j \sum_k D_{jk} I_{zj} S_{zk} \quad . \tag{I.31}$$

The angle-independent factor in D_{jk}, expressed in Hz, is $\frac{\hbar\gamma_j\gamma_k}{2\pi r_{jk}^3}$; for the interaction of two protons this becomes

$$\frac{120.067 \text{ kHz}}{[r_{jk}(\text{Å})]^3} \quad . \tag{I.32}$$

For a separation of 2.477 Å, the ortho H-H distance in benzene,

$$D_{jk} = (7.83)(1-\cos^2\theta_{jk})\text{kHz} \quad . \tag{I.33}$$

Such a coupling is reduced by molecular motion, as will be discussed in Chapter IV. For the rapid isotropic tumbling of normal liquids, the dipolar coupling has no effect on line positions or intensities since $\mathcal{H}_D$ contains no isotropic term.

1.5.6 Indirect Dipole-Dipole Hamiltonian

Indirect dipole-dipole coupling or J-coupling is the indirect interaction between magnetic nuclei mediated by the presence of

electrons. It can in general be written as follows [29]:

$$\mathcal{H}_J = \sum_{j<}^{N} \sum_{k}^{N} \underset{\sim}{I}_j \cdot \underset{\approx}{J}^{jk} \cdot \underset{\sim}{I}_k \quad . \tag{I.34}$$

This is similar to the previous expression for direct dipolar coupling (Eq. I.26), but $\underset{\approx}{J}$, unlike $\underset{\approx}{D}$, possesses a non-zero trace. Hence there is an isotropic component to J-coupling which is not averaged to zero by the rapid, isotropic molecular motion in liquids.

Invoking the high-field approximation and manipulating as in the previous section, one finds that [47]

$$\mathcal{H}_J = \sum_{j<}^{N} \sum_{k}^{N} J_{jk} \underset{\sim}{I}_j \cdot \underset{\sim}{I}_k + \sum_{j<}^{N} \sum_{k}^{N} J_{jk}^{aniso} [I_{zj} I_{zk} - \frac{1}{2} (I_{xj} I_{xk} + I_{yj} I_{yk})] \quad . \tag{I.35}$$

The anisotropic component of J_{jk} cannot be distinguished from a direct dipolar interaction (compare Eq.I.28) and furthermore is expected to be negligible for coupling between two hydrogens [48]. Thus we will assume that only the isotropic or scalar portion of the J-coupling is important and write

$$\mathcal{H}_J = \sum_{j<}^{N} \sum_{k}^{N} J_{jk} \underset{\sim}{I}_j \cdot \underset{\sim}{I}_k \quad . \tag{I.36}$$

The coupling constants J_{jk} are themselves small, on the order

of -20 to 20 Hz for protons [38]. In anisotropic phases, they are dwarfed by the direct dipole-dipole interactions. In liquids, however, they are the sole source of spin-spin coupling.

1.5.7 Other Terms

The most glaring omission in our overview of NMR interactions is any mention of relaxation effects. Relaxation is of course a fundamental and unavoidable aspect of spectroscopy, and several authors [13-18] have tackled its role in multiple-quantum NMR. Here, however, it will be almost completely ignored; for systems of interest (deuterium in solids, proton-bearing molecules in liquid crystal solvents), its effect on spectra is but a mild broadening, readily simulated by digital smoothing if desired. Only when a variant of a cw NMR experiment is analyzed (Chapter III) will relaxation be explicitly included in a calculation. Even then it will be treated phenomenologically using the Bloch equations [35].

Other Hamiltonian terms which have not been covered include spin-rotation coupling and antisymmetric chemical shielding components [29], but the effect of these terms is negligible on the types of spectra we will be considering.

1.6 The Density Matrix

When an appropriate set of basis functions has been chosen for the system of interest, each Hamiltonian discussed in the previous section can be written as a matrix, where the element $\mathcal{H}_{ab}$ (or $\langle a|\mathcal{H}|b\rangle$) is a measure of the overlap of state a with the result of operating $\mathcal{H}$ on state b. Another matrix, the density

matrix [37,49], is needed to describe the overall ensemble-averaged quantum-mechanical state of the system itself at each point in time. Because the density matrix formalism is central to all that transpires in the succeeding pages, a brief summary is perhaps in order.

Assume that the wavefunction ψ for a given isolated quantum-mechanical system can always be written as a linear combination of L basis functions ϕ_i:

$$\psi(t) = \sum_{i=1}^{L} c_i(t)\ \phi_i \tag{I.37}$$

The choice of states ϕ_i is arbitrary so long as they form a complete set. The L coefficients c_i, in general complex and time-dependent, can be used to fully describe the system. If we consider an ensemble of identical systems, as is appropriate for NMR, we need an ensemble-averaged description of the quantum mechanics. The ensemble-averaged expectation value of an operator F is given by

$$\begin{aligned} \langle\psi|F|\psi\rangle_{\text{ens.ave.}} &= \langle \sum_k c_k^* \phi_k |F| \sum_j c_j \phi_j \rangle_{\text{ens.ave.}} \\ &= \sum_j \sum_k \overline{c_j c_k^*}\ \langle\phi_k|F|\phi_j\rangle \\ &\equiv \sum_j \sum_k \overline{c_j c_k^*}\ F_{kj} \quad , \end{aligned} \tag{I.38}$$

where the bar indicates an ensemble average. A knowledge of all quantities $\overline{c_j c_k^*}$ suffices to calculate any <u>ensemble-averaged</u> expectation value. Hence these quantities are compiled in that most useful of constructs, the density matrix ρ, defined such that $\rho_{jk} = \overline{c_j c_k^*}$. The diagonal elements $\rho_{jj} = \overline{c_j c_j^*}$ describe ensemble-averaged populations of basis states ϕ_j and are always real numbers. Off-diagonal elements ρ_{jk} describe coherence between states ϕ_j and ϕ_k and are in general complex, each with a magnitude and phase in the complex plane. Since $\rho_{kj} = \rho_{jk}^*$, the density matrix is Hermitian.

Using the density matrix, it is simple to write the ensemble-averaged expectation value of an operator:

$$\langle F \rangle = \sum_j \sum_k \rho_{jk} F_{kj} = \mathrm{Tr}(\rho F) \quad . \tag{I.39}$$

The density matrix is thus the key to knowing what's going on in our ensemble of spin systems. The time dependence of ρ is given by the Liouville equation [20,21]:

$$\frac{d\rho}{dt} = i\,[\rho,\mathcal{H}] \quad . \tag{I.40}$$

If $\mathcal{H}$ is time-independent for an interval τ, this expression can be integrated to give

$$\rho(\tau) = e^{-i\mathcal{H}\tau}\,\rho(0)\,e^{i\mathcal{H}\tau} \tag{I.41}$$

(the most important equation for all that is to follow in this thesis). Quantum-mechanical evolution under a time-independent Hamiltonian is seen to be merely a unitary transformation of the density matrix.

A knowledge of evolution is not enough, however; we need to know also the initial equilibrium state of our ensemble of spin systems. Off-diagonal elements $\rho_{jk} = \overline{c_j c_k^*}$ are the averaged products of two different complex numbers; at equilibrium there is no reason to expect any special phase relationship, and hence off-diagonal elements are equal to zero (the random-phase hypothesis) [37]. Diagonal elements describing populations should at equilibrium satisfy a Boltzmann distribution:

$$(\rho_o)_{jj} = (\frac{1}{Z})\ e^{-E_j/kt} \quad , \tag{I.42}$$

or in operator form,

$$\rho_o = (\frac{1}{Z})\ e^{-\mathcal{H}/kT} \quad , \tag{I.43}$$

where Z is the partition function, the sum over all states of $e^{-\mathcal{H}/kT}$. It is traditional to first expand the exponential

$$\rho_o = (\frac{1}{Z})(\underset{\approx}{1} - \mathcal{H}/kT + \ldots) \quad , \tag{I.44}$$

and then realize that the spin-system energies described by this Hamiltonian are miniscule in comparison to kT for $T \gtrsim 1°K$,

(At T = 25°C, kT = 6.2×10^{12} Hz.) In the "high" temperature limit, therefore, one truncates the expansion:

$$\rho_o = (\frac{1}{Z})(\underset{\approx}{1} - \mathcal{H}/kT) \quad . \tag{I.45}$$

In this limit, Z is just the number of states in the system. If the system contains N spins of the same type with spin I, then $Z = (2I+1)^N$.

To simplify ρ_o further, recall that the Zeeman Hamiltonian $\mathcal{H}_z$ in the lab frame equals $-\omega_o I_z$ and is usually orders of magnitude larger than any other term in $\mathcal{H}$. Thus we can write

$$\rho_o = (\frac{1}{Z})(\underset{\approx}{1} + \omega_o I_z/kT) \quad . \tag{I.46}$$

Lastly we note that the unit matrix $\underset{\approx}{1}$ is unaltered by a unitary transformation and hence does not evolve. This excess baggage is therefore unceremoniously jettisoned, and ρ is re-defined as the <u>reduced</u> density matrix, with

$$\rho_o = \beta I_z \tag{I.47a}$$

and

$$\beta = (\frac{1}{Z})(\omega_0/kT) = (2I+1)^{-N}(\omega_0/kT) \quad . \tag{I.47b}$$

The reduced equilibrium density matrix in the rotating frame is also βI_z--the form of ρ_o is unchanged by the lab frame to rotating frame transformation [37].

1.7 The Basic Computational Approach

With the assumption that $\mathcal{H}$ is time-independent, determining the exact spin dynamics of a system of interest is equivalent to solving the matrix equation

$$\rho(t) = e^{-i\mathcal{H}t}\ \rho(0)\ e^{i\mathcal{H}t} \quad . \tag{I.48}$$

A brief outline of this procedure follows; more details can be found in Appendix D.

The first step is to set up the Hamiltonian as a matrix expressed in some convenient basis set--usually the set of spin-product states, e.g., $|++-\ldots+\rangle$. To calculate the propagator $e^{-i\mathcal{H}t}$ directly as a power series in $\mathcal{H}$ is possible only in special cases. In general, one first diagonalizes $\mathcal{H}$:

$$\mathcal{H} = U\ E\ U^{\dagger} \quad , \tag{I.49}$$

where E is a diagonal matrix of eigenvalues E_j and U is a unitary transformation matrix of column eigenvectors U_{*j} ($U^{\dagger}=U^{-1}$). An analytic solution for U and E using the secular equation $|\mathcal{H}-E_j\underset{\approx}{1}| = 0$ is possible and palatable for two- and three-level systems. More commonly, however, $\mathcal{H}$ is diagonalized numerically using a standard

algorithm [50,51]. (We have employed a Jacobi transformation program [52] that applies a series of unitary transformations on $\mathcal{H}$ to eliminate the largest remaining off-diagonal elements.)

Knowing U and E, one can then compute the propagator using the relationship

$$e^{-i\mathcal{H}t} = U\, e^{-iEt}\, U^{\dagger} \tag{I.50}$$

(see Appendix A). e^{-iEt} is diagonal with

$$(e^{-iEt})_{jj} = e^{-iEjt} \quad . \tag{I.51}$$

$\rho(t)$ is then given by the following:

$$\rho(t) = U\, e^{-iEt}\, U^{\dagger}\, \rho(0)\, U\, e^{iEt}\, U^{\dagger} \quad . \tag{I.52}$$

Mathematically, this expression is a series of matrix multiplications; physically it describes the transformation of $\rho(0)$ to the eigenbasis of $\mathcal{H}$, the simplified evolution of ρ in that basis, and then the transformation back to the original basis set.

If the Hamiltonian changes at a finite number of points during the evolution of ρ, the sequence of operations outlined above can be repeated for each step. If the Hamiltonian is time-dependent but periodic, an average Hamiltonian can be calculated using the Magnus expansion [23,24,53,54]. Alternately, a time-dependent Hamiltonian can be approximated by a string of time-independent

$\mathcal{H}_j$'s operating for very short intervals:

$$\mathcal{H}_j = \left(\frac{1}{\Delta t}\right)\int_{t_j}^{t_j+\Delta t} \mathcal{H}(t)\, dt \quad . \tag{I.53}$$

1.8 Assorted Thoughts

The past year has seen a veritable eruption of Pines group dissertations detailing the unfolding multiple-quantum saga [55-59]. Before plunging onward, I should perhaps describe the emphasis of this particular work. As the title suggests, I have dealt largely (though not entirely) with computer simulation of multiple-quantum processes. I like to think that I have succeeded in generating a somewhat better understanding of such phenomena as well as a glut of numbers, that the computer and I have sallied forth as Douglas Hofsteder has described this type of exploration [60]:

> It is a kind of experimental mathematics, in which the digital computer plays the role of Magellan's ship, the astronomer's telescope, and the physicist's accelerator. ... This way of doing mathematics builds powerful visual imagery and intuitions directly into one's understanding.

To continue in this philosophic vein, I would also like to note that the study of multiple-quantum spectroscopy using computers also gives rise to its own set of images and insights which complement those associated with experimentation or theoretical analysis. For one thing, the density matrix is seen

as no mere Greek symbol but rather as an actual matrix of numbers, a matrix whose elements depend critically on the basis set in use. Similarly, the physical concept of eigenstates becomes less important; instead the computer-adapted mind deals with the square arrays of unitary transformation matrices. Finally, the creation of multiple-quantum coherence is seen not as spikes on an oscilloscope screen or extra terms in an equation, but rather as a flow of coherence from the density matrix diagonal out into the normally forbidden and thus arid reaches of the matrix. As the system approaches the long-time "statistical limit" (see Chapter V), one can imagine this outward rush slowing into a gentle lapping of coherence waves as the matrix "levels off".

Lastly some thoughts on terminology. The power, elegance, and flexibility of pulsed NMR techniques are enough to inspire a search for some descriptive encompassing phrase. Mehring [23] has suggested "spin engineering", but this seems lacking in pizzazz. Others have put forth "spin gymnastics", yet this term tends to evoke the exploits of a single nucleus rather than an ensemble of them. To fully capture the sense of a vast sea of nuclei flipping and cavorting as the experimenter so desires, I propose ... "spin choreography".

CHAPTER II

DEUTERIUM DOUBLE-QUANTUM NMR IN SOLIDS

2.1 Introduction

Models play an important role in quantum mechanics. The harmonic oscillator, the particle in a box, and the hydrogen atom are conceptual building blocks with which more complicated problems can be understood. Similarly, the two-level system (as exemplified by a single spin-$\frac{1}{2}$ nucleus) introduces a vector description of the density matrix which can be used to explain a wide range of time-dependent spectroscopic phenomena: coherence evolution, spin echoes, population inversion, adiabatic demagnetization, etc. Feynman, Vernon, and Hellwarth in a famous paper [61] have generalized this two-level model beyond the bounds of NMR to a variety of spectroscopic applications.

In this chapter, the dynamics of a three-level system will be discussed. As the simplest system in which multiple-quantum coherence can occur, it serves as a prototype for the tangled networks of MQ coherence to be considered later. Moreover, a description of the quantum mechanics can be made very physically intuitive: an expansion of the density matrix as a linear combination of conveniently commuting operators simplifies the mathematics and generates a real "feel" for the effect of each term in the Hamiltonian. As such, the three-level system will perhaps take its place in quantum mechanics and spectroscopy texts as another "building block" of physics.

The particular three levels of interest in this chapter are those of a spin-one nucleus, specifically a deuteron. In the absence of applied rf fields, its Hamiltonian in the laboratory frame is simply

the sum of a Zeeman and a quadrupole term:

$$\mathcal{H} = \mathcal{H}_z + \mathcal{H}_Q = -\omega_0 I_z + \omega_Q (I_z^2 - \tfrac{2}{3}) \quad . \tag{II.1}$$

($\mathcal{H}_Q$ as written describes the first-order quadrupole shift; second-order effects will be considered later.) The energy levels of the three spin states are as follows:

$$\begin{aligned} m &= 1 & E_1 &= -\omega_0 + \tfrac{1}{3}\omega_Q \\ m &= 0 & E_0 &= -\tfrac{2}{3}\omega_Q \\ m &= -1 & E_{-1} &= \omega_0 + \tfrac{1}{3}\omega_Q \quad . \end{aligned} \tag{II.2}$$

These are illustrated in Fig. II.1, which also depicts the "cigar-shaped" deuterium nucleus.

When we jump aboard the rotating frame, the Hamiltonian becomes

$$\mathcal{H} = -\Delta\omega I_z + \omega_Q (I_z^2 - \tfrac{2}{3}) \quad , \tag{II.3}$$

where here we will not attempt to separate $\Delta\omega$ into a chemical shift and a deliberate frequency offset. The energies of this Hamiltonian are $E_1 = -\Delta\omega + \omega_Q/3$, $E_0 = -2\,\omega_Q/3$, and $E_{-1} = \Delta\omega + \omega_Q/3$. That the frequency of the double-quantum (DQ) transition between E_1 and E_{-1} equals $2\,\Delta\omega$ (and thus is independent of the quadrupole splitting) is crucial for much of what evolves in this chapter. Indeed, the fundamental experiment of interest is as follows. (1) Create a state of double-quantum coherence, a quantum-mechanical superposition of

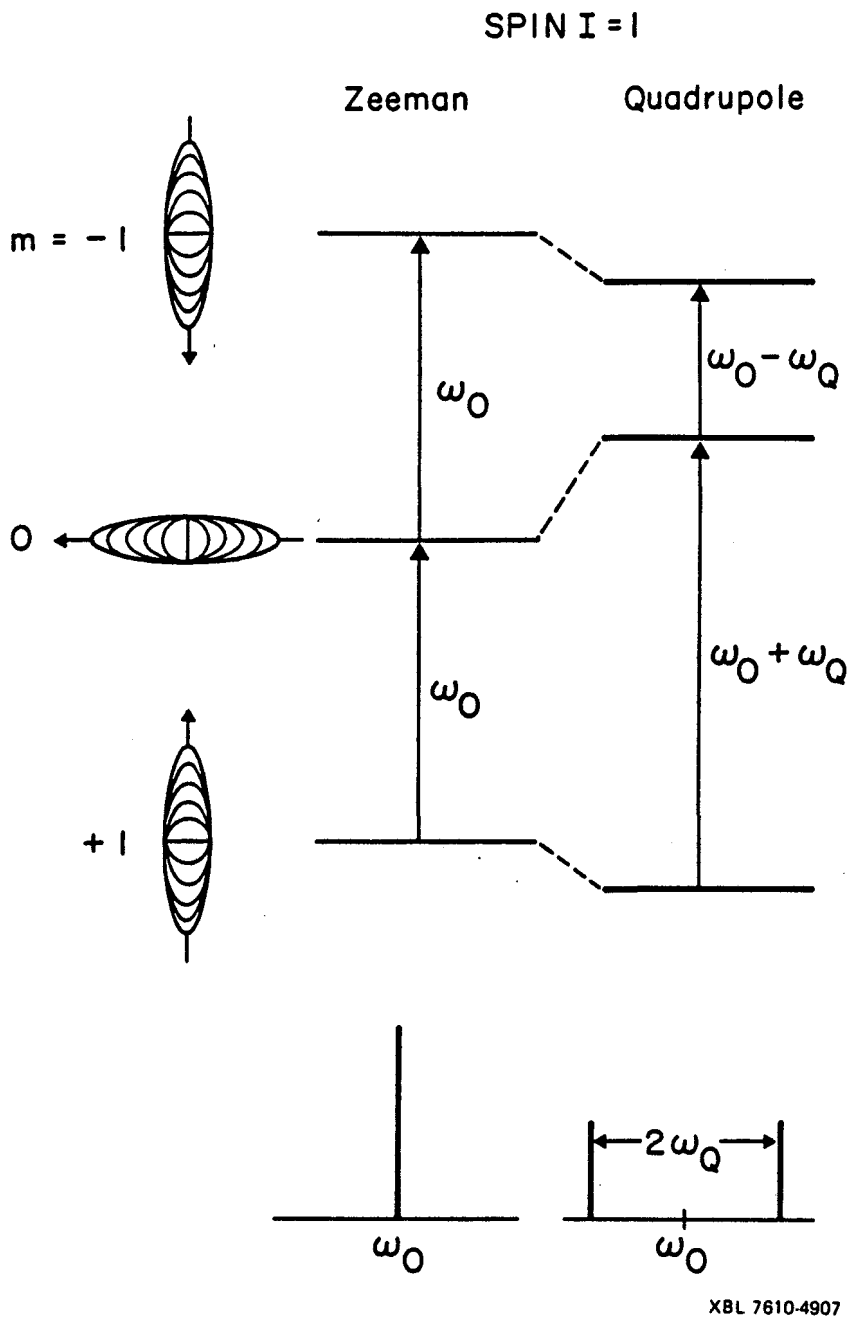

Figure II.1 Deuterium energy levels in the laboratory frame, along with the corresponding single-quantum spectra. It is assumed that the quadrupole shifts are a small perturbation of the Zeeman interaction.

states $|1\rangle$ and $|-1\rangle$ which does not average to zero over the sample. Both the rf Hamiltonian and the quadrupole Hamiltonian must be called upon to prepare this state. (2) Let the double-quantum coherence evolve at the frequency $2\,\Delta\omega$. This evolution is not directly observable; only single-quantum coherence gives rise to a macroscopic transverse magnetization detectable by the current it induces in the NMR coil. (An alternate explanation is that only single-quantum coherence can emit dipolar radiation.) (3) Apply additional rf pulses to transfer double-quantum coherence into single-quantum coherence that can be detected. By incrementing the DQ evolution time and Fourier transforming with respect to it, the double-quantum spectrum is obtained.

Before we plunge into a detailed analysis of the experiment, however, a brief description of applications and a bit of three-level history will be presented.

2.2 An Outline of Previous Work

A number of groups have probed and prodded three-level systems with FT-NMR since the mid-1970's. Among the most prolific have been Hatanaka, Hashi, and co-workers [62], who have performed the double-quantum analogs to a wide variety of conventional single-quantum NMR experiments. Using three of the six spin states of aluminum in Al_2O_3, they have observed double-quantum FID's, spin echoes, coherence transfer echoes, transient nutations, rotary echoes, spin locking, spin-locked echoes, and rotary saturation.

My Pines group colleagues, Shimon Vega and Tom Shattuck, investigated double-quantum cross-polarization and made the first practical use of Fourier transform DQ spectroscopy in the determination

of deuterium chemical shielding tensors [63a,b]. The shielding measurements were continued and expanded upon by Dave Wemmer [40]. Meanwhile, Vega and Pines reported the first observations of DQ spin locking [64] and presented an operator formalism that greatly facilitated analysis of three-level spin dynamics [65]. A revised set of operators was later developed by Vega [66] and independently by Wokaun and Ernst [67].

Along a second Berkeley axis of activity, Dave Gold and Erwin Hahn used three of the four sodium spin states in a single crystal of $NaNO_3$ as their three-level NMR domain [68]. They verified the form of the Brewer-Hahn equations [69] developed earlier for optical phenomena and studied the DQ analogs to spin locking, rotary saturation, and adiabatic fast passage. They also considered the effect of the fourth sodium state on these results and observed the three-quantum transition in a steady-state experiment.

The Volds and fold at San Diego [15,16] have studied the deuterium DQ spectra of small molecules dissolved in liquid crystal solvents; the lack of rotational isotropy in these ordered phases gives rise to non-zero quadrupole splittings. (See Chapter IV.) Their emphasis has been on the measurement of relaxation parameters in order to better determine the spectral densities of molecular motion. In other liquid crystal work, Hsi, Zimmerman, and Luz [70] have used the DQ spectra of isotopically substituted deuterons to investigate the ordering and motion of methylene chains. Hoatson and Packer, on the other hand, have used a deuteron in a lyotropic liquid crystal as their laboratory for testing various double-quantum pulse sequences [71].

In a very elegant study, Stoll, Wolff, and Mehring [72] applied the technique of NMR interferometry developed initially by Stoll, Vega, and Vaughan [14] to the three levels of deuterium in a d_{18}-hexamethylbenzene single crystal. They demonstrated that any pair of spin states, including the double-quantum pair $|+1\rangle$ and $|-1\rangle$, have spinor character when irradiated: a rotation of 2π causes wavefunctions to change sign. Fictitious spin-$\frac{1}{2}$ systems are thus fermions just like real spin-$\frac{1}{2}$ systems. Moreover, by varying the relative irradiation power at the two single-quantum frequencies, the authors were able to proceed continuously from an effective two-level system to a full three-level system with a corresponding continuous change in rotational symmetry from 4π to 2π. (Like a Cheshire cat, the middle state changes from a virtual to an actual intermediate.) The authors also detailed the variety of fictitious spin-$\frac{1}{2}$ frames present and pointed out the curious analogy between I=1 spin states and quarks.

The preceding is only a partial list of activities; further references can be found in the review article by Bodenhausen [10].

2.3 An Actual, Although Tenuous, Link to Chemistry

2.3.1 We Gaze Upon the Deuteron: Two-Quantum Yielding the Chemical Shielding

One of the most useful applications of NMR spectroscopy to the study of solids is the determination of chemical shielding tensors. Information gained on the distribution of electron density around the probe nucleus is difficult to obtain by other techniques. Moreover, accurately measured values of shielding anisotropies constitute a real acid test of orbital calculations, a means of separating good theory

from bad. In addition to what can be learned regarding structure and bonding, the extent, the symmetry, and even the mechanism of molecular motion can be revealed in shielding lineshapes and their temperature dependence [40].

Unfortunately, chemical shielding effects are usually masked by other spin interactions, so the perspicacious spectroscopist must weed out unwanted terms in his Hamiltonian; these include heteronuclear and homonuclear dipolar couplings, plus quadrupolar splittings when $I > \frac{1}{2}$. Different nuclei can be treated in different ways. For those with either small gyromagnetic ratios or low isotopic abundance (two chemically interesting examples are carbon-13 and silicon-29), homonuclear dipolar interactions are not a problem. High-powered decoupling of heteronuclei (most commonly protons) plus cross-polarization to improve sensitivity can be used most successfully in the pursuit of shielding tensors [23].

For protons and fluorines, however, the existence of sizeable homonuclear dipolar couplings entails more elaborate techniques. One option is the multiple pulse spin-space-averaging approach of WAHUHA and its complicated progeny [24], but the instrumental requirements in terms of pulse power, pulse accuracy, and pulse timing are formidable and set the heart to yearning for a simpler procedure.

Such yearning was soothed in 1976 when Vega, Shattuck, and Pines [63a] proposed the following alternative for investigation of hydrogen shielding tensors. First one isotopically substitutes deuterium for protons at a concentration of a few percent in chemical sites of interest. The deuterium NMR signal will not be plagued by homonuclear

dipolar couplings since the dilute deuterium nuclei will, on average, be far away from each other. Interaction with protons can be eliminated in turn by straightforward proton decoupling. Of course, the use of deuterium introduces a new source of broadening--the quadrupole splitting--but this impediment is overcome by exciting the double-quantum transition; as noted earlier, its frequency to first order depends only on $\Delta\omega$ and hence on the chemical shift. Idealized deuterium single-quantum and double-quantum lineshapes associated with a powdered sample are illustrated in Fig. II.2.

A number of shielding tensors have been studied using this DQ technique, including oxalic acid dihydrate [63a,b], plus benzene, p-methoxybenzoic acid (deuterated at the acid position), ferrocene, barium chlorate monohydrate, and hexamethylbenzene (all these described in Ref. 40). Measured values of the chemical shielding anisotropies agree well with the results of proton multiple pulse work [23,24].

2.3.2 Single Crystals vs. Powders

In the quest for chemical shielding data, one often has the choice of examining either a single crystal or a powdered sample. There are advantages and disadvantages to each. Only with single crystals, for example, can the orientation of the shielding tensor in general be established relative to the molecular framework. Single-crystal rotation experiments, however, are tedious, time-consuming, and often complicated by multiple molecular orientations in the unit cell. Moreover, many substances cannot be readily crystallized. This chapter will therefore focus largely on the line-shapes associated with powder spectra. Although the orientation of tensor principal axes cannot in general be learned with this approach

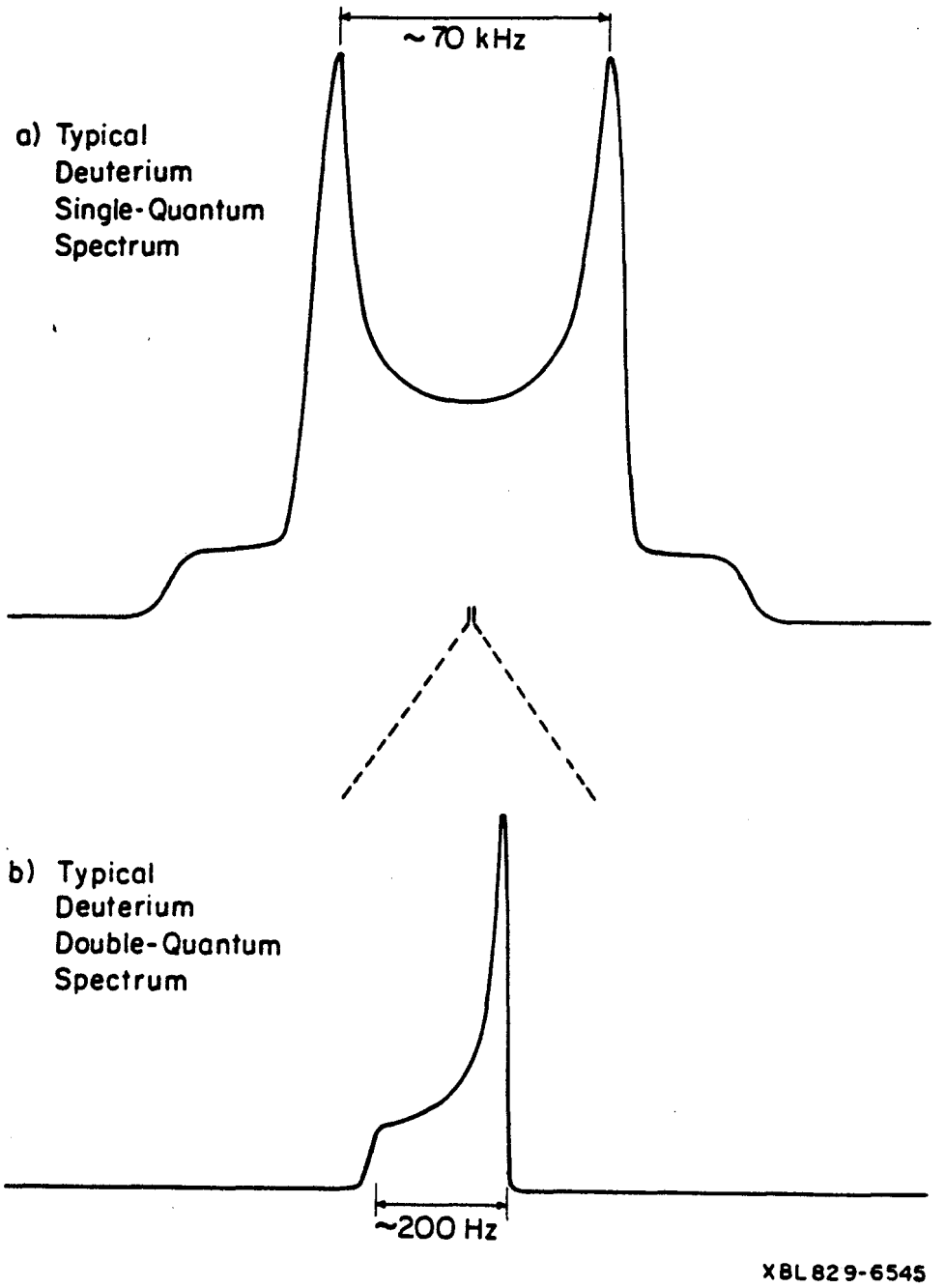

Figure II.2 Idealized deuterium powder spectra, with shielding anisotropies and quadrupole shifts appropriate for rotating ferrocene or benzene rings (σ_o=-2 ppm, ν_{Qc}=36 KHz, η_{cs}=η_Q=0, ν_o=28.4 MHz). The single-quantum spectrum features a quadrupole powder lineshape; the much more narrow chemical shielding lineshape appears in the DQ spectrum. Pulse sequence distortions are not included in either case.

(unless dictated by molecular symmetry or motion), the principal values of the chemical shielding tensor are readily determined from the discontinuities in the lineshape (Fig. II.3).

From Eq. I.20, an expression for the angular dependence of the chemical shielding can be written as follows:

$$\sigma = \bar{\sigma} + \sigma_0 \, [(3 \cos^2\theta - 1) + \eta_{cs} \sin^2\theta \cos 2\phi] \quad . \qquad \text{(II.4)}$$

The principal values of $\underset{\approx}{\sigma}$ are $\sigma_{xx} = \bar{\sigma} - \sigma_0 \, (1 + \eta_{cs})$, $\sigma_{yy} = \bar{\sigma} - \sigma_0 \, (1 - \eta_{cs})$, and $\sigma_{zz} = \bar{\sigma} + 2\sigma_0$. When $\eta_{cs} = 0$, the unbroadened powder lineshape has an edge of infinite intensity at $\sigma_{\perp} = \sigma_{xx} = \sigma_{yy}$ (the unique principal axis perpendicular to H_0) and a "normal" edge at $\sigma_{||} = \sigma_{zz}$ (the unique axis parallel to H_0). The width of the lineshape is $\Delta\sigma = \sigma_{||} - \sigma_{\perp} = 3\sigma_0$. When $\eta_{cs} \neq 0$, the edges of the powder lineshape lie at σ_{xx} and σ_{zz} with an interior discontinuity at σ_{yy}. The width is given by $\Delta\sigma = \sigma_{zz} - \sigma_{xx} = (3 + \eta_{cs})\sigma_0$.

As a follow-up to the pioneering efforts of Shattuck, Vega, and Wemmer, the work described in this chapter will deal mostly with computer simulation and optimization of DQ pulse sequences and their effect on chemical shielding powder lineshapes. A new model for spin-one evolution and a few experimental results will also be presented.

2.4 Operator Assistance for Studying Spin-System Evolution

A desire for chemical shielding data is only one reason for investigating the spin dynamics of a deuteron. A more basic motivation is that the details of spin evolution are fascinating in their own right, independent of any chemical applications. Much

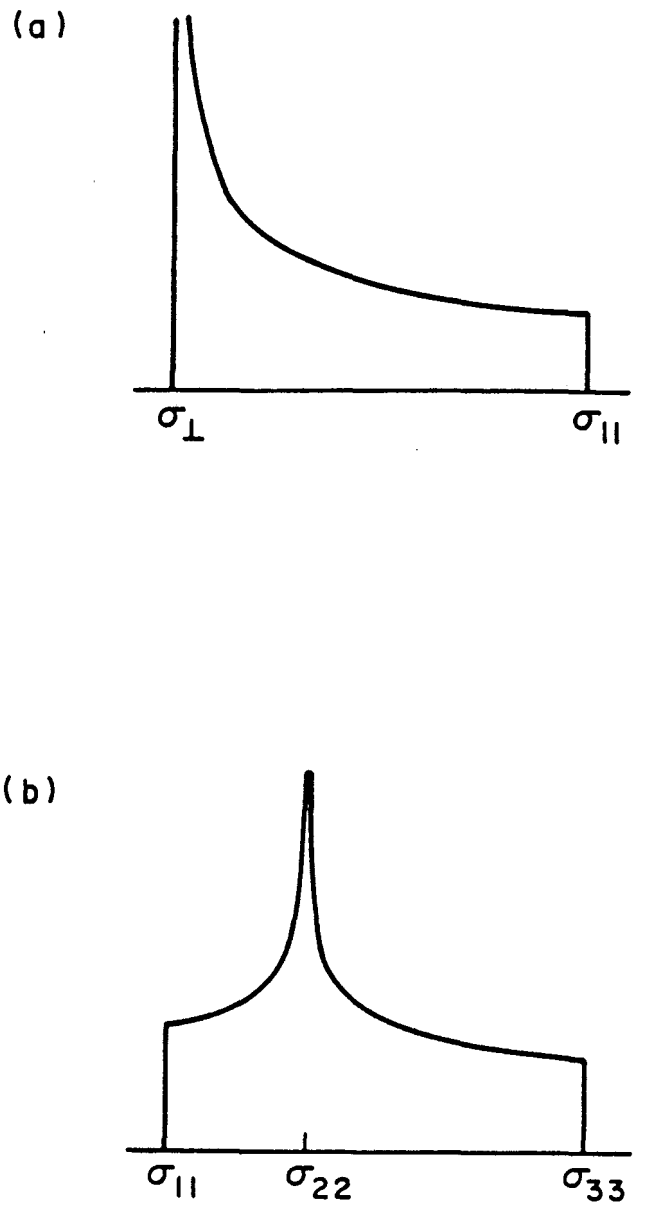

XBL 763-713

Figure II.3 Chemical shielding powder lineshapes. (a) An axially symmetric tensor (η_{cs}=0). (b) The general case of $\eta_{cs}\neq 0$.

of the aesthetics is associated with an operator formalism that can be used to describe the Hamiltonian and the density matrix. Before presenting this approach in terms of three levels, however, let us review the properties of the more familiar two-level system.

2.4.1 Starting Small: A Look Back at Two Levels

Where else to begin but the rotating frame Hamiltonian? In the general case of an offset frequency $\Delta\omega$ and rf irradiation of intensity ω_1 and phase ϕ, we have

$$\mathcal{H} = -\Delta\omega\, I_z - \cos\phi\, \omega_1\, I_x - \sin\phi\, \omega_1\, I_y \tag{II.5a}$$

$$\equiv -(\omega_z\, I_z + \omega_x\, I_x + \omega_y\, I_y) \quad . \tag{II.5b}$$

The second equation emphasizes that $\mathcal{H}$ can be expressed as a linear combination of the angular momentum operators I_x, I_y, and I_z. As a reminder, the form of these operators in the $\{|\frac{1}{2}\rangle, |-\frac{1}{2}\rangle\}$ basis set of a single spin-$\frac{1}{2}$ nucleus is as follows [73]:

$$I_x = \frac{1}{2}\begin{pmatrix} 0 & 1 \\ 1 & 0 \end{pmatrix}, \quad I_y = \frac{1}{2}\begin{pmatrix} 0 & -i \\ i & 0 \end{pmatrix}, \quad I_z = \frac{1}{2}\begin{pmatrix} 1 & 0 \\ 0 & -1 \end{pmatrix} \quad . \tag{II.6}$$

The reduced density matrix (see section 1.6) can also be written at all times as a linear combination of operators I_x, I_y, and I_z with real coefficients:

$$\rho(t) = \beta(a_x(t)\, I_x + a_y(t)\, I_y + a_z(t)\, I_z) \quad . \tag{II.7}$$

In other words, three operators span the "spin space" of a single $I = \frac{1}{2}$ nucleus. (In general, the constraint that ρ be hermitian and traceless implies that K^2-1 linearly independent operators are needed to fully describe a KxK density matrix.)

The most important advantage of this operator expansion is that ρ can be displayed geometrically as a vector with components a_x, a_y, and a_z. Moreover, there exists a beautiful and exact analogy between this "state-of-the-system" vector in spin space and the macroscopic magnetization vector $\underset{\sim}{M}$ in real space:

$$\underset{\sim}{M} = M_x\,\hat{x} + M_y\,\hat{y} + M_z\,\hat{z} \qquad \text{(II.8a)}$$

$$\equiv M_o(a_x\,\hat{x} + a_y\,\hat{y} + a_z\,\hat{z}) \quad . \qquad \text{(II.8b)}$$

A second advantage is that the evolution of ρ can be calculated by making use of the angular momentum commutation rules of Eq. I.2c or more conveniently by using the following simple formulas [73]:

$$e^{-i\theta I_p}\, I_p\, e^{i\theta I_p} = I_p \quad , \qquad \text{(II.9a)}$$

$$e^{-i\theta I_p}\, I_q\, e^{i\theta I_p} = \cos\theta\, I_q + \sin\theta\, I_r \quad , \qquad \text{(II.9b)}$$

$$e^{-i\theta I_p}\, I_r\, e^{i\theta I_p} = \cos\theta\, I_r - \sin\theta\, I_q \quad , \qquad \text{(II.9c)}$$

where p, q, and r represent x, y, and z or cyclical permutations thereof. Each of these expressions describes a rotation; indeed, $e^{\pm i\theta I_p}$ is the generator of rotations about the p-axis. The density

matrix evolution equation

$$\rho(t) = e^{-i\mathcal{H}t}\ \rho(0)\ e^{i\mathcal{H}t} \tag{II.10}$$

is itself the prescription for a rotation of the density matrix vector (a_x, a_y, a_z) about the Hamiltonian vector $(\omega_x, \omega_y, \omega_z)$ in spin space, or a rotation of the magnetization about the effective rotating-frame magnetic field in real space.

One quick run through the mathematics of Eq. II.10 will get us in the mood for manipulations to come. The Hamiltonian of Eq. II.5b describes rotation about three separate axes, but this is equivalent to a single rotation about the vector $(\omega_x, \omega_y, \omega_z)$. To express $\mathcal{H}$ in that simplified form, we must apply two successive transformations, one involving the rf phase angle ϕ, the other involving an angle $\theta = \tan^{-1}(\omega_1/\Delta\omega)$:

$$\mathcal{H}' = e^{i\phi I_z}\ \mathcal{H}\ e^{-i\phi I_z}$$

$$= -(\Delta\omega\ I_z + \omega_1\ I_x) \quad , \tag{II.11}$$

$$\mathcal{H}'' = e^{i\theta I_y}\ \mathcal{H}'\ e^{-i\theta I_y}$$

$$= -\omega_{eff}\ I_z \quad . \tag{II.12}$$

The primes and double-primes refer to transformed Hamiltonians and

$$\omega_{eff} = [\Delta\omega^2 + \omega_1{}^2]^{1/2} \quad . \tag{II.13}$$

Of course, if $\mathcal{H}$ is transformed, ρ must be too. Defining a transformation matrix $R = e^{-i\phi I_z} e^{-i\theta I_y}$, we can write

$$\rho(t) = e^{-i\mathcal{H}t}\ \rho(0)\ e^{i\mathcal{H}t}$$

$$= R\ e^{-i\mathcal{H}'t}\ R^{\dagger}\ \rho(0)\ R\ e^{i\mathcal{H}'t}\ R^{\dagger}$$

$$= R\ \exp(i\ \omega_{eff}\ t\ I_z)[R^{\dagger}\ \rho(0)\ R]\ \exp(-i\ \omega_{eff}\ t\ I_z)R^{\dagger} \quad . \tag{II.14}$$

Each successive transformation of $\rho(0)$ involves rotation by a single angular momentum operator; because $\rho(0)$ is itself a linear combination of these operators, solving for $\rho(t)$ merely entails repeated use of Eqs. II.9a-II.9c.

So much for the evolution of a two-level system--now on to bigger game ... .

2.4.2 The Three-Level Circus

With the addition of an rf term (assumed for now to be aligned with the x-axis of the rotating frame), the Hamiltonian of Eq. II.3 becomes

$$\mathcal{H} = -\ \Delta\omega\ I_z - \omega_1\ I_x + \omega_Q\ (I_z^{\ 2} - \tfrac{2}{3}) \quad . \tag{II.15}$$

When the quadrupole splitting is zero, $\mathcal{H}$ is the same as for the two-level system, and ρ is again a linear combination of I_x, I_y, and I_z. In general, however, $\omega_Q \neq 0$ and evolution is more involved and more interesting. The presence of a bilinear operator ($I_z^{\ 2}$) in $\mathcal{H}$ insures

that $\exp(-i\mathcal{H}t)\ \rho\ \exp(i\mathcal{H}t)$ cannot describe the simple rotation of a density matrix vector in three dimensions. Indeed, an operator expansion of $\rho(t)$ can no longer be limited to three linearly independent terms; at least $3^2-1 = 8$ operators are needed to span the 3x3 density matrix.

As to which operators should be used in this expansion, the choice is arbitrary: convenience, simplicity, and generality are the deciding criteria. Two sets have been presented in the literature. The first was developed by Shimon Vega [74] originally for the analysis of pure NQR spectra of nitrogen-14 and later applied to spin-one NMR [65]. This set of nine operators $I_{p,i}$ ($p \equiv x,y,z$; $i \equiv 1,2,3$; one linear dependence in that $I_{x,3} + I_{y,3} + I_{z,3} = 0$) will be discussed at great length in the pages to come. Subsequently Vega [66] as well as Wokaun and Ernst [67] recast the spin-one problem in terms of a second set of operators. For each pair of states $|j\rangle$ and $|k\rangle$ they defined fictitious spin-$\frac{1}{2}$ operators I_x^{j-k}, I_y^{j-k}, and I_z^{j-k}:

$$I_x^{j-k} = \frac{1}{2}\,[\,|j\rangle\langle k| + |k\rangle\langle j|\,] \quad ,$$

$$I_y^{j-k} = -\frac{i}{2}\,[\,|j\rangle\langle k| - |k\rangle\langle j|\,] \quad ,$$

$$I_z^{j-k} = \frac{1}{2}\,[\,|j\rangle\langle j| - |k\rangle\langle k|\,] \quad , \qquad \text{(II.16)}$$

with $I_x^{k-j} = I_x^{j-k}$, $I_y^{k-j} = -I_y^{j-k}$, $I_z^{k-j} = -I_z^{j-k}$, and the following commutation relationships:

$$[I_p^{j-k}, I_q^{j-k}] = i\, I_r^{j-k} \qquad (p,q,r \equiv x,y,z;\ y,z,x;\ z,x,y)\ ,$$

$$[I_x^{j-k}, I_x^{\ell-k}] = [I_y^{j-k}, I_y^{\ell-k}] = \frac{i}{2}\, I_y^{j-\ell}\ ,$$

$$[I_z^{j-k}, I_z^{\ell-k}] = 0\ ,$$

$$[I_x^{j-k}, I_y^{\ell-k}] = \frac{i}{2}\, I_x^{j-\ell}\ ,$$

$$[I_x^{j-k}, I_z^{\ell-k}] = -\frac{i}{2}\, I_y^{j-k}\ ,$$

$$[I_y^{j-k}, I_z^{\ell-k}] = \frac{i}{2}\, I_x^{j-k}\ . \qquad \text{(II.17)}$$

As there are three ways of choosing two states in a spin-one system, the total number of operators is again nine, with one linear dependence: $I_z^{1-0} + I_z^{0-(-1)} = I_z^{1-(-1)}$. Not surprisingly, these fictitious spin-$\frac{1}{2}$ operators are most useful when the spin-one system most resembles a real spin-$\frac{1}{2}$ system; that is, when one level can be largely ignored. This is the case, for example, when the system is irradiated at one of the single-quantum frequencies ($\Delta\omega \approx \pm\, \omega_Q$) or when the double-quantum transition is excited. If both single-quantum transitions must be considered simultaneously, however, the operator expressions become somewhat awkward. In contrast, the $I_{p,i}$ operators are admirably suited for any sort of coherence when $\Delta\omega \approx 0$ but prove to be unwieldy when $\Delta\omega \approx \omega_Q$.

The two sets of operators differ also in their applicability to other, more complicated systems. The newer formalism is the more general and has been used in the description of density matrices for

a spin-$\frac{3}{2}$ particle and for two coupled spin-$\frac{1}{2}$ nuclei [66,67]. The $I_{p,i}$ operators are not readily adapted to anything but the three-level system; nonetheless, it is this set of operators that will be used here--mostly for the sake of familiarity but also because they <u>are</u> the more useful formalism for the $\Delta\omega \approx 0$ experiments we will consider.

2.4.3 The World According to $I_{p,i}$ Operators

From this point onward, our analysis of the three-level system will be couched entirely in terms of the following linear and bilinear angular momentum operators [65]:

$$I_{x,1} = \frac{1}{2} I_x \quad , \qquad I_{z,1} = \frac{1}{2} I_z \quad ,$$

$$I_{x,2} = \frac{1}{2} (I_y I_z + I_z I_y) \quad , \qquad I_{z,2} = \frac{1}{2} (I_x I_y + I_y I_x) \quad ,$$

$$I_{x,3} = \frac{1}{2} (I_z^2 - I_y^2) \quad , \qquad I_{z,3} = \frac{1}{2} (I_y^2 - I_x^2) \quad . \qquad \text{(II.18)}$$

$$I_{y,1} = \frac{1}{2} I_y \quad ,$$

$$I_{y,2} = \frac{1}{2} (I_z I_x + I_x I_z) \quad ,$$

$$I_{y,3} = \frac{1}{2} (I_x^2 - I_z^2) \quad ,$$

In addition, we will for convenience define

$$I_{xy,3} = I_{x,3} - I_{y,3} = \frac{1}{2}\,[3\,I_z^{\,2} - 2] \quad ,$$

$$I_{yz,3} = I_{y,3} - I_{z,3} \quad ,$$

$$I_{zx,3} = I_{z,3} - I_{x,3} \quad . \tag{II.19}$$

The Hamiltonian of Eq. II.15 in its new incarnation becomes

$$\mathcal{H} = -2\Delta\omega\, I_{z,1} - 2\omega_1\, I_{x,1} + \frac{2}{3}\,\omega_Q\,(I_{x,3} - I_{y,3}) \quad ; \tag{II.20}$$

we will examine its effect on the system shortly. First, however, a closer look at the operators themselves is warranted. They are most neatly expressed in terms of a basis set $\{|x\rangle, |y\rangle, |z\rangle\}$ where

$$|x\rangle = -\frac{i}{\sqrt{2}}\,[\,|1\rangle - |-1\rangle] \quad , \tag{II.21a}$$

$$|y\rangle = \frac{1}{\sqrt{2}}\,[\,|1\rangle + |-1\rangle] \quad , \tag{II.21b}$$

$$|z\rangle = |0\rangle \quad . \tag{II.21c}$$

The matrix form of the operators in this basis set can be found in Table II.1. Additional Vega-tables summarize their commutation and rotation properties and present the matrix form of the exponential operators $\exp(-i\theta\, I_{p,i})$. Note that rotations which involve the three operators $I_{p,1}$, $I_{p,2}$, and $I_{p,3}$ of the p-frame (p = x, y, or z) occur with twice the intrinsic angular frequency of rotations

$$I_{x,1} = \frac{1}{2} I_x \qquad \frac{1}{2}\begin{pmatrix} 0 & 0 & 0 \\ 0 & 0 & 1 \\ 0 & 1 & 0 \end{pmatrix}$$

$$I_{x,2} = \frac{1}{2}(I_y I_z + I_z I_y) \qquad \frac{1}{2}\begin{pmatrix} 0 & 0 & 0 \\ 0 & 0 & -i \\ 0 & i & 0 \end{pmatrix}$$

$$I_{x,3} = -\frac{1}{2}(I_y^2 - I_z^2) \qquad \frac{1}{2}\begin{pmatrix} 0 & 0 & 0 \\ 0 & 1 & 0 \\ 0 & 0 & -1 \end{pmatrix}$$

$$I_{y,1} = \frac{1}{2} I_y \qquad \frac{1}{2}\begin{pmatrix} 0 & 0 & 1 \\ 0 & 0 & 0 \\ 1 & 0 & 0 \end{pmatrix}$$

$$I_{y,2} = \frac{1}{2}(I_z I_x + I_x I_z) \qquad \frac{1}{2}\begin{pmatrix} 0 & 0 & i \\ 0 & 0 & 0 \\ -i & 0 & 0 \end{pmatrix}$$

$$I_{y,3} = -\frac{1}{2}(I_z^2 - I_x^2) \qquad \frac{1}{2}\begin{pmatrix} -1 & 0 & 0 \\ 0 & 0 & 0 \\ 0 & 0 & 1 \end{pmatrix}$$

$$I_{z,1} = \frac{1}{2} I_z \qquad \frac{1}{2}\begin{pmatrix} 0 & i & 0 \\ -i & 0 & 0 \\ 0 & 0 & 0 \end{pmatrix}$$

$$I_{z,2} = \frac{1}{2}(I_x I_y + I_y I_x) \qquad \frac{1}{2}\begin{pmatrix} 0 & 1 & 0 \\ 1 & 0 & 0 \\ 0 & 0 & 0 \end{pmatrix}$$

$$I_{z,3} = -\frac{1}{2}(I_x^2 - I_y^2) \qquad \frac{1}{2}\begin{pmatrix} 1 & 0 & 0 \\ 0 & -1 & 0 \\ 0 & 0 & 0 \end{pmatrix}$$

$$\boxed{[I_{p,j}, I_{p,k}] = i I_{p,\ell}}$$

$p = x, y, z$
$j, k, \ell = 1, 2, 3$ or cyclic permutation

XBL 7611-9877 a

Table II.1

Table II.2

Properties of the $I_{p,i}$ Operators

COMMUTATORS

$$[I_{p,i}, I_{p,j}] = iI_{p,k} \qquad [I_{p,1}, I_{q,1}] = \frac{i}{2} I_{r,1}$$

$$[I_{p,1}, I_{q,2}] = -\frac{i}{2} I_{r,2} \qquad [I_{p,2}, I_{q,2}] = -\frac{i}{2} I_{r,1}$$

$$[I_{p,2}, I_{q,1}] = -\frac{i}{2} I_{r,2} \qquad [I_{p,1}, (I_{q,3}-I_{r,3})] = 0$$

$$[I_{p,3}, I_{q,3}] = 0$$

ROTATIONS

$$\exp(-i\theta I_{p,i})\, I_{p,j}\, \exp(i\theta I_{p,i}) = \cos\theta\, I_{p,j} + \sin\theta\, I_{p,k}$$

$$\exp(-i\theta I_{p,1})\, I_{q,1}\, \exp(i\theta I_{p,1}) = \cos\frac{\theta}{2}\, I_{q,1} + \sin\frac{\theta}{2}\, I_{r,1}$$

$$\exp(-i\theta I_{p,1})\, I_{q,2}\, \exp(i\theta I_{p,1}) = \cos\frac{\theta}{2}\, I_{q,2} - \sin\frac{\theta}{2}\, I_{r,2}$$

$$\exp(-i\theta I_{p,2})\, I_{q,1}\, \exp(i\theta I_{p,2}) = \cos\frac{\theta}{2}\, I_{q,1} - \sin\frac{\theta}{2}\, I_{r,2}$$

$$\exp(-i\theta I_{p,2})\, I_{q,2}\, \exp(i\theta I_{p,2}) = \cos\frac{\theta}{2}\, I_{q,2} - \sin\frac{\theta}{2}\, I_{r,1}$$

where $p, q, r = x, y, z$ or cyclic permutation

and $i, j, k = 1, 2, 3$ or cyclic permutation.

Table II.2 continued

RELATIONSHIP TO SINGLE-TRANSITION OPERATORS [67]

$$I_{x,1} = \frac{1}{\sqrt{2}} (I_x^{1-2} + I_x^{2-3})$$

$$I_{x,2} = \frac{1}{\sqrt{2}} (I_y^{1-2} - I_y^{2-3})$$

$$I_{x,3} = \frac{1}{2} (I_x^{1-3} + I_z^{1-2} - I_z^{2-3})$$

$$I_{y,1} = \frac{1}{\sqrt{2}} (I_y^{1-2} + I_y^{2-3})$$

$$I_{y,2} = \frac{1}{\sqrt{2}} (I_x^{1-2} - I_x^{2-3})$$

$$I_{y,3} = \frac{1}{2} (I_x^{1-3} - I_z^{1-2} + I_z^{2-3})$$

$$I_{z,1} = I_z^{1-3}$$

$$I_{z,2} = I_y^{1-3}$$

$$I_{z,3} = - I_x^{1-3}$$

Table II.3

Rotations Generated by Fictitious Spin-$\frac{1}{2}$ Operators

$$R_{p,j}(\theta)\ I_{q,k} \equiv \exp(-i\theta I_{p,j})\ I_{q,k}\ \exp(i\theta I_{p,j})$$

$R_{x,1}(\theta)$

$$I_{x,1} \rightarrow I_{x,1}$$

$$I_{x,2} \rightarrow \cos\theta\ I_{x,2} + \sin\theta\ I_{x,3}$$

$$I_{x,3} \rightarrow -\sin\theta\ I_{x,2} + \cos\theta\ I_{x,3}$$

$$I_{y,1} \rightarrow \cos\theta/2\ I_{y,1} + \sin\theta/2\ I_{z,1}$$

$$I_{y,2} \rightarrow \cos\theta/2\ I_{y,2} - \sin\theta/2\ I_{z,2}$$

$$I_{y,3} \rightarrow I_{y,3} + \frac{1}{2}\sin\theta\ I_{x,2} + \sin^2\theta/2\ I_{x,3}$$

$$= \frac{1}{2}(I_{x,2}\sin\theta - I_{x,3}\cos\theta) + \frac{1}{2}(I_{y,3} - I_{z,3})$$

$$I_{z,1} \rightarrow \cos\theta/2\ I_{z,1} - \sin\theta/2\ I_{y,1}$$

$$I_{z,2} \rightarrow \cos\theta/2\ I_{z,2} + \sin\theta/2\ I_{y,2}$$

$$I_{z,3} \rightarrow I_{z,3} + \frac{1}{2}\sin\theta\ I_{x,2} + \sin^2\theta/2\ I_{x,3}$$

$$= \frac{1}{2}(I_{x,2}\sin\theta - I_{x,3}\cos\theta) - \frac{1}{2}(I_{y,3} - I_{z,3})$$

$R_{x,2}(\theta)$

$$I_{x,1} \rightarrow \cos\theta\ I_{x,1} - \sin\theta\ I_{x,3}$$

$$I_{x,2} \rightarrow I_{x,2}$$

$$I_{x,3} \rightarrow \sin\theta\ I_{x,1} + \cos\theta\ I_{x,3}$$

Table II.3 continued

$$I_{y,1} \rightarrow \cos\theta/2\ I_{y,1} - \sin\theta/2\ I_{z,2}$$

$$I_{y,2} \rightarrow \cos\theta/2\ I_{y,2} - \sin\theta/2\ I_{z,1}$$

$$I_{y,3} \rightarrow I_{y,3} - \frac{1}{2}\sin\theta\ I_{x,1} + \sin^2\theta/2\ I_{x,3}$$

$$= -\frac{1}{2}(I_{x,1}\sin\theta + I_{x,3}\cos\theta) + \frac{1}{2}(I_{y,3} - I_{z,3})$$

$$I_{z,1} \rightarrow \cos\theta/2\ I_{z,1} + \sin\theta/2\ I_{y,2}$$

$$I_{z,2} \rightarrow \cos\theta/2\ I_{z,2} + \sin\theta/2\ I_{y,1}$$

$$I_{z,3} \rightarrow I_{z,3} - \frac{1}{2}\sin\theta\ I_{x,1} + \sin^2\theta/2\ I_{x,3}$$

$$= -\frac{1}{2}(I_{x,1}\sin\theta + I_{x,3}\cos\theta) - \frac{1}{2}(I_{y,3} - I_{z,3})$$

$R_{x,3}(\theta)$

$$I_{x,1} \rightarrow \cos\theta\ I_{x,1} + \sin\theta\ I_{x,2}$$

$$I_{x,2} \rightarrow -\sin\theta\ I_{x,1} + \cos\theta\ I_{x,2}$$

$$I_{x,3} \rightarrow I_{x,3}$$

$$I_{y,1} \rightarrow \cos\theta/2\ I_{y,1} - \sin\theta/2\ I_{y,2}$$

$$I_{y,2} \rightarrow \cos\theta/2\ I_{y,2} + \sin\theta/2\ I_{y,1}$$

$$I_{y,3} \rightarrow I_{y,3}$$

$$I_{z,1} \rightarrow \cos\theta/2\ I_{z,1} - \sin\theta/2\ I_{z,2}$$

$$I_{z,2} \rightarrow \cos\theta/2\ I_{z,2} + \sin\theta/2\ I_{z,1}$$

$$I_{z,3} \rightarrow I_{z,3}$$

Table II.3 continued

$R_{y,1}(\theta)$

$$I_{x,1} \to \cos\theta/2\ I_{x,1} - \sin\theta/2\ I_{z,1}$$

$$I_{x,2} \to \cos\theta/2\ I_{x,2} + \sin\theta/2\ I_{z,2}$$

$$I_{x,3} \to I_{x,3} + \frac{1}{2}\sin\theta\ I_{y,2} + \sin^2\theta/2\ I_{y,3}$$

$$= \frac{1}{2}(I_{y,2}\sin\theta - I_{y,3}\cos\theta) - \frac{1}{2}(I_{z,3} - I_{x,3})$$

$$I_{y,1} \to I_{y,1}$$

$$I_{y,2} \to \cos\theta\ I_{y,2} + \sin\theta\ I_{y,3}$$

$$I_{y,3} \to -\sin\theta\ I_{y,2} + \cos\theta\ I_{y,3}$$

$$I_{z,1} \to \cos\theta/2\ I_{z,1} + \sin\theta/2\ I_{x,1}$$

$$I_{z,2} \to \cos\theta/2\ I_{z,2} - \sin\theta/2\ I_{x,2}$$

$$I_{z,3} \to I_{z,3} + \frac{1}{2}\sin\theta\ I_{y,2} + \sin^2\theta/2\ I_{y,3}$$

$$= \frac{1}{2}(I_{y,2}\sin\theta - I_{y,3}\cos\theta) + \frac{1}{2}(I_{z,3} - I_{x,3})$$

$R_{y,2}(\theta)$

$$I_{x,1} \to \cos\theta/2\ I_{x,1} + \sin\theta/2\ I_{z,2}$$

$$I_{x,2} \to \cos\theta/2\ I_{x,2} + \sin\theta/2\ I_{z,1}$$

$$I_{x,3} \to I_{x,3} - \frac{1}{2}\sin\theta\ I_{y,1} + \sin^2\theta/2\ I_{y,3}$$

$$= -\frac{1}{2}(I_{y,1}\sin\theta + I_{y,3}\cos\theta) - \frac{1}{2}(I_{z,3} - I_{x,3})$$

Table II.3 continued

$$I_{y,1} \rightarrow \cos\theta\ I_{y,1} - \sin\theta\ I_{y,3}$$

$$I_{y,2} \rightarrow I_{y,2}$$

$$I_{y,3} \rightarrow \sin\theta\ I_{y,1} + \cos\theta\ I_{y,3}$$

$$I_{z,1} \rightarrow \cos\theta/2\ I_{z,1} - \sin\theta/2\ I_{x,2}$$

$$I_{z,2} \rightarrow \cos\theta/2\ I_{z,2} - \sin\theta/2\ I_{x,1}$$

$$I_{z,3} \rightarrow I_{z,3} - \frac{1}{2}\sin\theta\ I_{y,1} + \sin^2\theta/2\ I_{y,3}$$

$$= -\frac{1}{2}(I_{y,1}\sin\theta + I_{y,3}\cos\theta) + \frac{1}{2}(I_{z,3} - I_{x,3})$$

$R_{y,3}(\theta)$

$$I_{x,1} \rightarrow \cos\theta/2\ I_{x,1} - \sin\theta/2\ I_{x,2}$$

$$I_{x,2} \rightarrow \cos\theta/2\ I_{x,2} + \sin\theta/2\ I_{x,1}$$

$$I_{x,3} \rightarrow I_{x,3}$$

$$I_{y,1} \rightarrow \cos\theta\ I_{y,1} + \sin\theta\ I_{y,2}$$

$$I_{y,2} \rightarrow -\sin\theta\ I_{y,1} + \cos\theta\ I_{y,2}$$

$$I_{y,3} \rightarrow I_{y,3}$$

$$I_{z,1} \rightarrow \cos\theta/2\ I_{z,1} - \sin\theta/2\ I_{z,2}$$

$$I_{z,2} \rightarrow \cos\theta/2\ I_{z,2} + \sin\theta/2\ I_{z,1}$$

$$I_{z,3} \rightarrow I_{z,3}$$

Table II.3 continued

$R_{z,1}(\theta)$

$$I_{x,1} \rightarrow \cos\theta/2\ I_{x,1} + \sin\theta/2\ I_{y,1}$$

$$I_{x,2} \rightarrow \cos\theta/2\ I_{x,2} - \sin\theta/2\ I_{y,2}$$

$$I_{x,3} \rightarrow I_{x,3} + \frac{1}{2}\sin\theta\ I_{z,2} + \sin^2\theta/2\ I_{z,3}$$

$$= \frac{1}{2}(I_{z,2}\sin\theta - I_{z,3}\cos\theta) + \frac{1}{2}(I_{x,3} - I_{y,3})$$

$$I_{y,1} \rightarrow \cos\theta/2\ I_{y,1} - \sin\theta/2\ I_{x,1}$$

$$I_{y,2} \rightarrow \cos\theta/2\ I_{y,2} + \sin\theta/2\ I_{x,2}$$

$$I_{y,3} \rightarrow I_{y,3} + \frac{1}{2}\sin\theta\ I_{z,2} + \sin^2\theta/2\ I_{z,3}$$

$$= \frac{1}{2}(I_{z,2}\sin\theta - I_{z,3}\cos\theta) - \frac{1}{2}(I_{x,3} - I_{y,3})$$

$$I_{z,1} \rightarrow I_{z,1}$$

$$I_{z,2} \rightarrow \cos\theta\ I_{z,2} + \sin\theta\ I_{z,3}$$

$$I_{z,3} \rightarrow -\sin\theta\ I_{z,2} + \cos\theta\ I_{z,3}$$

$R_{z,2}(\theta)$

$$I_{x,1} \rightarrow \cos\theta/2\ I_{x,1} - \sin\theta/2\ I_{y,2}$$

$$I_{x,2} \rightarrow \cos\theta/2\ I_{x,2} - \sin\theta/2\ I_{y,1}$$

$$I_{x,3} \rightarrow I_{x,3} - \frac{1}{2}\sin\theta\ I_{z,1} + \sin^2\theta/2\ I_{z,3}$$

$$= -\frac{1}{2}(I_{z,1}\sin\theta + I_{z,3}\cos\theta) + \frac{1}{2}(I_{x,3} - I_{y,3})$$

Table II.3 continued

$$I_{y,1} \rightarrow \cos\theta/2\ I_{y,1} + \sin\theta/2\ I_{x,2}$$

$$I_{y,2} \rightarrow \cos\theta/2\ I_{y,2} + \sin\theta/2\ I_{x,1}$$

$$I_{y,3} \rightarrow I_{y,3} - \frac{1}{2}\sin\theta\ I_{z,1} + \sin^2\theta/2\ I_{z,3}$$

$$= -\frac{1}{2}(I_{z,1}\sin\theta + I_{z,3}\cos\theta) - \frac{1}{2}(I_{x,3} - I_{y,3})$$

$$I_{z,1} \rightarrow \cos\theta\ I_{z,1} - \sin\theta\ I_{z,3}$$

$$I_{z,2} \rightarrow I_{z,2}$$

$$I_{z,3} \rightarrow \sin\theta\ I_{z,1} + \cos\theta\ I_{z,3}$$

$R_{z,3}(\theta)$

$$I_{x,1} \rightarrow \cos\theta/2\ I_{x,1} - \sin\theta/2\ I_{x,2}$$

$$I_{x,2} \rightarrow \cos\theta/2\ I_{x,2} + \sin\theta/2\ I_{x,1}$$

$$I_{x,3} \rightarrow I_{x,3}$$

$$I_{y,1} \rightarrow \cos\theta/2\ I_{y,1} - \sin\theta/2\ I_{y,2}$$

$$I_{y,2} \rightarrow \cos\theta/2\ I_{y,2} + \sin\theta/2\ I_{y,1}$$

$$I_{y,3} \rightarrow I_{y,3}$$

$$I_{z,1} \rightarrow \sin\theta\ I_{z,2} + \cos\theta\ I_{z,1}$$

$$I_{z,2} \rightarrow \cos\theta\ I_{z,2} - \sin\theta\ I_{z,1}$$

$$I_{z,3} \rightarrow I_{z,3}$$

Table II.3 continued

$R_{xy,3}(\theta)$

$$I_{x,1} \rightarrow \cos\tfrac{3}{2}\theta\ I_{x,1} + \sin\tfrac{3}{2}\theta\ I_{x,2}$$

$$I_{x,2} \rightarrow \cos\tfrac{3}{2}\theta\ I_{x,2} - \sin\tfrac{3}{2}\theta\ I_{x,1}$$

$$I_{y,1} \rightarrow \cos\tfrac{3}{2}\theta\ I_{y,1} - \sin\tfrac{3}{2}\theta\ I_{y,2}$$

$$I_{y,2} \rightarrow \cos\tfrac{3}{2}\theta\ I_{y,2} + \sin\tfrac{3}{2}\theta\ I_{y,1}$$

$R_{yz,3}(\theta)$

$$I_{y,1} \rightarrow \cos\tfrac{3}{2}\theta\ I_{y,1} + \sin\tfrac{3}{2}\theta\ I_{y,2}$$

$$I_{y,2} \rightarrow \cos\tfrac{3}{2}\theta\ I_{y,2} - \sin\tfrac{3}{2}\theta\ I_{y,1}$$

$$I_{z,1} \rightarrow \cos\tfrac{3}{2}\theta\ I_{z,1} - \sin\tfrac{3}{2}\theta\ I_{z,2}$$

$$I_{z,2} \rightarrow \cos\tfrac{3}{2}\theta\ I_{z,2} + \sin\tfrac{3}{2}\theta\ I_{z,1}$$

$R_{zx,3}(\theta)$

$$I_{x,1} \rightarrow \cos\tfrac{3}{2}\theta\ I_{x,1} - \sin\tfrac{3}{2}\theta\ I_{x,2}$$

$$I_{x,2} \rightarrow \cos\tfrac{3}{2}\theta\ I_{x,2} + \sin\tfrac{3}{2}\theta\ I_{x,1}$$

$$I_{z,1} \rightarrow \cos\tfrac{3}{2}\theta\ I_{z,1} + \sin\tfrac{3}{2}\theta\ I_{z,2}$$

$$I_{z,2} \rightarrow \cos\tfrac{3}{2}\theta\ I_{z,2} - \sin\tfrac{3}{2}\theta\ I_{z,1}$$

Table II.4

Rotation Matrices $U_{p,j} = \exp(-i\theta I_{p,j})$

$$U_{x,1} = \begin{pmatrix} 1 & 0 & 0 \\ & \cos\theta/2 & -i\sin\theta/2 \\ 0 & -i\sin\theta/2 & \cos\theta/2 \end{pmatrix} \qquad U_{x,2} = \begin{pmatrix} 1 & 0 & 0 \\ 0 & \cos\theta/2 & -\sin\theta/2 \\ 0 & \sin\theta/2 & \cos\theta/2 \end{pmatrix}$$

$$U_{x,3} = \begin{pmatrix} 1 & 0 & 0 \\ 0 & e^{-i\theta/2} & 0 \\ 0 & 0 & e^{i\theta/2} \end{pmatrix}$$

$$U_{y,1} = \begin{pmatrix} \cos\theta/2 & 0 & -i\sin\theta/2 \\ 0 & 1 & 0 \\ -i\sin\theta/2 & 0 & \cos\theta/2 \end{pmatrix} \qquad U_{y,2} = \begin{pmatrix} \cos\theta/2 & 0 & \sin\theta/2 \\ 0 & 1 & 0 \\ -\sin\theta/2 & 0 & \cos\theta/2 \end{pmatrix}$$

$$U_{y,3} = \begin{pmatrix} e^{i\theta/2} & 0 & 0 \\ 0 & 1 & 0 \\ 0 & 0 & e^{-i\theta/2} \end{pmatrix}$$

$$U_{z,1} = \begin{pmatrix} \cos\theta/2 & \sin\theta/2 & 0 \\ -\sin\theta/2 & \cos\theta/2 & 0 \\ 0 & 0 & 1 \end{pmatrix} \qquad U_{z,2} = \begin{pmatrix} \cos\theta/2 & -i\sin\theta/2 & 0 \\ -i\sin\theta/2 & \cos\theta/2 & 0 \\ 0 & 0 & 1 \end{pmatrix}$$

$$U_{z,3} = \begin{pmatrix} e^{-i\theta/2} & 0 & 0 \\ 0 & e^{i\theta/2} & 0 \\ 0 & 0 & 1 \end{pmatrix}$$

$$U_{xy,3} = \begin{pmatrix} e^{-i\theta/2} & 0 & 0 \\ 0 & e^{-i\theta/2} & 0 \\ 0 & 0 & e^{i\theta} \end{pmatrix} \qquad U_{yz,3} = \begin{pmatrix} e^{i\theta} & 0 & 0 \\ 0 & e^{-i\theta/2} & 0 \\ 0 & 0 & e^{-i\theta/2} \end{pmatrix}$$

$$U_{zx,3} = \begin{pmatrix} e^{-i\theta/2} & 0 & 0 \\ 0 & e^{i\theta} & 0 \\ 0 & 0 & e^{-i\theta/2} \end{pmatrix}$$

Table II.5

What the $I_{p,i}$ Operators Signify as Density Matrix Components

$I_{z,1}$	equilibrium Zeeman population manifested as magnetization along the z-axis.
$I_{x,1}$, $I_{y,1}$	single-quantum coherence states giving rise to transverse magnetization. The two transitions $\|-1\rangle \leftrightarrow \|0\rangle$ and $\|0\rangle \leftrightarrow \|1\rangle$ have the same phase, either 0° ($I_{x,1}$) or 90° ($I_{y,1}$).
$I_{x,2}$, $I_{y,2}$	single-quantum coherence states in which the two transitions are completely out of phase with each other, aligned along either the y-axis ($I_{x,2}$) or the x-axis ($I_{y,2}$). No magnetization results.
$I_{z,2}$, $I_{z,3}$	states of double-quantum coherence with no magnetization.
$I_{xy,3}$	describes a population characteristic of quadrupolar order (no magnetization).
$I_{x,3}$, $I_{y,3}$	entail both double-quantum coherence and quadrupolar order: $I_{x,3} = \frac{1}{2}(I_{xy,3}-I_{z,3})$ $I_{y,3} = -\frac{1}{2}(I_{xy,3}+I_{z,3})$

that "mix letters". This difference will be discussed in more detail shortly.

The density matrix can also be expressed as a linear combination of the $I_{p,i}$ operators:

$$\rho(t) = \beta \sum_{p,i} a_{p,i}(t)\, I_{p,i} \quad . \tag{II.22}$$

[The constant β equals $(1/3)\,(\omega_0/kT)$ and shouldn't really be omitted or forgotten--but will be for the remainder of the chapter.] The nine coefficients $a_{p,i}(t)$ completely describe the system, but to make sense of these numbers, we must know the meaning of each operator component of ρ in terms of populations and coherences. This sort of information is presented in Table II.5. Note that only the three operators $I_{x,1}$, $I_{y,1}$, and $I_{z,1}$ correspond to a macroscopic magnetization.

The coefficients $a_{p,i}(t)$ also describe the position of a state-of-the-system vector in a nine-dimensional space. The evolution of the density matrix is mirrored by the motion of this vector. Figure II.4 shows typical projections into the three fictitious spin-$\frac{1}{2}$ frames X, Y, and Z. ("X" is the three-dimensional space spanned by $I_{x,1}$, $I_{x,2}$, and $I_{x,3}$, with analogous definitions for Y and Z.)

The vector representation of density matrix evolution will be used extensively in the pages to come, especially when only two components of ρ are of interest at a time. Nonetheless, there is a fundamental conceptual problem with the vector model: one's inability in any but the most altered of mental states to fully visualize nine dimensions. We would like a three-dimensional model, something to tie a vivid concrete image to an abstract state of coherence. Clearly a

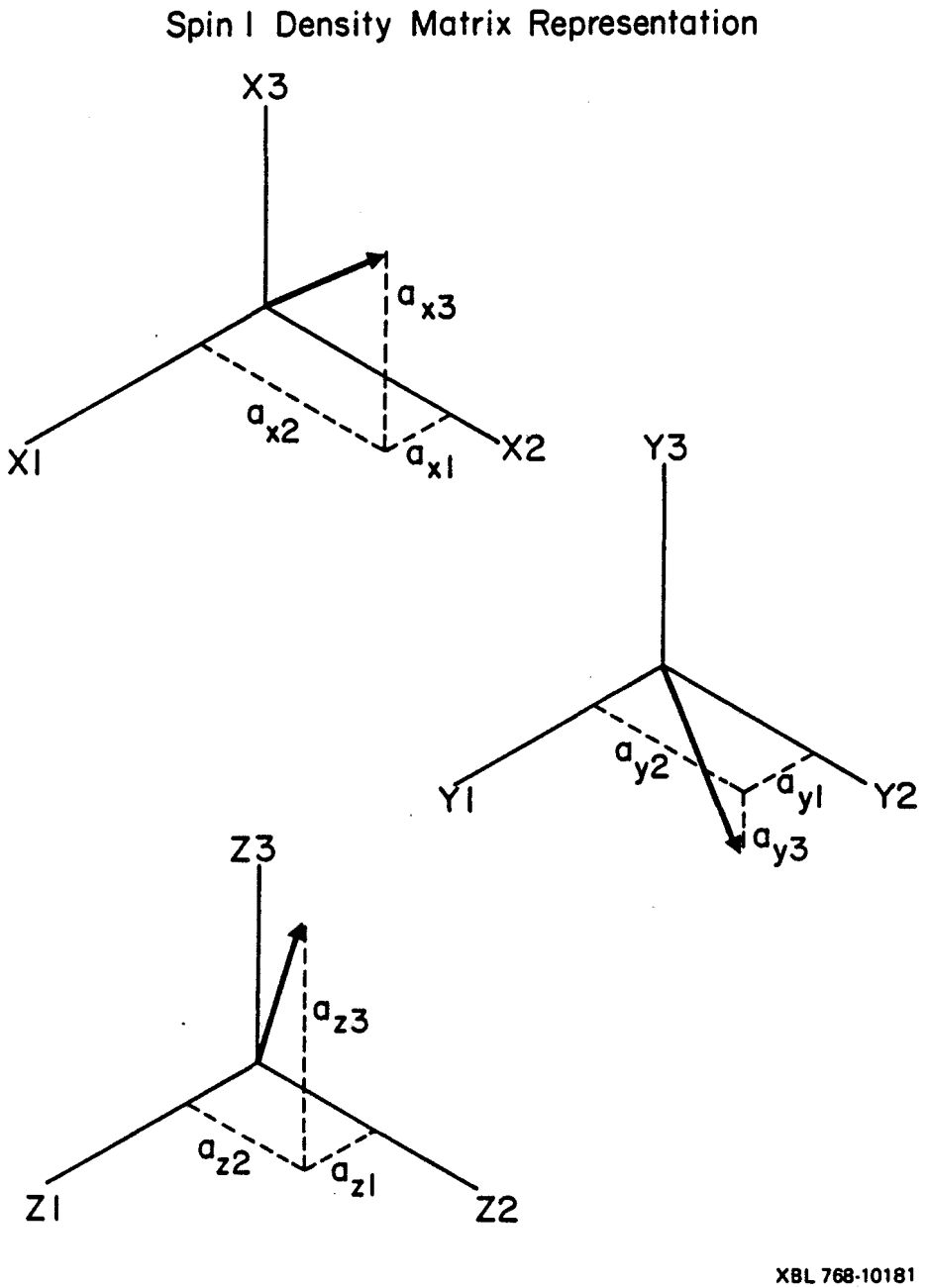

Figure II.4 A typical projection of the state-of-the-system vector in the X, Y, and Z frames spanned by the spin-1 $I_{p,i}$ operators.

vector in three dimensions does not provide enough information; it can only specify the coefficients of three operators. To model a three-level system in three dimensions requires a more complicated "state-of-the-system object".

2.4.4 Additional Models for the Three-Level System

In the quest for physical insight, several other pictorial representations have been proposed for the three-level system. Hoatson and Packer [71] suggested the use of two vectors in an x-y plane to signify the two single-quantum coherences. After a hard 90° pulse with phase = 0° ($\omega_1 >> \omega_Q$, $\Delta\omega$), the two vectors are collinear along the y-axis of the rotating frame. They then precess at the single-quantum frequencies $\Delta\omega + \omega_Q$ and $\Delta\omega - \omega_Q$, growing out of phase with one another. The transverse magnetization at any time is proportional to the vector sum. When the two vectors are 180° out of phase and pointing in opposite directions along the x-axis ($\rho = I_{y,2}$), a second hard 90° x-pulse creates double-quantum coherence ($I_{z,2}$). [For a general orientation of the SQ vectors v_1 and v_2, $a_{x,1} = \hat{x}\cdot(v_1+v_2)$, $a_{y,1} = \hat{y}\cdot(v_1+v_2)$, $a_{x,2} = \hat{y}\cdot(v_1-v_2)$, and $a_{y,2} = \hat{x}\cdot(v_1-v_2)$.] The DQ coherence then evolves as a two-headed arrow in a separate axis system. Although Hoatson and Packer were able to accurately model the density matrix in this fashion, the need for two axis systems and the somewhat magical appearance of the two-headed DQ coherence vector are aesthetic disadvantages.

Vega, Pines, and co-workers [64], in the spirit of the Wigner-Eckhardt theorem [21], have related the $I_{p,i}$ operators to the familiar p and d orbitals (Fig. II.5):

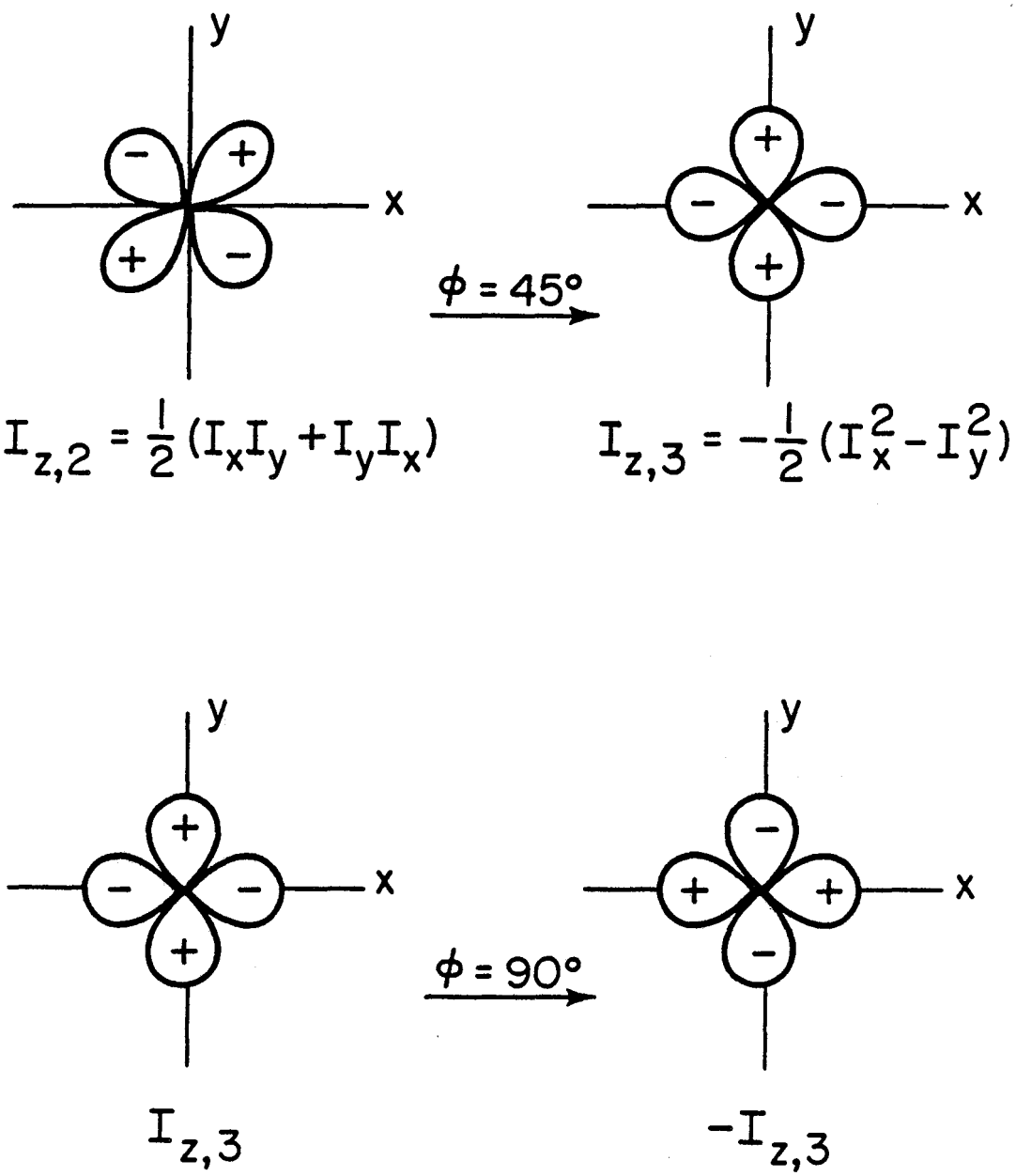

XBL 7610-4973

Figure II.5 d-orbital representations of the operators $I_{z,2}$ and $I_{z,3}$. Only a 45° rotation is needed to interconvert the two; in contrast, the p_x and p_y orbitals that represent $I_{x,1}$ and $I_{y,1}$ are related by a 90° rotation.

$$I_{x,1} \leftrightarrow p_x \;,\quad I_{x,2} \leftrightarrow d_{yz} \;,\quad I_{x,3} \leftrightarrow d_{y^2-z^2} \;,$$

$$I_{y,1} \leftrightarrow p_y \;,\quad I_{y,2} \leftrightarrow d_{xz} \;,\quad I_{y,3} \leftrightarrow d_{z^2-x^2} \;,$$

$$I_{z,1} \leftrightarrow p_z \;,\quad I_{z,2} \leftrightarrow d_{xy} \;,\quad I_{z,3} \leftrightarrow d_{x^2-y^2} \;,$$

$$I_{xy,3} \leftrightarrow d_{z^2} \;.$$

This analogy is of great help in illuminating the rotation properties of the operators. Consider an initial density matrix proportional to $I_{z,2}$ (i.e., a state of double-quantum coherence). Application of an rf pulse along the x-axis ($\mathcal{H}_{rf} = -2\omega_1 I_{x,1}$) rotates $I_{z,2}$ to $I_{y,2}$ with an angular frequency of ω_1 (see Table II.3). In terms of the model, a d_{xy} orbital is rotated 90° to become a d_{xz} orbital. In contrast, the offset Hamiltonian, $-2\Delta\omega\, I_{z,1}$, rotates $I_{z,2}$ to $I_{z,3}$ with an angular frequency of $2\Delta\omega$. The orbital picture makes clear the reason for the faster rate of rotation: only 45° is needed to convert a d_{xy} orbital to a $d_{x^2-y^2}$ orbital.

The limitation of this operator representation is the difficulty in displaying the effects of the quadrupolar Hamiltonian. As stated earlier, $\mathcal{H}_Q$ contains a bilinear operator, and therefore it cannot be modeled as a simple rotation in three dimensions. Indeed, $\mathcal{H}_Q$ acts to interconvert p-orbital and d-orbital operators. After much thought, I have sadly concluded that there is no simple way of simulating this transmutation of first-rank and second-rank tensors without unappealing and arbitrary restrictions. If one accepts its inelegancies, however, the following scheme <u>can</u> be used to incorporate the effects of the

quadrupole Hamiltonian into the orbital picture.

Central to this approach is the mimicking of a p-orbital by an adulterated d-orbital. Imagine the d_{xz} orbital, for example, with its positive lobes in the first and third quadrants of the x-z plane and its negative lobes in the second and fourth quadrants of the x-z plane. Now imagine keeping the shape and position of the lobes the same but swapping the sign of the second-quadrant and third-quadrant lobes. The resulting "four-leaf clover" is positive above the x-y plane, negative below. As such, it is reminiscent of a p_z orbital, although certainly lacking the appropriate cylindrical symmetry about the z-axis. To compensate for this symmetry problem, certain restrictions will have to be applied to the rotation of "pseudo-p-orbitals", as we shall see below.

Rather than toiling with various manipulations on two-dimensional figures, let us instead play with a very real and no doubt familiar object: a Rubik's cube. Only four edge "cubelets" interest us, those lying on any given plane passing through the center of the cube and parallel to a face. Two of these cubelets are marked with a plus sign (positive lobes), two with a minus sign (negative lobes); none of the colors matter. Different arrangements of the marked cubelets and different orientations of the entire cube generate the nine $I_{p,i}$ operators, as shown in Fig. II.6. Those operators analogous to d-orbitals (any $I_{p,2}$ or $I_{p,3}$ operator) are unambiguously defined by four cubelets signifying lobes. With $I_{p,1}$ operators a problem arises: should $I_{x,1}$, for example, be depicted as a "sign-swapped" d_{xy} orbital or "sign-swapped" d_{xz} orbital? For the model to work correctly, the choice must always be d_{xz}. Similarly, $I_{y,1}$ is depicted

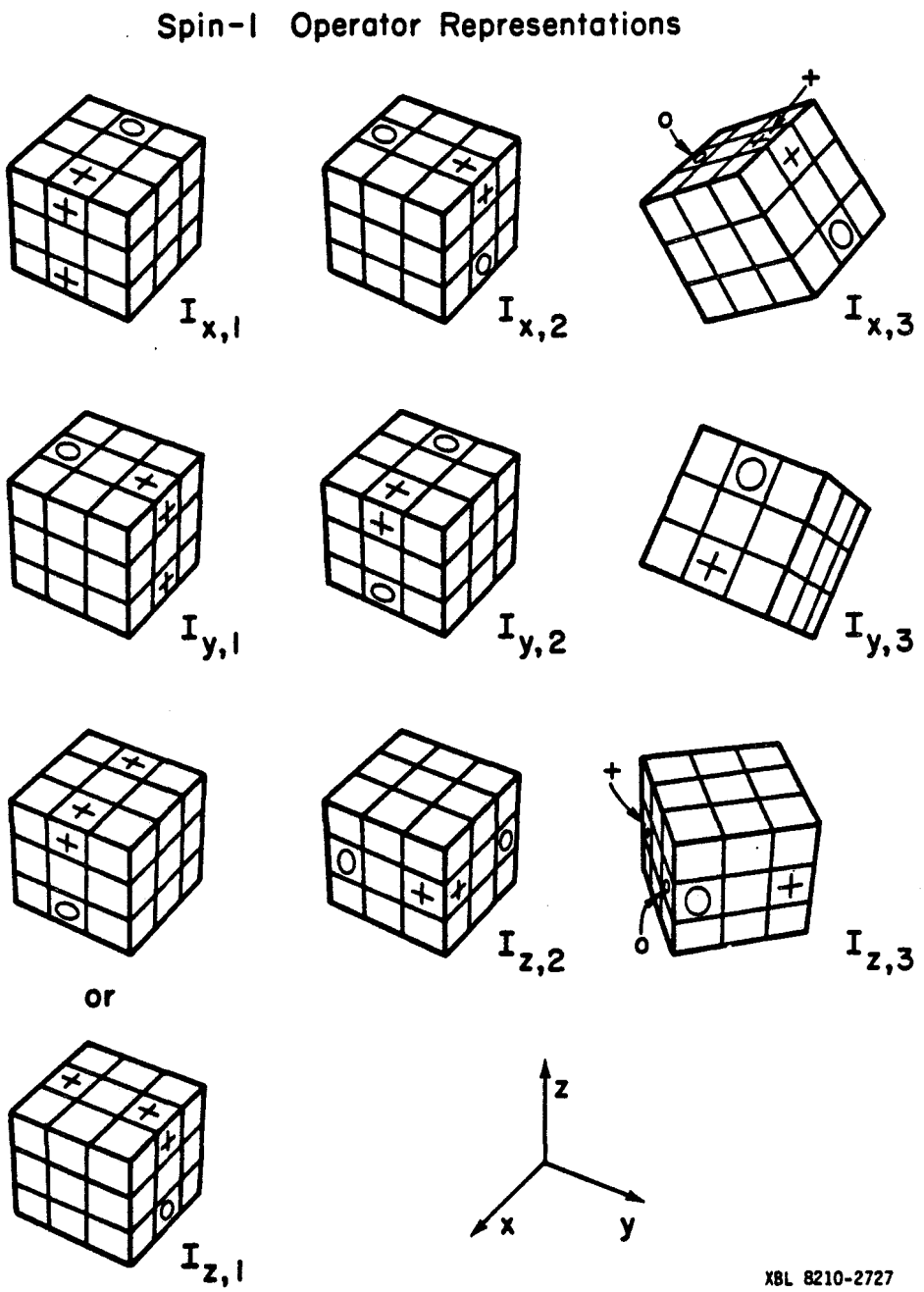

Figure II.6 A Rubik's cube representation of the $I_{p,i}$ operators used in the expansion of the spin-1 density matrix. Cubelets marked with a "+" signify positive lobes; those marked with an "o" signify negative lobes. (The remaining cubelets are blank.) $I_{z,1}$ can be represented in two different ways.

as a sign-swapped d_{yz} orbital. For $I_{z,1}$ either choice (d_{xz} or d_{yz}) is allowed.

Now for the rules of the game. The effects of various terms in the Hamiltonian are as follows. $\mathcal{H}_{off}$ and $\mathcal{H}_{rf}$ cause simple rotations of the entire cube, but the I_z^2 term in $\mathcal{H}_Q$ induces <u>internal</u> rotation about the z-axis. To be specific, $\mathcal{H}_Q$ acts to rotate the top third of the cube clockwise and the bottom third counterclockwise; the middle third is unaffected. This rule is arbitrary to say the least, but it bears some conceptual links to the counter-rotating single-quantum vectors of Hoatson and Packer.

Let us check to see if the model correctly simulates the properties of $\mathcal{H}_Q$: interconverting $I_{x,1}$ and $I_{x,2}$ as well as $I_{y,1}$ and $I_{y,2}$ but leaving all other operator components of the density matrix unchanged. A look at Fig. II.6 reveals that a 90° twist of the top third of the cube and a -90° twist of the bottom third convert $I_{x,1}$ to $\pm I_{x,2}$ and vice-versa. (The signs are unimportant at this stage.) A similar relationship holds for $I_{y,1}$ and $I_{y,2}$. In contrast, $I_{z,2}$ and $I_{z,3}$ lie entirely within the middle third of the cube and are unaffected by the twisting. The form of $I_{z,1}$ switches from a sign-swapped d_{xz} to a sign-swapped d_{yz} orbital, but these both represent the operator. As for $I_{x,3}$ and $I_{y,3}$, their orientation does not allow the concept of top, middle, and bottom thirds, but we do note that the marked cubelets lie either in the x-y plane or along the z-axis. Were counter-rotations about the z-axis possible with this cube configuration, these operator representations would be unchanged.

Subject to a certain amount of hand-waving, then, the model does mimic the effects of $\mathcal{H}_Q$. Note, however, that if $I_{x,1}$ were depicted

as a sign-swapped d_{xy} orbital, our rules would predict it to be unaltered by a quadrupole term. Such inelegancies are unfortunately unavoidable.

But enough background--let's move on to applications. With cube in hand (or in mind) let us follow the course of a few pulse sequences. For simplicity, we will assume that only one term of the Hamiltonian acts on the system at a time. (This assumption is not at all unreasonable when hard pulses are used and $\omega_Q >> \Delta\omega$.) The cases we will consider are as follows. For each, the initial density matrix is proportional to $I_{z,1}$.

(1) Preparation of double-quantum coherence with the pulse sequence 90x-τ-90x. The first 90° pulse along the x-axis converts $I_{z,1}$ (sign-swapped d_{yz} representation) to $I_{y,1}$. Between pulses the quadrupole Hamiltonian converts $I_{y,1}$ to $I_{y,2}$. The second x-pulse then flips the d_{xz} orbital signifying $I_{y,2}$ to the d_{xy} orbital representing $I_{z,2}$. This operator is unaffected by $\mathcal{H}_Q$ but is rotated to $I_{z,3}$ by the offset term.

(2) The quadrupole echo sequence 90x-τ-90y-τ. As before, the first pulse rotates $I_{z,1}$ to $I_{y,1}$, and in the interval τ $I_{y,1}$ is twisted by $\mathcal{H}_Q$ to become $I_{y,2}$. The second pulse along the <u>y-axis</u> spins the $I_{y,2}$ pinwheel by 90°, creating $-I_{y,2}$. (Because $I_{y,1}$ and $I_{y,2}$ are two components of the same fictitious spin-$\frac{1}{2}$ frame, this 90° pulse has the inverting effect of a 180° pulse.) Subsequent twisting by $\mathcal{H}_Q$ returns the density matrix to $I_{y,1}$. Were different quadrupole frequencies ω_Q acting on different molecules in a sample (as would be expected in a powder), single-quantum coherences would dephase during the first delay, twisting at different rates from $I_{y,1}$ to $I_{y,2}$, but

would refocus during the second delay and echo after a total delay of 2τ.

(3) Creation of quadrupolar order via the Jeener-Brockaert sequence 90x-τ-45y [75]. Once again, the first pulse creates $I_{y,1}$ from $I_{z,1}$ and the delay permits $\mathcal{H}_Q$ to twist $I_{y,1}$ into $I_{y,2}$. The 45° pulse along the y-axis then rotates $I_{y,2}$ to $I_{y,3}$. This latter operator, we recall, equals $-(I_{xy,3} + I_{z,3})/2$. The system is thus characterized by the presence of both quadrupolar order (populations proportional to $\mathcal{H}_Q$) and double-quantum coherence, as noted by Hoatson and Packer [71].

Many other sequences can of course be simulated with the Rubik's cube model. It is hoped that this approach gives the reader a literal feel for the density matrix properties of the three-level system and a hands-on familiarity with the $I_{p,i}$ operators. In addition, those for whom three levels are passé might wish to think about the marvelous cube as a model for more complicated spin systems--after all, only 4 out of 26 cubelets were used here.

2.5 Expressions for the Effects of Various Hamiltonians

Time now to put the models aside and return to the more abstract and less colorful realm of operator algebra. We wish to derive expressions for the evolution of the density matrix when acted upon by all or part of the Hamiltonian in Eq. II.20. In the simplest case, two out of three terms in $\mathcal{H}$ are zero. The effect of the remaining term on ρ is then found by calculating simple operator rotations, as compiled in Table II.3. The value of θ to be used when the Hamiltonian is applied for a time t is $-2\Delta\omega t$ for $\mathcal{H}_{off}$, $-2\omega_1 t$ for $\mathcal{H}_{rf}$, and

$2\omega_Q t/3$ for $\mathcal{H}_Q$. Density matrix expressions are derived below for the more general circumstance of at least two non-zero terms in $\mathcal{H}$.

2.5.1 $\mathcal{H}_{off} \neq 0, \mathcal{H}_{rf} \neq 0, \mathcal{H}_Q = 0$

This case is not really very interesting--when there is no quadrupolar splitting, the density matrix remains a linear combination of I_x, I_y, and I_z. (There is no need for $I_{p,i}$ operators.) Its evolution is exactly that of the two-level system described earlier--see Eqs. II.9a-II.9c. Explicit expressions for operator coefficients can be found in the literature [73].

2.5.2 $\mathcal{H}_{off} \neq 0, \mathcal{H}_{rf} = 0, \mathcal{H}_Q \neq 0$

The equation describing density matrix evolution in the absence of a pulse is as follows:

$$\rho(\tau) = \exp[-i(\mathcal{H}_{off}+\mathcal{H}_Q)\tau]\ \rho(0)\ \exp[i(\mathcal{H}_{off}+\mathcal{H}_Q)\tau]$$

$$= \exp[-i(-2\Delta\omega\ I_{z,1} + \frac{2}{3}\omega_Q\ I_{xy,3})\tau]\ \rho(0)$$

$$\exp[i(-2\Delta\omega\ I_{z,1} + \frac{2}{3}\omega_Q\ I_{xy,3})\tau] \quad . \quad \text{(II.23)}$$

Because $[I_{z,1}, I_{xy,3}] = 0$, these two rotations can be applied successively:

$$\rho(\tau) = \exp(-\frac{2}{3}\ i\ \omega_Q\tau\ I_{xy,3})[\exp(2i\Delta\omega\tau\ I_{z,1})\ \rho(0)\ \exp(-2i\Delta\omega\tau\ I_{z,1})]$$

$$\exp(\frac{2}{3}\ i\ \omega_Q\tau\ I_{xy,3}) \quad . \quad \text{(II.24)}$$

As a sample calculation, let $I_{x,1}$ be the initial density matrix. Using the rotation expressions listed in Table II.3,

$$\rho(\tau) = \exp(-\frac{2}{3}\, i\, \omega_Q \tau\, I_{xy,3})[\cos\Delta\omega\tau\, I_{x,1} - \sin\Delta\omega\tau\, I_{y,1}]$$

$$\exp(\frac{2}{3}\, i\, \omega_Q \tau\, I_{xy,3})$$

$$= \cos\Delta\omega\tau\, \cos\omega_Q\tau\, I_{x,1} + \cos\Delta\omega\tau\, \sin\omega_Q\tau\, I_{x,2}$$

$$- \sin\Delta\omega\tau\, \cos\omega_Q\tau\, I_{y,1} + \sin\Delta\omega\tau\, \sin\omega_Q\tau\, I_{y,2} \quad . \tag{II.25}$$

Complete results (in frequency units) can be found in Table II.6 .

2.5.3 $\mathcal{H}_{off} = 0,\ \mathcal{H}_{rf} \neq 0,\ \mathcal{H}_Q \neq 0$

In this case, the two non-zero terms of the Hamiltonian do not commute ($[I_{x,1}, I_{xy,3}] = -3i\, I_{x,2}/2$) so an immediate separation of $\mathcal{H}_{rf}$ and $\mathcal{H}_Q$ in the exponentials is not possible. Instead we proceed as follows. Since $I_{x,3} + I_{y,3} + I_{z,3} = 0$, we can write

$$\mathcal{H} = -2\omega_1\, I_{x,1} + \frac{2}{3}\,\omega_Q\,(I_{x,3}-I_{y,3})$$

$$= -2\omega_1\, I_{x,1} + \frac{2}{3}\,\omega_Q\,(I_{x,3}-I_{y,3}) + \frac{1}{3}\,\omega_Q\,(I_{x,3}+I_{y,3}+I_{z,3})$$

$$= -2\omega_1\, I_{x,1} + \omega_Q\, I_{x,3} - \frac{1}{3}\,\omega_Q(I_{y,3}-I_{z,3}) \quad . \tag{II.26}$$

Next transform the Hamiltonian and the density matrix by rotating about $I_{x,2}$:

Table II.6

Spin-1 Evolution Under the Hamiltonian $\mathcal{H}_{off} + \mathcal{H}_Q$

$$\mathcal{H} = -2\Delta\nu\ I_{z,1} + \frac{2}{3}\ \nu_Q\ (I_{x,3} - I_{y,3})$$

various initial density matrices

$\rho(0) = I_{x,1}$

$$a_{x,1} = (\cos 2\pi\Delta\nu t)(\cos 2\pi\nu_Q t)$$

$$a_{x,2} = (\cos 2\pi\Delta\nu t)(\sin 2\pi\nu_Q t)$$

$$a_{y,1} = -\ (\sin 2\pi\Delta\nu t)(\cos 2\pi\nu_Q t)$$

$$a_{y,2} = (\sin 2\pi\Delta\nu t)(\sin 2\pi\nu_Q t)$$

$\rho(0) = I_{x,2}$

$$a_{x,2} = (\cos 2\pi\Delta\nu t)(\cos 2\pi\nu_Q t)$$

$$a_{x,1} = -(\cos 2\pi\Delta\nu t)(\sin 2\pi\nu_Q t)$$

$$a_{y,2} = (\sin 2\pi\Delta\nu t)(\cos 2\pi\nu_Q t)$$

$$a_{y,1} = (\sin 2\pi\Delta\nu t)(\sin 2\pi\nu_Q t)$$

$\rho(0) = I_{y,1}$

$$a_{y,1} = (\cos 2\pi\Delta\nu t)(\cos 2\pi\nu_Q t)$$

$$a_{y,2} = -(\cos 2\pi\Delta\nu t)(\sin 2\pi\nu_Q t)$$

$$a_{x,1} = (\sin 2\pi\Delta\nu t)(\cos 2\pi\nu_Q t)$$

$$a_{x,2} = (\sin 2\pi\Delta\nu t)(\sin 2\pi\nu_Q t)$$

Table II.6 continued

$\rho(0) = I_{y,2}$

$$a_{y,2} = (\cos 2\pi\Delta\nu t)(\cos 2\pi\nu_Q t)$$

$$a_{y,1} = (\cos 2\pi\Delta\nu t)(\sin 2\pi\nu_Q t)$$

$$a_{x,2} = -\ (\sin 2\pi\Delta\nu t)(\cos 2\pi\nu_Q t)$$

$$a_{x,1} = (\sin 2\pi\Delta\nu t)(\sin 2\pi\nu_Q t)$$

$\rho(0) = I_{z,2}$

$$a_{z,2} = \cos 4\pi\Delta\nu t$$

$$a_{z,3} = -\sin 4\pi\Delta\nu t$$

$\rho(0) = I_{z,3}$

$$a_{z,2} = \sin 4\pi\Delta\nu t$$

$$a_{z,3} = \cos 4\pi\Delta\nu t$$

$$\mathcal{H}' = e^{-i\theta I_{x,2}}\, \mathcal{H}\, e^{i\theta I_{x,2}} \quad , \tag{II.27}$$

$$\rho'(0) = e^{-i\theta I_{x,2}}\, \rho(0)\, e^{i\theta I_{x,2}} \quad , \tag{II.28a}$$

$$\begin{aligned} \rho(t) &= e^{-i\mathcal{H}t}\, \rho(0)\, e^{i\mathcal{H}t} \\ &= e^{i\theta I_{x,2}}\, e^{-i\mathcal{H}'t}\, \rho'(0)\, e^{i\mathcal{H}'t}\, e^{-i\theta I_{x,2}} \quad . \end{aligned} \tag{II.28b}$$

The calculation of $\mathcal{H}'$ is straightforward:

$$\begin{aligned} \mathcal{H}' &= -2\omega_1 (\cos\theta\, I_{x,1} - \sin\theta\, I_{x,3}) + \omega_Q (\sin\theta\, I_{x,1} + \cos\theta\, I_{x,3}) \\ &\qquad - \frac{1}{3}\omega_Q (I_{y,3} - I_{z,3}) \\ &= (\omega_Q \sin\theta - 2\omega_1 \cos\theta) I_{x,1} + (\omega_Q \cos\theta + 2\omega_1 \sin\theta) I_{x,3} \\ &\qquad - \frac{1}{3}\omega_Q (I_{y,3} - I_{z,3}) \quad . \end{aligned} \tag{II.29}$$

When θ is chosen such that $\omega_Q \sin\theta = 2\omega_1 \cos\theta$, the term proportional to $I_{x,1}$ vanishes. We define

$$\omega_{eff} = [\omega_Q^{\,2} + 4\omega_1^{\,2}]^{1/2} \quad , \tag{II.30a}$$

$$\cos\theta = \frac{\omega_Q}{\omega_{eff}} \quad , \tag{II.30b}$$

$$\sin\theta = \frac{2\omega_1}{\omega_{eff}} \quad , \tag{II.30c}$$

and the rotated Hamiltonian becomes

$$\mathcal{H}' = \omega_{eff}\, I_{x,3} - \frac{1}{3}\,\omega_Q\,(I_{y,3} - I_{z,3}) \tag{II.31a}$$

$$\equiv \mathcal{H}_1' + \mathcal{H}_2' \quad . \tag{II.31b}$$

The reason for performing the rotation is now apparent: $[\mathcal{H}_1', \mathcal{H}_2'] = 0$ and thus

$$\rho(\tau) = e^{i\theta I_{x,2}}\, e^{-i\mathcal{H}_2' t}\, e^{-i\mathcal{H}_1' t}\, \rho'(0)\, e^{i\mathcal{H}_1' t}\, e^{i\mathcal{H}_2' t}\, e^{-i\theta I_{x,2}} \quad . \tag{II.32}$$

The effect of the Hamiltonian is described by a series of simple rotations. For illustrative purposes, let's calculate the value of $a_{z,2}$ in the expansion of $\rho(t)$ when $\rho(0) = I_{z,1}$:

$$\rho'(0) = \cos\frac{\theta}{2}\, I_{z,1} + \sin\frac{\theta}{2}\, I_{y,2} \quad , \tag{II.33}$$

$$e^{-i\mathcal{H}_1' t}\, \rho'(0)\, e^{i\mathcal{H}_1' t} = (\cos\frac{\theta}{2})[\cos\frac{\omega_{eff} t}{2}\, I_{z,1} - \sin\frac{\omega_{eff} t}{2}\, I_{z,2}]$$

$$+ (\sin\frac{\theta}{2})[\cos\frac{\omega_{eff} t}{2}\, I_{y,2} + \sin\frac{\omega_{eff} t}{2}\, I_{y,1}] \ , \tag{II.34}$$

$$e^{-i\mathcal{H}_2' t}\, e^{-i\mathcal{H}_1' t}\, \rho'(0)\, e^{i\mathcal{H}_1' t}\, e^{i\mathcal{H}_2' t}$$

$$= (\cos\frac{\theta}{2})\{\cos\frac{\omega_{eff} t}{2}\, [\cos\frac{\omega_Q t}{2}\, I_{z,1} + \sin\frac{\omega_Q t}{2}\, I_{z,2}]$$

$$- \sin \frac{\omega_{eff} t}{2} [\cos \frac{\omega_Q t}{2} I_{z,2} - \sin \frac{\omega_Q t}{2} I_{z,1}]\}$$

$$+ (\sin \frac{\theta}{2}) \{\cos \frac{\omega_{eff} t}{2} [\cos \frac{\omega_Q t}{2} I_{y,2} + \sin \frac{\omega_Q t}{2} I_{y,1}]$$

$$+ \sin \frac{\omega_{eff} t}{2} [\cos \frac{\omega_Q t}{2} I_{y,1} + \sin \frac{\omega_Q t}{2} I_{y,2}]\}$$

$$= (\cos \frac{\theta}{2}) [\cos \frac{(\omega_{eff} - \omega_Q) t}{2} I_{z,1} + \sin \frac{(\omega_{eff} + \omega_Q) t}{2} I_{z,2}]$$

$$+ (\sin \frac{\theta}{2}) [\cos \frac{(\omega_{eff} + \omega_Q) t}{2} I_{y,2} + \sin \frac{(\omega_{eff} + \omega_Q) t}{2} I_{y,1}] \quad . \quad (II.35)$$

The effect on the operators of the last rotation about $I_{x,2}$ is as follows:

$$I_{y,1} \rightarrow \cos \frac{\theta}{2} I_{y,1} + \sin \frac{\theta}{2} I_{z,2} \quad ,$$

$$I_{y,2} \rightarrow \cos \frac{\theta}{2} I_{y,2} + \sin \frac{\theta}{2} I_{z,1} \quad ,$$

$$I_{z,1} \rightarrow \cos \frac{\theta}{2} I_{z,1} - \sin \frac{\theta}{2} I_{y,2} \quad ,$$

$$I_{z,2} \rightarrow \cos \frac{\theta}{2} I_{z,2} - \sin \frac{\theta}{2} I_{y,1} \quad .$$

We find $a_{z,2}$ at last by picking out terms proportional to $I_{z,2}$:

$$a_{z,2}(t) = -\cos^2\frac{\theta}{2}\left[\sin\frac{(\omega_{eff}-\omega_Q)t}{2}\right] + \sin^2\frac{\theta}{2}\left[\sin\frac{(\omega_{eff}+\omega_Q)t}{2}\right]$$

$$= -\frac{1}{2}\left(1+\frac{\omega_Q}{\omega_{eff}}\right)\sin\frac{(\omega_{eff}-\omega_Q)t}{2} + \frac{1}{2}\left(1-\frac{\omega_Q}{\omega_{eff}}\right)\sin\frac{(\omega_{eff}+\omega_Q)t}{2}$$

(II.36a)

$$= \left(\cos\frac{\omega_{eff}t}{2}\right)\left(\sin\frac{\omega_Q t}{2}\right) - \left(\frac{\nu_Q}{\nu_{eff}}\right)\left(\sin\frac{\omega_{eff}t}{2}\right)\left(\cos\frac{\omega_Q t}{2}\right)$$

(II.36b)

$$= (\cos\pi\,\nu_{eff}\,t)\,(\sin\pi\,\nu_Q\,t) - \left(\frac{\nu_Q}{\nu_{eff}}\right)(\sin\pi\,\nu_{eff}\,t)\,(\cos\pi\,\nu_Q\,t)\ .$$

(II.36c)

Needless to say, one sample calculation is enough! Complete results (in frequency units) can be found in Table II.7.

Three additional points should be made concerning these equations. The first is what to do if your rf phase is not zero but rather some value ϕ, so that

$$\mathcal{H}_\phi = -2\omega_1\,(\cos\phi\ I_{x,1} + \sin\phi\ I_{y,1}) + \frac{2}{3}\,\omega_Q\ I_{xy,3}\quad . \qquad \text{(II.37)}$$

Relief is but a rotation away: since $[I_{z,1}, I_{xy,3}] = 0$,

$$\mathcal{H}_\phi = e^{-2i\phi I_{z,1}}\,\mathcal{H}_0\,e^{2i\phi I_{z,1}}\quad , \qquad \text{(II.38)}$$

where $\mathcal{H}_0$ here signifies our familiar Hamiltonian with $\phi = 0$.

By rewriting

Table II.7

Spin-1 Evolution Under the Hamiltonian $\mathcal{H}_Q+\mathcal{H}_{rf}$

$$\mathcal{H} = -2\nu_1 I_{x,1} + \frac{2}{3}\nu_Q (I_{x,3}-I_{y,3})$$

$$\Delta\nu = 0 \qquad \nu_{eff} = [\nu_Q^2 + 4\nu_1^2]^{1/2}$$

various initial density matrices

$\rho(0) = I_{z,1}$

$$a_{z,1} = (\cos\pi\nu_{eff}t)(\cos\pi\nu_Q t) + \frac{\nu_Q}{\nu_{eff}}(\sin\pi\nu_{eff}t)(\sin\pi\nu_Q t)$$

$$a_{z,2} = (\cos\pi\nu_{eff}t)(\sin\pi\nu_Q t) - \frac{\nu_Q}{\nu_{eff}}(\sin\pi\nu_{eff}t)(\cos\pi\nu_Q t)$$

$$a_{y,1} = \frac{2\nu_1}{\nu_{eff}}(\sin\pi\nu_{eff}t)(\cos\pi\nu_Q t)$$

$$a_{y,2} = -\frac{2\nu_1}{\nu_{eff}}(\sin\pi\nu_{eff}t)(\sin\pi\nu_Q t)$$

$\rho(0) = I_{z,2}$

$$a_{z,1} = -(\cos\pi\nu_{eff}t)(\sin\pi\nu_Q t) + \frac{\nu_Q}{\nu_{eff}}(\sin\pi\nu_{eff}t)(\cos\pi\nu_Q t)$$

$$a_{z,2} = (\cos\pi\nu_{eff}t)(\cos\pi\nu_Q t) + \frac{\nu_Q}{\nu_{eff}}(\sin\pi\nu_{eff}t)(\sin\pi\nu_Q t)$$

$$a_{y,1} = -\frac{2\nu_1}{\nu_{eff}}(\sin\pi\nu_{eff}t)(\sin\pi\nu_Q t)$$

$$a_{y,2} = -\frac{2\nu_1}{\nu_{eff}}(\sin\pi\nu_{eff}t)(\cos\pi\nu_Q t)$$

$\rho(0) = I_{y,1}$

$$a_{y,1} = (\cos\pi\nu_{eff}t)(\cos\pi\nu_Q t) - \frac{\nu_Q}{\nu_{eff}}(\sin\pi\nu_{eff}t)(\sin\pi\nu_Q t)$$

$$a_{y,2} = -(\cos\pi\nu_{eff}t)(\sin\pi\nu_Q t) - \frac{\nu_Q}{\nu_{eff}}(\sin\pi\nu_{eff}t)(\cos\pi\nu_Q t)$$

$$a_{z,1} = -\frac{2\nu_1}{\nu_{eff}}(\sin\pi\nu_{eff}t)(\cos\pi\nu_Q t)$$

$$a_{z,2} = -\frac{2\nu_1}{\nu_{eff}}(\sin\pi\nu_{eff}t)(\sin\pi\nu_Q t)$$

Table II.7 continued

$\rho(0) = I_{y,2}$

$$a_{y,1} = (\cos\pi\nu_{eff}t)(\sin\pi\nu_Q t) + \frac{\nu_Q}{\nu_{eff}}(\sin\pi\nu_{eff}t)(\cos\pi\nu_Q t)$$

$$a_{y,2} = (\cos\pi\nu_{eff}t)(\cos\pi\nu_Q t) - \frac{\nu_Q}{\nu_{eff}}(\sin\pi\nu_{eff}t)(\sin\pi\nu_Q t)$$

$$a_{z,1} = -\frac{2\nu_1}{\nu_{eff}}(\sin\pi\nu_{eff}t)(\sin\pi\nu_Q t)$$

$$a_{z,2} = \frac{2\nu_1}{\nu_{eff}}(\sin\pi\nu_{eff}t)(\cos\pi\nu_Q t)$$

$\rho(0) = I_{x,1}$

$$a_{x,1} = \frac{\nu_Q^2}{\nu_{eff}^2}(\cos 2\pi\nu_{eff}t) + \frac{4\nu_1^2}{\nu_{eff}^2}$$

$$a_{x,2} = \frac{\nu_Q}{\nu_{eff}}(\sin 2\pi\nu_{eff}t)$$

$$a_{x,3} = -\frac{2\nu_1\nu_Q}{\nu_{eff}^2}[1 - \cos 2\pi\nu_{eff}t]$$

$\rho(0) = I_{x,2}$

$$a_{x,1} = -\frac{\nu_Q}{\nu_{eff}}(\sin 2\pi\nu_{eff}t)$$

$$a_{x,2} = \cos 2\pi\nu_{eff}t$$

$$a_{x,3} = -\frac{2\nu_1}{\nu_{eff}}(\sin 2\pi\nu_{eff}t)$$

$\rho(0) = I_{z,3}$

$$a_{x,1} = \frac{\nu_1\nu_Q}{\nu_{eff}^2}[1 - \cos 2\pi\nu_{eff}t]$$

$$a_{x,2} = -\frac{\nu_1}{\nu_{eff}}(\sin 2\pi\nu_{eff}t)$$

$$a_{x,3} = \frac{2\nu_1^2}{\nu_{eff}^2}[1 - \cos 2\pi\nu_{eff}t]$$

$$a_{z,3} = 1$$

Table II.7 continued

$\rho(0) = I_{y,3}$

$$a_{x,1} = \frac{\nu_1 \nu_Q}{\nu_{eff}^2} [1 - \cos 2\pi\nu_{eff} t] \qquad a_{y,3} = 1$$

$$a_{x,2} = - \frac{\nu_1}{\nu_{eff}} (\sin 2\pi\nu_{eff} t)$$

$$a_{x,3} = \frac{2\nu_1^2}{\nu_{eff}^2} [1 - \cos 2\pi\nu_{eff} t]$$

$\rho(0) = I_{x,3}$

$$a_{x,1} = - \frac{2\nu_1 \nu_Q}{\nu_{eff}^2} [1 - \cos 2\pi\nu_{eff} t]$$

$$a_{x,2} = \frac{2\nu_1}{\nu_{eff}} (\sin 2\pi\nu_{eff} t)$$

$$a_{x,3} = \frac{4\nu_1^2}{\nu_{eff}^2} (\cos 2\pi\nu_{eff} t) + \frac{\nu_Q^2}{\nu_{eff}^2}$$

$$\rho(t) = e^{-i\mathcal{H}_\phi t}\, \rho(0)\, e^{i\mathcal{H}_\phi t} \tag{II.39a}$$

as

$$\rho(t) = e^{-2i\phi I_{z,1}}\, e^{-i\mathcal{H}_0 t}\, [e^{2i\phi I_{z,1}}\, \rho(0)\, e^{-2i\phi I_{z,1}}]\, e^{i\mathcal{H}_0 t}\, e^{2i\phi I_{z,1}} \quad , \tag{II.39b}$$

the expressions in Table II.7 can be used in the case of general rf phase <u>if</u> the initial density matrix is first rotated about the z-axis and the resulting evolved operators are then rotated back to the initial frame.

The second point to make regarding these expressions is that they are equivalent to equations derived by Brewer and Hahn [69] for optical three-level systems and later modified by Gold and Hahn [68] for NMR. A term-by-term concordance will not be given here; instead what is interesting is to compare the method of solution. Hahn and co-workers solved for the eight unknowns in a set of eight coupled differential equations (Bloch equations without relaxation terms). We on the other hand started with the integrated equation of motion for ρ and manipulated its form so that the effect of the Hamiltonian could be expressed as a series of rotations based on the properties of angular momentum operators.

The final point worth noting with regard to the results in Tables II.6 and II.7 is their usefulness in analyzing real pulse sequences. True, the three-level Hamiltonian in general contains non-zero offset, rf, and quadrupole terms, and for this general Hamiltonian

neither set of equations is applicable. For the deuterium chemical shielding experiments we are interested in, however, it is usually the case that $\omega_Q \approx \omega_1 >> \Delta\omega$. During rf pulses (typically 3 to 30 μsec long), the puny effects of $\mathcal{H}_{off}$ can be ignored, and Table II.7 provides a nearly exact description of density matrix evolution. During the longer periods of time between pulses when $\mathcal{H}_{rf} = 0$, the equations of Table II.6 govern the evolution. An analytical expression for an entire pulse sequence can thus be generated by stringing together the appropriate two-term-Hamiltonian formulas. Only when a pulse is exceptionally long or when $\Delta\omega$ is on purpose made large is the exact solution discussed in the next section necessary.

2.5.4 The General Hamiltonian

The most general three-level Hamiltonian,

$$\mathcal{H} = -2\Delta\omega\, I_{z,1} - 2\omega_1\, (\cos\phi\, I_{x,1} + \sin\phi\, I_{y,1}) + \frac{2}{3}\,\omega_Q\, I_{xy,3} \quad ,(II.40)$$

can be expressed in the basis set $\{|x\rangle, \ |y\rangle, \ |z\rangle\}$ as

$$\mathcal{H} = \begin{pmatrix} \omega_Q/3 & -i\Delta\omega & -\omega_1 \sin\phi \\ i\Delta\omega & \omega_Q/3 & -\omega_1 \cos\phi \\ -\omega_1 \sin\phi & -\omega_1 \cos\phi & -2\omega_Q/3 \end{pmatrix} \quad . \qquad (II.41)$$

This 3x3 hermitian matrix can be diagonalized numerically (using the Jacobi transformation method, for example) or analytically (using the formula for the roots of a cubic equation); the result is

$$\mathcal{H} = U \Lambda U^{\dagger} \quad , \tag{II.42}$$

where Λ is the diagonal matrix of energy eigenvalues and U is the complex and unitary matrix of eigenvectors. As stated in Chapter I and in Appendix A, the density matrix equation of motion is

$$\rho(t) = U e^{-i\Lambda t} U^{\dagger} \rho(0) U e^{i\Lambda t} U^{\dagger} \quad , \tag{II.43}$$

where $e^{-i\Lambda t}$ is diagonal with $(e^{-i\Lambda t})_{jj} = e^{-i\Lambda_{jj} t}$. Successive steps in the pulse sequence are computed by successive application of Eq. II.43. Although an analytical solution for $\rho(t)$ is possible, it will in general be so complicated and so heavy laden with inverse trigonometric functions that no trace of physical insight is extractable. Instead we will use computed values of the operator coefficients $a_{p,i}$ that characterize $\rho(t)$ to graph the course of evolution through the nine dimensions of "Vega space".

2.6 Pulse Sequences for Creation and Detection of Double-Quantum Coherence

Our reasons for studying double-quantum deuterium spectra were discussed in section 2.3, and the operator algebra techniques needed to analyze the dynamics of a spin-one system were presented in the previous section. We now wish to consider specific pulse sequences to excite and detect double-quantum coherence. Our strategy is shaped both by the nature of the sample and the capabilities of our spectrometer. Typically we will be interested in examining powdered samples because they are easier to prepare and easier to study than single

crystals. Hence there will be a wide range of ν_Q values (and on a much smaller scale, a range of $\Delta\nu$ values) for the pulse sequence to accomodate. (Note that our change in focus from theory to applications is mirrored by a switch from ω's to ν's.)

It is helpful to get a feel for the magnitude of the quantities $\Delta\nu$, ν_1, and ν_Q which appear in the Hamiltonian. As discussed in section 1.5.4, the quadrupole frequency experienced by a given nucleus depends on the angles θ and ϕ which describe the orientation of the magnetic field H_0 in the principal axis system of the local electric field gradient tensor:

$$\nu_Q(\mathrm{Hz}) = \nu_{Qc}\,[(3\cos^2\theta-1) + \eta_Q \sin^2\theta \cos 2\phi] \quad , \qquad \text{(II.44)}$$

where η_Q is the asymmetry parameter of the field gradient. Some representative values of ν_{Qc} are 7.1 KHz for the methyl deuterons in hexamethylbenzene (subject to $\hat{C}_3$ methyl group rotation and $\hat{C}_6$ ring rotation), 36 KHz for aromatic deuterons on a rapidly spinning ring, and 72 KHz for aromatic deuterons on a stationary molecule [40].

The size of $\Delta\nu$ is largely in the hands of the spectroscopist, but a typical value is 1-2 KHz in a double-quantum experiment. The chemical shift is the interesting contribution to the offset frequency, and the range in chemical shift values due to molecular orientation is on the order of 5-20 ppm, or 140-550 Hz in a field of 42 kilogauss (180 MHz proton resonance).

Finally, the size of ν_1 is governed by the technical specifications of the spectrometer: amplifier power, the Q factor of the coil, its

propensity to arc at high voltage, etc. I found the usual upper limit for ν_1 to be on the order of 80 KHz, corresponding to a 3 μsec 90° pulse length.

These numbers have been paraded to support the statement made earlier that ν_Q and ν_1 are likely to be comparable in magnitude, whereas $\Delta\nu$ is apt to be considerably smaller. Because ν_1 is not gigantic compared to other terms in the Hamiltonian, we are not in the hard pulse regime (as will be the case in Chapters IV and V when the proton NMR of molecules dissolved in liquid crystals is considered). That is to say, the effect of a pulse is not governed solely by $\mathcal{H}_{rf}$--terms of similar size, in particular $\mathcal{H}_Q$, must be included in the analysis.

With this in mind, we turn at last to the four pulse sequences shown in Fig. II.7. (These have been discussed before [40,65], but a brief recapitulation here will make subsequent sections clearer.) Sequence A is the simplest means of preparing and detecting double-quantum coherence. The weak pulse at the beginning is "tailored" in terms of pulse length and rf strength to rotate the initial density matrix $I_{z,1}$ directly into the double-quantum coherence state $I_{z,2}$. (The effective rotation axis is in fact $I_{z,3}$; see section 2.8.1.) During the interval τ, the double-quantum coherence evolves but cannot be detected until a second pulse transfers coherence to $I_{x,1}$ or $I_{y,1}$. The transverse magnetization which accompanies single-quantum coherence is sampled as a function of τ; the Fourier transform of this point-by-point FID is the desired double-quantum spectrum.

Although simple, sequence A has its problems. The first is the difficulty of measuring an NMR signal directly after an rf pulse:

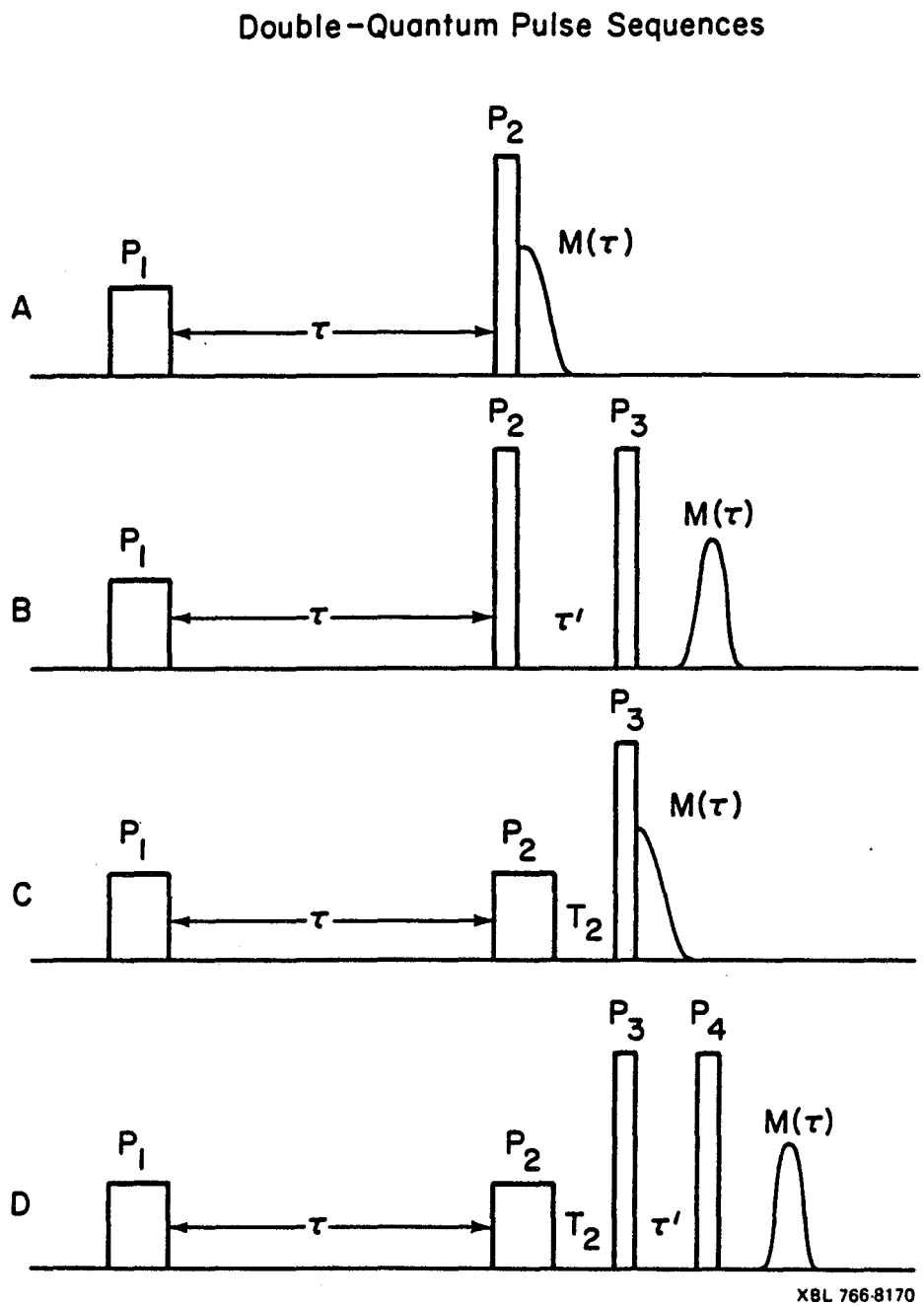

Figure II.7 Four possible pulse sequences for the excitation and detection of double-quantum coherence. Sequence A is most convenient if the sample is a single crystal, but sequence D works best for a powder. In each case, DQ coherence evolves during the variable delay τ.

probe "ringing" due to slow dissipation of rf energy in the tuned probe circuit can completely swamp any sample response. If one waits 20-30 μsec for the ringing to go away, the signal often disappears too: deuterons subject to different values of ν_Q evolve at differing rates from $I_{x,1}$ to $I_{x,2}$ or $I_{y,1}$ to $I_{y,2}$. This dephasing destroys the signal. As mentioned earlier, the cure is the quadrupole echo of Sequence B. The additional pulse after a delay τ' refocuses the errant single-quantum coherences, which then echo after an additional time τ'. (See section 2.9 for details.) If τ' is greater than the ringdown time, the transverse magnetization can be cleanly sampled.

The second problem with Sequence A is that there is no guarantee the entire chemical shielding powder pattern will appear with the same sign. As we will see, a certain amount of distortion of the powder lineshape is unavoidable, but it helps to avoid undue zero-crossing and cancellation of positive and negative intensity. One way of bettering our chances is to use a second weak pulse after DQ evolution to rotate $I_{z,2}$ back to $I_{z,1}$. If the first and second pulses are the same, and on resonance, then spin-inversion transition arguments as in section 4.6.3 indicate that all transitions comprising the DQ lineshape will have the same phase. Of course, another pulse must be applied as in Sequence C to rotate double-quantum-dependent population into double-quantum-dependent magnetization. (Inadequencies in this pulse may also bring about cancellation of intensity, but that can't be helped.) An additional advantage to Sequence C accrues if the time between the second and third pulses is made greater than the transverse relaxation time T_2: unwanted single-quantum coherences inadvertently created by the weak pulses will die away while the double-quantum

information is stored as a longer-lived population.

Saving the best for last, Sequence D combines the improvements introduced in B and C and thus is the DQ pulse sequence we will concentrate on henceforth.

2.7 On the Nature of Powders

In going from a fixed value of ν_Q to the continuous range of ν_Q values in a polycrystalline sample, it is best to remember this maxim: a powder, like politics, requires the art of compromise. No given combination of pulse length and strength can be ideal for all crystallites; instead we seek the pulse or pulse sequence with the best average performance. To be specific, we want the chemical shielding tensor lineshape with as much overall intensity and as little distortion as possible.

In the absence of broadening, the lineshape $L(\sigma)$ that results from a particular experiment is given by

$$L(\sigma) = L_0(\sigma)\ T(\sigma) \quad , \qquad \text{(II.45)}$$

where $L_0(\sigma)$ is the undistorted and characteristic powder lineshape associated with a particular set of principal values for the chemical shielding tensor (as in Fig. II.3) and $T(\sigma)$ is a <u>transfer function</u> which describes the efficiency of the pulse sequence for each value of σ ($-1.0 \leq T(\sigma) \leq 1.0$).

The functional form of $L_0(\sigma)$ depends on the value of the chemical shielding asymmetry parameter; when $\eta_{cs} = 0$, one finds [24]

$$L_0(\sigma) = \frac{1}{2}\,[(3\sigma_0)(\sigma-\bar{\sigma}+\sigma_0)]^{-1/2} \quad . \tag{II.46}$$

As noted earlier, a discontinuity (modified in "real life" by broadening) occurs at one end of the lineshape where $\sigma = \sigma_{\perp} = \bar{\sigma} - \sigma_0$. To generate an L_0 on the computer that is n points wide, the following non-normalized formula is useful:

$$L_0(1) = [2(n-1)]^{1/2} \quad , \tag{II.47a}$$

$$L_0(i) = \left(\frac{n-1}{i-1}\right)^{1/2} \quad , \quad i = 2,3,\ldots,n \quad . \tag{II.47b}$$

When $\eta_{cs} \neq 0$, $L_0(\sigma)$ is described by an elliptic integral that can be readily approximated by three-term polynomials of σ [40].

The transfer function $T(\sigma)$ cannot be obtained <u>directly</u> from the pulse sequence because σ (a component of the offset frequency $\Delta\nu$) is small in comparison to that other variable quantity, ν_Q. Indeed it is $T(\nu_Q)$, the efficiency of the sequence as a function of the quadrupole splitting, that must be calculated first, using either the equations of Table II.6 and II.7 or the numerical solution provided by the computer. The relationship between the chemical shielding transfer function and the quadrupole transfer function is governed by the relative orientation of the chemical shielding and electric field gradient tensors. For each crystallite, the orientation of the external field H_0 relative to the two sets of principal axes generates a value for ν_Q and for σ. The former determines the efficiency of the pulse sequence and thus the intensity associated with the crystallite; the latter determines at what point in the chemical

shielding lineshape this intensity makes a contribution.

In the general case, the computation of $T(\sigma)$ requires extensive averaging over orientation. For the sake of clarity and speed, however, we will mainly focus on only the simplest case: both tensors axially symmetric ($\eta_Q = \eta_{cs} = 0$) with unique principal axes parallel, as would be expected in the case of rapid molecular motion about an n-fold axis ($n > 2$). We then can write

$$\nu_Q = \nu_{Qc} \ (3 \cos^2\theta - 1) \quad , \qquad \text{(II.48a)}$$

$$\Delta\nu = \sigma = \bar{\sigma} + \sigma_0 \ (3 \cos^2\theta - 1) \quad . \qquad \text{(II.48b)}$$

Values for ν_Q range from $-\nu_{Qc}$ to $2\nu_{Qc}$; values for σ range from $\bar{\sigma} - \sigma_0$ to $\bar{\sigma} + 2\sigma_0$. Because the tensors are aligned, only one ν_Q value is associated with each σ value; as a result, $T(\sigma)$ is identical in form to $T(\nu_Q)$.

More complicated tensor orientations will be considered briefly in section 2.11.

2.8 Preparing Double-Quantum Coherence: An In-Depth Report

Double-quantum coherence...we know what it is, we know what it's good for, but how can we get as much of it as we want? How best can we succumb to the lure of forbidden transitions? That is the question which will dominate our thoughts in the pages to come. The answer will depend largely on two factors: the nature of the sample (powder or single crystal) and the relative size of ν_1 and ν_Q.

2.8.1 Results for a Fixed Value of ν_Q

Before taking on a powder, we will first consider the details of double-quantum excitation for a single value of ν_Q with $\Delta\nu = 0$, a problem discussed by several of my Pines group colleagues [40,63b, 65]. For the hard-pulse limit ($\nu_1 >> \nu_Q$) a preparation sequence was presented earlier during our Rubik's cube ruminations: x-pulse, delay, ± x-pulse, with the length of the delay given by

$$\sin\omega_Q\tau = 1 \quad \text{or} \quad \tau = \frac{\pi}{2\omega_Q} = \frac{1}{4\nu_Q} \quad . \tag{II.49}$$

An effective Hamiltonian (see section 4.6 and Appendix A) can be readily calculated when the two pulses are 180° out of phase:

$$\begin{aligned}\mathcal{H}_{eff} &= e^{-i\pi I_{x,1}}[\tfrac{2}{3}\,\omega_Q\,(I_{x,3}-I_{y,3})]e^{i\pi I_{x,1}} \\ &= \tfrac{2}{3}\,\omega_Q\,(I_{z,3}-I_{x,3}) \\ &= \omega_Q\,I_{z,3} - \tfrac{1}{3}\,\omega_Q\,(I_{x,3}-I_{y,3}) \quad .\end{aligned} \tag{II.50}$$

The $I_{z,3}$ term in $\mathcal{H}_{eff}$ rotates the initial density matrix $I_{z,1}$ into double-quantum coherence described by $I_{z,2}$.

When $\nu_1 \approx \nu_Q$, a single pulse can be used to create DQ coherence; by choosing ν_1 and the pulse length t correctly, 100% efficiency is achieved. The key is Eq. II.36c. To make $|a_{z,2}| = 1$ requires

$$|\sin\pi\,\nu_Q t| = 1 \tag{II.51a}$$

and

$$|\cos\pi\ \nu_{eff}\ t| = 1 \quad . \tag{II.51b}$$

The first condition puts a limitation on t in terms of an integer m:

$$t = \frac{2m-1}{2\ \nu_Q} \quad , \quad m = 1,2,\ldots \tag{II.52a}$$

The second condition then determines allowed values for ν_1:

$$\nu_{eff} = [\nu_Q{}^2 + 4\nu_1{}^2]^{1/2} = \frac{k}{t}\ , \ k = 1,2,\ldots$$

$$= \frac{2k}{2m-1}\ \nu_Q \quad , \tag{II.52b}$$

$$\nu_1 = \frac{1}{2}\ [(\frac{2k}{2m-1})^2 - 1]^{1/2}\ \nu_Q \qquad (k \geq m) \quad . \tag{II.52c}$$

With two "knobs" to turn, it's easy experimentally to conveniently convert Zeeman populations totally into DQ coherence.

As an aside, the same method can be used to create perfect 180° pulses for $I_{z,1}$ or $I_{z,2}$, with applications to inversion-recovery T_1 measurements or double-quantum spin echoes. In Table II.7, the same formula describes $a_{z,1}(t)$ for $\rho_0 = I_{z,1}$ and $a_{z,2}(t)$ for $\rho_0 = I_{z,2}$:

$$\left.\begin{matrix} a_{z,1}(t) \\ a_{z,2}(t) \end{matrix}\right\} = (\cos\pi\ \nu_{eff}\ t)(\cos\pi\ \nu_Q t) + \frac{\nu_Q}{\nu_{eff}}\ (\sin\pi\ \nu_{eff}\ t)(\sin\pi\ \nu_Q t). \tag{II.53}$$

Inverting the sign of the coefficient requires

$$\cos\pi\,\nu_{eff}\,t = 1 \quad \text{and} \quad \cos\pi\,\nu_Q t = -1$$

<u>or</u>

$$\cos\pi\,\nu_{eff}\,t = -1 \quad \text{and} \quad \cos\pi\,\nu_Q t = 1 \quad . \tag{II.54}$$

The first set of conditions leads to

$$t = \frac{2m-1}{\nu_Q} \quad \nu_1 = \frac{1}{2}\,[(\frac{2k}{2m-1})^2-1]^{1/2}\,\nu_Q \qquad k,m=1,2,\ldots,k \geq m \tag{II.55a}$$

whereas the second set implies

$$t = \frac{2m}{\nu_Q} \quad \nu_1 = \frac{1}{2}\,[(\frac{2k+1}{2m})^2-1]^{1/2}\,\nu_Q \qquad k,m=1,2,\ldots,k \geq m\,. \tag{II.55b}$$

Back now to the preparation of DQ coherence. When $\nu_1 << \nu_Q$, it is possible to simplify Eq. II.36a as follows:

$$\frac{\omega_Q}{\omega_{eff}} \approx 1 \quad ,$$

$$\omega_{eff}-\omega_Q = [\omega_Q{}^2+4\omega_1{}^2]^{1/2} - \omega_Q$$

$$= \omega_Q[1 + (\frac{1}{2})(\frac{4\omega_1{}^2}{\omega_Q{}^2}) + \ldots] - \omega_Q$$

$$\approx \frac{2\omega_1{}^2}{\omega_Q} \quad ,$$

$$a_{z,2}(t) \approx - \sin \frac{\omega_1^2}{\omega_Q} t \quad . \tag{II.56}$$

A weak pulse thus acts as a rotation about the $I_{z,3}$ axis with an effective frequency $-\nu_1^2/\nu_Q$. Vega and Pines [65] discuss this limiting case in detail.

For a more graphic understanding of evolution during a double-quantum preparation pulse, let us beam down to the $I_{z,1}$, $I_{z,2}$ plane of Vega space. Figure II.8 shows the idealized trajectory of the state-of-the-system vector for $\nu_1 << \nu_Q$: a 90° rotation about the $I_{z,3}$ axis lying perpendicular to the plane. An actual trajectory for ν_Q = 50 KHz and ν_1 = 10 KHz appears in Fig. II.9; the trajectory for ν_Q = 50 KHz and ν_1 = 20 KHz is shown in Fig. II.10. In each case the length of the pulse (125 μsec and 31.25 μsec, respectively) was chosen by the weak-pulse criterion

$$\sin \frac{\omega_1^2}{\omega_Q} t = 1 \quad . \tag{II.57}$$

The scalloped indentations are due to periodic creation of single-quantum coherence; these grow broader and deeper as ν_1 increases. Moreover, it can be seen that Eq. II.57 is, as one would expect, a less accurate guide to good pulse lengths for larger values of ν_1. We can instead use Eqs. II.52a and II.52c with m = k = 2 to optimize the pulse in Fig. II.10:

$$t = \frac{3}{2\nu_Q} = 30 \text{ μsec} \quad , \tag{II.58a}$$

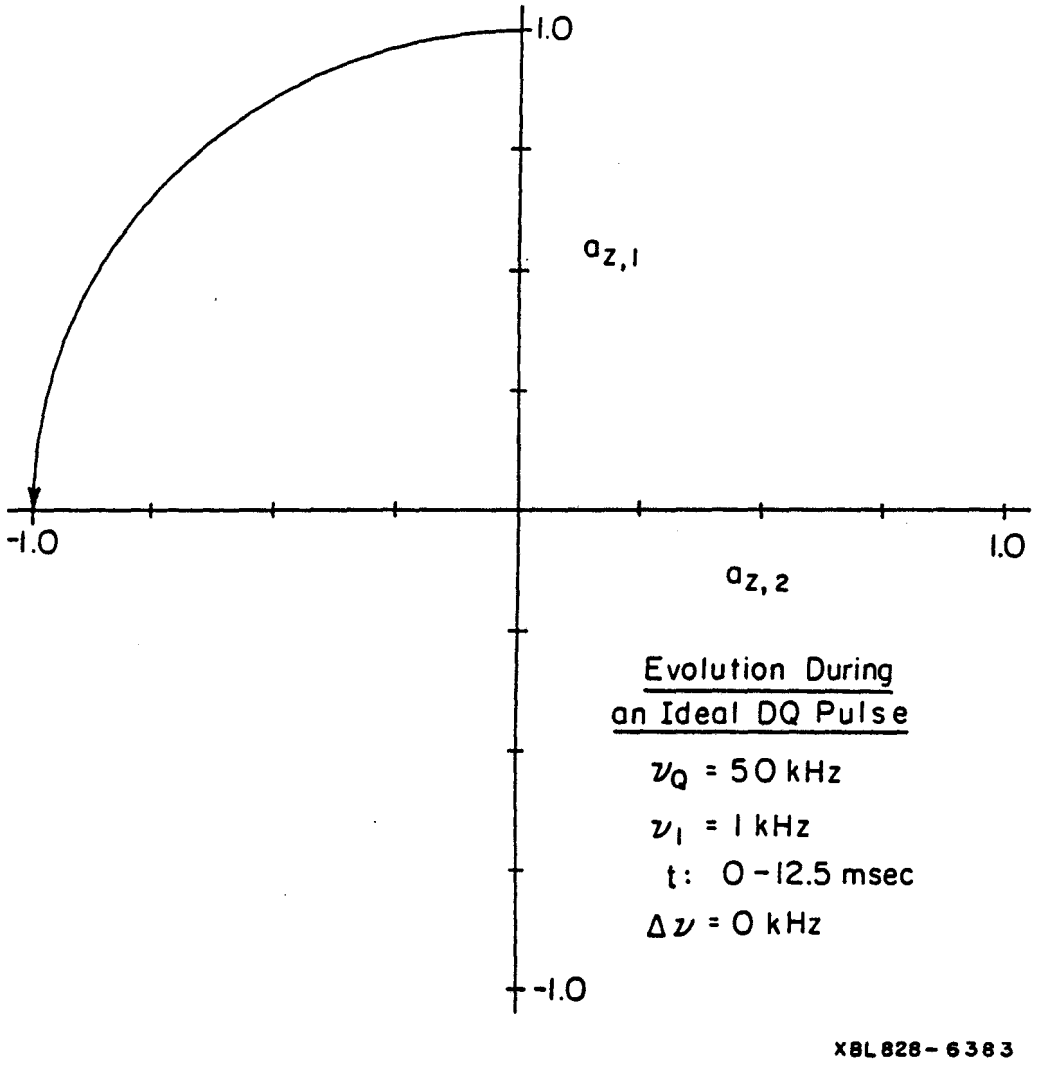

Figure II.8 Spin-system evolution during a double-quantum excitation pulse in the limit that $\nu_1 \ll \nu_Q$. The pulse length t was chosen such that $\sin(2\pi\ \nu_1^2 t/\nu_Q) = 1$. It is seen that the effect of the Hamiltonian is a rotation about the $I_{z,3}$ axis.

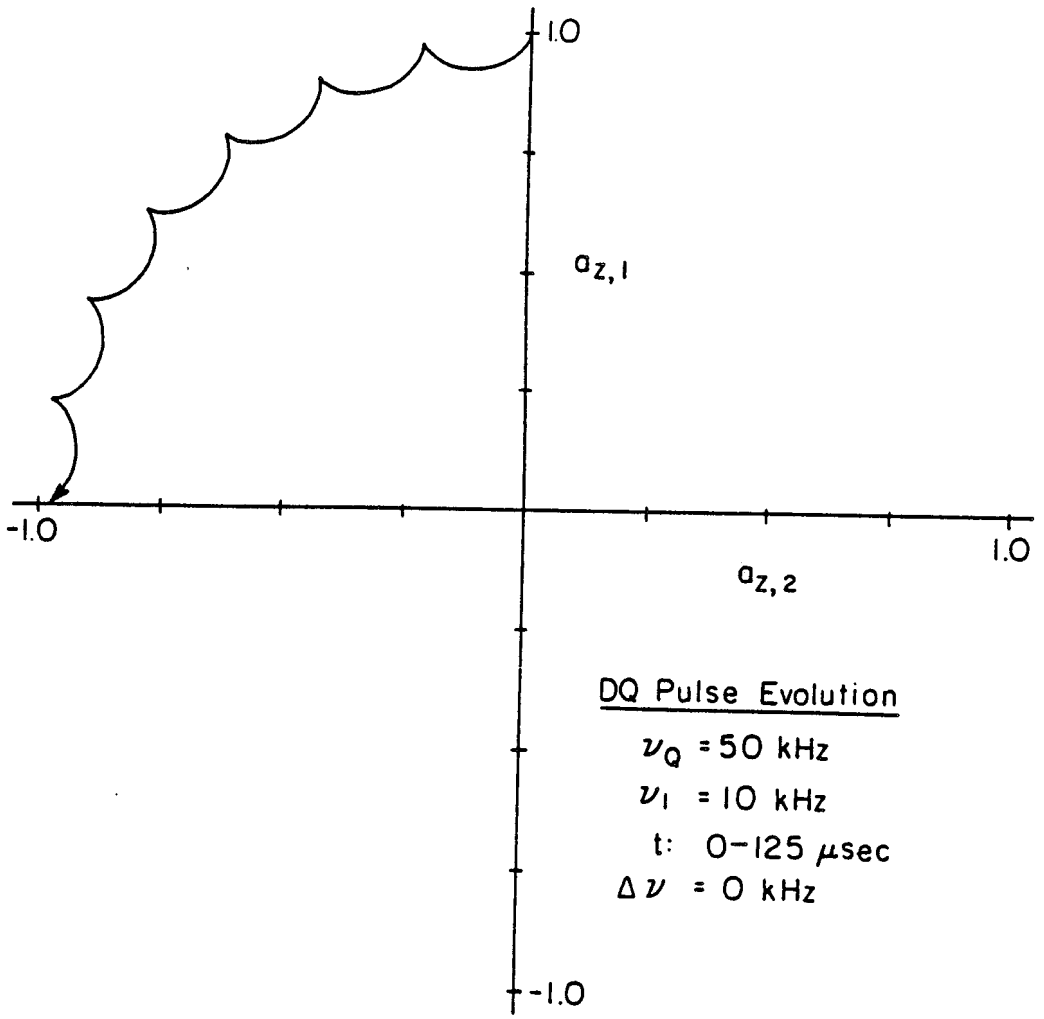

XBL 828-6385

Figure II.9 Spin-system evolution during a DQ excitation pulse for a larger value of ν_1 than in Figure II.8. Again the pulse length t was chosen such that $\sin(2\pi\ \nu_1^2 t/\nu_Q) = 1$. Indentations in the trajectory represent periodic creation of single-quantum coherence.

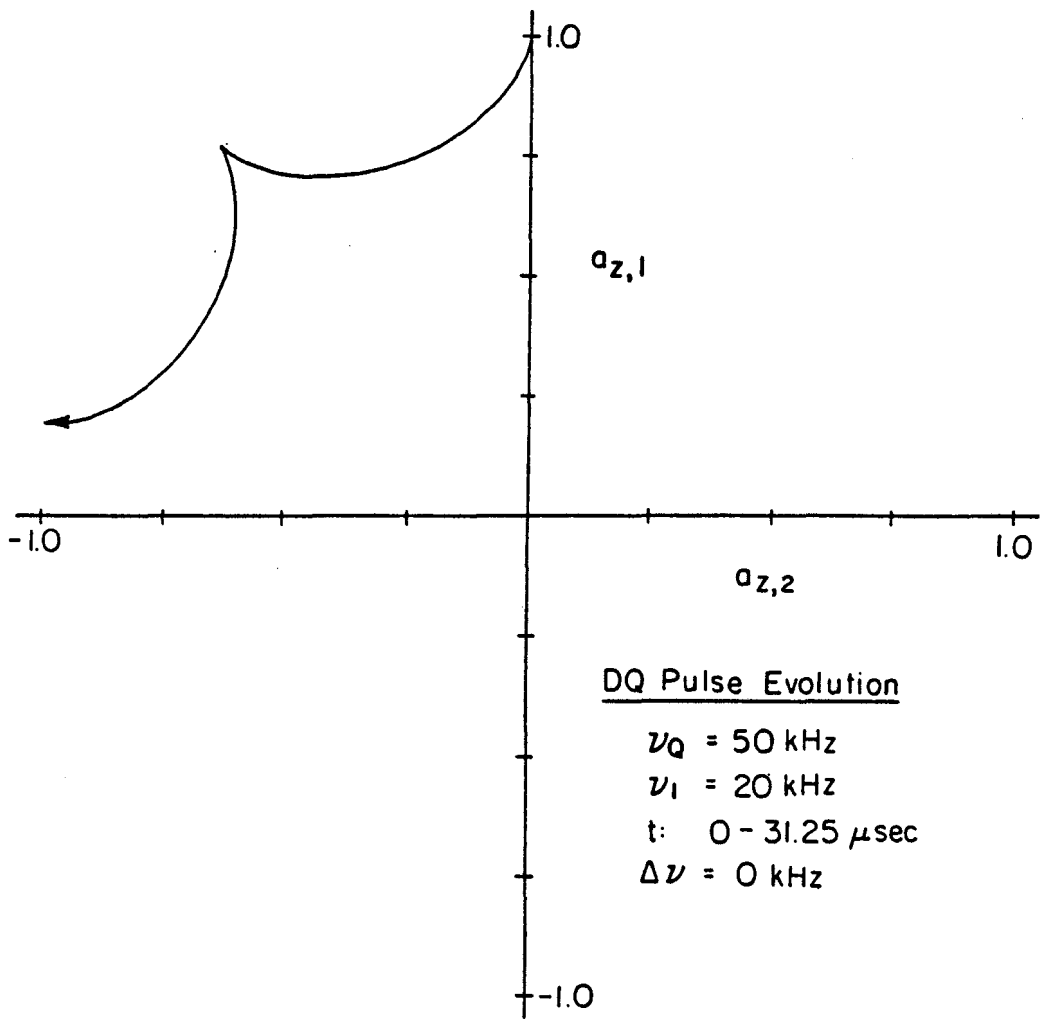

XBL 828-6384

Figure II.10 Another example of a spin vector trajectory in the $I_{z,1}$, $I_{z,2}$ plane during DQ preparation. The weak-pulse formula for creation of DQ coherence [$\sin(2\pi\ \nu_1^2 t/\nu_Q) = 1$] was used, but its growing inaccuracy as ν_1 increases is apparent.

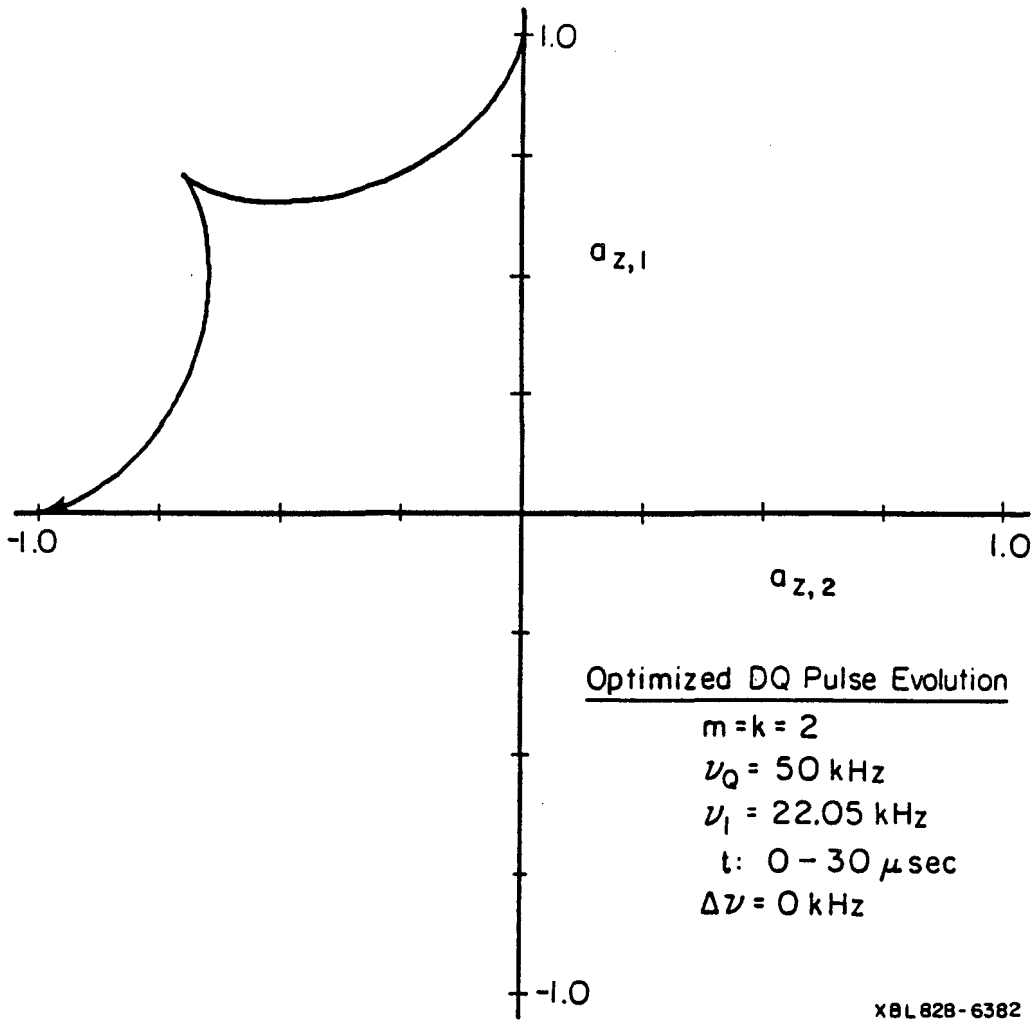

Figure II.11 Double-quantum coherence can be fully prepared ($|a_{z,2}=1|$) for a given value of ν_Q when Eqs. II.52a and II.52c are used to find optimal t and ν_1 values. Integers m and k were chosen to yield t and ν_1 values close to those in Figure II.10.

$$\nu_1 = \frac{1}{2}\,[(\tfrac{4}{3})^2 - 1]^{1/2}\,\nu_Q$$

$$= \frac{\sqrt{7}}{6}\,\nu_Q = 22 \text{ KHz} \quad . \qquad \text{(II.58b)}$$

The result of this adjustment can be seen in Fig. II.11.

Another way to present the effect of an optimized DQ pulse is to plot the operator coefficients $a_{y,1}$, $a_{y,2}$, $a_{z,1}$ and $a_{z,2}$ as a function of time. For ν_Q = 20 KHz and m = k = 1, the optimized pulse strength is ν_1 = 17.3 KHz; $a_{p,i}(t)$ values are plotted in Fig. II.12 versus the length of this pulse, from 0-60 μsec. The optimal point for double-quantum coherence is t = 25 μsec, when $a_{z,2} = -1$. When the pulse is twice as long, the initial density matrix is inverted. At other times, the single-quantum coherences described by $I_{y,1}$ and $I_{y,2}$ are present in addition to DQ coherence.

It is constructive at this point to define the following frame-projection coefficients:

$$a_p \equiv [a_{p,1}^2 + a_{p,2}^2 + a_{p,3}^2]^{1/2} \quad , \quad p = x,y,z;$$

$$a_i \equiv [a_{x,i}^2 + a_{y,i}^2 + a_{z,i}^2]^{1/2} \quad , \quad i = 1,2,3 \quad . \qquad \text{(II.59)}$$

For evolution during an x-phase pulse with $\Delta\nu = 0$, the only non-zero frame-projection coefficients are

$$a_y = [a_{y,1}^2 + a_{y,2}^2]^{1/2} \quad , \quad a_z = [a_{z,1}^2 + a_{z,2}^2]^{1/2} \quad ,$$

$$a_1 = [a_{y,1}^2 + a_{z,1}^2]^{1/2} \quad , \quad a_2 = [a_{y,2}^2 + a_{z,2}^2]^{1/2} \quad . \qquad \text{(II.60)}$$

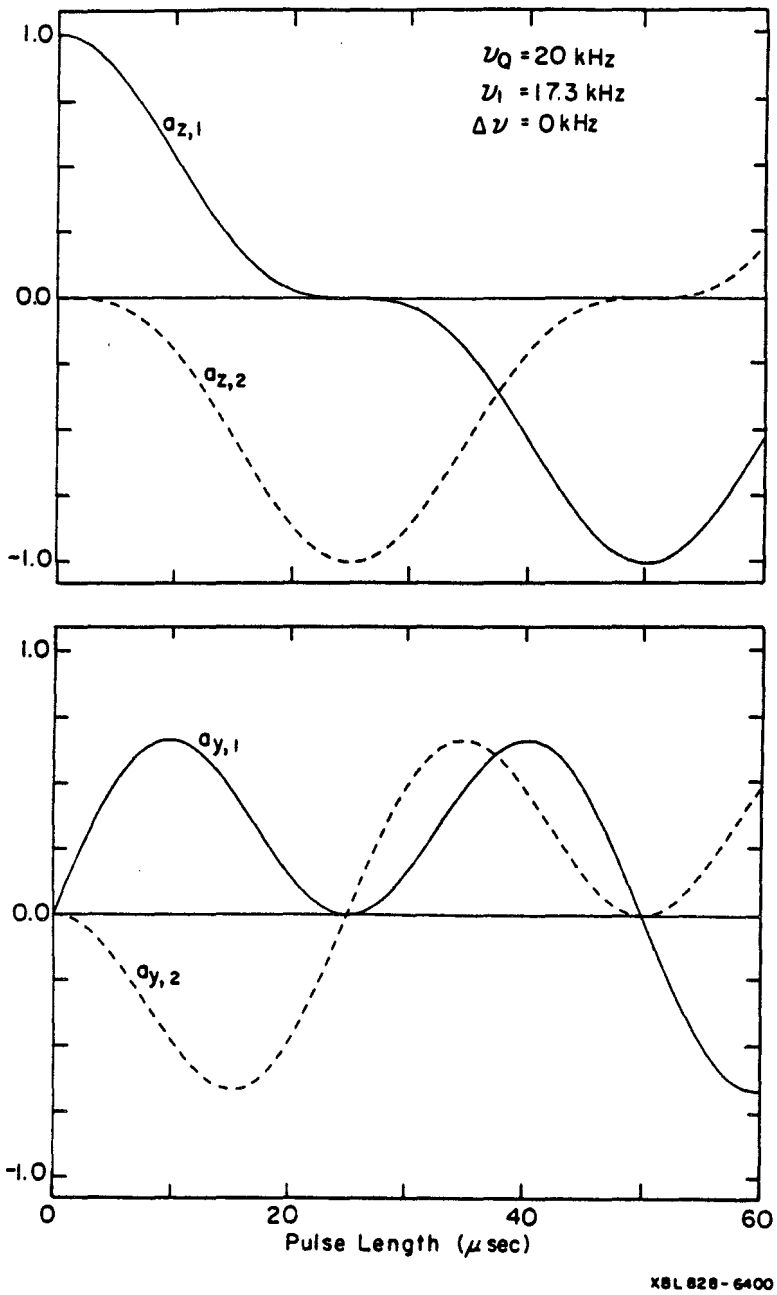

Figure II.12 Evolution during a DQ preparation pulse with ν_1 optimized using m=k=1 in Eq. II.52c ($\nu_1 = \sqrt{3}\,\nu_Q/2$). The initial density matrix is $I_{z,1}$, and because $\Delta\nu$ is zero, only four operators--$I_{z,1}$, $I_{z,2}$, $I_{y,1}$, and $I_{y,2}$--are needed in an expansion of ρ. Maximum creation of DQ coherence ($a_{z,2}$=-1) occurs at t=25 μsec.

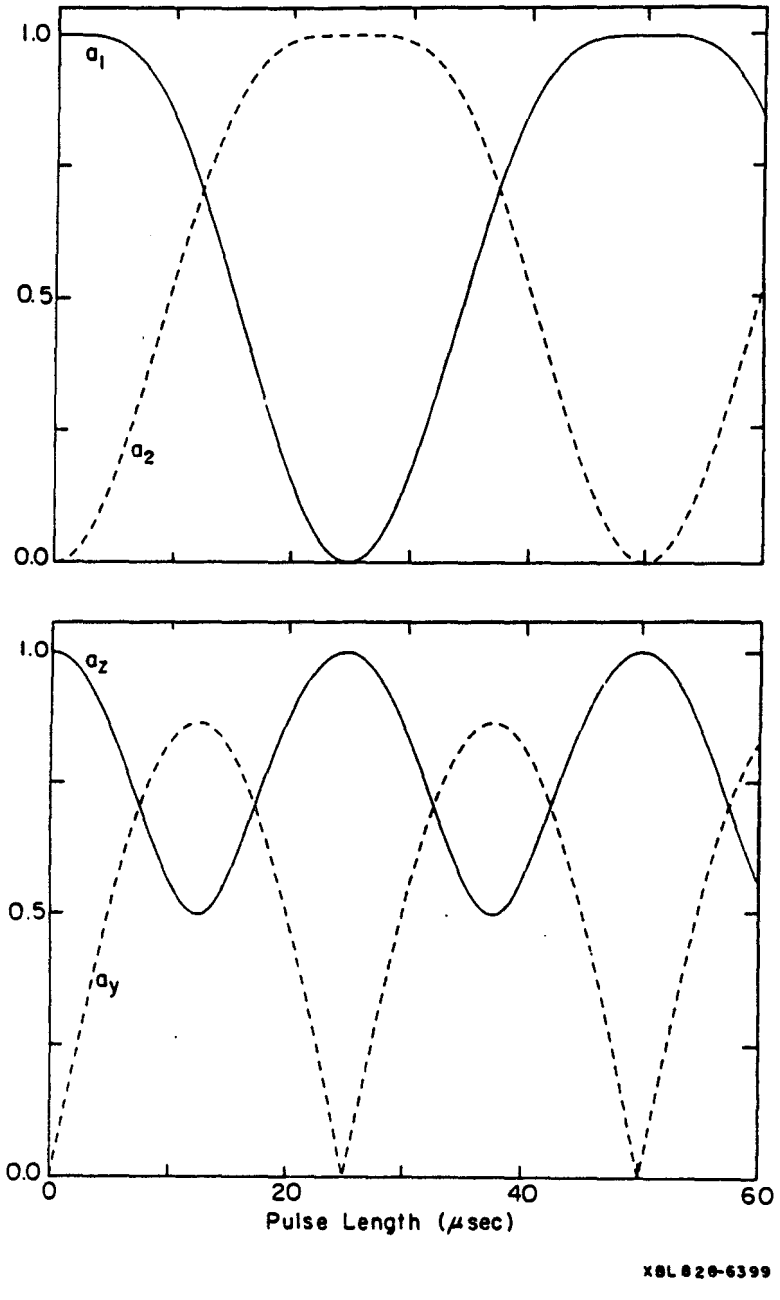

Figure II.13 Frame-projection coefficients a_y, a_z, a_1, and a_2 during the optimized DQ pulse of Figure II.12. Note that a_1 and a_2 are related merely by a shift along the time axis; in contrast, a_z oscillates from 1 to ν_Q/ν_{eff} while a_y varies from 0 to $2\nu_1/\nu_{eff}$.

These are plotted in Fig. II.13 for the pulse and system parameters of the previous paragraph. Note that the time-averaged projections of the state-of-the-system vector in frames "1" and "2" are equal--in fact, $a_1(t)$ and $a_2(t)$ have the same functional form, only shifted in time. There is no such symmetry with respect to its travels through the "Z" and "Y" frames, however:

$$a_z(t) = [\cos^2\pi\,\nu_{eff}\,t + \frac{\nu_Q^{\,2}}{\nu_{eff}^{\,2}}\,\sin^2\pi\,\nu_{eff}\,t]^{1/2} \quad ,$$

$$a_y(t) = \left|\frac{2\nu_1}{\nu_{eff}}\,\sin\pi\,\nu_{eff}\,t\right| \quad . \qquad \text{(II.61)}$$

The value of a_z oscillates between 1 and $\frac{\nu_Q}{\nu_{eff}}$ whereas a_y never rises higher than $\frac{2\nu_1}{\nu_{eff}}$. (For an optimized pulse with $m = k = 1$, $\nu_Q/\nu_{eff} = 1/2$ and $2\nu_1/\nu_{eff} = \sqrt{3}/2$.) This dichotomy simply reflects the fact that rf irradiation with $\Delta\nu = 0$ is resonant for the double-quantum transition and not so for the single-quantum transitions. Only in the limit of $\nu_1 \gg \nu_Q$ is this off-resonance discrimination overcome and symmetry achieved between Z and Y frames.

2.8.2 Preparing Double-Quantum Coherence in Powders

Our starting point is again the equation describing the time evolution of $a_{z,2}$ for $\rho_0 \propto I_{z,1}$ and $\Delta\nu \approx 0$:

$$a_{z,2}(t) = (\cos\pi\,\nu_{eff}\,t)(\sin\pi\,\nu_Q t) - (\frac{\nu_Q}{\nu_{eff}})(\sin\pi\,\nu_{eff}\,t)(\cos\pi\,\nu_Q t). \qquad \text{(II.62)}$$

Note that at all times $a_{z,2}$ is an <u>odd</u> function of ν_Q and thus,

as mentioned earlier, no double-quantum coherence can be prepared when $\nu_Q = 0$. (This latter statement is true no matter what the value of $\Delta\nu$.) A typical plot of $a_{z,2}$ vs. ν_Q is shown in Fig. II.14.

We wish now to find the best pulse or pulse sequence for excitation of DQ coherence over the entire range of ν_Q values, realizing of course that there is nothing we can do about $\nu_Q = 0$. One technique, proposed by Dave Wemmer [40], utilizes two hard pulses separated by a delay τ'. The value of $a_{z,2}$ after this sequence is given by

$$a_{z,2} = -\sin 2\pi\, \nu_Q \tau' \quad . \qquad \text{(II.63)}$$

We would like $a_{z,2}$ to be a square-wave function of ν_Q: $a_{z,2} = 1$ for $-\nu_{Qc} \leq \nu_Q < 0$ and $a_{z,2} = -1$ for $0 < \nu_Q \leq 2\nu_{Qc}$. This idealized form for $a_{z,2}$ can be expanded as a Fourier sum of sine terms like Eq. II.63 above with $\tau' = (2k-1)/(4\nu_{Qc})$ and $k=1,2,3,\ldots$ Preparation delay times can then be chosen on the basis of this Fourier series expansion and resulting spectra combined using the appropriate weighting functions. The first three terms of the expansion,

$$-\left\{\sin\left(\frac{\pi}{2}\frac{\nu_Q}{\nu_{Qc}}\right) + \frac{1}{3}\sin\left(\frac{3\pi}{2}\frac{\nu_Q}{\nu_{Qc}}\right) + \frac{1}{5}\sin\left(\frac{5\pi}{2}\frac{\nu_Q}{\nu_{Qc}}\right)\right\} \quad , \qquad \text{(II.64)}$$

approximate a square wave reasonably well; to create the look experimentally, results from sequences with $\tau' = 1/(4\nu_{Qc})$, $3/(4\nu_{Qc})$, and $5/(4\nu_{Qc})$ are added together in the proper ratio.

The simple relationship of $a_{z,2}$, ν_Q, and τ' breaks down

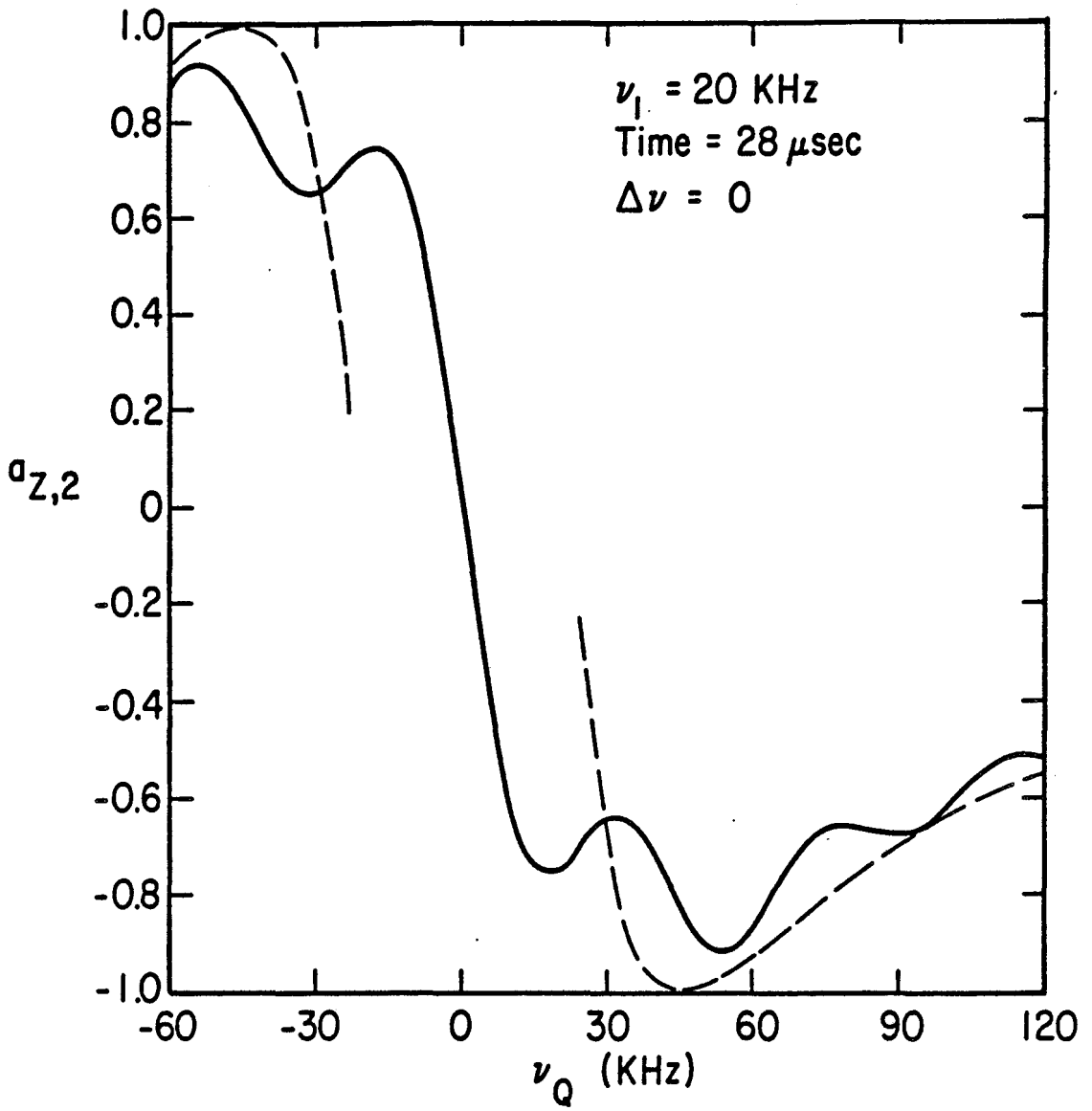

Figure II.14 Creation of double-quantum coherence as a function of ν_Q. The solid line represents the exact response; the dashed line is based on the weak-pulse formula $a_{z,2} = -\sin(2\pi\ \nu_1^2 t/\nu_Q)$. This formula is naturally most accurate when $\nu_Q \gg \nu_1$.

when $\nu_1 \approx \nu_Q$ and the rf pulses are more complicated than simple rotations. For the record, the prepared value of $a_{z,2}$ is given by the following hefty expression, where t is the length of each of the pulses:

$$a_{z,2}(\nu_Q) = [\cos^2\pi\,\nu_{eff}t - (\frac{\nu_Q}{\nu_{eff}})^2 \sin^2\pi\,\nu_{eff}\,t](\sin 2\pi\,\nu_Q t)$$

$$- (\frac{\nu_Q}{\nu_{eff}})(\sin 2\pi\,\nu_{eff}\,t)(\cos 2\pi\,\nu_Q t)$$

$$- (\frac{2\nu_1}{\nu_{eff}})^2(\sin^2\nu_{eff}\,\pi\,t)[\sin 2\pi\,\nu_Q(t + \tau')] \quad . \quad \text{(II.65)}$$

One could try to extract some useful analytical corrections to the Fourier series expansion from this tangle of sines and cosines, but it is easier to vary pulse and delay lengths on the computer to numerically fit the desired sine wave components, as was done for Fig. II.15.

In a similar fashion, the computer can be used to find the best <u>single</u> pulse for DQ excitation in a powder. The idea is to try a variety of pulse lengths and ν_1 values, seeking the combination that yields the best least-squares fit to a step function for $a_{z,2}(\nu_Q)$. The results of this computerized search through a two-dimensional parameter space are the following "powder-optimized" values:

$$\nu_1 \approx 0.571\,\nu_{Qc}$$

$$t \approx \frac{0.862}{\nu_{Qc}} \approx \frac{.492}{\nu_1} \quad . \qquad \text{(II.66)}$$

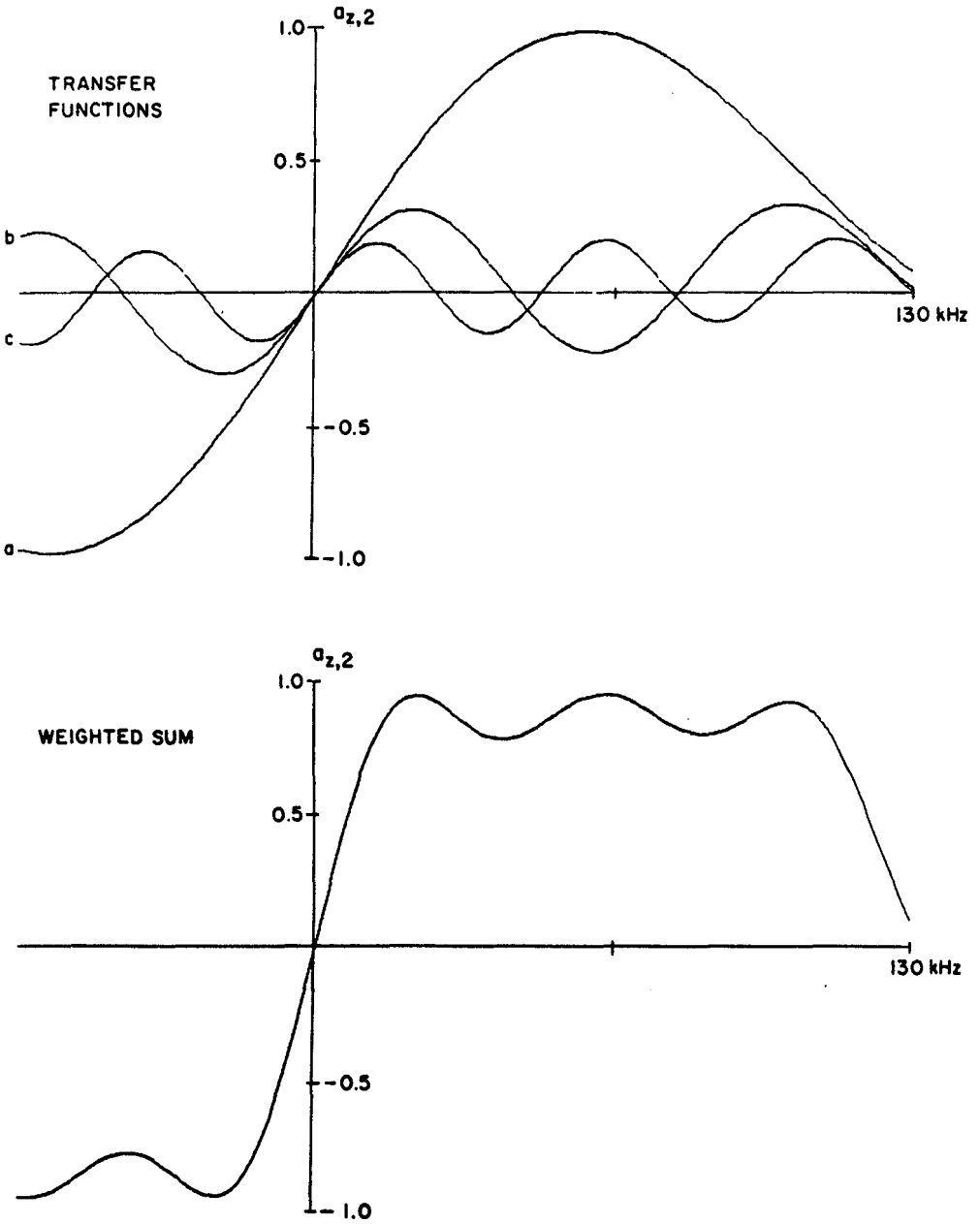

XBL 788-10111

Figure II.15 A weighted sum of three actual pulse-delay-pulse transfer functions for the creation of DQ coherence in a powder with ν_{Qc} = 65 kHz and $\Delta\nu$ = 0. These ideally are sine functions, the lowest three terms in a Fourier series expansion of a square wave. (The overall sign of each is opposite that used in the text.) Were $\nu_1 >> \nu_{Qc}$, one would simply choose three delays given by $\tau' = (2k-1)/(4\nu_{Qc})$ with k = 1, 2, 3. Instead, ν_1 was fixed at 100 kHz, and the computer was used to find pulse and delay times to best reproduce the appropriate sines. Details can be found in Ref. 40.

In quicker and dirtier terms, the best choice for single-pulse DQ excitation in a powder is an apparent pi pulse ($\nu_1 t \approx \frac{1}{2}$) with ν_1 somewhat less than 60% of the characteristic quadrupole frequency. For ν_{Qc} = 36 KHz (the value for rotating benzene and ferrocene rings), a good DQ pulse is 25 μsec long with ν_1 = 20 KHz. A plot of $a_{z,2}$ vs. ν_Q for this pulse is featured in Fig. II.16.

Double-quantum coherence must of course be detected as well as created. For our favorite pulse sequence, model D in Fig. II.7, a transfer function $T_{DQ}(\nu_Q)$ can be defined to describe the efficiency of the two weak pulses in transforming $I_{z,1}$ into $I_{z,2}$ and then back into $I_{z,1}$. As one might expect, the dependence on ν_Q is nearly identical for these two related operations, differing only by an overall sign which we will ignore. (Compare the equations for $a_{z,2}(t)$ evolving from $\rho_0 = I_{z,1}$ and for $a_{z,1}(t)$ evolving from $\rho_0 = I_{z,2}$ in Table II.7.) The expression for $T_{DQ}(\nu_Q)$ is therefore just the square of Eq. II.62, and a plot of the transfer function for ν_{Qc} = 36 KHz, ν_1 = 20 KHz, and t = 25 μsec can be found in Fig. II.17. Note the unavoidable "big dip" centered at $\nu_Q = 0$.

For the sake of insight and aesthetics, it is worthwhile to plot the spin-space trajectories of a powder under the influence of a DQ preparation pulse. To be specific, Figs. II.18-II.20 present "snapshots" at 5 sec intervals of the evolution of a powder (ν_{Qc} and ν_1 as in the previous paragraph). For a slightly different view of the proceedings, Fig. II.21 features the microsecond by microsecond development in the $I_{z,1}$, $I_{z,2}$ plane associated with four values of ν_Q.

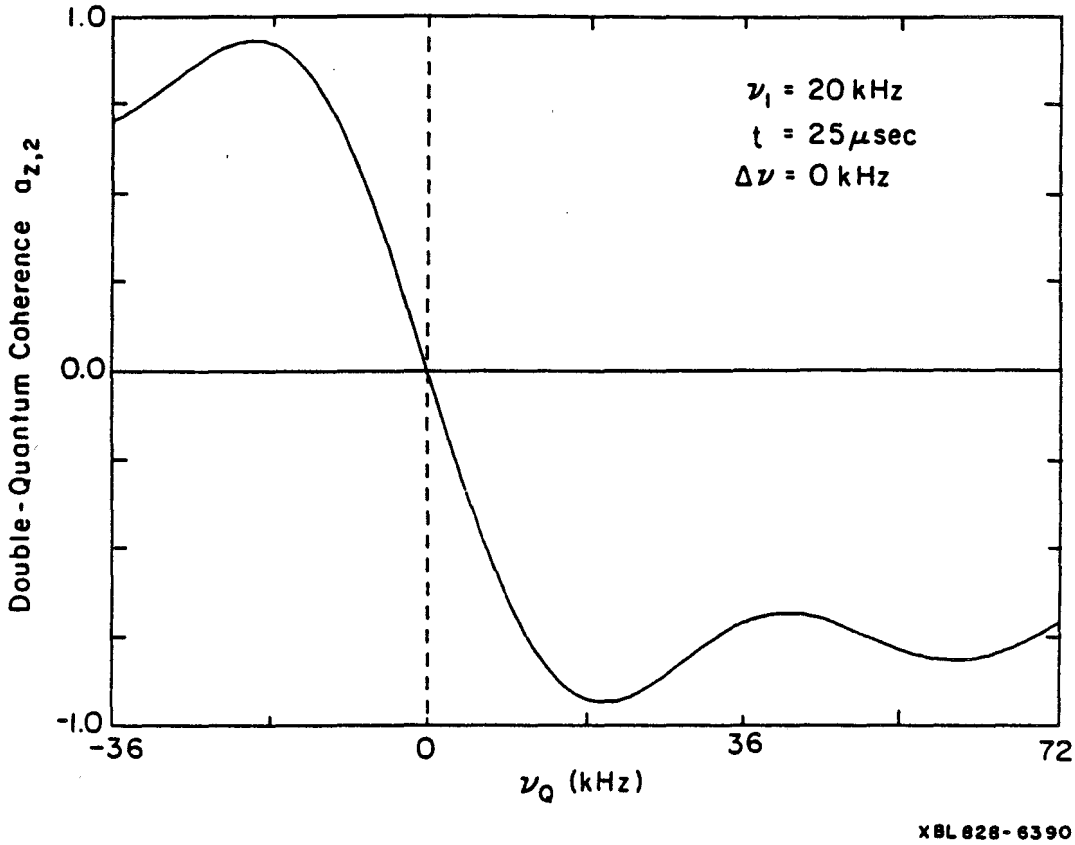

Figure II.16 Creation of DQ coherence as a function of ν_Q for a powder-optimized preparation pulse. With ν_{Qc}=36 KHz, one should choose $\nu_1 \approx 0.57\ \nu_{Qc}$ = 20.6 KHz and $t \approx 0.86/\nu_{Qc}$ = 23.9 μsec. These values were rounded to 20 KHz and 25 μsec for convenience.

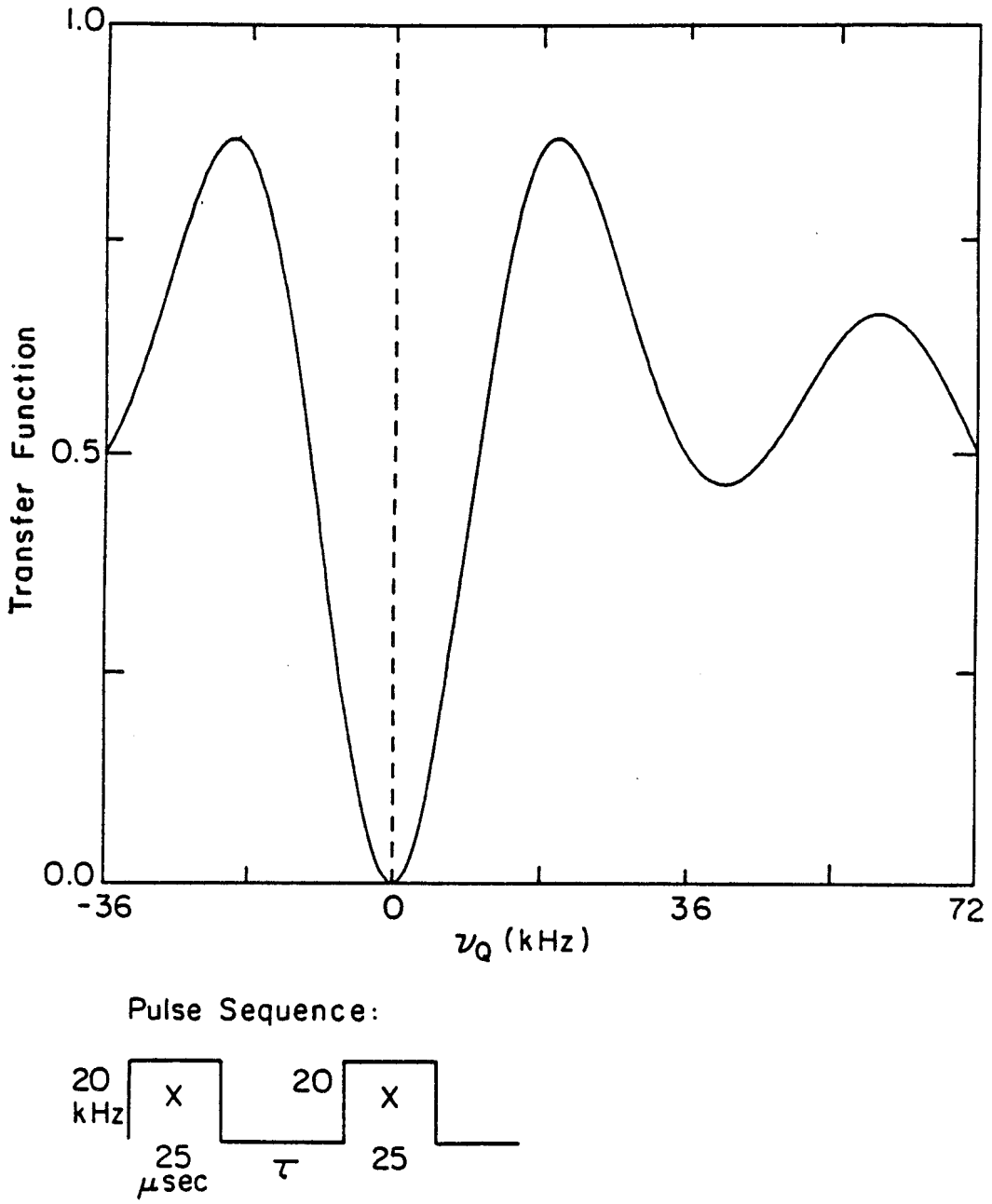

XBL 828-6392

Figure II.17 A transfer function for creation of DQ coherence and subsequent return of the density matrix to $I_{z,1}$ (Zeeman populations). This function is merely the square of the $a_{z,2}$ vs. ν_Q plot in Figure II.16. Note the "big dip" at ν_Q=0.

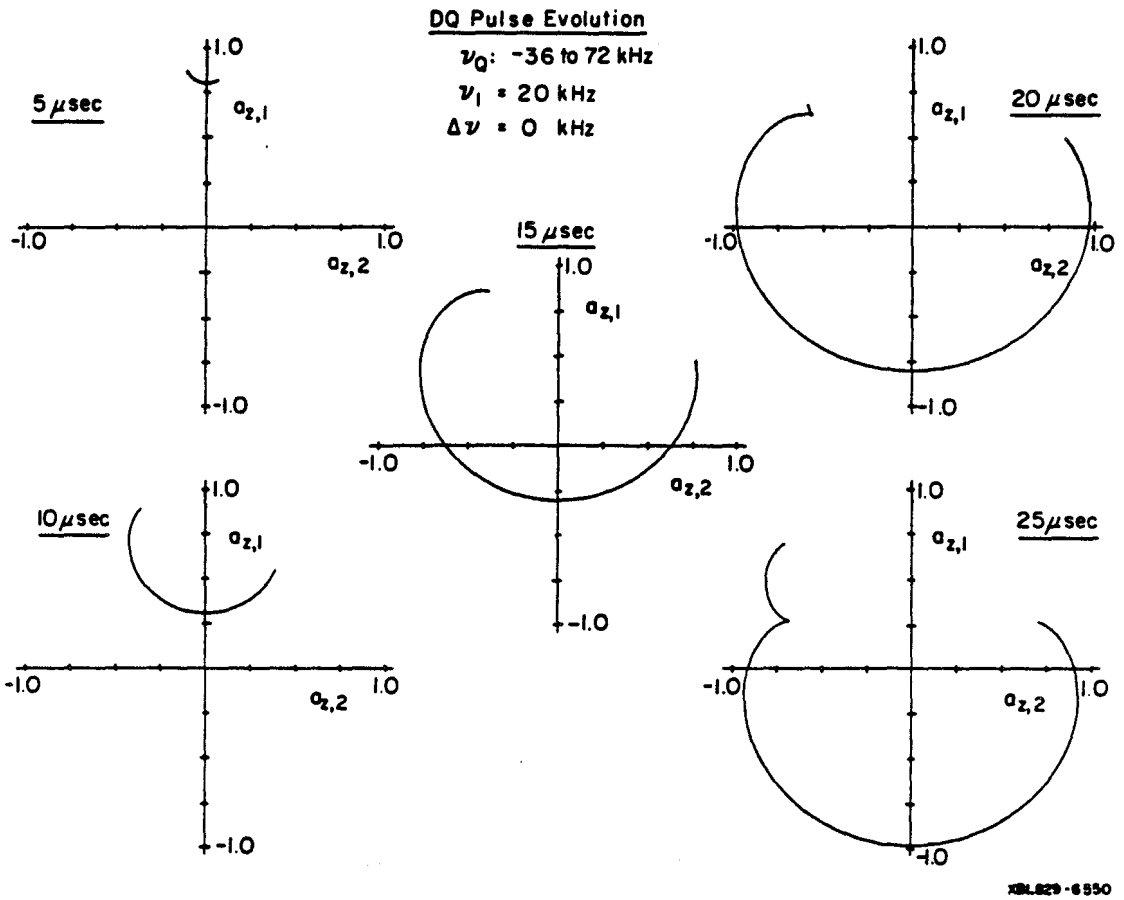

Figure II.18 Snapshots of density matrix coefficients $a_{z,1}$ and $a_{z,2}$ captured at 5 μsec intervals during an optimized DQ preparation pulse. Each curve represents the projection in the $I_{z,1}$, $I_{z,2}$ plane of the spin vectors for a powder with ν_{Qc}=36 KHz and η_Q=0. Values for ν_Q thus range from -36 KHz to 72 KHz. Note that $a_{z,1}(\nu_Q) = a_{z,1}(-\nu_Q)$ and $a_{z,2}(\nu_Q) = -a_{z,2}(-\nu_Q)$.

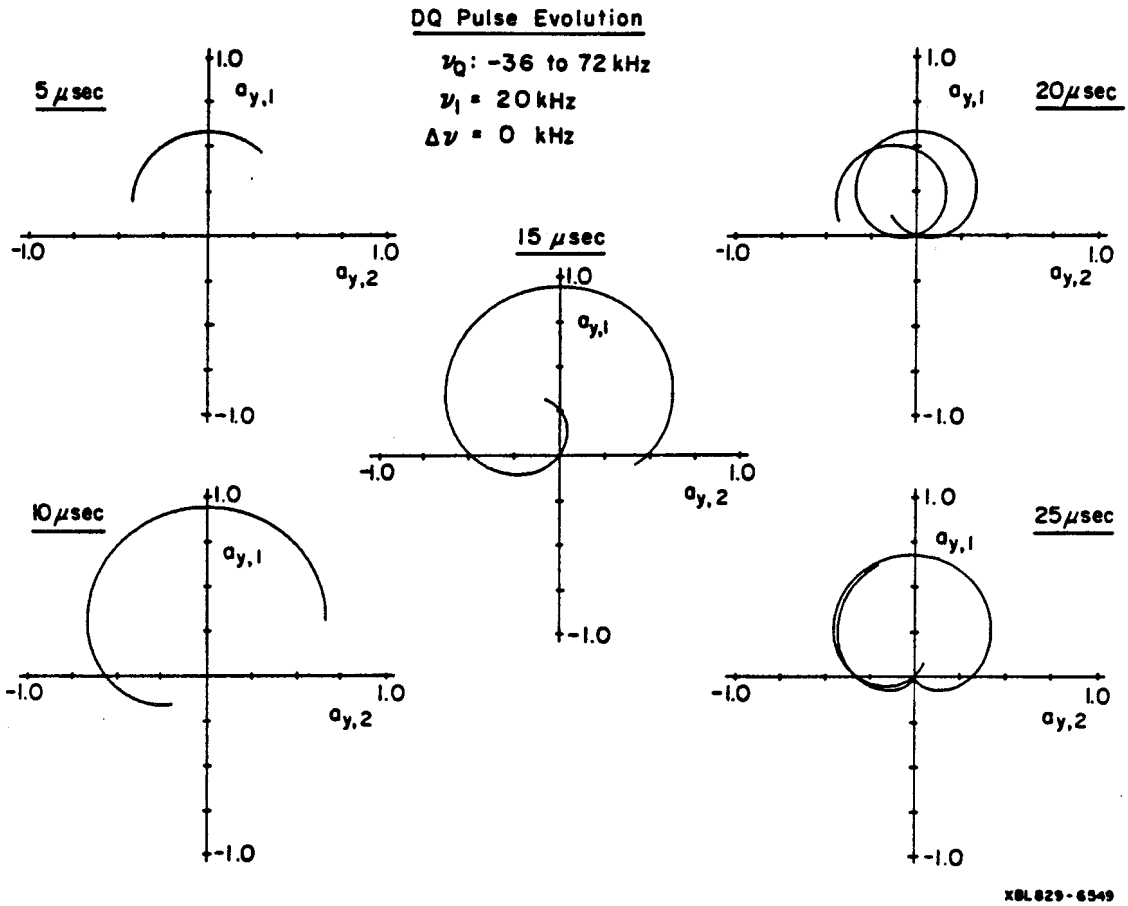

Figure II.19 The growth of single-quantum coherence during a DQ preparation pulse with $\Delta\nu=0$--a companion to Figure II.18. Note that $a_{y,1}(\nu_Q) = a_{y,1}(-\nu_Q)$ and $a_{y,2}(\nu_Q) = -a_{y,2}(-\nu_Q)$.

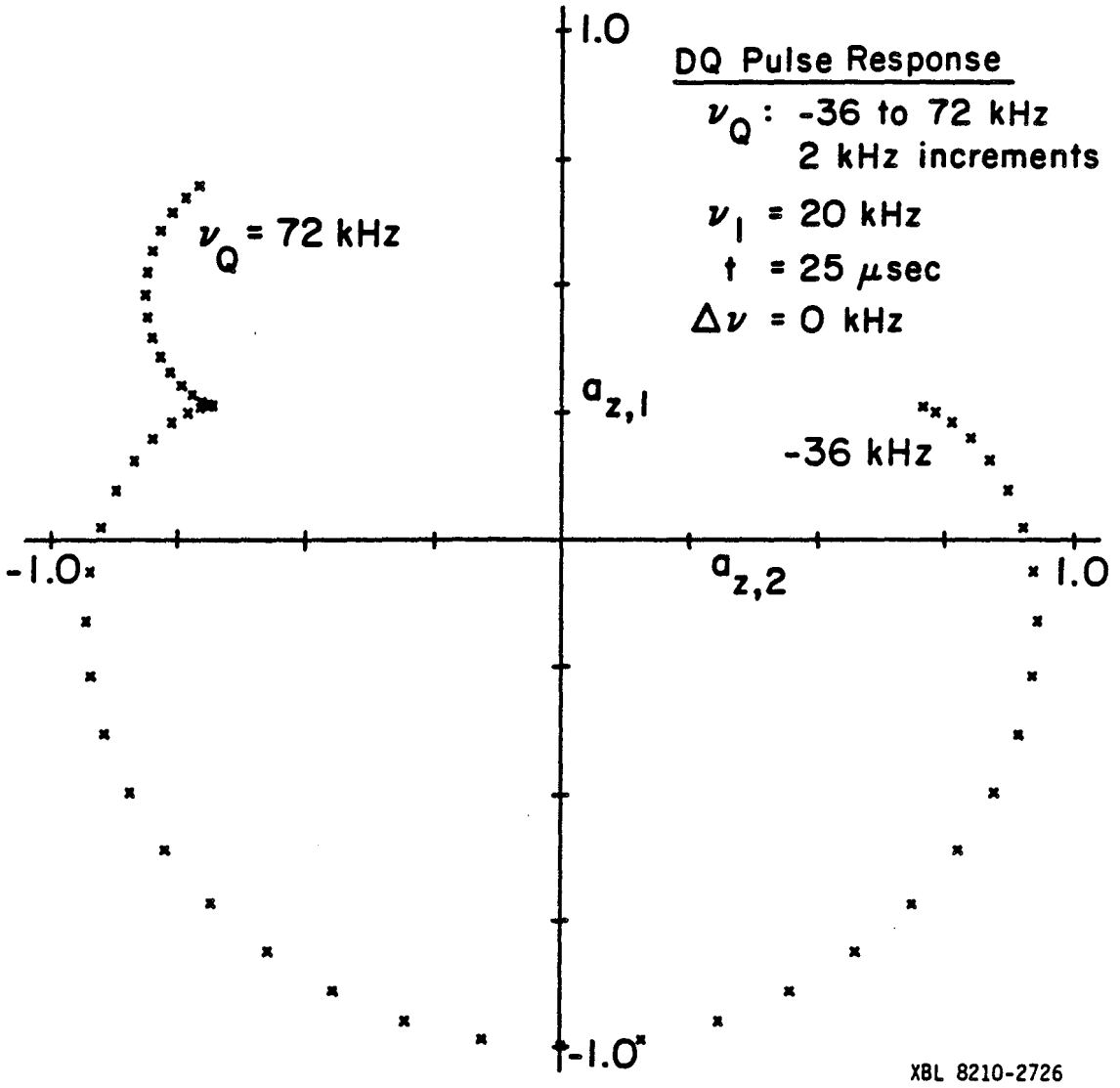

Figure II.20 The spread of spin vector projections in the $I_{z,1}$, $I_{z,2}$ plane resulting from a powder-optimized double-quantum preparation pulse. This plot is a more detailed version of the final frame in Figure II.18.

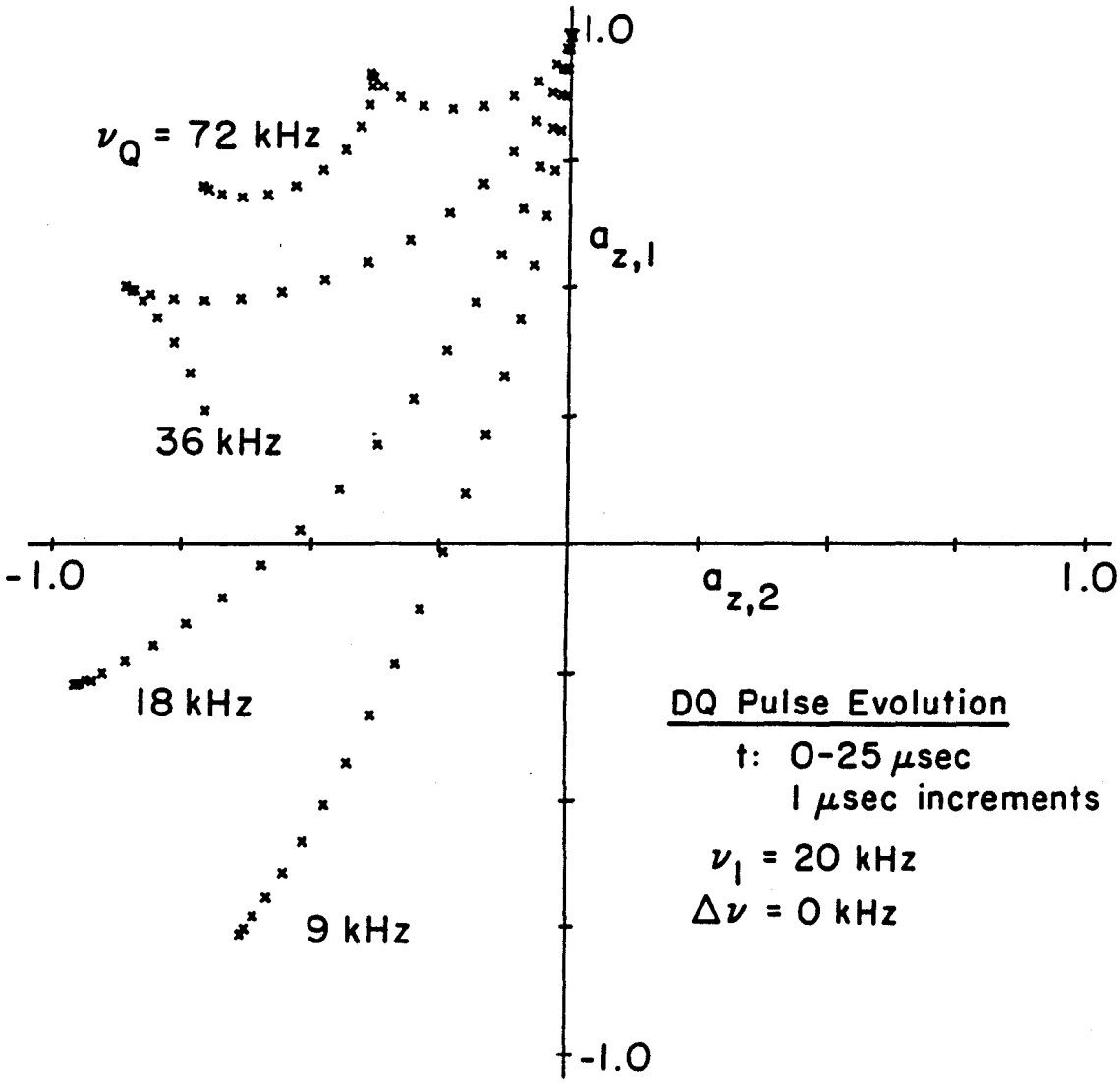

XBL 829-11685

Figure II.21 Yet another view of evolution during a powder-optimized DQ preparation pulse--trajectories in the $I_{z,1}$, $I_{z,2}$ plane associated with four values of ν_Q.

2.9 Analysis of the Quadrupole Echo Sequence

We now focus attention on the second half of our double-quantum pulse sequence (and a useful construct all by itself), the quadrupole echo. Its purpose is to transform Zeeman population $I_{z,1}$ into measurable single-quantum coherence for a powder. A $90x-\tau_1-90y-\tau_2$ sequence works as follows. The first pulse rotates $I_{z,1}$ into $I_{y,1}$, which due to probe ringing cannot be readily detected. Instead, spin vectors associated with different values of ν_Q fan out in the $I_{y,1}$, $I_{y,2}$ plane under the influence of $\mathcal{H}_Q$ for a time τ_1. A 90y pulse is then applied that acts within the Y frame as a 180° pulse, flipping the spin pancake [20]. The wandering vectors then refocus and echo along $I_{y,1}$ after a time τ_2. For perfect pulses with $\nu_1 >> \nu_Q$, τ_2 equals τ_1.

We, however, must adapt to the real world, where among other imperfections it is often the case that $\nu_1 \approx \nu_Q$. A naively chosen quadrupole echo sequence with both pulse flip angles equal to 90° and signal detection set at $\tau_2 = \tau_1$ might not work very well at all.

To optimize the sequence for a particular value of ν_{Qc}, we turn to the two-term-Hamiltonian equations of evolution in Tables II.6 and II.7. An analytical expression for $a_{y,1}$ after the second delay is readily obtained as a function of ν_1, ν_Q, $\Delta\nu$, the pulse lengths t_1 and t_2, and the delays τ_1 and τ_2. It is the job of the computer then to vary each of the pulse sequence parameters independently over a specified range to determine the largest <u>average</u> value of $a_{y,1}$, averaged over a specified number of quadrupole frequencies from $-\nu_{Qc}$ to $2\nu_{Qc}$. (In practice, the values

of ν_1 and τ_1 are constrained by the properties of the spectrometer, so there is less "playing" with these parameters than with the others.)

Before considering some of the optimized results, let's examine the effect of the two pulses individually. Figure II.22 displays the growth of single-quantum coherence in the $I_{y,1}$, $I_{y,2}$ plane for a powder with ν_{Qc} = 36 KHz. As the 50 KHz pulse lengthens microsecond by microsecond, the curves representing the spin-vector projections grow out from the origin towards $a_{y,1} = 1$, as we would expect for an x-pulse. However, the effect of $\mathcal{H}_Q$ during this pulse is to twist the spin vectors of those systems with large values of $|\nu_Q|$ away from the $I_{y,1}$ axis. By the time we are close to a 90° pulse (t_1 = 5 μsec), a sizeable arc has developed. It is to compensate for this initial dephasing that the optimal value of τ_2 is usually roughly equal to $\tau_1 + (t_1/2)$.

Another view of the problem is provided by plotting $a_{y,1}$ as a function of ν_Q for different values of the pulse length (Fig. II.23). The unhappy choice between narrow bandwidth ($\omega_1 t \approx \pi/2$) and broad but mediocre excitation ($\omega_1 t < \pi/2$) is readily apparent. Indeed the major stumbling block to effective DQ spectroscopy when $\nu_1 < \nu_{Qc}$ is <u>not</u> double-quantum preparation or even the echo in the $I_{y,1}$, $I_{y,2}$ plane; it is in the creation of single-quantum coherence from $I_{z,1}$. (As a remedy, however, modulation of the amplitude, the frequency, or the phase of the single-quantum preparation pulse could be used to increase its effective bandwidth--see Chapter III.)

The spin vectors arrayed in the $I_{y,1}$, $I_{y,2}$ plane as a legacy of the first pulse continue to evolve during the first delay. As

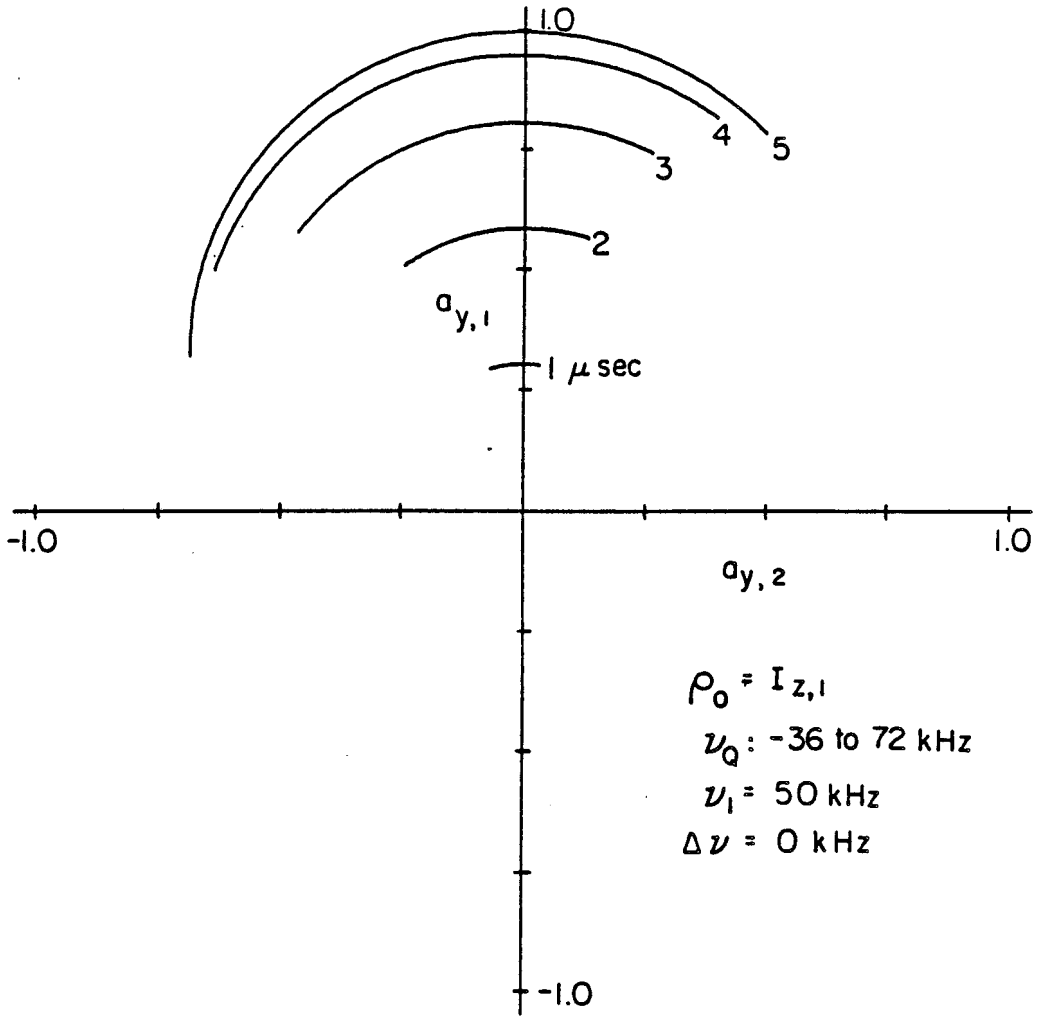

XBL 828-6386

Figure II.22 Microsecond-by-microsecond growth of $a_{y,1}$ and $a_{y,2}$ during a 90° pulse for a powder with ν_{Qc}=36 KHz and η_Q=0.

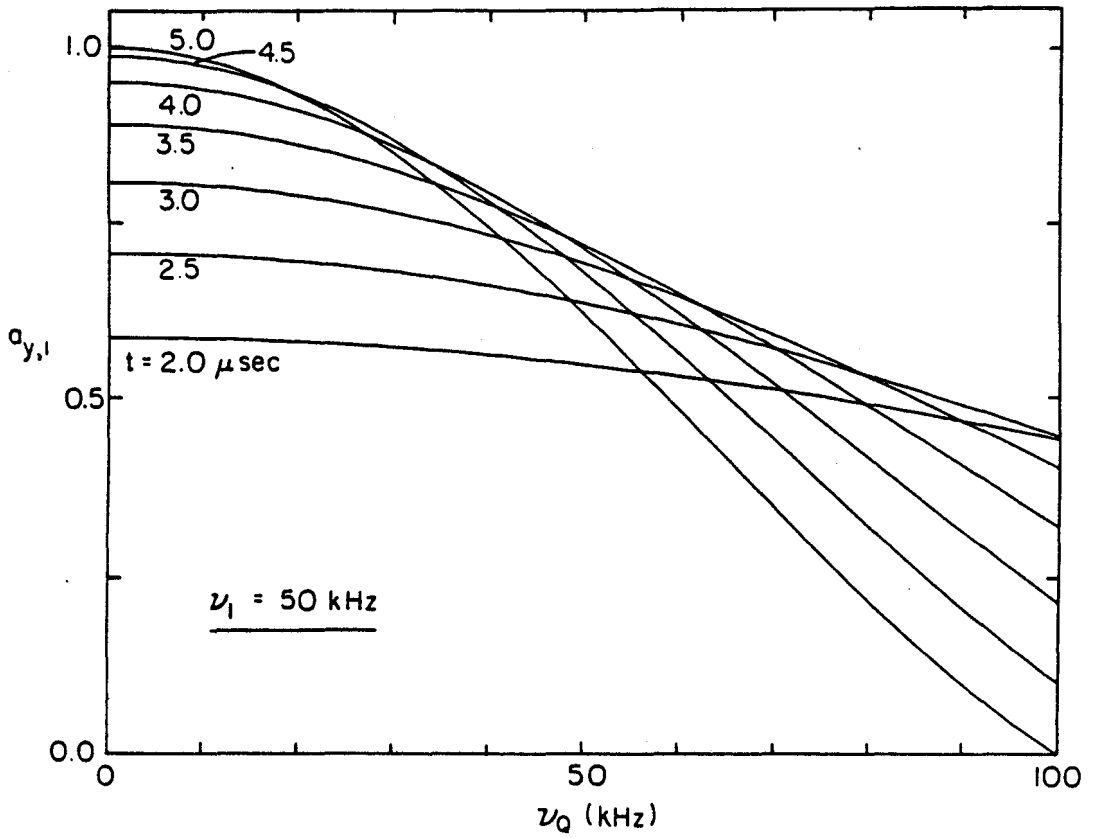

XBL 828-6389

Figure II.23 The creation of single-quantum coherence as a function of ν_Q for various pulse lengths ($\Delta\nu = 0$).

noted earlier, the effect of $\mathcal{H}_Q$ is a rotation about $I_{y,3}$, spreading the vectors throughout the plane. If an offset term is present in the Hamiltonian, coherence will appear in the X-frame as well--$\mathcal{H}_{off}$ converts $I_{y,1}$ and $I_{y,2}$ to $I_{x,1}$ and $I_{x,2}$. These operators are in turn rotated to $I_{z,1}$ and $I_{z,2}$ by the second pulse of the quadrupole echo sequence; as a consequence, any X-frame coherence created during the first delay is not subsequently observable.

Now for a look at the effects of the echoing pulse in the Y-frame. Ideally, this pulse should act as a 180° rotation about the $I_{y,1}$ axis, changing the sign of $a_{y,2}$ for each spin vector but keeping $a_{y,1}$ intact. In reality, the presence of $\mathcal{H}_Q$ modifies the simple rotation picture. Figure II.24 depicts the microsecond-by-microsecond evolution of the spin vectors for a powder with ν_{Qc} = 36 KHz. The pulse strength ν_1 is 50 KHz and the initial density matrix for each vector is $I_{y,2}$ (an unlikely situation in practice, but useful in showing what happens to $I_{y,2}$ <u>components</u>). Although only the vector with $\nu_Q = 0$ remains in the $I_{y,2}$, $I_{y,3}$ plane during its journey, the pulse actually works quite well when its length is 4-5 μsec--every value of $a_{y,2}$ is close to -1. The effect of $\mathcal{H}_Q$ seems first to be a divergence of spin vectors and then a refocusing of coherence around $-I_{y,2}$.

In fact, the echoing pulse is more effective in general when a spin vector is initially along the $I_{y,2}$ axis than when it is aligned with the $I_{y,1}$ axis, as illustrated in Fig. II.25. There the spread of spin vector positions after a 4.5 μsec 50 KHz pulse is compared for two different initial density matrices, $I_{y,1}$ and $I_{y,2}$. The

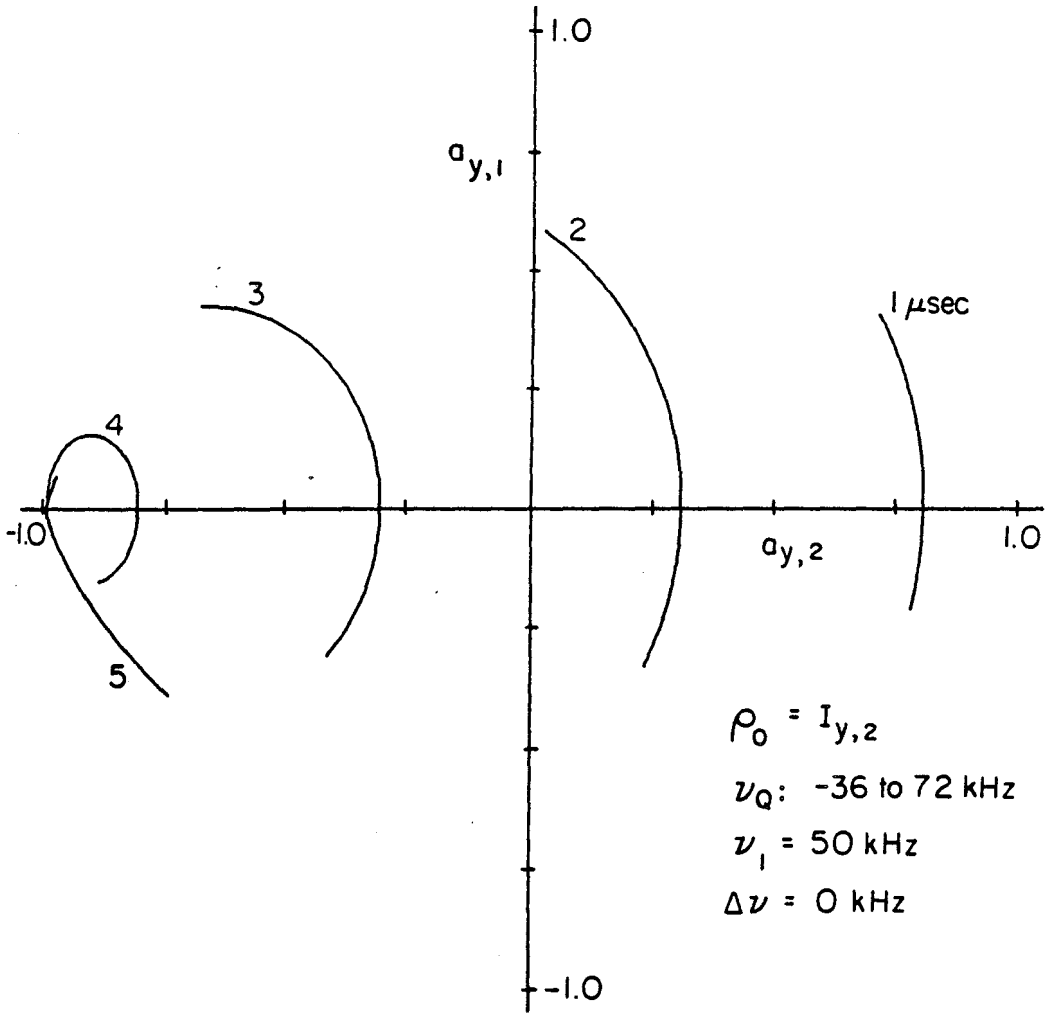

XBL 828-6387

Figure II.24. Microsecond-by-microsecond evolution in the $I_{y,1}$, $I_{y,2}$ plane during a quadrupole echo pulse. Each curve represents a range of ν_Q values from -36 KHz to 72 KHz.

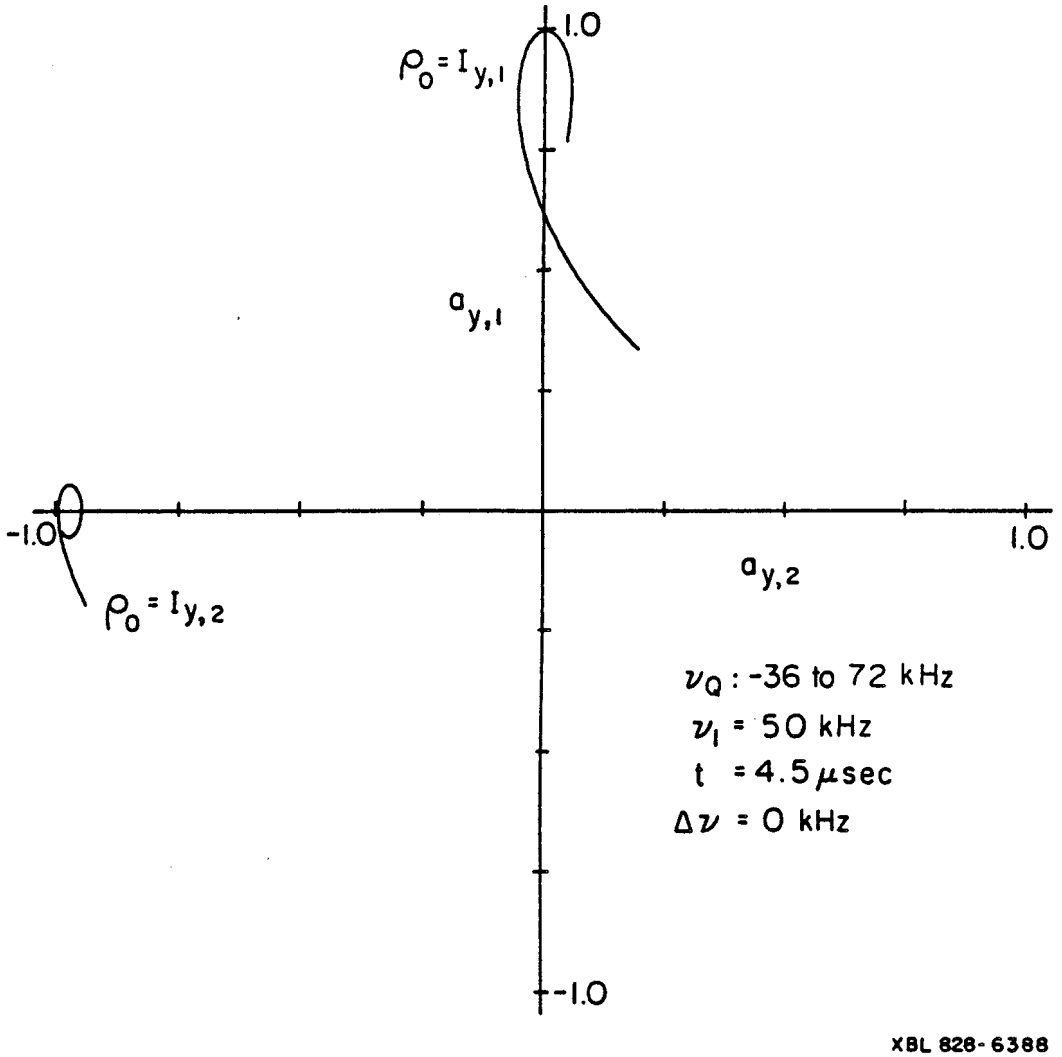

Figure II.25 A demonstration that the quadrupole echo is more effective when a spin vector is initially along the $I_{y,2}$ axis than along the $I_{y,1}$ axis, particularly for large values of ν_Q. [Wiggles in quadrupole echo transfer functions (as in Figure II.27) are due to this difference.] Each curve represents a spread in spin vector projections following an echoing pulse for -36 KHz $\leq \nu_Q \leq$ 72 KHz and a given ρ_o.

$\rho_0 = I_{y,1}$ curve is indicative of better echoing for $\nu_Q \approx 0$ but drops noticeably in efficiency relative to the $\rho_0 = I_{y,2}$ curve for ν_Q values on the order of ν_{Qc} (36 KHz) and beyond.

The overall efficiency of the quadrupole echo sequence can be described by a transfer function $T_{QE}(\nu_Q)$. In the limit of large ν_1, the use of 90° pulses insures that $T_{QE}(\nu_Q) \approx 1.0$ for all ν_Q values. When ν_1 does not dominate ν_{Qc} the computer can be used to select an optimized sequence for a powder. An example is the following, for ν_{Qc} = 36 KHz, ν_1 fixed arbitrarily at 50 KHz, and τ_1 set at 40 μsec:

1.	x-pulse	4.5 μsec	50 KHz	3.	y-pulse	4.5 μsec	50 KHz
2.	delay	40 μsec		4.	delay	41.5 μsec.	

The transfer function for the first pulse of this sequence is shown in Fig. II.26, and the overall $T_{QE}(\nu_Q)$ appears in Fig. II.27. Notice that the latter function is essentially a series of wiggles superimposed on the $a_{y,1}$ vs. ν_Q response to the first pulse. The wiggles reflect the difference in echoing efficiency for a spin vector aligned with either the $I_{y,1}$ or $I_{y,2}$ axis just prior to the echo pulse; they go roughly as $\sin^2 [2\pi \nu_Q(\tau_1+t_1/2)]$ except for small ν_Q values.

The computer can in addition be trained to generate pulse sequences optimized over a limited range of ν_Q values or for a single value of ν_Q. An application suggested by Gary Drobny [76] involved a deuterated liquid crystal for which ν_Q was measured to be 44 KHz. The available rf power was ν_1 = 35 KHz. A quadrupole echo sequence with two 90° pulses ($t_1 = t_2$ = 7 μsec) and $\tau_1 = \tau_2$ =

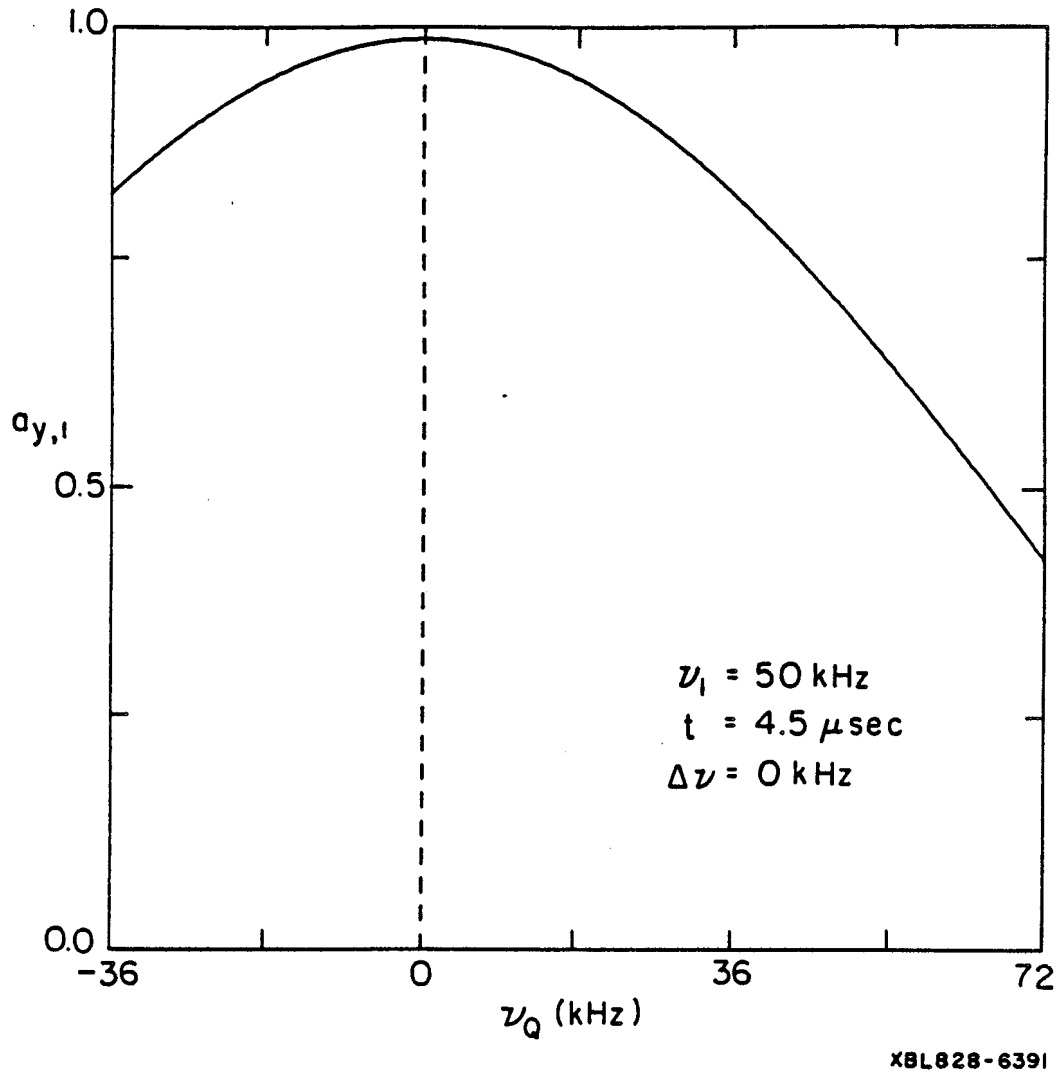

Figure II.26 Creation of single-quantum coherence as a function of ν_Q following the first pulse of an optimized quadrupole echo sequence. The initial density matrix is $I_{z,1}$.

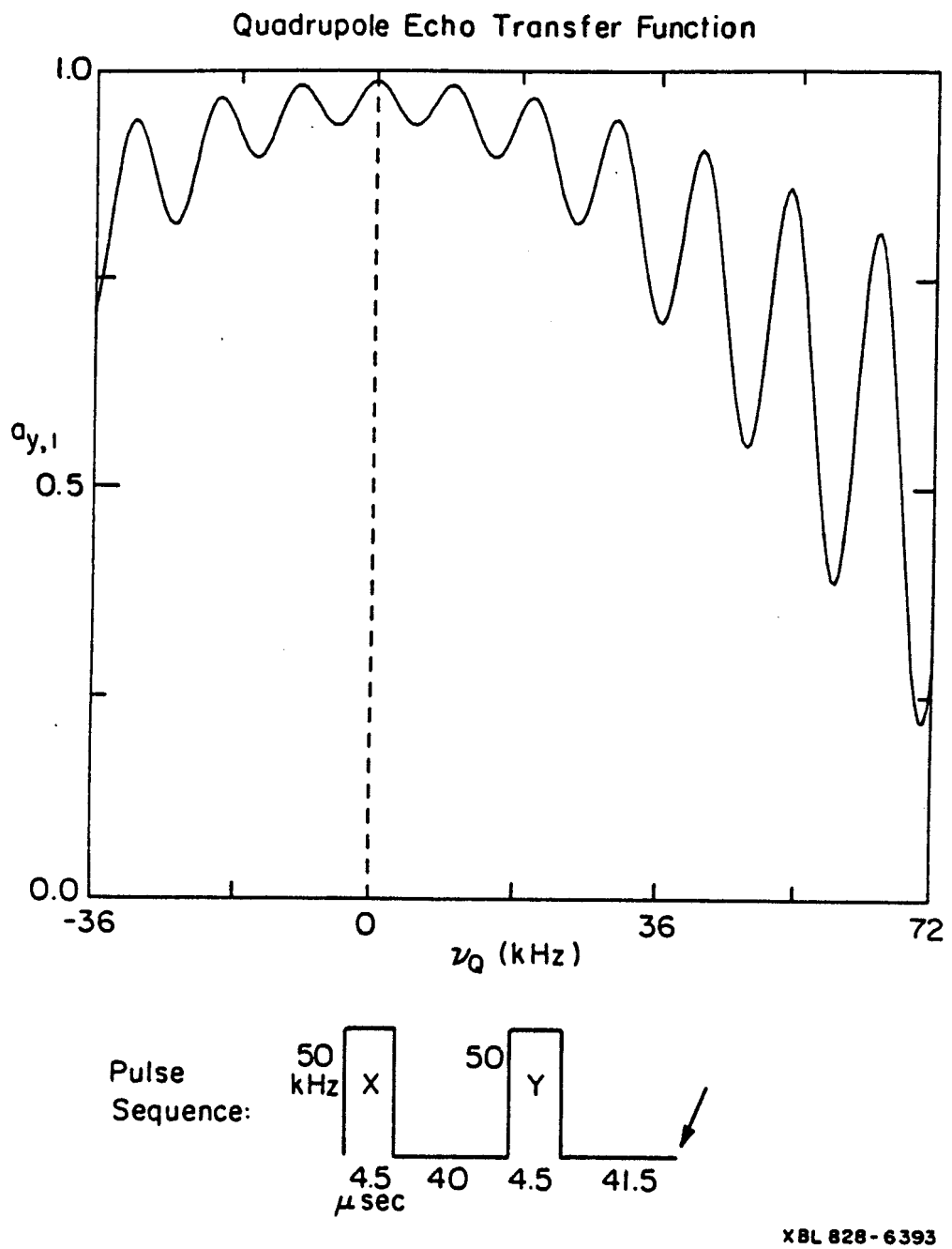

Figure II.27 The transfer function ($I_{z,1} \rightarrow I_{y,1}$) for an optimized quadrupole echo sequence with $\Delta\nu=0$. Comparison with Figure II.26 reveals that the basic shape is governed by response to the first pulse; superimposed wiggles result from the fact that the second pulse can in general convert $a_{y,2}$ to $-a_{y,2}$ more efficiently than it can maintain a value of $a_{y,1}$.

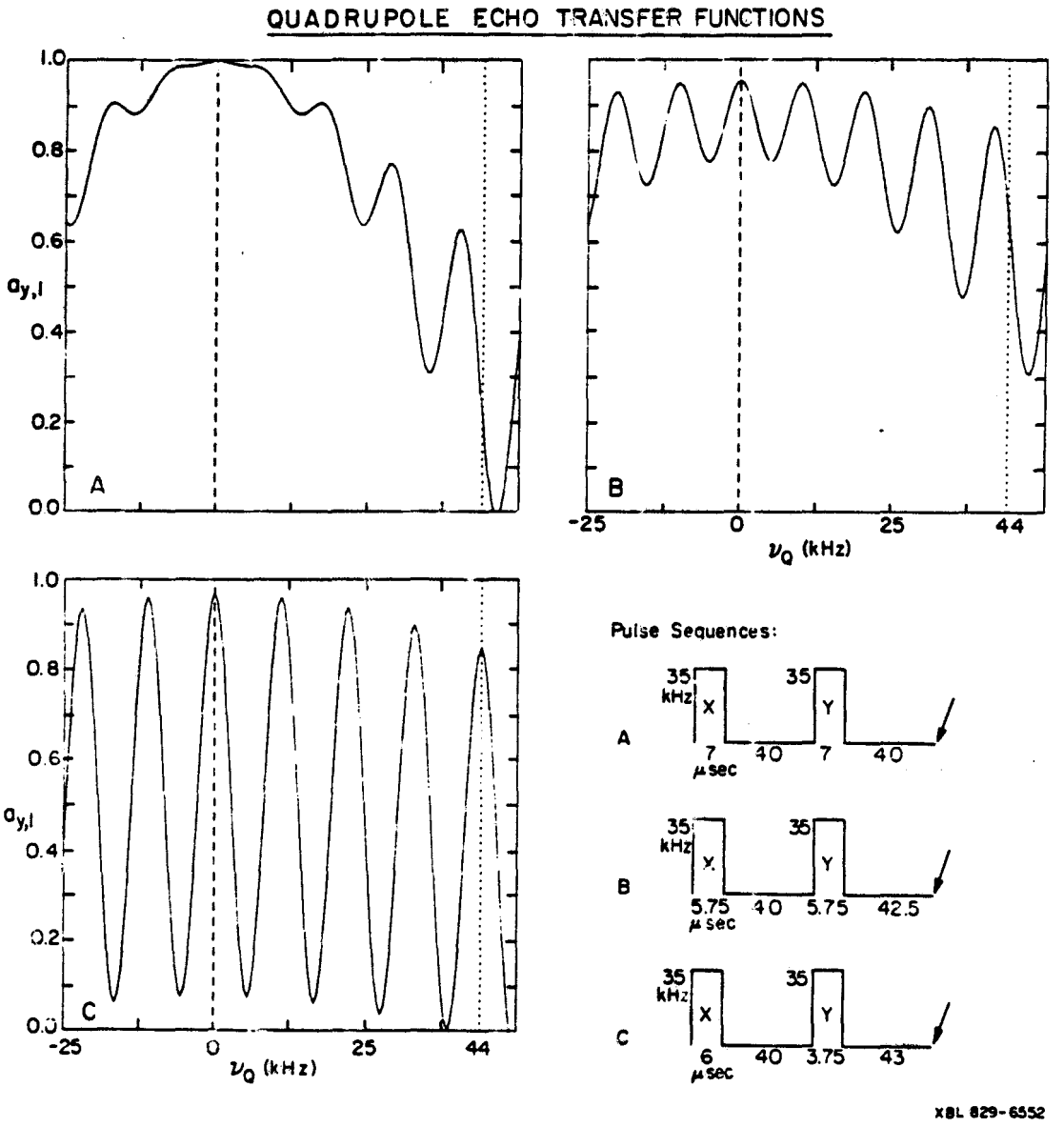

Figure II.28 Three different quadrupole echo pulse sequences and corresponding transfer functions, inspired by Gary Drobny's liquid crystal experiment for which ν_Q=44 KHz and $\nu_1 \leq 35$ KHz. Sequence A uses 90° pulses and equal delay lengths τ_1 and τ_2. Sequence B is computer-optimized for 40 KHz $\leq \nu_Q \leq$ 44 KHz; sequence C is optimized for ν_Q=44 KHz. Final $a_{y,1}$ values at ν_Q=44 KHz are 0.19, 0.64, and 0.85, respectively.

40 μsec yielded a puny final $a_{y,1}$ value of 0.19. A sequence optimized over the range 40-44 KHz gave rise to a final $a_{y,1}$ value of 0.64; optimization solely for ν_Q = 44 KHz resulted in $a_{y,1}$ = 0.85. The three transfer functions are compared in Fig. II.28.

Bloom and co-workers [77] have also used the equations of Table II.7 to determine the spectral distortions due to finite pulse width in the quadrupole echo sequence and to choose the best pulse flip angles in order to minimize the distortion.

2.10 At Long Last Lineshapes

2.10.1 Aligned and Axially Symmetric EFG and Chemical Shielding Tensors

For pulse sequence D, the overall quadrupole transfer function $T(\nu_Q)$ is the product of the double-quantum transfer function $T_{DQ}(\nu_Q)$ and the quadrupole echo transfer function $T_{QE}(\nu_Q)$. $T(\nu_Q)$ is illustrated in Fig. II.29 for the following familiar set of pulse parameters:

1.	x-pulse	25 μsec	20 KHz	5.	x-pulse	4.5 μsec	50 KHz
2.	delay	τ		6.	delay	40 μsec	
3.	x-pulse	25 μsec	20 KHz	7.	y-pulse	4.5 μsec	50 KHz
4.	delay	$t > T_2$		8.	delay	41.5 μsec.	

Assuming that the electric field gradient (EFG) and shielding tensors are aligned and that $\eta_Q = \eta_{cs}$, the chemical shielding transfer function $T(\sigma)$ is identical in form to $T(\nu_Q)$. The chemical shielding powder lineshape (for an axial tensor and ν_{Qc} = 36 KHz) that would result from the pulse sequence above is

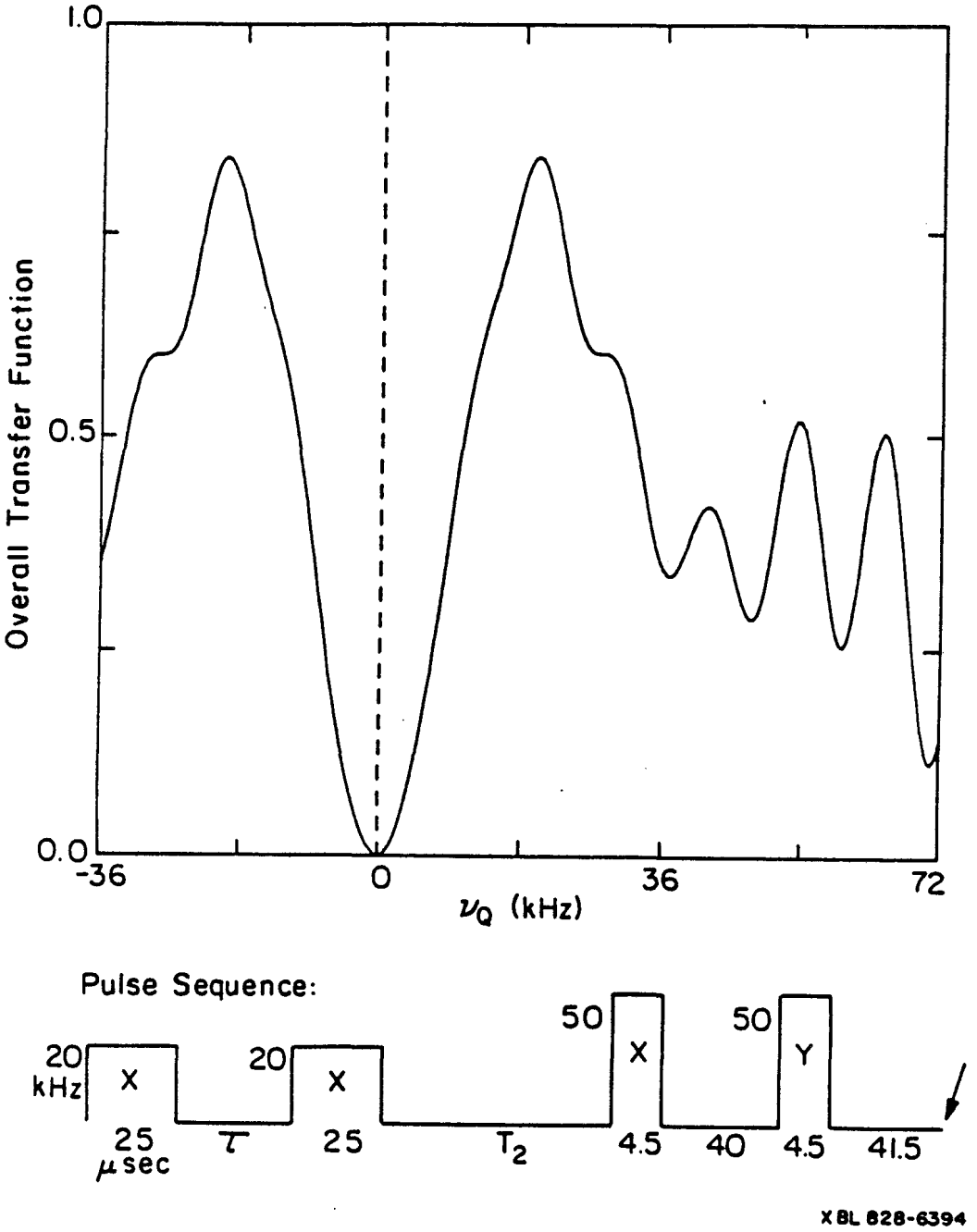

Figure II.29 An overall four-pulse transfer function for DQ preparation and detection, optimized for ν_{Qc}=36 KHz. A delay on the order of T_2 between the second and third pulses allows any unwanted coherences to die away.

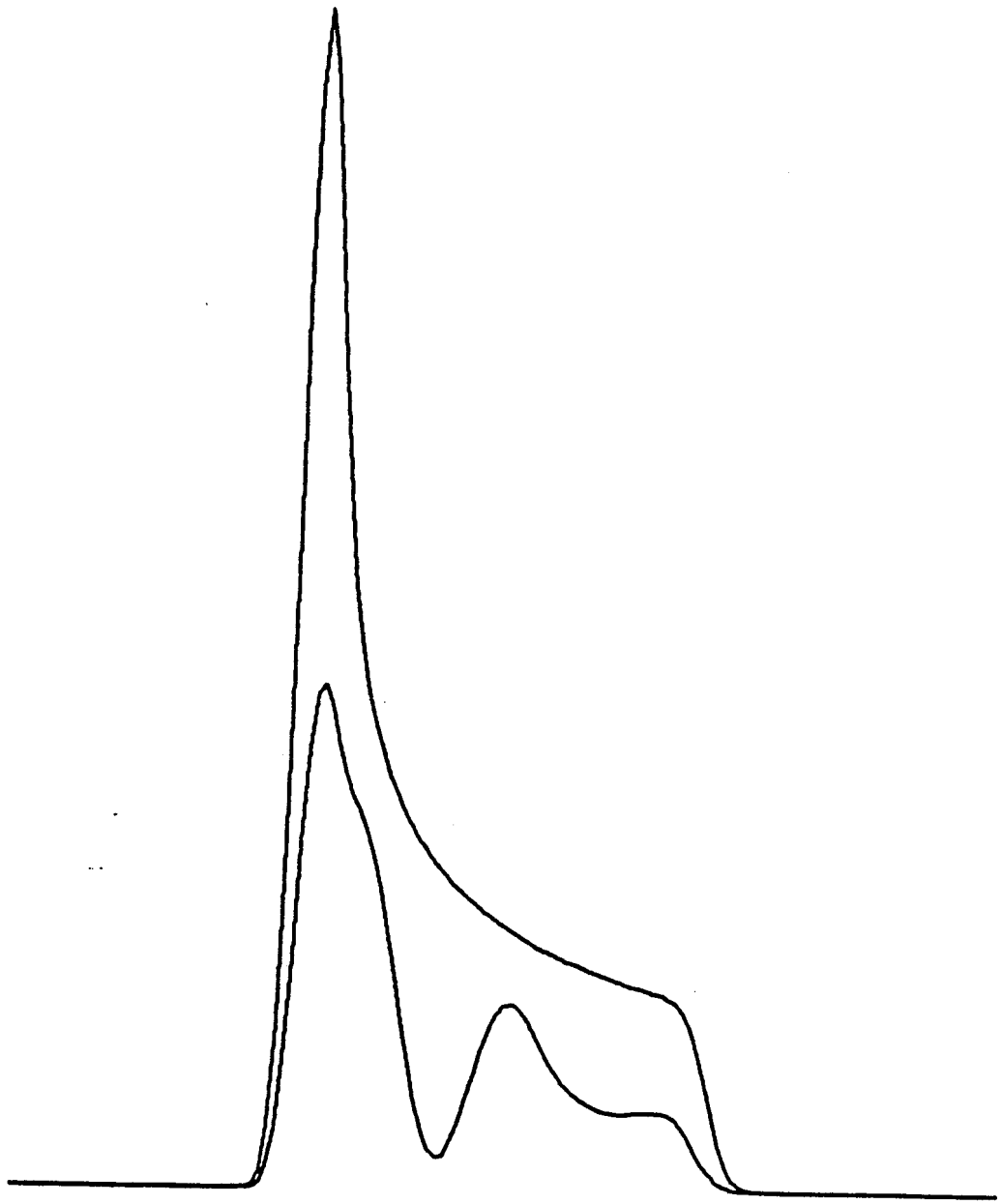

XBL 811-7666

Figure II.30 Simulated and slightly broadened chemical shielding powder lineshapes, with and without the distortions due to the transfer function in Figure II.29. The shielding and electric field gradient tensors are assumed to be axial and aligned.

shown in Fig. II.30, modified by a small amount of simulated broadening. Higher overall intensity and less distortion would be expected if a larger value of ν_1 were used in the quadrupole echo sequence.

To match any of the experimental spectra obtained thus far, a good deal more broadening must be applied to the distorted lineshape. (The distinctive bumps and wiggles in the simulation have never been seen experimentally due to residual dipolar couplings, magnetic field inhomogeneities, and other ravishers of resolution.) The most accurate way of introducing a certain degree of Gaussian broadening into a computed lineshape is to make use of the convolution theorem [78]: (1) Inverse Fourier transform the lineshape. (2) Multiply the resulting function of time by a Gaussian decay (itself the inverse FT of the desired Gaussian frequency broadening). (3) Fourier transform the product back into frequency space. A much easier technique of sufficient accuracy for our work is to use a three-point smoothing algorithm, which replaces each point s(i) in the lineshape with the quantity [s(i-1) + 2s(i) + s(i+1)]/4. After n smooths, the broadening of a sharp line of unit intensity at i=0 is described by the following formula for intensity at i=m:

$$s(m) = \frac{(n!)^2}{(n+m)!(n-m)!} \; s(0) \quad , \qquad \text{(II.67a)}$$

where

$$s(0) = \frac{(2n)!}{4^n (n!)^2} \quad \text{and} \quad |m| \leq n \quad . \qquad \text{(II.67b)}$$

The function $s(m)/s(0)$ approximates the Gaussian $\exp(-m^2/n)$ in the limit of large n and small m. The standard deviation of $s(m)/s(0)$ is thus on the order of $(n/2)^{1/2}$ points, corresponding to a full width at half maximum (FWHM) of $\sim 2(n \ln 2)^{1/2}$ points. Because these quantities are measured in points, the effective broadening of a computed lineshape is governed both by the number of smooths and by the number of points used to represent the lineshape.

2.10.2 Comparison with Experiments

A number of axially symmetric chemical shielding powder lineshapes have been measured experimentally by Dave Wemmer [40]--a typical result obtained with pulse sequence D appears in Fig. II.31 along with an "ultra-smoothed" simulation. As one searches vainly for pulse sequence distortions in the 6.5 ppm wide experimental spectrum (in particular the "big dip" corresponding to $\nu_Q = 0$), it is clear that an appreciable amount of broadening is present that washes away the resolution. As such, it is impossible to actually verify the computed transfer functions experimentally; moreover, an accurate determination of $\Delta\sigma$ is difficult and subject to ambiguity.

Wemmer [40] lists a variety of possible sources for broadening--magnetic field inhomogeneity, residual homonuclear or heteronuclear dipolar couplings, second order quadrupole shifts, and T_1 lifetime broadening--to which can be added the sample-shape dependence of the bulk magnetic susceptibility [79]. Many of these peak plumpers can be minimized, however, by time- and labor-intensive devotion to experimental detail. Conscientious shimming can reduce the

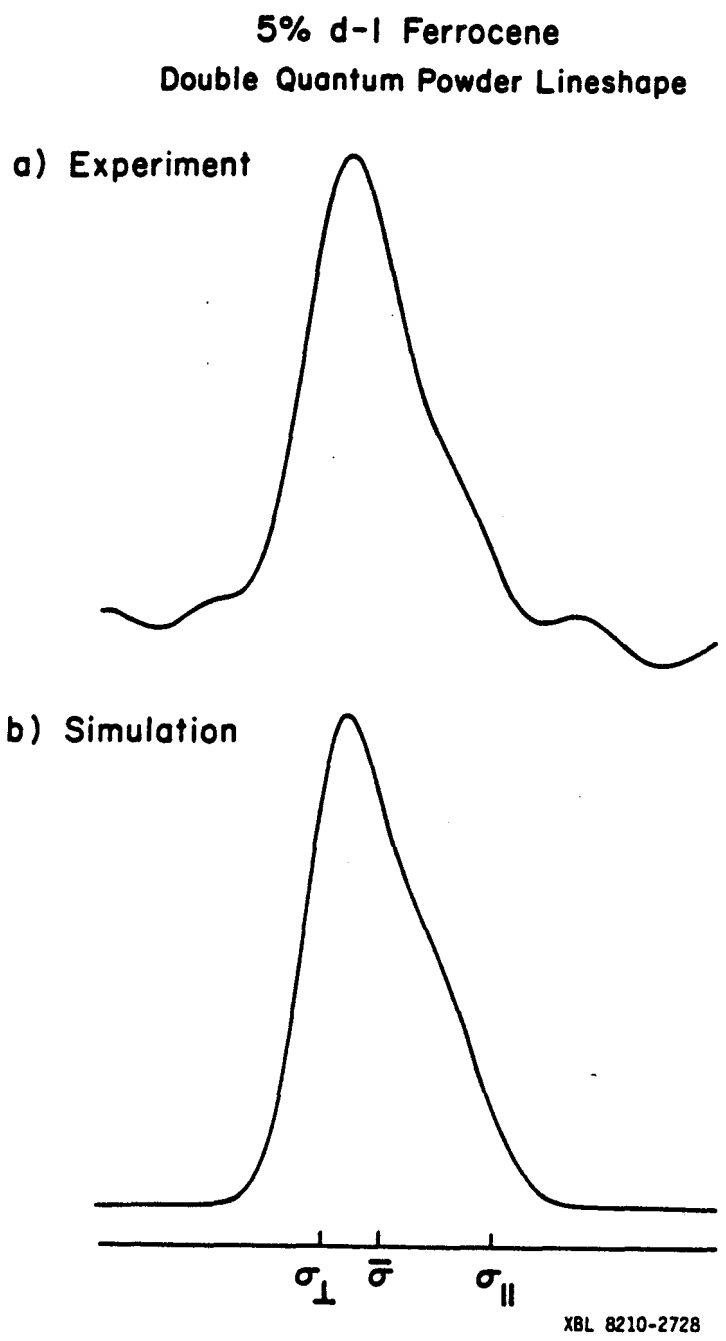

Figure II.31 (a) The DQ chemical shielding powder lineshape for d-1 ferrocene (5% in normal ferrocene), obtained by Dave Wemmer [40]. (b) A simulation assuming axial and aligned shielding and EFG tensors, ν_{Qc}= 36 KHz, and a four-pulse DQ sequence (weak pulses: ν_1=20 KHz, t=25 μsec; strong pulses: ν_1=62.5 KHz, t=4 μsec). The positions of $\sigma_\perp$, $\bar{\sigma}$, and $\sigma_{||}$ were obtained from the unbroadened lineshape. 150 points wide initially, it was smoothed 2000 times, equivalent to a convolution with a Gaussian of standard deviation ≈ 32 points. Experimentally, $|\sigma_\perp - \sigma_{||}|$ = 6.5 ppm.

magnet inhomogeneity to a fraction of a ppm, especially if both room-temperature and superconducting shims are used. Linewidth measurements at several different deuterium concentrations will indicate if homonuclear dipolar coupling is an important source of broadening. If so, the concentration can be lowered, although this reduction entails a longer acquisition time. In a similar manner, a study of linewidth vs. proton decoupling power will reveal if heteronuclear dipolar coupling is a problem. A spherical sample will minimize broadening due to the bulk susceptibility, and the use of as high a magnetic field as possible will shrink second-order quadrupole effects (as well as increasing the chemical shielding range relative to the size of the dipolar couplings). Therefore, despite the considerable effort required, I am confident that someday someone will see a trace experimentally of the dips and wiggles my computer programs predict.

2.10.3 Non-Axial But Aligned Tensors: A Simulated Lineshape for $Ba(ClO_3)_2 \cdot HDO$

At the suggestion of Dave Wemmer, the DQ transfer function for $Ba(ClO_3)_2 \cdot HDO$ has also been computed. Chiba [80] has studied the single-quantum spectrum of a single crystal of $Ba(ClO_3)_2 \cdot D_2O$ and determined the orientation and magnitude of the electric field gradient tensor. At low temperature ($\sim -130°C$), the EFG tensor is almost perfectly axial ($\eta_Q \approx 0.0$) with $e^2qQ/h = 243.5$ KHz and the unique principal axis parallel to the O-D bond--a result consistent with a stationary D_2O molecule. At room temperature, water molecules make rapid two-fold jumps about their C_2 axes. To describe the effect of this motion on the spectrum, we first recall

that an axial EFG tensor $\underset{\approx}{V}$ can be written in its principal axis system X, Y, Z as

$$\underset{\approx}{V} = eq \begin{pmatrix} -\frac{1}{2}(1+\eta_Q) & 0 & 0 \\ 0 & -\frac{1}{2}(1-\eta_Q) & 0 \\ 0 & 0 & 1 \end{pmatrix} = eq \begin{pmatrix} -\frac{1}{2} & 0 & 0 \\ 0 & -\frac{1}{2} & 0 \\ 0 & 0 & 1 \end{pmatrix} . \tag{II.68}$$

In an axis system with $\hat{x}$ perpendicular to the C_2 symmetry axis but in the plane of the water molecule, $\hat{y}$ parallel to the C_2 axis, and $\hat{z}$ perpendicular to the plane of the molecule, the EFG tensors of the two deuteron sites are

$$\underset{\approx}{V}_1 = eq \begin{pmatrix} \sin^2\theta - \frac{1}{2}\cos^2\theta & \frac{3}{2}\cos\theta\sin\theta & 0 \\ \frac{3}{2}\cos\theta\sin\theta & \cos^2\theta - \frac{1}{2}\sin^2\theta & 0 \\ 0 & 0 & -\frac{1}{2} \end{pmatrix} \tag{II.69a}$$

and

$$\underset{\approx}{V}_2 = eq \begin{pmatrix} \sin^2\theta - \frac{1}{2}\cos^2\theta & -\frac{3}{2}\cos\theta\sin\theta & 0 \\ -\frac{3}{2}\cos\theta\sin\theta & \cos^2\theta - \frac{1}{2}\sin^2\theta & 0 \\ 0 & 0 & -\frac{1}{2} \end{pmatrix} , \tag{II.69b}$$

where θ is half of the D-O-D bond angle. When rapid 180° flips occur about the C_2 axis, the deuterons see the average of $\underset{\approx}{V}_1$ and $\underset{\approx}{V}_2$:

$$\underset{\approx}{V}_{ave} = \frac{1}{2}(V_1 + V_2) = eq\begin{pmatrix} \sin^2\theta - \frac{1}{2}\cos^2\theta & 0 & 0 \\ 0 & \cos^2\theta - \frac{1}{2}\sin^2\theta & 0 \\ 0 & 0 & -\frac{1}{2} \end{pmatrix} \tag{II.70}$$

The D-O-D bond angle is 105°; half of this is approximately the magic angle, 54.7°, for which $\cos^2\theta = \frac{1}{3}$ and $\sin^2\theta = \frac{2}{3}$. With this choice of θ,

$$V_{ave} = \frac{1}{2}\, eq\begin{pmatrix} 1 & 0 & 0 \\ 0 & 0 & 0 \\ 0 & 0 & -1 \end{pmatrix} \quad . \tag{II.71}$$

Thus when the tensor is motionally averaged, the coupling constant e^2qQ/h drops by a factor of two and η_Q becomes approximately equal to one, as Chiba indeed observed in the single-quantum spectrum.

Our interest lies, however, in the double-quantum spectrum of $Ba(ClO_3)_2{\cdot}HDO$. The deuterium chemical shielding tensor at low temperature is also expected to be axial and aligned with the O-D bond. The effect of motional averaging will be the same for this tensor as for the EFG tensor; hence $\eta_{cs} \approx 1.0$ at room temperature as well. That the two averaged tensors have the same principal axis system orientation and the same asymmetry parameter means that only one value of ν_Q corresponds to each value of σ--thus $T(\nu_Q)$ and $T(\sigma)$ are identical functions.

An optimized transfer function has naturally been calculated and appears in Fig. II.32. The value of ν_{Qc} is 45 KHz [80] and the pulse sequence is as follows:

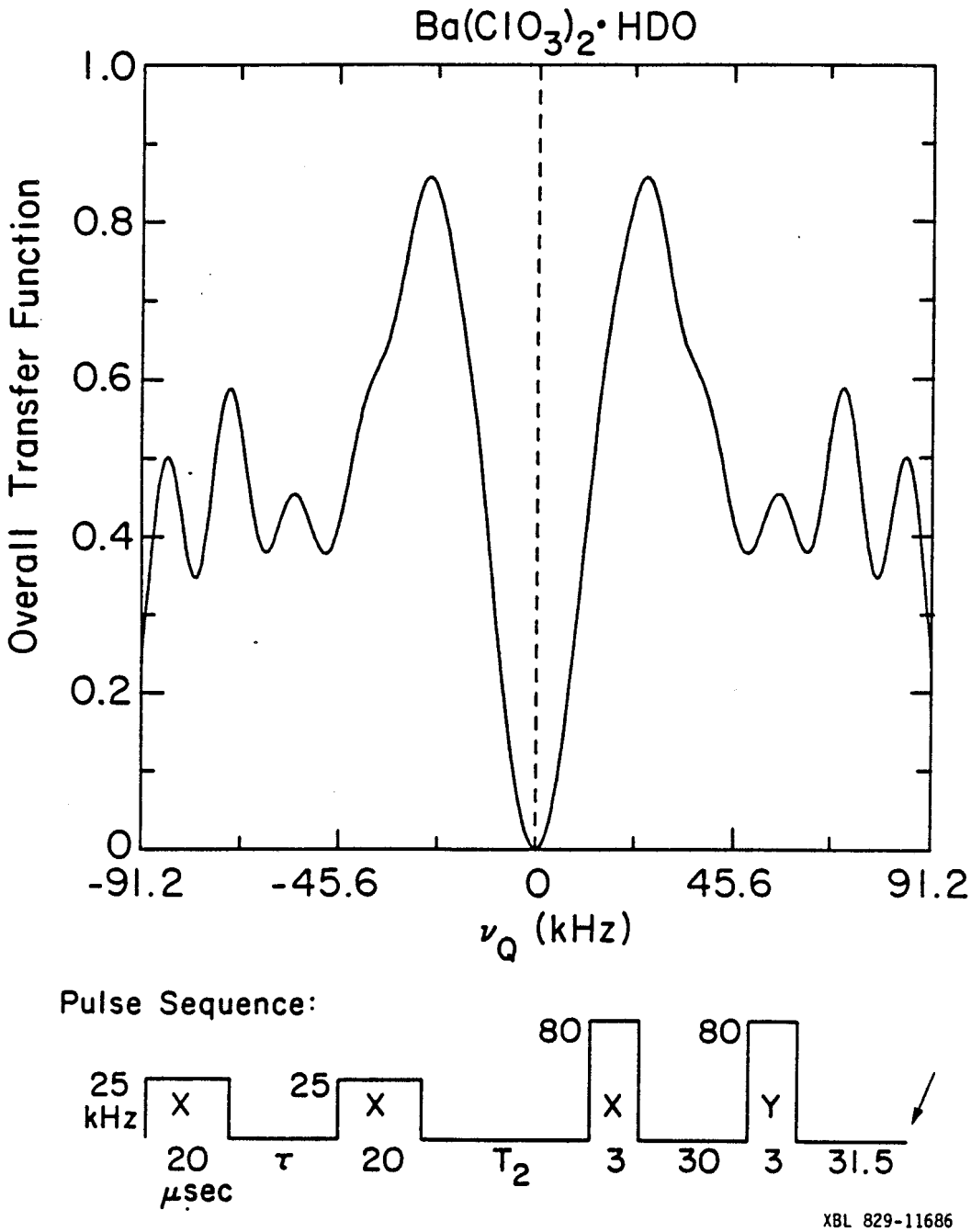

Figure II.32 An optimized four-pulse transfer function for preparation and detection of deuterium DQ coherence in polycrystalline $Ba(ClO_3)_2 \cdot HDO$. Additional numbers: ν_{Qc}=45.6 KHz, $\eta_Q \approx 1.0$, $\eta_{cs} \approx 1.0$, and $\Delta\nu=0$.

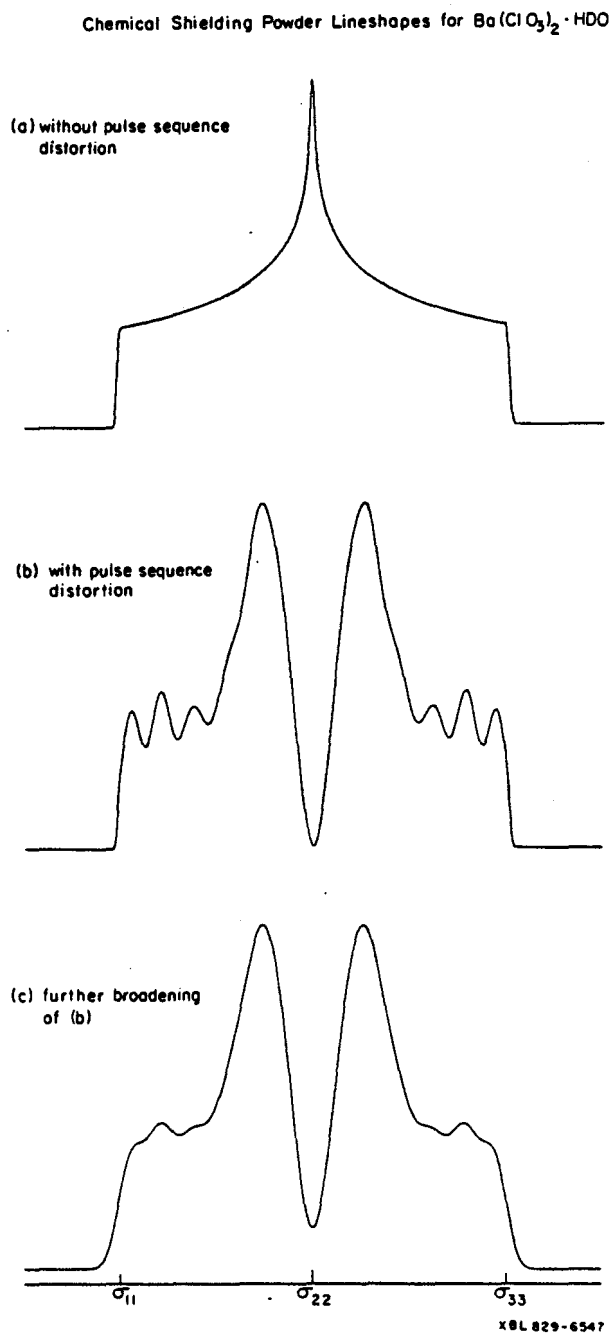

Figure II.33 Three simulated chemical shielding powder lineshapes for $Ba(ClO_3)_2 \cdot HDO$. (a) An $\eta = 0$ lineshape without pulse sequence distortion. (b) The lineshape in (a) multiplied by the transfer function of Fig. II.32. (c) A smoothed and hence broadened version of (b).

1.	x-pulse	20 μsec	25 KHz	5.	x-pulse	3 μsec	80 KHz
2.	delay	τ		6.	delay	30 μsec	
3.	x-pulse	20 μsec	25 KHz	7.	y-pulse	3 μsec	80 KHz
4.	delay	$t > T_2$		8.	delay	31.5 μsec	

Appropriate distorted lineshapes with $\eta_{cs} = 1.0$ appear in Fig. II.33. Notice that the "big dip" associated with $\nu_Q = 0$ eliminates the central peak of the undistorted powder pattern. The resulting double-humped structure should be readily detected experimentally; unfortunately, the experiment has not yet been done.

2.11 Lineshapes for General Tensor Orientations

Thus far we have only considered shielding tensor lineshapes for systems in which the principal axis frames of the quadrupole and chemical shielding tensors are aligned and for which $\eta_{cs} = \eta_Q$. In these cases, there is a one-to-one correspondence between σ and ν_Q and thus $T(\sigma) \equiv T(\nu_Q)$. For the general case of non-congruent tensors at an arbitrary relative orientation, the relationship of $T(\sigma)$ and $T(\nu_Q)$ is not at all simple--a range of ν_Q values will correspond to a particular value of σ. As a result, each point of $T(\sigma)$ involves an integral over portions of $T(\nu_Q)$, and the two functions can thus be very different.

The most general case of non-axial and non-aligned shielding and quadrupole tensors requires a knowledge of the three Euler angles which relate the two principal axis frames. To preserve a shred of simplicity, however, we will assume that the chemical shielding tensor is axially symmetric. The relative orientation of the two tensor frames can then be specified by only two angles

α and β describing the position of the unique shielding axis in the EFG principal axis system. [The coordinates of the shielding "vector" are ($\sin\beta \cos\alpha$, $\sin\beta \sin\alpha$, $\cos\beta$).]

Calculation of $T(\sigma)$ for a given pair of angles α and β, a given set of parameters η_Q, ν_{Qc}, σ_0, and $\bar{\sigma}$, and a given pulse sequence proceeds as follows. (1) $T(\nu_Q)$ is determined for the pulse sequence using either the two-term-Hamiltonian evolution equations of Tables II.6 and II.7 or the exact computer results. (2) A large number ($\sim$ 20 000) of nearly equally spaced points are chosen on the unit sphere, each point representing a magnetic field orientation characterized by polar angles θ and ϕ relative to the EFG frame. (3) The values of ν_Q and σ are calculated for each point, i.e., each combination of θ and ϕ . (4) If ν_{Qi} and σ_i are the quantities so obtained, then the value of $T(\nu_{Qi})$ is added to an output "bin" specified by the value of σ_i. (5) The <u>average</u> contribution to each bin is calculated at the last step to yield a point-by-point trace of $T(\nu_Q)$.

There are obviously too many variables in this procedure for any sort of definitive study here; instead only a few examples will be presented. We will once again assume ν_{Qc} = 36 KHz and choose a pulse sequence very much like the one discussed in section 2.10.1:

1.	x-pulse	25 μsec	20 KHz	5.	x-pulse	3 μsec	80 KHz
2.	delay	τ		6.	delay	30 μsec	
3.	x-pulse	25 μsec	20 KHz	7.	y-pulse	3 μsec	80 KHz
4.	delay	$t > T_2$		8.	delay	31.5 μsec.	

When the two tensors are axially symmetric and aligned, a familiar $T(\sigma)$ and lineshape result (Fig. II.34). Keeping both tensors axially symmetric but separating the unique axes by 10° markedly changes the appearance of $T(\sigma)$ and the powder lineshape (Fig. II.35). In particular, the big dip at $\sigma = \bar{\sigma}$ fills in since intensity from crystallites with $\nu_Q \neq 0$ can contribute there. The same effect is achieved by keeping $a = \beta = 0°$ but setting $\eta_Q \neq 0$. Fig. II.36 shows the shielding transfer function and lineshape for $\eta_Q = 0.5$.

These powder lineshapes (and <u>many</u> more that could be generated) are of interest for the following reason: if experimental resolution were sufficiently good, the nature and location of chemical shielding powder pattern distortions could possibly reveal the relative orientation of the shielding and EFG tensors. Since the orientation of the latter with respect to the molecule is often known or can be surmised, one would therefore have a handle on the orientation of the former relative to molecular axes.

This sort of information, however, is much more easily and unambiguously obtained via two-dimensional NMR. Linder, Hohener, and Ernst [81] have demonstrated the technique with some beautiful 2-D powder spectra, including a carbon-13 spectrum of benzene showing the ^{13}C chemical shielding lineshape along one axis and the ^{13}C-^{1}H dipolar powder pattern along the other.

In our case, we would collect a single-quantum FID beginning at the quadrupolar echo point for each value of τ. A double Fourier transform with respect to τ and with respect to the FID time would then yield the 2-D spectrum. Simulated lineshapes for the case of axial and aligned tensors appear in Fig. II.37 and Fig. II.38, with

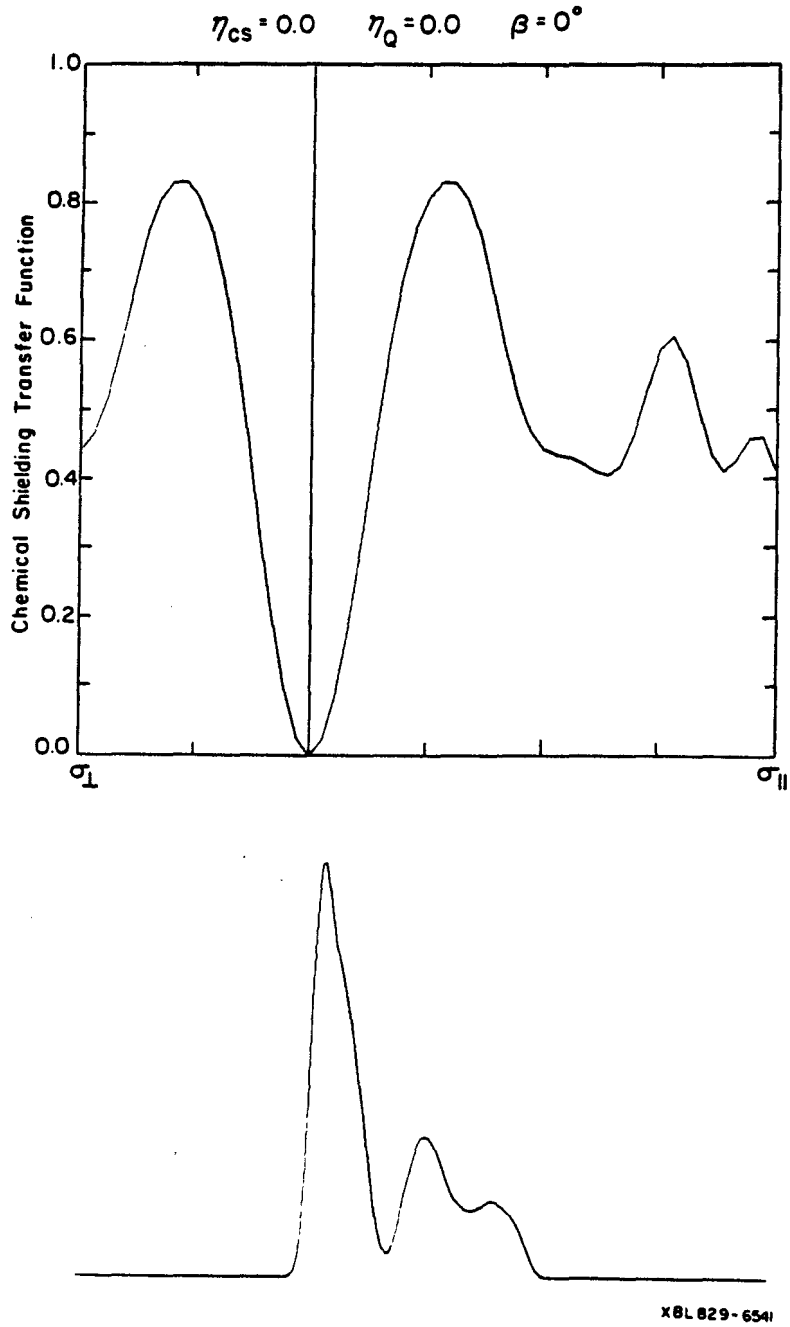

Figure II.34 A chemical shielding transfer function and corresponding powder lineshape for axial and aligned shielding and EFG tensors. A four-pulse DQ sequence was used (weak pulses: ν_1=20 KHz, t=25 μsec; strong pulses: ν_1=80 KHz, t=3 μsec) with ν_{Qc}=36 KHz.

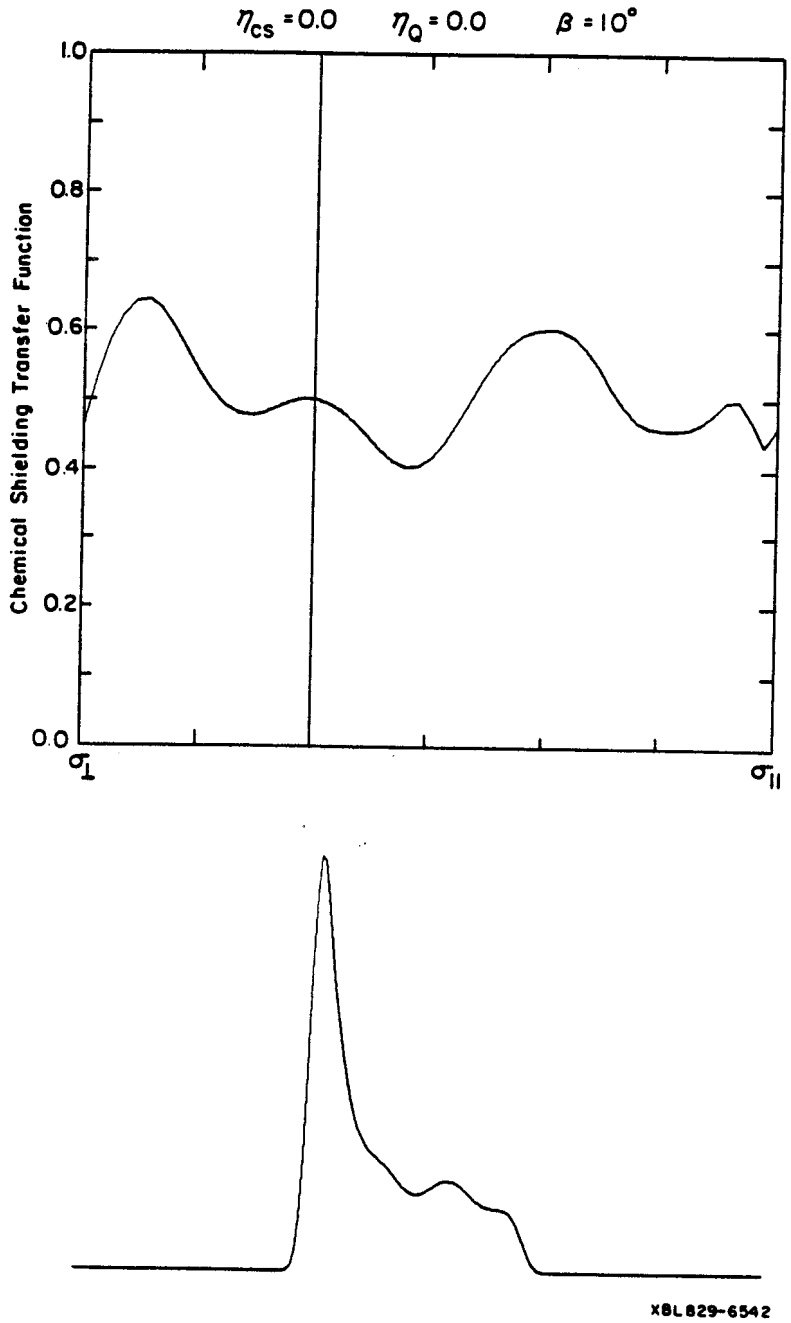

Figure II.35 The DQ chemical shielding transfer function and powder lineshape for axial shielding and EFG tensors with unique principal axes separated by an angle β=10°. Pulse sequence parameters as in Figure II.34. Unlike Figure II.34, there is no dip in intensity at $\bar{\sigma}$.

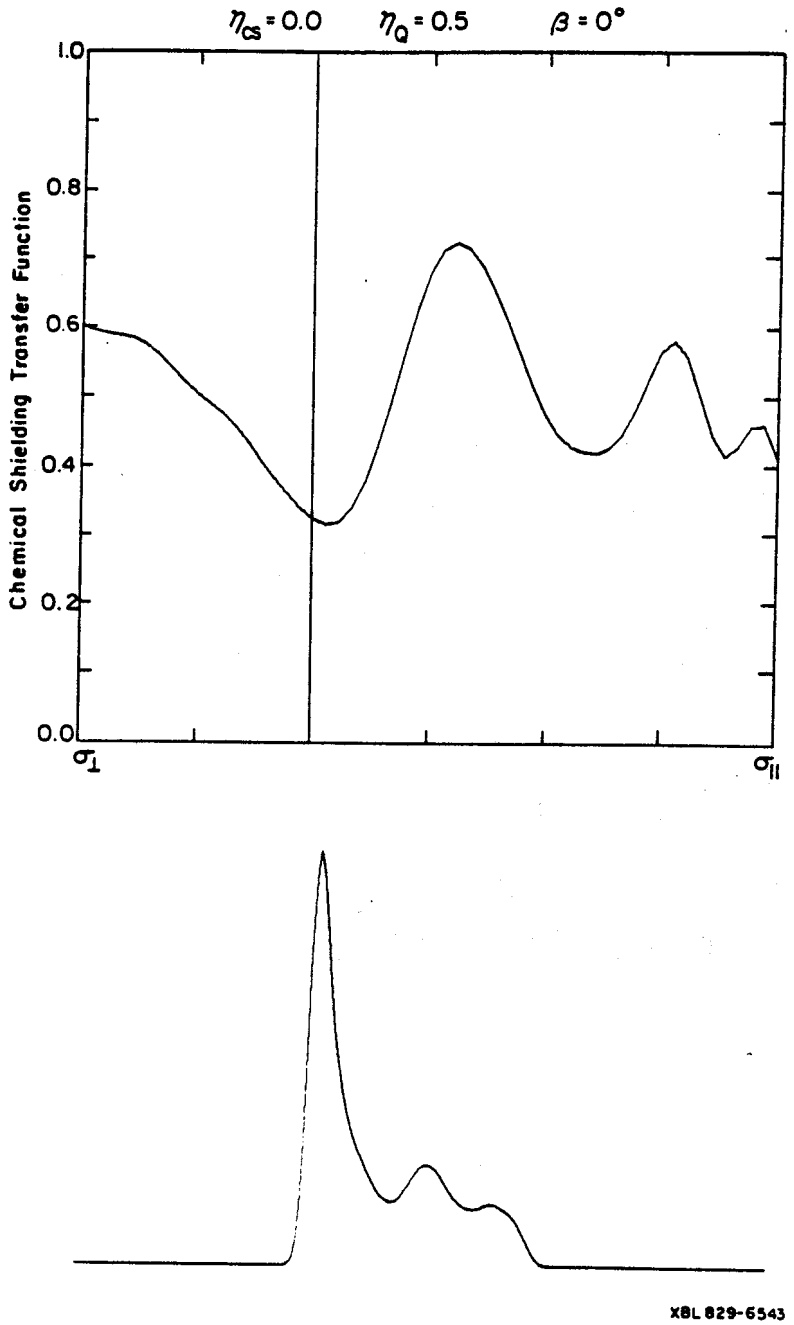

Figure II.36 The DQ chemical shielding transfer function and powder lineshape for an axial shielding tensor and an EFG tensor with η_Q=0.5. The z principal axes of the two tensors are aligned (β=0°). Pulse sequence parameters as in Figure II.34.

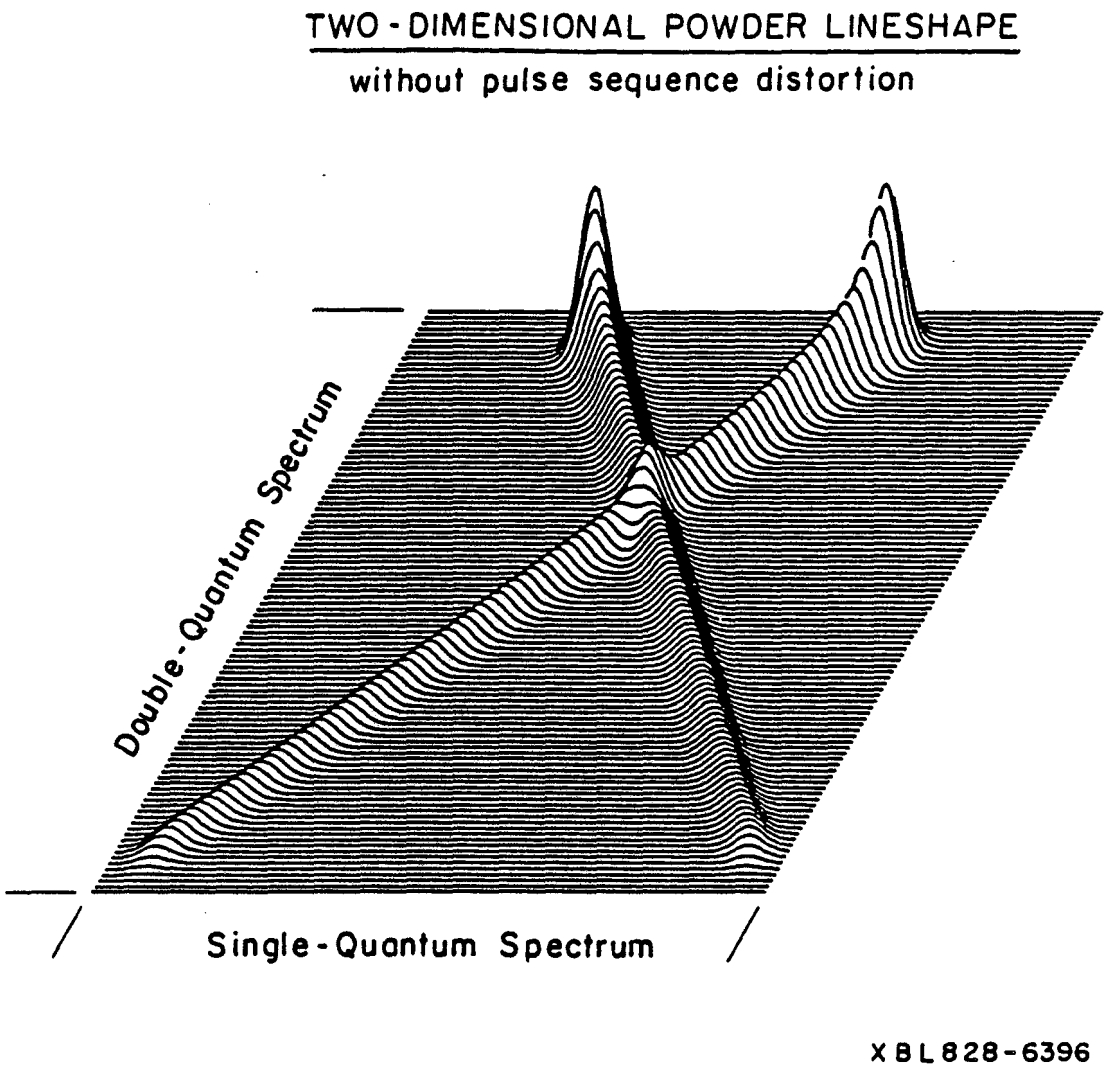

Figure II.37 An idealized two-dimensional magnitude spectrum for a polycrystalline deuterium sample--no transfer function distortions are considered, and the shielding and EFG tensors are assumed to be axial and aligned. A projection onto the single-quantum axis yields the quadrupole powder lineshape; a projection onto the double-quantum axis yields the chemical shielding powder lineshape.

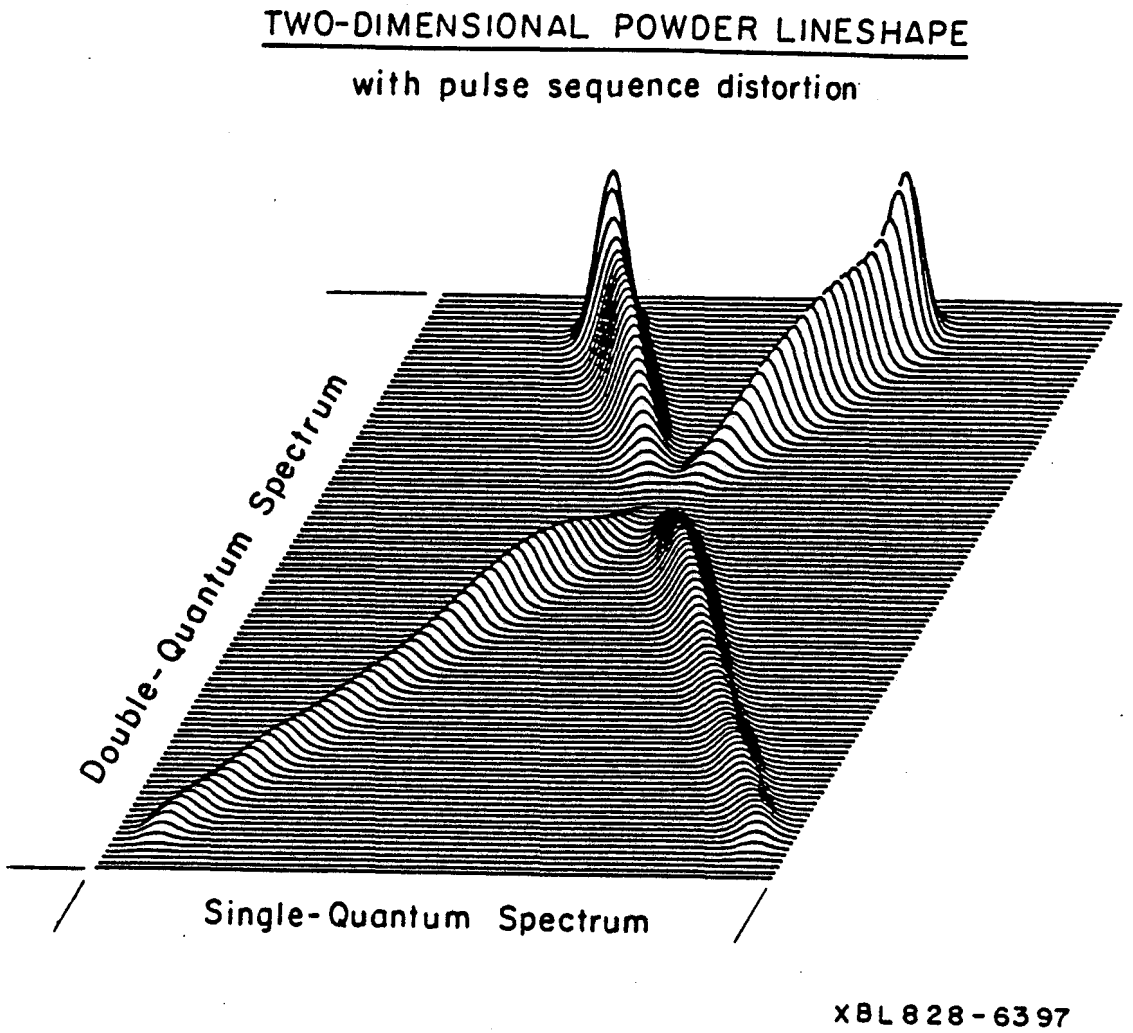

Figure II.38 Another two-dimensional deuterium magnitude spectrum, this time including the distortions inherent in a four-pulse DQ sequence. As in Figure II.37, the shielding and EFG tensors were chosen to be axial and aligned with ν_{Qc}=36 KHz. The resulting loss of intensity at ν_Q=0 and $\sigma=\bar{\sigma}$ is apparent where the "ridges" cross.

and without the distortions caused by the pulse sequence described earlier in this section. In both spectra, the projection along one axis is the single-quantum quadrupole powder lineshape; the projection along the other axis is the DQ chemical shielding pattern.

2.12 Effect of the Second-Order Quadrupole Shift

One complication in the measurement of chemical shielding tensors by double-quantum spectroscopy has only been alluded to thus far, but will now be laid bare: the second-order quadrupole shift Hamiltonian. The effect of this term is to increase the spacing between the $|1\rangle$ and $|-1\rangle$ energy levels; second-order energy corrections for $\eta_Q = 0$ are as follows [20]:

$$m = -1 \qquad E_{-1}^{(2)} = \frac{1}{2}\left(\frac{\nu_{Qc}}{\nu_0}\right)^2(\sin^2\theta)(3\cos^2\theta+1) \quad ,$$

$$m = 0 \qquad E_0^{(2)} = 0 \quad ,$$

$$m = 1 \qquad E_1^{(2)} = -\frac{1}{2}\left(\frac{\nu_{Qc}}{\nu_0}\right)^2(\sin^2\theta)(3\cos^2\theta+1) \quad , \qquad \text{(II.72)}$$

where ν_0 is the deuterium Larmor frequency. The second-order shift thus acts like a <u>chemical</u> shift during free evolution and must be taken into account for an accurate analysis of DQ powder lineshapes.

For simplicity, let us assume once again that the quadrupole and chemical shielding tensors are axially symmetric and aligned. The double-quantum precession frequency, $E_{-1}-E_1$ in the rotating frame, is then

$$2\,\nu_{DQ} = 2\bar{\sigma} + 2\sigma_0(3\cos^2\theta-1) + \left(\frac{\nu_{Qc}^{\;2}}{\nu_0}\right)(\sin^2\theta)(3\cos^2\theta+1)\ . \quad \text{(II.73)}$$

The frequency per photon is half this quantity.

Now for some typical numbers. In a magnet for which the proton Larmor frequency is 180 MHz, ν_0 for deuterium is 28.4 MHz. If we consider rapidly spinning benzene or ferrocene, ν_{Qc} = 36 KHz and $\Delta\sigma = \sigma_{||}-\sigma_{\perp}$ = -6.5 ppm = -185 Hz. The corresponding value of σ_0 is -2.2 ppm = -62 Hz, and we have

$$\nu_{DQ} - \bar{\sigma} = (-62\text{ Hz})(3\cos^2\theta-1) + (23\text{ Hz})(\sin^2\theta)(3\cos^2\theta+1)\ . \quad \text{(II.74)}$$

Even at a relatively low ν_{Qc} value of 36 KHz, the second-order shift term is non-negligible. The situation is worse of course if the benzene or ferrocene rings are not spinning; in that case, both σ_0 and ν_{Qc} are twice as large, but the <u>square</u> of the characteristic quadrupole frequency appears in the expression for ν_{DQ}:

$$\nu_{DQ} - \bar{\sigma} = (-125\text{ Hz})(3\cos^2\theta-1) + (91\text{ Hz})(\sin^2\theta)(3\cos^2\theta+1)\ . \quad \text{(II.75)}$$

A few simulated lineshapes will bring Eq. II.73 more fully to life. For simplicity, no pulse sequence distortions are included. Figure II.39 displays the pure second-order quadrupole powder lineshapes (σ_0 = 0) for ν_{Qc} = 36 KHz (top) and 72 KHz (bottom). The center peak of each corresponds to θ = 90°, the peak on the

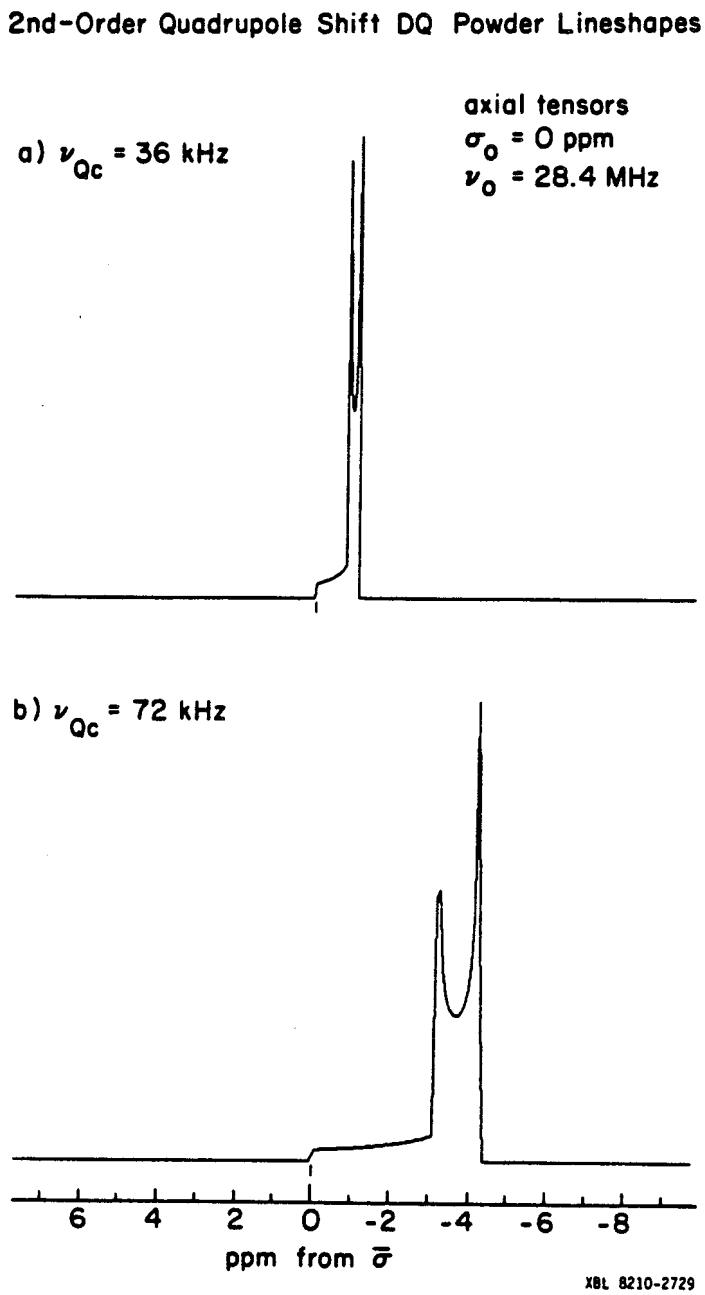

Figure II.39 Two simulated deuterium DQ spectra featuring second-order quadrupole powder lineshapes for different values of ν_{Qc}. No chemical shielding anisotropy or pulse sequence distortions are included and η_Q is assumed to be zero. Overall linewidths are 1.07 ppm in (a) and 4.28 ppm in (b).

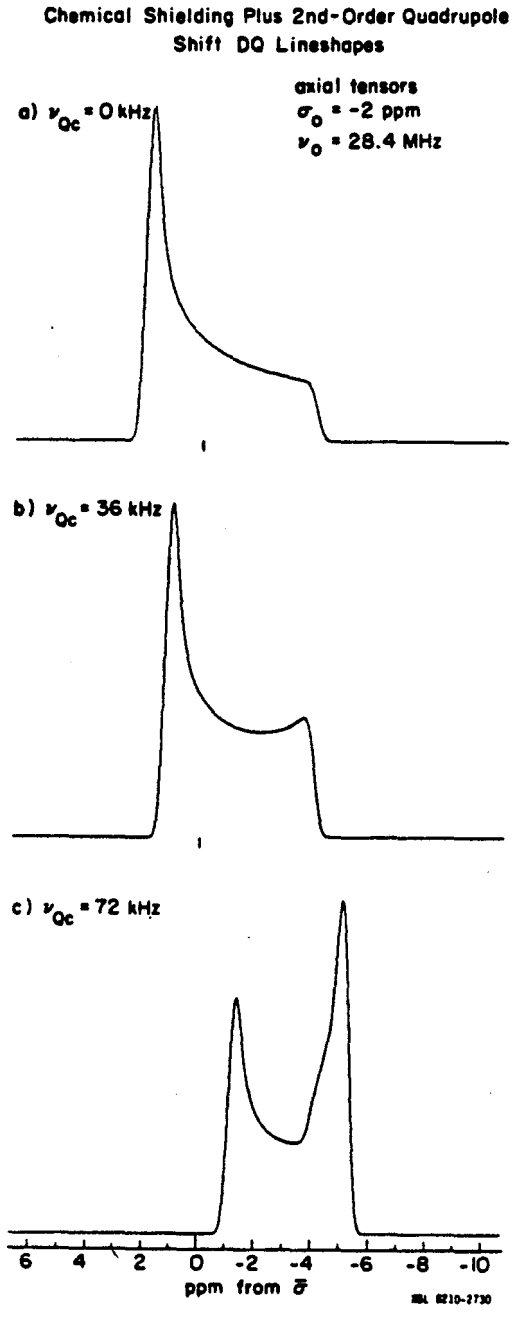

Figure II.40 Simulated and slightly broadened deuterium DQ powder lineshapes featuring a chemical shielding anisotropy σ_o of -2 ppm and varying amounts of second-order quadrupole broadening. The EFG and shielding tensors are assumed to be axial and aligned, and no pulse sequence distortions are included. As ν_{Qc} increases, the overall unbroadened linewidth drops from 6.0 ppm to 5.2 ppm to 4.0 ppm.

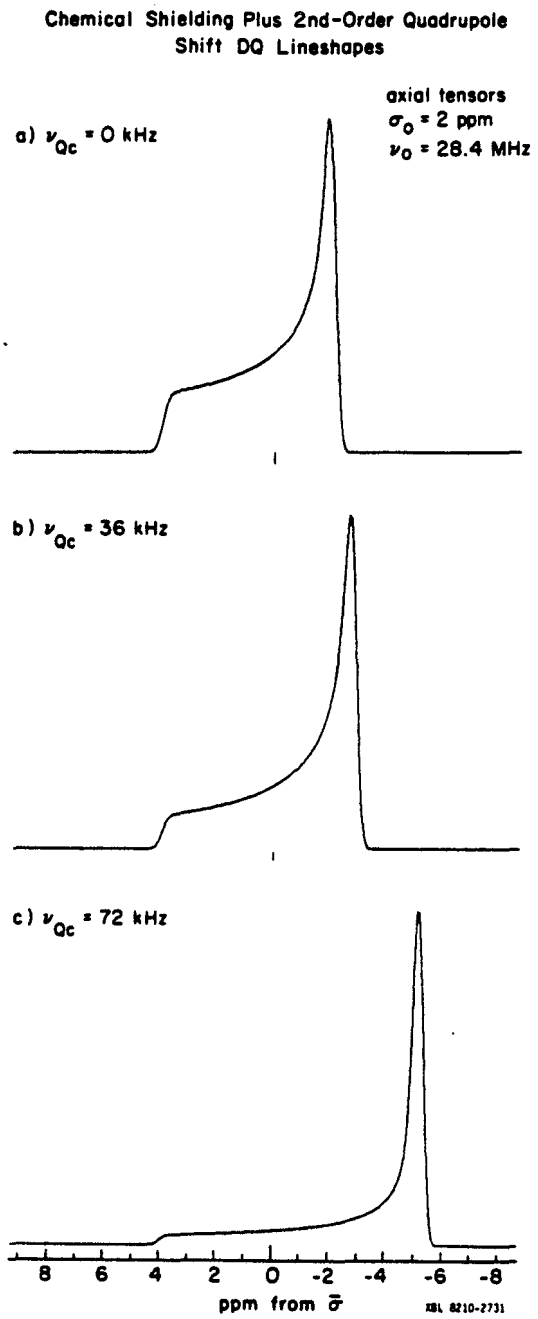

Figure II.41 Deuterium DQ powder lineshapes as in Figure II.40, but with a chemical shielding anisotropy σ_o=+2 ppm. As ν_{Qc} increases, the overall unbroadened linewidth expands from 6.0 ppm to 6.8 ppm to 9.2 ppm.

right to $\theta = \theta_m = 54.7°$, and the low shoulder on the left to $\theta = 0°$. The overall linewidths are 1.07 ppm and 4.28 ppm respectively.

In Fig. II.40, the value of σ_0 is fixed at -2 ppm (roughly the value for rotating benzene or ferrocene). The characteristic quadrupole frequency ν_{Qc} varies from 0 KHz (top) to 36 KHz (middle) to 72 KHz (bottom), substantially changing both the lineshape and the overall linewidth (which drops from 6.00 ppm to 5.20 ppm to 4.00 ppm). In contrast, when σ_0 equals +2 ppm, the effect of the second-order shift is to stretch the powder lineshape, as illustrated in Fig. II.41. As ν_{Qc} increases from 0 KHz to 36 KHz to 72 KHz, the overall linewidth expands from 6.00 ppm to 6.80 ppm to 9.22 ppm.

2.13 Double-Quantum Spin-Locking

In the spirit of Vega and Pines [64], Gold [68], and Hatanaka and Hashi [62], I too have explored the eminently curious phenomenon of double-quantum spin-locking. My sample was a single crystal of d-18 hexamethylbenzene oriented for maximum quadrupolar splitting (ν_Q = 16.7 KHz). Both the short-term and long-term properties of DQ spin-locking were investigated.

The conventional single-quantum spin-locking experiment begins with a 90° x-pulse to create transverse magnetization along the y-axis of the rotating frame. A 90° rf phase shift leads to a parallel configuration of H_1 and the magnetization. Then as long as the rf field stays on, the decay of the locked magnetization requires energy exchange with the lattice and is characterized by a relaxation time $T_{1\rho}$ that is on the order of T_1 rather than T_2.

As noted in section 2.4.3, the DQ operators $I_{z,2}$ and $I_{z,3}$

interconvert under rotation about the $I_{z,1}$ axis with twice the frequency of the SQ operators $I_{z,1}$ and $I_{y,1}$. Therefore a DQ preparation pulse followed by rf irradiation at a 45° phase shift will result in double-quantum spin-locking. Although there is no magnetization associated with DQ coherence, its decay is nonetheless a type of T_1 process.

When $\nu_1 << \nu_Q$, spin locking can be understood as follows. As detailed in section 2.8.1, a weak pulse acts like a rotation about $I_{z,3}$, converting the density matrix from $I_{z,1}$ to $I_{z,2}$. Specifically,

$$\mathcal{H} \approx -\left(\frac{\nu_1^2}{\nu_Q}\right) I_{z,3} + \frac{2}{3}\nu_Q I_{xy,3} \qquad \text{(II.76a)}$$

Shifting the rf phase by 45° converts this Hamiltonian to

$$\mathcal{H} \approx \left(\frac{\nu_1^2}{\nu_Q}\right) I_{z,2} + \frac{2}{3}\nu_Q I_{xy,3} \qquad \text{(II.76b)}$$

That both the phase-shifted Hamiltonian and the prepared DQ density matrix are proportional to $I_{z,2}$ leads to locking.

A more involved analysis of an evolving spin-locked spin-one system is made easier if the phase of the DQ preparation pulse is 45°. The prepared density matrix is then $I_{z,3}$. Its subsequent evolution during a spin-locking y-pulse can be obtained from the well-worn equations of Table II.7 if it is assumed that $\Delta\nu = 0$:

$$a_{z,3}(t) = 1 - \frac{\nu_1^2}{\nu_{eff}^2}\,[1 - \cos 2\pi\,\nu_{eff}\,t]$$

$$= \frac{\nu_Q^2 + 3\nu_1^2}{\nu_Q^2 + 4\nu_1^2} + \frac{\nu_1^2}{\nu_Q^2 + 4\nu_1^2}\cos 2\pi\,\nu_{eff}\,t \quad ,$$

$$a_{y,1}(t) = -\frac{\nu_1\nu_Q}{\nu_{eff}^2}\,[1 - \cos 2\pi\,\nu_{eff}\,t] \quad ,$$

$$a_{y,2}(t) = -\frac{\nu_1}{\nu_{eff}}\sin 2\pi\,\nu_{eff}\,t \quad ,$$

$$a_{xy,3}(t) = -\frac{\nu_1^2}{\nu_{eff}^2}\,[1 - \cos 2\pi\,\nu_{eff}\,t] \quad . \qquad \text{(II.77)}$$

For comparison, the evolution of a single-quantum coherence $I_{y,1}$ locked by a y-pulse is given by the following set of operator coefficients:

$$a_{y,1}(t) = \frac{\nu_Q^2}{\nu_{eff}^2}\cos 2\pi\,\nu_{eff}\,t + \frac{4\nu_1^2}{\nu_{eff}^2} \quad ,$$

$$a_{y,2}(t) = -\frac{\nu_Q}{\nu_{eff}}\sin 2\pi\,\nu_{eff}\,t \quad ,$$

$$a_{xy,3}(t) = -\frac{\nu_1\nu_Q}{\nu_{eff}^2}\,[1 - \cos 2\pi\,\nu_{eff}\,t] \quad ,$$

$$a_{z,3}(t) = -\frac{\nu_1 \nu_Q}{\nu_{eff}^2} [1 - \cos 2\pi \nu_{eff} t] \quad , \tag{II.78}$$

where again $\Delta\nu$ is assumed to be zero. Note that the same four operators are involved in both cases, including $I_{xy,3}$, the operator describing quadrupolar order. (The situation is definitely more complicated than in a spin-$\frac{1}{2}$ system, for which $\rho = I_y$, $\mathcal{H} = -\omega_1 I_y$, and no evolution occurs other than relaxation.)

The extent of double-quantum spin-locking as a function of time can be monitored by first applying a second DQ preparation pulse of 45° phase to rotate $I_{z,3}$ back to $I_{z,1}$, waiting a time on the order of T_2 for extraneous coherences to fade, and then applying a 90° pulse to create measurable single-quantum coherence. In this fashion the evolution of $I_{z,3}$ was put under surveillance for both small and large values of the spin-locking time. For short times, the detected magnetization should be proportional to $a_{z,3}(t)$:

$$a_{z,3}(t) = 1 - \frac{\nu_1^2}{\nu_{eff}^2} [1 - \cos 2\pi \nu_{eff} t] \quad . \tag{II.79}$$

The oscillations in the magnetization are in fact seen experimentally, as shown in Fig. II.42, along with a simulation. The spin-locking field ν_1 was roughly 60 KHz, hard to measure exactly due to pulse drooping. Agreement of simulation and experiment can be optimized by varying the ν_1 value used in the calculation; despite the stigma of a "fudge factor", the close spectral match is gratifying.

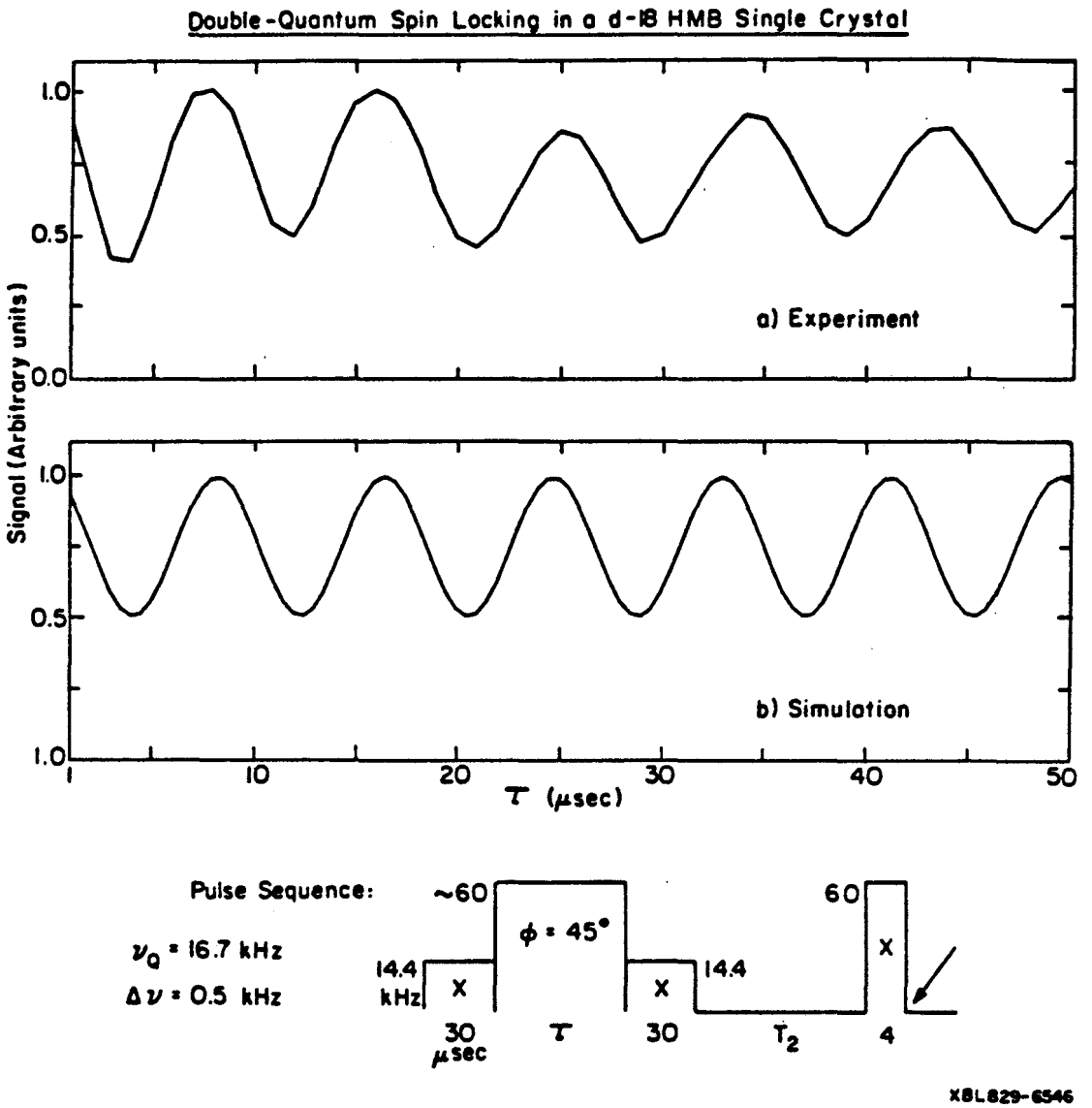

Figure II.42 Short-time oscillations in DQ coherence $a_{z,2}$ during spin-locking. The sample was a single crystal of perdeuterated hexamethylbenzene oriented such that ν_Q=16.7 KHz. The spin-locking field was ∿ 60 KHz for extremely short τ values, but drooped to ∿ 50 KHz as τ increased. This drop in ν_1 is mirrored in the experimental plot by a decreasing oscillation frequency as τ grows larger. 60 KHz was chosen for ν_1 in the simulation.

For longer spin-locking times, these oscillations damp out due to inhomogeneities in H_1 and H_0, but a value for the double-quantum $T_{1\rho}$ can be obtained from the slow exponential decay of the detected magnetization. I found $(T_{1\rho})_{DQ}$ = 38 msec for perdeuterated hexamethylbenzene. In contrast, a conventional single-quantum spin-locking experiment gave $(T_{1\rho})_{SQ}$ = 64 msec, a factor of 1.7 times longer.

CHAPTER III

CONTINUOUS-WAVE NMR WITH PHASE-CYCLED PULSES

3.1 Introduction

Time now for a little relaxation before making the leap to big spin systems in Chapters IV and V. Yes, for the first and only time in this dissertation, finite T_1 and T_2 values will be more than just a vaguely troubling complication in the experimental verification of our calculations. Instead, relaxation times will be explicitly included in our computations, although in a very simple-minded way.

The problem to be addressed in this chapter is as follows: can a particular multiple-quantum order (all transitions that involve a specified value of ΔM) be selectively excited in some sort of cw NMR experiment. If this feat is possible, such selectivity would circumvent the major drawback to cw multiple-quantum experiments: overlap of the sharp higher-quantum lines of interest with the saturation-broadened remains of lower-quantum transitions. The equations developed will be applicable to any order of coherence, but the pulse sequences these equations inspire will be tested on that scarred veteran from Chapter II, the three-level system.

The detailed theory of lineshapes for cw multiple quantum NMR was first worked out by Yatsiv [82] in a paper not noted for its appeal to the casual reader. More accessible descriptions were later put forth by both Anderson, Freeman, and Reilly [6] and Cohen and Whiffen [9]. They likened cw MQ NMR to a special case of nuclear double resonance in which the same rf field is used both to perturb energy levels (mixing eigenstates of the internal Hamiltonian with

different values of M) and to observe transitions between the levels.

The conceptual link to double resonance suggests the use of multiple frequencies for MQ NMR. This approach was first described by Yatsiv, who analyzed the effect of audio-modulated rf irradiation (giving rise to frequencies ω, $\omega-\omega_{aud}$, and $\omega+\omega_{aud}$) on the size of double-quantum intensity. For three states $|a\rangle$, $|b\rangle$, and $|c\rangle$ in successive Zeeman manifolds, one can enhance the two-quantum transition $|a\rangle \leftrightarrow |c\rangle$ by setting $\omega \approx \omega_{ac}/2$ and $\omega_{aud} \approx |\omega_{ab}-\omega_{bc}|/2$. (SQ excitation arises if the rf frequencies resulting from modulation are exactly resonant with the single-quantum transitions.) Cohen and Whiffen pointed out that rf frequency modulation or audio-oscillation of H_0 can also provide a spread in $\Delta\omega$ values, and they used the latter method to boost the double-quantum transition in an AX system.

Our approach to the problem of enhancing MQ transitions will be to modulate rf phase instead of amplitude or frequency. Indeed, the relationship between rf pulse phase and the phase of ΔM-quantum coherence will be the recurrent theme of our manipulations. As discussed at length in section 4.6.2, a change in rf phase of $\Delta\phi$ results in a coherence phase change of $(\Delta M)(\Delta\phi)$. The following scenario can thus be put forth. Imagine a system of three coupled protons or just a single spin-$\frac{3}{2}$ nucleus. First apply a very weak pulse with $\phi = 0°$ to an initial density matrix ρ_0 proportional to I_z. The evolution that occurs can be described schematically as follows:

$$U_0\, \rho_0\, U_0^{\dagger} \approx \rho_0 + c_0\, P_{0Q} + c_1\, P_{1Q} + c_2\, P_{2Q} + c_3\, P_{3Q}\,, \quad \text{(III.1)}$$

where U_0 is a pulse propagator for $\phi = 0°$, P_{nQ} is a shorthand for the operators representing n-quantum coherence, and c_n is a small number proportional in some loose sense to the amount of n-quantum coherence created. Now consider applying a second pulse to the system, but phase-shifting it by 120°. The density matrix after this second pulse is given by the following, where only linear terms in the small quantities are retained:

$$U_{120}U_0\rho_0U_0^{\dagger}U_{120}^{\dagger} \approx \rho_0 + [c_0P_{0Q}+c_1P_{1Q}+c_2P_{2Q}+c_3P_{3Q}]$$

$$+ [c_0P_{0Q} + e^{i2\pi/3}\, c_1P_{1Q} + e^{i4\pi/3}\, c_2P_{2Q} + c_3P_{3Q}] \; . \qquad \text{(III.2)}$$

Note that the coherences created by each pulse simply add in this linear regime. The effect of a third pulse with $\phi = 240°$ is to create coherences given by

$$c_0P_{0Q} + e^{i4\pi/3}\, c_1P_{1Q} + e^{i8\pi/3}\, c_2P_{2Q} + c_3P_{3Q} \; . \qquad \text{(III.3)}$$

When the three sets of coherences spawned by the three pulses are added together, the coefficients for single- and double-quantum coherences vanish since

$$(1 + e^{i2\pi/3} + e^{i4\pi/3}) = (1 + e^{i4\pi/3} + e^{i8\pi/3}) = 0 \; . \qquad \text{(III.4)}$$

In comparison, zero- and three-quantum coherences add constructively, as illustrated schematically in Figure III.1. (If the system under

Effect of a 3k-Quantum Selective Sequence

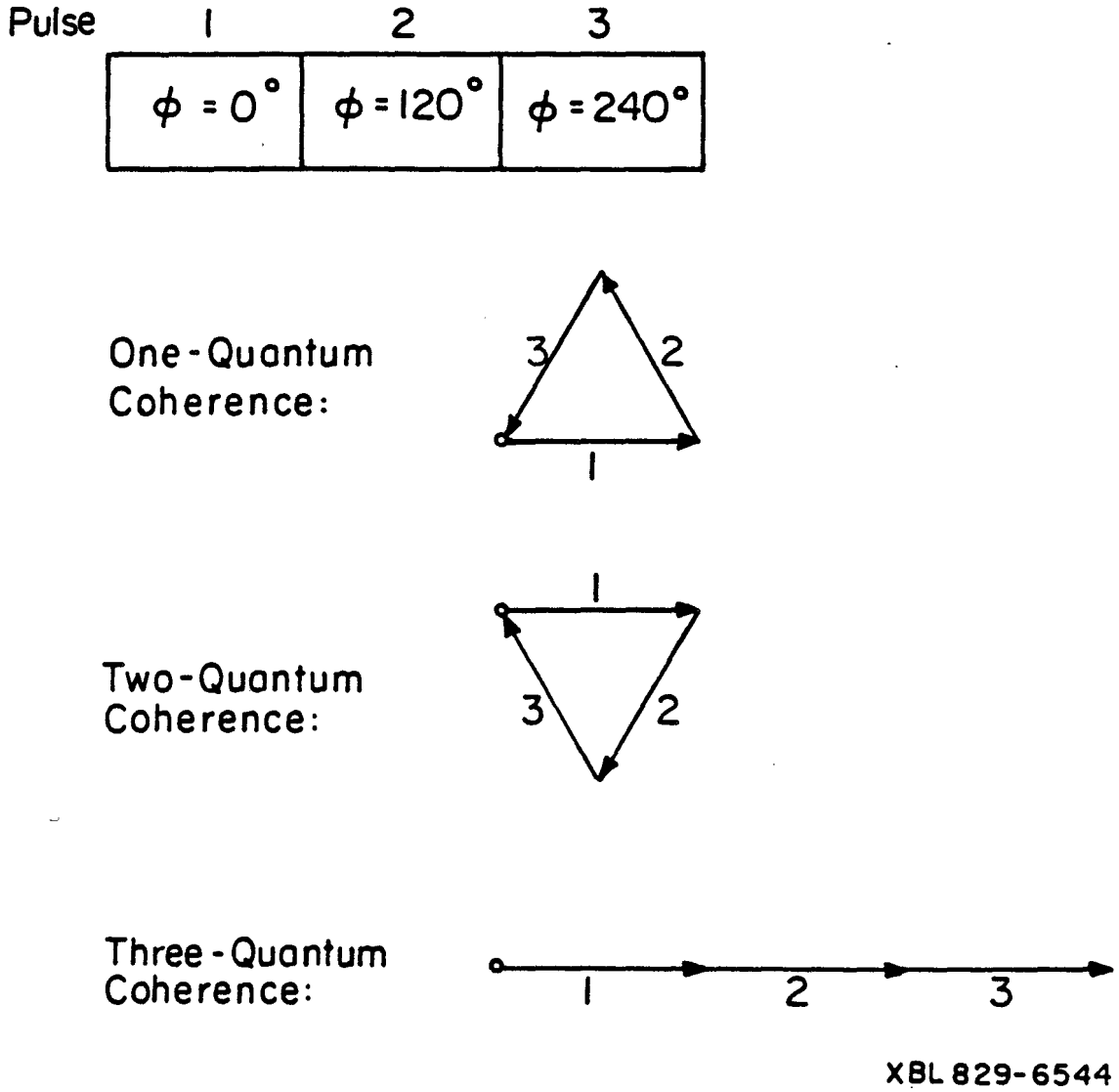

XBL 829-6544

Figure III.1 A schematic depiction of the coherences resulting from a 3k-quantum selective sequence. Each arrow represents the overall phase $\Delta M\phi$ of the ΔM-quantum coherence produced by a pulse of phase ϕ. For one- and two-quantum orders, these arrows add to zero in the complex plane; the selected 3Q arrows add constructively.

consideration is a single nucleus, then zero-quantum transitions do not exist.) The sequence is in fact 3k-quantum selective, with $k = 0,1,2,\ldots$.

This admittedly simplistic argument at least makes the selective preparation of n-quantum coherence seem qualitatively possible. Exciting the coherence is only half the battle, however, because ultimately the transverse magnetization associated with single-quantum transitions must be affected as well or nothing is detected.

Only a few preliminary calculations are included here--much work remains to be done to fully investigate the use of weak pulses in MQ NMR. The following scatter of topics will be considered in this chapter. In section 3.2, the frequency spectrum of a phase-shifted rf pulse cycle is analyzed with an eye towards multiple-quantum applications. In section 3.3, the Bloch equations are put to use in a superoperator describing the cw NMR lineshape of our favorite three-level system, the deuteron. A method for calculating the steady-state response to phase-shifted rf cycles is presented in section 3.4, and the method is applied to deuterium in section 3.5.

3.2 The Frequency Spectrum of a Phase-Cycled Sequence

Consider a continuous succession of rf pulses, each with the same length and ω_1 value, but with phases incremented by $2\pi/N$ radians at each step. As discussed earlier, this sequence is expected to be Nk-quantum selective. We now wish to see if this selectivity is mirrored in frequency space.

The sequence can be decomposed as shown in Figure III.2 into the sum of N periodically amplitude-modulated pulse trains with constant

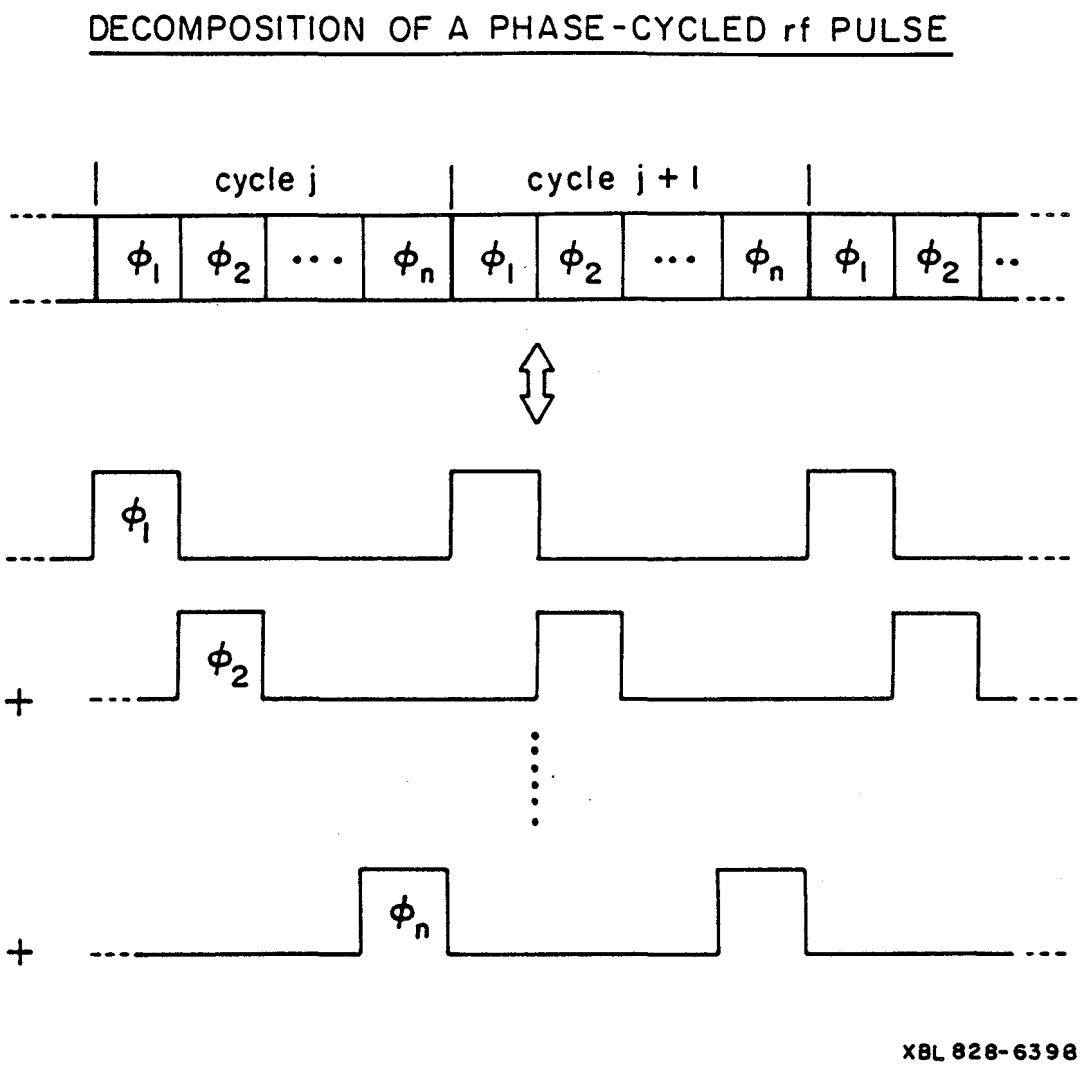

Figure III.2 A continuous but phase-cycled rf pulse can be treated as a sum of amplitude-modulated components, each with constant phase.

phase. Let $S_k(t)$ describe the on-off envelope of component k, and let ω_0 be the rf carrier frequency. The sum of the N components yields the complete waveform f as a function of time:

$$f(t) = \sum_{k=1}^{N} S_k(t) \cos(\omega_0 t + \phi_k)$$

$$= \frac{1}{2} \sum_{k=1}^{N} S_k(t) \cdot (e^{i(\omega_0 t+\phi_k)} + e^{-i(\omega_0 t+\phi_k)}) \quad , \qquad \text{(III.5)}$$

where $\phi_k = 2\pi k/N$. We are interested in the Fourier transform $g(\omega)$ of the function $f(t)$:

$$g(\omega) = \frac{1}{2} \sum_{k=1}^{N} \hat{S}_k(\omega) \times \int_{-\infty}^{\infty} (e^{i(\omega_0 t+\phi_k)} + e^{-i(\omega_0 t+\phi_k)}) e^{-i\omega t} \, dt, \qquad \text{(III.6)}$$

where "x" stands for convolution [78] and $\hat{S}_k(\omega)$ is itself the Fourier transform of $S_k(t)$:

$$\hat{S}_k(\omega) = \int_{-\infty}^{\infty} S_k(t) \, e^{-i\omega t} \, dt \quad . \qquad \text{(III.7)}$$

The integral in Eq. III.6 can be simplified by keeping only the non-oscillating term for $\omega_0 > 0$:

$$\int_{-\infty}^{\infty} e^{i(\omega_0 t+\phi_k)} + e^{-i(\omega_0 t+\phi_k)} \, e^{-i\omega t} dt = e^{i\phi_k} \, \delta(\omega-\omega_0) \quad . \qquad \text{(III.8)}$$

With this reduction,

$$g(\omega) = \frac{1}{2} \sum_{k=1}^{N} \hat{S}_k(\omega) \times e^{i\phi_k} \delta(\omega-\omega_0) \quad . \tag{III.9}$$

We turn now to an evaluation of $\hat{S}_k(\omega)$, noting first that

$$S_k(t) = S_1[t + (k-1)\tau] \quad , \tag{III.10}$$

where τ is the length of each pulse. $\hat{S}_k(\omega)$ can then be written as follows:

$$\hat{S}_k(\omega) = \int_{-\infty}^{\infty} S_1[t + (k-1)\tau]e^{-i\omega t}\, dt \quad . \tag{III.11}$$

With $u = t + (k-1)\tau$,

$$\begin{aligned}\hat{S}_k(\omega) &= \int_{-\infty}^{\infty} S_1(u) \exp\{-i\omega[u-(k-1)\tau]\}du \\ &= \exp[i\omega(k-1)\tau]\int_{-\infty}^{\infty} S_1(u)\, e^{-i\omega u}\, du \\ &\equiv \exp[i\omega(k-1)\tau]\, \hat{S}_1(\omega) \quad .\end{aligned} \tag{III.12}$$

The Fourier transform of the amplitude function for component k is simply a phase factor times the Fourier transform of the amplitude function for the first component.

Now for the evaluation of $\hat{S}_1(\omega)$. Over one cycle, $S_1(t) = 2\omega_1$ for $0 \leq t \leq \tau$ and $S_1(t) = 0$ for $\tau < t < N\tau$. The periodicity of $S_1(t)$ implies that $S_1(t + N\tau) = S_1(t)$. Straightforward use of the Fourier series expansion yields

$$S_1(t) = B_0 + \sum_{n=1}^{\infty} A_n \sin n\omega_c t + \sum_{n=1}^{\infty} B_n \cos n\omega_c t \quad , \tag{III.13}$$

where $\omega_c = 2\pi/N\tau$ is the angular cycle frequency and

$$B_0 = \frac{2\omega_1}{N} \quad , \tag{III.14a}$$

$$B_n = \frac{4\omega_1}{2\pi n} \sin(\frac{2\pi n}{N}) \quad , \tag{III.14b}$$

$$A_n = \frac{4\omega_1}{2\pi n} [1 - \cos(\frac{2\pi n}{N})] \quad . \tag{III.14c}$$

Alternately,

$$S_1(t) = \sum_{n=-\infty}^{\infty} c_n e^{in\omega_c t} \quad , \tag{III.15}$$

with

$$c_0 = \frac{2\omega_1}{N} \quad , \tag{III.16a}$$

$$c_n = \frac{2\omega_1 i}{2\pi n} [\exp(-2\pi i n/N)-1] \quad . \tag{III.16b}$$

The Fourier transform of $S_1(t)$ is then simply

$$\hat{S}_1(\omega) = \sum_{n=-\infty}^{\infty} c_n \ \delta(\omega-n\omega_c) \quad . \tag{III.17}$$

We now can plug Eqs. III.12 and III.17 into Eq. III.9 and obtain

$$g(\omega) = \frac{1}{2} \sum_{k=1}^{N} \exp[i\omega(k-1)\tau] \; \hat{S}_1(\omega) \; x \; e^{i\phi_k} \; \delta(\omega-\omega_0)$$

$$= \frac{1}{2} \sum_{k=1}^{N} \exp[i\omega(k-1)\tau] \; (\sum_{n=-\infty}^{\infty} c_n \; \delta(\omega-n\omega_c)) \; x$$

$$e^{i\phi_k} \; \delta(\omega-\omega_0) \quad . \qquad \text{(III.18)}$$

The convolution in $g(\omega)$ can be evaluated at this stage. Recalling that [78]

$$\hat{f}_1(\omega) \; x \; \hat{f}_2(\omega) = \int_{-\infty}^{\infty} \hat{f}_1(\Omega) \; \hat{f}_2(\omega-\Omega) \, d\Omega \quad , \qquad \text{(III.19)}$$

we have

$$g(\omega) = \frac{1}{2} \sum_{n=-\infty}^{\infty} c_n \sum_{k=1}^{N} e^{i\phi_k} \int_{-\infty}^{\infty} \exp[i\Omega(k-1)\tau] \; \delta(\Omega-n\omega_c)$$

$$\delta(\omega-\Omega-\omega_0) \, d\Omega$$

$$= \frac{1}{2} \sum_{n=-\infty}^{\infty} c_n \sum_{k=1}^{N} e^{i\phi_k} \exp[in(k-1)\omega_c\tau] \; \delta[\omega-(\omega_0+n\omega_c)]$$

$$= \frac{1}{2} \sum_{n=-\infty}^{\infty} c_n \sum_{k=1}^{N} \exp(\frac{2\pi ik}{N}) \; \exp(\frac{2\pi in(k-1)}{N}) \; \delta[\omega-(\omega_0+n\omega_c)] \quad ,$$

$$\text{(III.20)}$$

where the relations $\omega_c\tau = 2\pi/N$ and $\phi_k = 2\pi k/N$ have been used. Mushing onward,

$$g(\omega) = \frac{1}{2} \sum_{n=-\infty}^{\infty} c_n \exp(-i2\pi n/N) \left[\sum_{k=1}^{N} \exp\left(\frac{2\pi i(n+1)k}{N}\right) \delta[\omega-(\omega_0+n\omega_c)]\right] . \tag{III.21}$$

At this juncture, a crucial simplification takes place: the sum in brackets equals zero unless

$$n+1 = mN \quad , \quad m = 0, \pm 1, \pm 2 \quad .... \tag{III.22a}$$

or

$$n = \ldots -(2N+1), -(N+1), -1, N-1, 2N-1, \ldots \tag{III.22b}$$

When these conditions are met, the sum in brackets equals N.

From this point on, manipulation of $g(\omega)$ is straightforward algebraic slogging. The result (at last) is

$$g(\omega) = -\omega_1 \left(\frac{N}{\pi}\right) \sin\left(\frac{\pi}{N}\right) e^{i3\pi/N} \sum_{n=-\infty}^{\infty} \left(\frac{1}{n}\right) \delta[\omega-(\omega_0+n\omega_c)]\, \delta_{n,mN-1} \quad . \tag{III.23}$$

The component magnitudes are given by

$$|g(\omega)| = \omega_1 \left(\frac{N}{\pi}\right) \sin\left(\frac{\pi}{N}\right) \sum_{n=-\infty}^{\infty} \left(\frac{1}{|n|}\right) \delta[\omega-(\omega_0+n\omega_c)]\, \delta_{n,mN-1} \quad . \tag{III.24}$$

The two largest (and closest to ω_0) are as follows:

$$\omega = \omega_0-\omega_c \qquad |g(\omega)| = \omega_1\left[\frac{N}{\pi} \sin\left(\frac{\pi}{N}\right)\right] \quad , \tag{III.25a}$$

$$\omega = \omega_0 + (N-1)\omega_c \qquad |g(\omega)| = \frac{1}{N-1}\ \omega_1\ [\frac{N}{\pi}\sin(\frac{\pi}{N})] \quad . \qquad \text{(III.25b)}$$

Although the frequency spectrum of our phase-modulated pulse contains an infinite number of terms, there is a pleasing relationship concerning these two. If one adds (N-1) photons of frequency $\omega_0-\omega_c$ and one photon of frequency $\omega_0 + (N-1)\omega_c$, the result is $N\omega_0$--exact resonance with the N-quantum transition. Moreover, the intensities of the Fourier components at $\omega = \omega_0-\omega_c$ and $\omega = \omega_0 + (N-1)\omega_c$ are in <u>precisely</u> the correct ratio for this combination. This seems to auger well for N-quantum selectivity.

Figure III.3a displays $|g(\omega)|$ vs. ω for N=4. It was calculated not from Eq. III.24 but for convenience by a fast Fourier transform of the pulse phase envelope (using a spectrometer computer). The unavoidable restriction of a finite sampling length introduces some small peak amplitude error, particularly at larger frequencies, but Fig. III.3a is qualitatively correct.

The frequency spectra of fancier pulse sequences have also been investigated. It has been shown in the theory of selective excitation by <u>pulsed</u> NMR that more complicated phase patterns than a simple "forward roll" lead to better selectivity [55]. To be specific, the phase-cycling we have considered thus far is described as being zero-order selective because the zero-order term $\bar{\mathcal{H}}^{(0)}$ in the average Hamiltonian expansion [24,53,54] of the pulse propagator is purely nk-quantum selective. A first-order selective sequence results, i.e., an additional term in the average Hamiltonian is rendered nk-quantum selective, when the pulse cycle is symmetrized. [Symmetrization

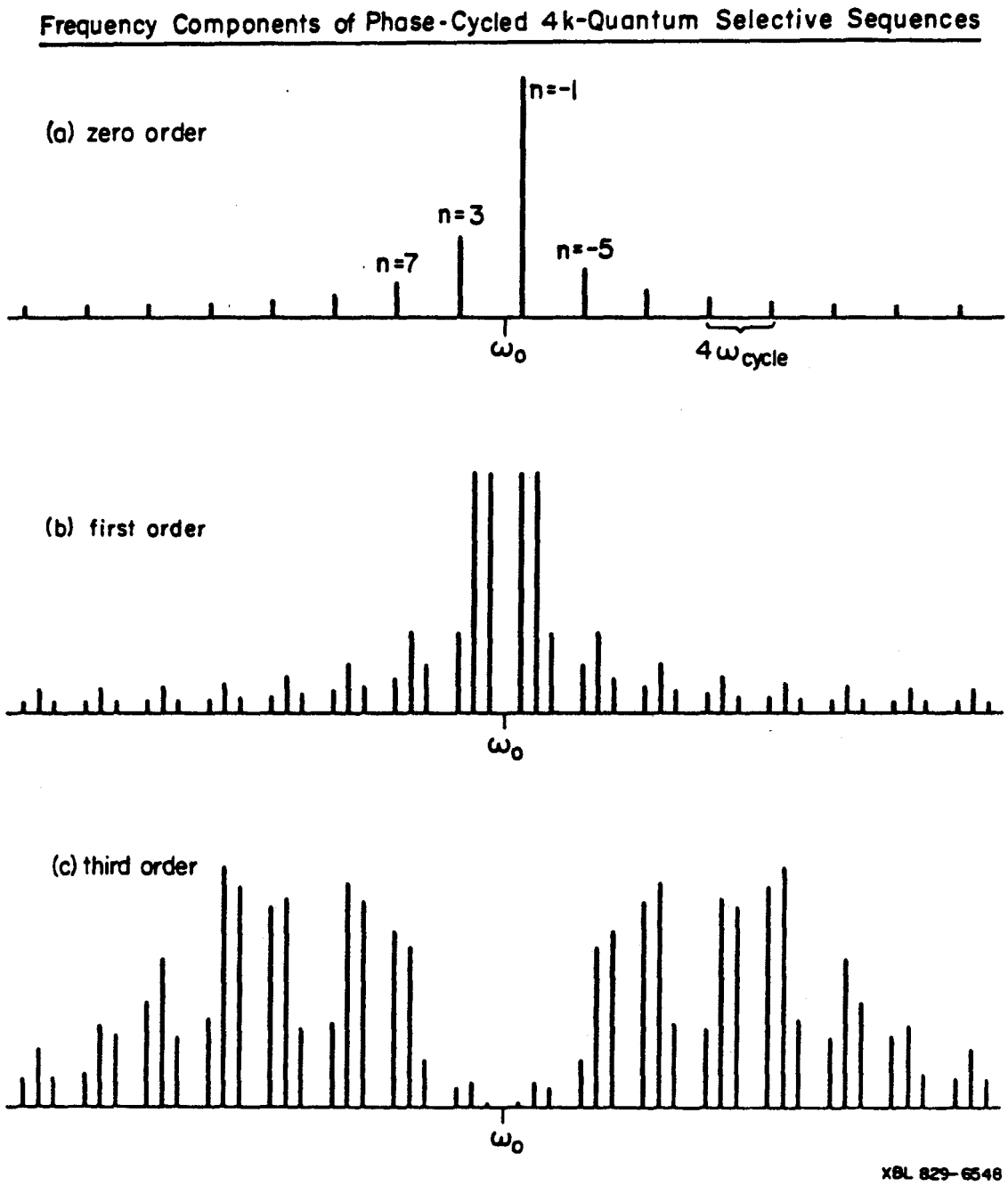

Figure III.3 The frequency components of three phase-cycled 4k-quantum selective cw pulse sequences with the same overall cycle time. (a) A simple phase roll (0123) is zero-order selective. The intensity at $\omega = \omega_o - \omega_c$ (n = -1) is three times that at $\omega = \omega_o + 3\omega_c$ (n = 3). (b) A first-order sequence results when the phases are symmetrized: (0123) (3210). (c) A second level of phase cycling combined with a second symmetrization yields a 64-step third-order sequence: (0123) (3210) (1230) (0321) (2301) (1032) (3012) (2103) (3012) (2103) (2301) (1032) (1230) (0321) (0123) (3210).

entails following a pulse cycle by its mirror image in time. For example, a three-quantum zero-order selective cycle can be symbolized by (012), where each integer j signifies a pulse of phase $2\pi j/N$ radians, with N=3 in this case. The corresponding first-order selective symmetrized cycle is written (012)(210).] Combining symmetrization and additional phase-shifting leads to higher orders of selectivity: the 36-step cycle (012)(210) (120)(021) (201)(102) (201)(102) (120)(021) (012)(210) is third-order selective.

Figure III.4 illustrates these cycle-building concepts schematically for n=4. The pulse sequence in Fig. III.4a is the simple progression of phases examined earlier; its frequency spectrum appears in Fig. III.3a. Sequence b is first-order selective and its frequency spectrum (calculated numerically as the fast Fourier transform of its pulse phase envelope) is displayed in Fig. III.3b. (More accurately, Fig. III.3b shows the frequency spectrum of a first-order sequence with the same cycle time as sequence a; hence the individual pulses are half as long.) Similarly, the frequency spectrum of a third-order sequence like Fig. III.4c but with a cycle time equal to that of sequence a (entailing pulses one-sixteenth the length of those in a) is presented in Fig. III.3c. It is immediately apparent that symmetrization of the pulse sequence is mirrored by a symmetric distribution of frequencies about ω_0, but other than this observation, no physical insight into the reasons for improved selectivity as we go from a to c is available. (Components with the largest intensity tend to move outward from ω_0 in progressing from a to c, but the relationship of this redistribution to multiple-quantum selectivity is not obvious.)

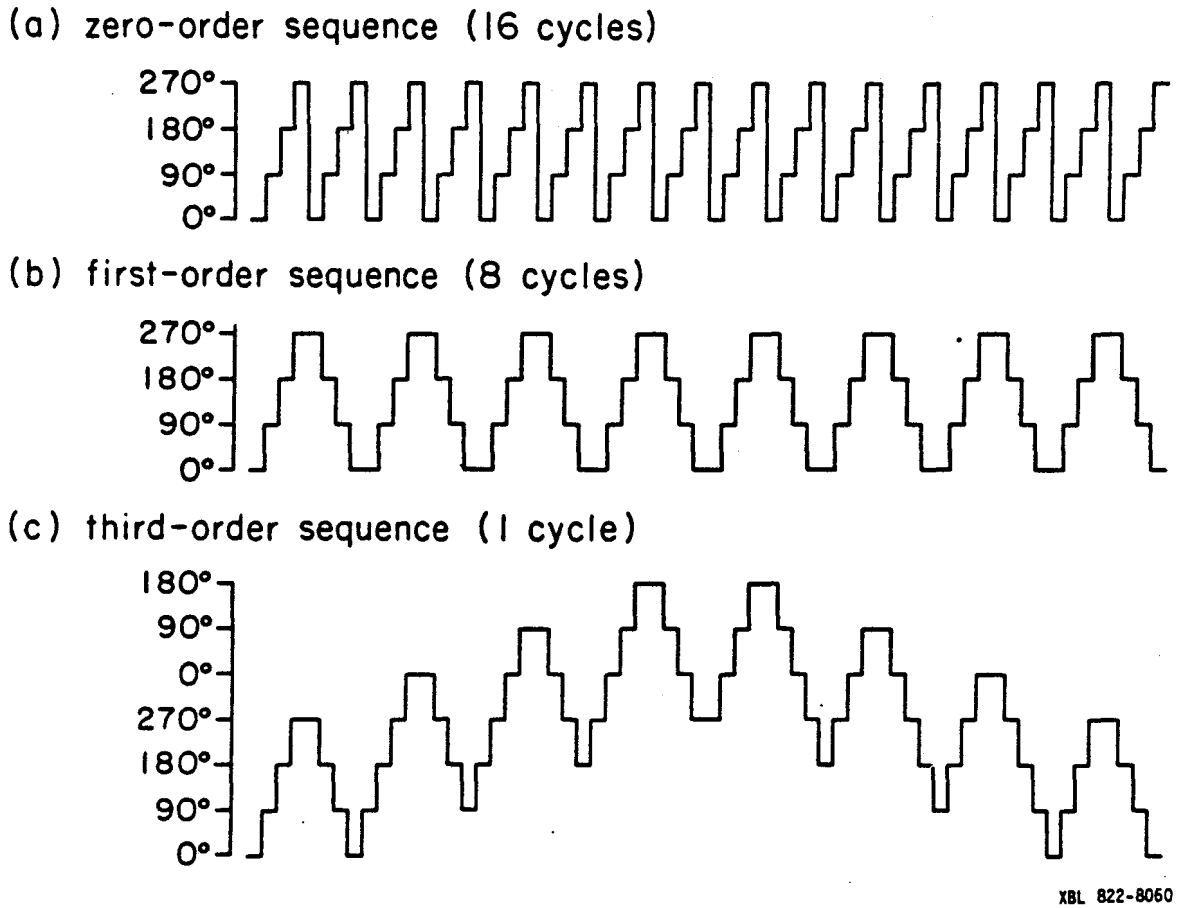

Figure III.4 A representation of the rf phases used in the zero-order, first-order, and third-order 4k-quantum selective sequences of Fig. III.3. There is one important difference, however -- in Fig. III.3, the overall cycle times are the same for each sequence; here the individual pulse lengths are equal.

3.3 Calculation of Conventional cw NMR Spectra for a Three-Level System

Now that phase-cycled pulse sequences have been analyzed in frequency space, it is time to calculate their actual effect on spin systems. We will be interested in the steady-state response to a large number of pulse cycles; therefore the equation of motion for the density matrix must be modified to take relaxation into account [20]:

$$\frac{d\rho}{dt} = i[\rho,\mathcal{H}] - \hat{\hat{\Gamma}}\,(\rho-\rho_0) \quad . \tag{III.26}$$

The mysterious $\hat{\hat{\Gamma}}$ is the relaxation superoperator; when it is expressed as a matrix, ρ must be expressed as a column vector. In a similar fashion, a Hamiltonian superoperator can be defined:

$$\hat{\hat{\mathcal{H}}}\,\rho \equiv i[\rho,\mathcal{H}] \tag{III.27}$$

and thus

$$\frac{d\rho}{dt} = (\hat{\hat{\mathcal{H}}}-\hat{\hat{\Gamma}})\rho + \hat{\hat{\Gamma}}\,\rho_0 \quad . \tag{III.28}$$

The introduction of relaxation and the concomitant use of superoperators greatly increases the size of the calculation. If there are L spin states, the undamped equation of motion, $d\rho/dt = i[\rho,\mathcal{H}]$, requires complex LxL matrices for ρ and $\mathcal{H}$. In contrast, superoperators $\hat{\hat{\mathcal{H}}}$ and $\hat{\hat{\Gamma}}$ are on the order of $L^2 \times L^2$ matrices and

quickly become enormous as L increases. In the interest of finite computing time (and to benefit from a well-established formalism), we will therefore focus on the familiar case of L = 3.

Relaxation will also be approached in the spirit of simplicity by making use of the Bloch equations [11,20-22], which describe the decay of coherences to zero at a rate characterized by a spin-spin relaxation time T_2, and which describe the return of populations to their equilibrium Zeeman values in terms of a spin-lattice relaxation time T_1. As such, our analysis is valid only for isolated three-level systems, such as deuterons in low isotopic abundance in a proton-decoupled solid or adrift on molecules dissolved in a liquid crystal solvent. In particular, phenomena involving the establishment of a spin temperature, such as spin locking, cannot be handled at all.

With these limitations in mind, let us begin our investigation of a relaxable three-level system. The $I_{p,i}$ operators introduced in Chapter II will again serve as a framework for our algebraic constructions. The density matrix ρ will be expressed as a vector with eight coefficients for the operators $I_{x,1}$, $I_{x,2}$, $I_{y,1}$, $I_{y,2}$, $I_{xy,3}$, $I_{z,1}$, $I_{z,2}$, and $I_{z,3}$ that span the three-level spin system. (The operator $I_{xy,3} = I_{x,3}-I_{y,3}$ is used instead of $I_{x,3}$ and $I_{y,3}$ separately in order to minimize the size of the superoperator matrix.)

The Hamiltonian to be considered is a familiar one:

$$\mathcal{H} = -2\Delta\nu\, I_{z,1} - 2\nu_1\, I_{x,1} + \frac{2}{3}\,\nu_Q\, I_{xy,3} \quad . \qquad \text{(III.29)}$$

Because $\mathcal{H}$ and ρ are both expanded in terms of $I_{p,i}$ operators, the commutation rules of Table II.2 can be used to evaluate $[\rho,\mathcal{H}]$.

As for relaxation, let us first distinguish single-quantum and double-quantum spin-spin relaxation times, T_{2SQ} and T_{2DQ} (expected to be comparable quantities). Furthermore, let us define relaxation rates $R_1 = 1/T_1$, $R_{2SQ} = 1/T_{2SQ}$, and $R_{2DQ} = 1/T_{2DQ}$. Equation III.28 for the evolution of ρ can then be written as eight coupled differential equations:

$$\frac{da_{x,1}}{dt} = -R_{2SQ}\, a_{x,1} - \nu_Q\, a_{x,2} + \Delta\nu\, a_{y,1}$$

$$\frac{da_{x,2}}{dt} = \nu_Q\, a_{x,1} - R_{2SQ}\, a_{x,2} - \Delta\nu\, a_{y,2} - \nu_1\, a_{z,3} + 3\nu_1\, a_{xy,3}\ ,$$

$$\frac{da_{y,1}}{dt} = -\Delta\nu\, a_{x,1} + \nu_Q\, a_{y,2} + \nu_1\, a_{z,1} - R_{2SQ}\, a_{y,1}\ ,$$

$$\frac{da_{y,2}}{dt} = \Delta\nu\, a_{x,2} - \nu_Q\, a_{y,1} - R_{2SQ}\, a_{y,2} - \nu_1\, a_{z,2}\ ,$$

$$\frac{da_{xy,3}}{dt} = -\nu_1\, a_{x,2} - R_1\, a_{xy,3}\ ,$$

$$\frac{da_{z,1}}{dt} = (-\nu_1\, a_{y,1} - R_1\, a_{z,1}) + R_1\ ,$$

$$\frac{da_{z,2}}{dt} = \nu_1\, a_{y,2} + 2\Delta\nu\, a_{z,3} - R_{2DQ}\, a_{z,2}\ ,$$

$$\frac{da_{z,3}}{dt} = \nu_1\, a_{x,2} - 2\Delta\nu\, a_{z,2} - R_{2DQ}\, a_{z,3}\ . \qquad \text{(III.30)}$$

In terms of a matrix and vector description in the operator basis set described above,

$$\dot{\rho} = \underset{\approx}{M}\rho + \underset{\sim}{r} \quad , \tag{III.31}$$

with

$$\rho = (a_{x,1}, a_{x,2}, a_{y,1}, a_{y,2}, a_{xy,3}, a_{z,1}, a_{z,2}, a_{z,3})^T \quad , \tag{III.32}$$

$$\underset{\sim}{r} = (0, 0, 0, 0, 0, R_1, 0, 0)^T \quad , \tag{III.33}$$

and

$$\underset{\approx}{M} = \begin{bmatrix} -R_{2SQ} & -\nu_Q & \Delta\nu & 0 & 0 & 0 & 0 & 0 \\ \nu_Q & -R_{2SQ} & 0 & -\Delta\nu & 3\nu_1 & 0 & 0 & -\nu_1 \\ -\Delta\nu & 0 & -R_{2SQ} & \nu_Q & 0 & \nu_1 & 0 & 0 \\ 0 & \Delta\nu & -\nu_Q & -R_{2SQ} & 0 & 0 & -\nu_1 & 0 \\ 0 & -\nu_1 & 0 & 0 & -R_1 & 0 & 0 & 0 \\ 0 & 0 & -\nu_1 & 0 & 0 & -R_1 & 0 & 0 \\ 0 & 0 & 0 & \nu_1 & 0 & 0 & -R_{2DQ} & 2\Delta\nu \\ 0 & \nu_1 & 0 & 0 & 0 & 0 & -2\Delta\nu & -R_{2DQ} \end{bmatrix} \tag{III.34}$$

Before pondering the effects of phase-cycled pulses, let us first consider the simplest case of spin-system response to rf irradiation with constant phase. The steady-state solution is easily found by setting all elements of $\dot{\rho}$ equal to zero:

$$0 = \underset{\approx}{M}\rho + \underset{\sim}{r} \quad \text{or} \quad \rho = -\underset{\approx}{M}^{-1}\underset{\sim}{r} \quad . \tag{III.35}$$

A standard matrix-inversion routine [52] can be used to solve for the steady-state elements of ρ as a function of ν_Q, ν_1, and $\Delta\nu$. Spectra can be generated by calculating the value of $a_{y,1}$, the single-quantum coherence perpendicular to the applied field, versus $\Delta\nu$ for fixed values of ν_1 and ν_Q. Figure III.5 displays four such spectra. In each case ν_Q = 30 KHz, T_1 = 50 msec, and $T_{2SQ} = T_{2DQ}$ = 1 msec, roughly appropriate values for deuterium in solids. As ν_1 increases, the single-quantum lines broaden and saturate, and as expected, a sharp double-quantum peak appears at $\Delta\nu = 0$. A different view of the process can be found in Fig. III.6: spectral intensities at the single quantum transition frequency ($\Delta\nu=\pm\nu_Q$) and the double-quantum frequency ($\Delta\nu=0$) plotted as a function of ν_1.

These results are well known and are included here to illustrate both the basic computational approach and the basic problem of cw multiple-quantum NMR: high-quantum transitions of interest are mired in a morass of broadened lower-quantum transitions. Cycling of rf pulse phase will improve matters, but before spectra are displayed, a means for determining the steady-state response of the system will be presented.

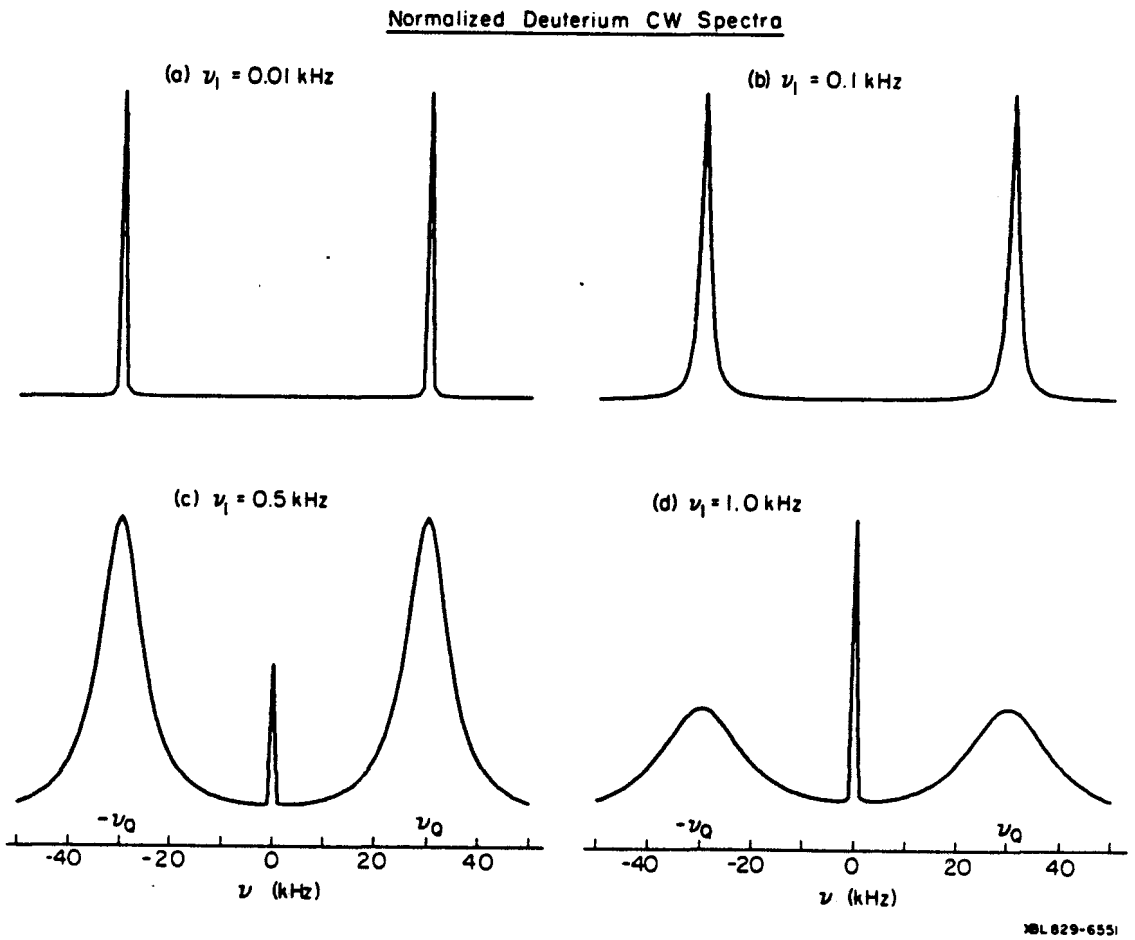

Figure III.5 Four deuterium cw spectra, calculated in steady state ($\dot{\rho}$ = 0) with no rf phase shifts and each normalized to the same height. As ν_1 increases, SQ transitions saturate and broaden while a sharp DQ transition grows in. System parameters are as follows: ν_Q = 30 KHz, T_1 = 50 msec, T_{2SQ} = T_{2DQ} = 1 msec. Maximum intensity for each spectrum in terms of an $a_{y,1}$ value: (a) 0.0225, (b) 0.0078, (c) 0.0016, (d) 0.0022.

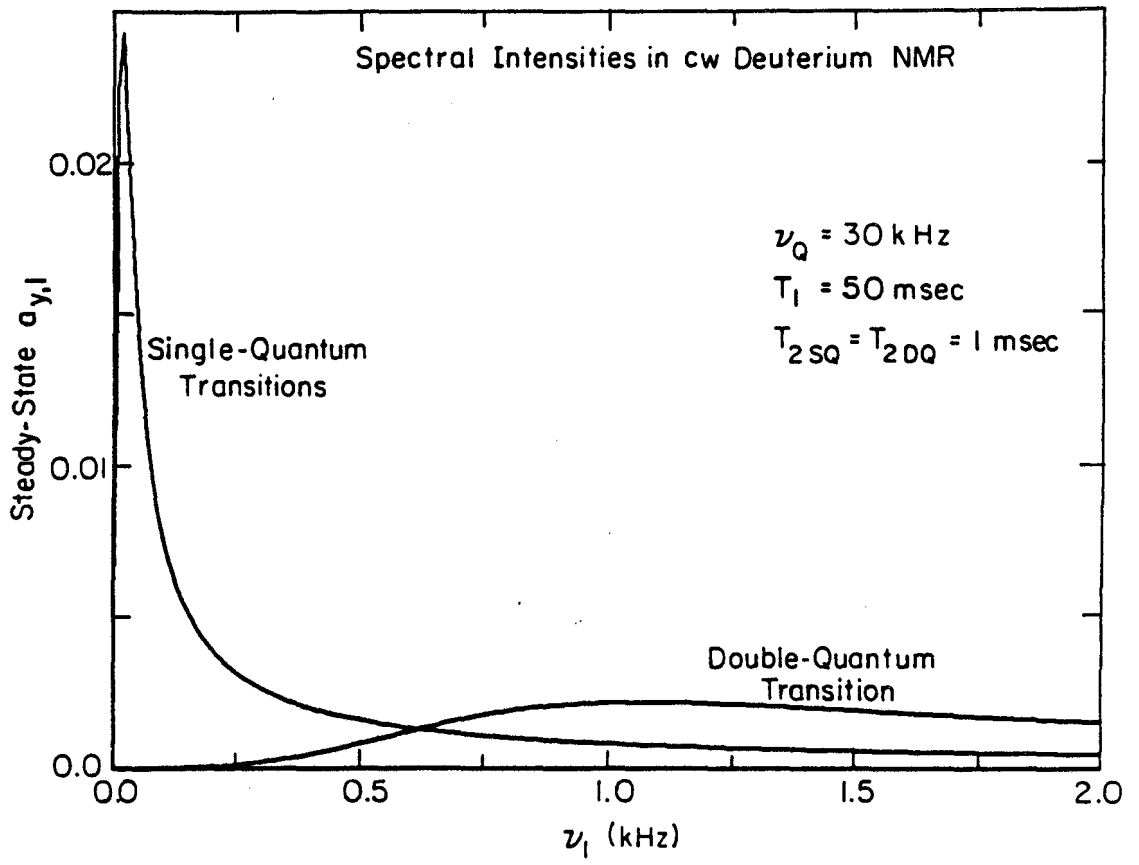

Figure III.6 Steady-state spectral intensities at the SQ and DQ resonance frequencies of deuterium as a function of rf pulse strength ν_1 in conventional cw NMR. The system parameters are those of Fig. III.5.

3.4 Calculating the Steady-State Response to Phase-Cycled rf Irradiation

The starting point for calculating the steady-state response to phase-cycled irradiation is the superoperator matrix equation discussed in the last section:

$$\dot{\rho} = \underset{\approx}{M}\rho + \underset{\sim}{r} \quad , \qquad \text{(III,36)}$$

This equation can be formally integrated over a pulse length τ to give

$$\rho(\tau) = \exp(\underset{\approx}{M}\tau)\rho(0) + \underset{\approx}{M}^{-1}[\exp(\underset{\approx}{M}\tau) - \underset{\approx}{1}]\underset{\sim}{r} \quad . \qquad \text{(III.37)}$$

This can be written as

$$\rho(\tau) = \underset{\approx}{B}\ \rho(0) + \underset{\approx}{C}\ \underset{\sim}{r} \quad , \qquad \text{(III.38)}$$

where

$$\underset{\approx}{\beta} = \exp(\underset{\approx}{M}\tau) \text{ and } \underset{\approx}{C} = \underset{\approx}{M}^{-1}(\underset{\approx}{B}-\underset{\approx}{1}) \quad . \qquad \text{(III.39)}$$

To select double-quantum coherence in a three-level system requires only two rf phases and thus two Hamiltonians:

$$\mathcal{H}_1 = -2\Delta\nu\ I_{z,1} - 2\nu_1\ I_{x,1} + \frac{2}{3}\nu_Q\ I_{xy,3} \quad , \qquad \text{(III.40a)}$$

$$\mathcal{H}_2 = -2\Delta\nu\ I_{z,1} + 2\nu_1\ I_{x,1} + \frac{2}{3}\nu_Q\ I_{xy,3} \quad . \tag{III.40b}$$

The damped evolution of ρ under $\mathcal{H}_1$ is described above. An analogous set of equations holds for $\mathcal{H}_2$. Let N be the superoperator matrix corresponding to M but with the sign of ν_1 reversed. The integrated equation of motion for ρ is then

$$\rho(\tau) = \exp(\underset{\approx}{N}\tau)\ \rho(0) + \underset{\approx}{N}^{-1}\ [\exp(\underset{\approx}{N}\tau) - \underset{\approx}{1}]\underset{\sim}{r} \tag{III.41a}$$

$$\equiv \underset{\approx}{F}\ \rho(0) + \underset{\approx}{G}\ \underset{\sim}{r} \quad , \tag{III.41b}$$

with

$$F = \exp(\underset{\approx}{N}\tau) \text{ and } \underset{\approx}{G} = \underset{\approx}{N}^{-1}(\underset{\approx}{F}-\underset{\approx}{1}) \quad . \tag{II.42}$$

After two pulses described by $\mathcal{H}_1$ and $\mathcal{H}_2$, we have

$$\begin{aligned}\rho(2\tau) &= \underset{\approx}{F}\ \rho(\tau) + \underset{\approx}{G}\ \underset{\sim}{r} \\ &= \underset{\approx}{F}\ \underset{\approx}{B}\ \rho(0) + \underset{\approx}{F}\ \underset{\approx}{C}\ \underset{\sim}{r} + \underset{\approx}{G}\ \underset{\sim}{r} \quad .\end{aligned} \tag{III.43}$$

Similarly,

$$\rho(3\tau) = \underset{\approx}{B}\ \underset{\approx}{F}\ \underset{\approx}{B}\ \rho(0) + \underset{\approx}{B}\ \underset{\approx}{F}\ \underset{\approx}{C}\ \underset{\sim}{r} + \underset{\approx}{B}\ \underset{\approx}{G}\ \underset{\sim}{r} + \underset{\approx}{C}\ \underset{\sim}{r} \tag{III.44a}$$

and

$$\rho(4\tau) = \underset{\approx}{F}\,\underset{\approx}{B}\,\underset{\approx}{F}\,\underset{\approx}{B}\,\rho(0) + \underset{\approx}{F}\,\underset{\approx}{B}\,\underset{\approx}{F}\,\underset{\approx}{C}\,\underset{\sim}{r} + \underset{\approx}{F}\,\underset{\approx}{B}\,\underset{\approx}{G}\,\underset{\sim}{r} + \underset{\approx}{F}\,\underset{\approx}{C}\,\underset{\sim}{r} + \underset{\approx}{G}\,\underset{\sim}{r}$$

$$\equiv \underset{\approx}{L}^2\,\rho(0) + (\underset{\approx}{L} + \underset{\approx}{1})(\underset{\approx}{F}\,\underset{\approx}{C} + \underset{\approx}{G})\underset{\sim}{r} \quad . \qquad \text{(III.44b)}$$

where $\underset{\approx}{L} = \underset{\approx}{F}\,\underset{\approx}{B} = \exp(\underset{\approx}{M})\,\exp(\underset{\approx}{N})$. Continuing the process one finds

$$\rho(2n\tau) = \underset{\approx}{L}^n\,\rho(0) + (\underset{\approx}{L}^{n-1} + \underset{\approx}{L}^{n-2} + \ldots + \underset{\approx}{L} + \underset{\approx}{1})(\underset{\approx}{F}\,\underset{\approx}{C} + \underset{\approx}{G})\underset{\sim}{r}$$

$$= \underset{\approx}{L}^n\,\rho(0) + (\underset{\approx}{L}-\underset{\approx}{1})^{-1}\,(\underset{\approx}{L}^n-\underset{\approx}{1})\,(\underset{\approx}{F}\,\underset{\approx}{C} + \underset{\approx}{G})\underset{\sim}{r} \quad , \qquad \text{(III.45)}$$

where the sum rule for geometric series is applied to the matrix $\underset{\approx}{L}$.

In the steady-state limit at long times, the form of ρ must be <u>independent of initial conditions</u>--all $\rho(0)$ density matrices for a given system will evolve to the same final $\rho(2n\tau)$. (Actually the steady-state ρ will oscillate between two sets of operator coefficients corresponding to the two pulses in the cycle. If we look at the system only after an even number of pulses, this steady-state oscillation will not be seen.) Because the final density matrix is independent of $\rho(0)$, it must be the case that $\underset{\approx}{L}^n \to \underset{\approx}{0}$ as $n \to \infty$. With this assumption, the steady-state density matrix after an even number of pulses is given by

$$\rho_{ss} = -(\underset{\approx}{L}-\underset{\approx}{1})^{-1}(\underset{\approx}{F}\,\underset{\approx}{C} + \underset{\approx}{G})\underset{\sim}{r} \tag{III.46a}$$

$$= -[\exp(\underset{\approx}{N}\tau)\ \exp(\underset{\approx}{M}\tau) - \underset{\approx}{1}]^{-1}$$

$$\times\ \{\exp(\underset{\approx}{N}\tau)\underset{\approx}{M}^{-1}\ [\exp(\underset{\approx}{M}\tau)-\underset{\approx}{1}] + \underset{\approx}{N}^{-1}\ [\exp(\underset{\approx}{N}\tau)-1]\}\underset{\sim}{r} \quad . \tag{III.46b}$$

As a check on this formula, note what happens when $\underset{\approx}{N} = \underset{\approx}{M}$:

$$\rho_{ss} = -[\exp(2\underset{\approx}{M}\tau) - \underset{\approx}{1}]^{-1}$$

$$\times\ \{\exp(\underset{\approx}{M}\tau)\ [\exp(\underset{\approx}{M}\tau) - \underset{\approx}{1}] + \exp(\underset{\approx}{M}\tau) - \underset{\approx}{1}\}\underset{\approx}{M}^{-1}\ \underset{\sim}{r}$$

$$= [\exp(2\underset{\approx}{M}\tau) - \underset{\approx}{1}]^{-1}\ [\exp(2\underset{\approx}{M}\tau) - 1]\underset{\approx}{M}^{-1}\ \underset{\sim}{r}$$

$$= \underset{\approx}{M}^{-1}\ \underset{\sim}{r} \quad , \tag{III.47}$$

the steady-state result for constant rf phase derived earlier.

Equation III.46b is an exact solution for ρ_{ss}, but it was not used in the calculations reported here because a computer algorithm for diagonalization (and subsequent exponentiation) of a non-hermitian matrix was not available at the time. Instead the first-order response to short time intervals was compounded to simulate continuous evolution. Starting with

$$\dot{\rho} = \underset{\approx}{M}\ \rho + \underset{\sim}{r} \quad ,$$

one can write for small Δt,

$$\rho(\Delta t) = \rho(0) + \dot{\rho}\,\Delta t$$

$$= (\underset{\approx}{1} + \underset{\approx}{M}\,\Delta t)\,\rho(0) + (\Delta t)\underset{\sim}{r}$$

$$\equiv \underset{\approx}{P}\,\rho(0) + \underset{\sim}{s} \quad , \tag{III.48}$$

with

$$\underset{\approx}{P} = \underset{\approx}{1} + \underset{\approx}{M}\,\Delta t$$

and

$$\underset{\sim}{s} = \Delta t\,\underset{\sim}{r} \quad .$$

Continued evolution under the same pulse results in

$$\rho(2\Delta t) = \underset{\approx}{P}^2\,\rho(0) + \underset{\approx}{P}\,\underset{\sim}{s} + \underset{\sim}{s} \quad ,$$

$$\rho(3\Delta t) = \underset{\approx}{P}^3\,\rho(0) + (\underset{\approx}{P}^2 + \underset{\approx}{P} + \underset{\approx}{1})\underset{\sim}{s} \quad ,$$

$$\rho(m\Delta t) = \underset{\approx}{P}^m\,\rho(0) + (\underset{\approx}{P}-\underset{\approx}{1})^{-1}(\underset{\approx}{P}^m-\underset{\approx}{1})\underset{\sim}{s} \quad . \tag{III.49}$$

In analogous fashion, evolution during $\mathcal{H}_2$ is described by

$$\rho(m\Delta t) = \underset{\approx}{Q}^m\,\rho(0) + (\underset{\approx}{Q}-\underset{\approx}{1})^{-1}\,(\underset{\approx}{Q}^m-\underset{\approx}{1})\underset{\sim}{s} \quad , \tag{III.50}$$

where $\underset{\approx}{Q} = \underset{\approx}{1} + \underset{\approx}{N}\,\Delta t$. With the additional substitutions $\underset{\approx}{B} = \underset{\approx}{P}^m$, $\underset{\approx}{C} = (\underset{\approx}{P}-\underset{\approx}{1})^{-1}\,(\underset{\approx}{B}-\underset{\approx}{1})\Delta t$, $\underset{\approx}{F} = \underset{\approx}{Q}^m$, and $\underset{\approx}{G} = (\underset{\approx}{Q}-\underset{\approx}{1})^{-1}\,(\underset{\approx}{F}-\underset{\approx}{1})\Delta t$, the two equations of evolution become, for $\tau = m\Delta t$,

$$\rho(\tau) = \underset{\approx}{B}\,\rho(0) + \underset{\approx}{C}\,\underset{\sim}{r} \quad \text{for} \quad \mathcal{H} = \mathcal{H}_1 \quad , \tag{III.51a}$$

$$\rho(\tau) = \underset{\approx}{F}\,\rho(0) + \underset{\approx}{G}\,\underset{\sim}{r} \quad \text{for} \quad \mathcal{H} = \mathcal{H}_2 \quad . \tag{III.51b}$$

These equations are used to estimate the actual evolution during a pulse and are most accurate when m is large. To calculate the steady-state response to phase-cycling, note that Eqs. III.51a and III.51b are identical in form to the previously examined Eqs. III.38 and III.41b. Hence the solution in Eq. III.46a is applicable with the appropriate substitutions. One finds

$$\rho_{ss} = -[(\underset{\approx}{1} + \underset{\approx}{N}\Delta t)^m(\underset{\approx}{1} + \underset{\approx}{M}\,\Delta t)^m - \underset{\approx}{1}]^{-1}$$

$$\times\ \{(\underset{\approx}{1} + \underset{\approx}{N}\Delta t)^m\,\underset{\approx}{M}^{-1}\,[(\underset{\approx}{1} + \underset{\approx}{M}\,\Delta t)^m - \underset{\approx}{1}] + \underset{\approx}{N}^{-1}[(\underset{\approx}{1} + \underset{\approx}{N}\,\Delta t)^m - \underset{\approx}{1}]\}\underset{\sim}{r} \quad , \tag{III.52}$$

where it should be mentioned again that each pulse is divided into m small steps for the purpose of calculating the evolution. A comparison of this approximate formula with the exact solution of Eq. III.46b reveals that the difference lies in the use of $(\underset{\approx}{1} + \underset{\approx}{M}\,\Delta t)^m$ here to simulate $\exp(\underset{\approx}{M}\tau)$, plus similar relations for $\underset{\approx}{N}$. Expansions of the two expressions,

$$(1 + \underset{\approx}{M}\,\Delta t)^m = \underset{\approx}{1} + m\Delta t\,\underset{\approx}{M} + \frac{(m)(m-1)}{2}\,\Delta t^2\,\underset{\approx}{M}^2 + \ldots$$

$$= \underset{\approx}{1} + \tau\underset{\approx}{M} + [\tfrac{1}{2}(\tau^2 - \tau\Delta t)]\underset{\approx}{M}^2 + \ldots \qquad \text{(III.53a)}$$

and

$$\exp(\underset{\approx}{M}\tau) = \underset{\approx}{1} + \tau\underset{\approx}{M} + \frac{1}{2}\tau^2\,\underset{\approx}{M}^2 + \ldots \qquad \text{(III.53b)}$$

indicate that when m is large, the approximate formula should perform satisfactorily.

3.5 Phase-cycled cw Spectra for a Three-Level System

With Eq. III.52 as the heart of our computer program, we now hope to generate double-quantum selective spectra in a three-level system using phase-cycled cw NMR. For system parameters we will choose ν_Q = 2 KHz, T_1 = 50 msec, and $T_{2SQ} = T_{2DQ}$ = 1 msec. The time increment Δt over which evolution is assumed to be linear will usually be set to 2 μsec. A typical pulse length will be 32 μsec, giving a cycle time t_c of 64 μsec (only two-pulse zero-order-selective cycles will be considered here).

Figure III.7 displays coefficients $a_{y,1}$ and $a_{z,2}$ as a function of the number of applied cycles (0-400) for $|\nu_1|$ = 2 KHz, $\Delta\nu$ = 0 (double-quantum resonance), and cycle time t_c = 64 μsec. Initial oscillations of each coefficient are damped by the relaxation terms in the Hamiltonian as the system approaches a steady state. Note that the final magnitudes of $a_{y,1}$ and $a_{z,2}$ in this plot are roughly the same size.

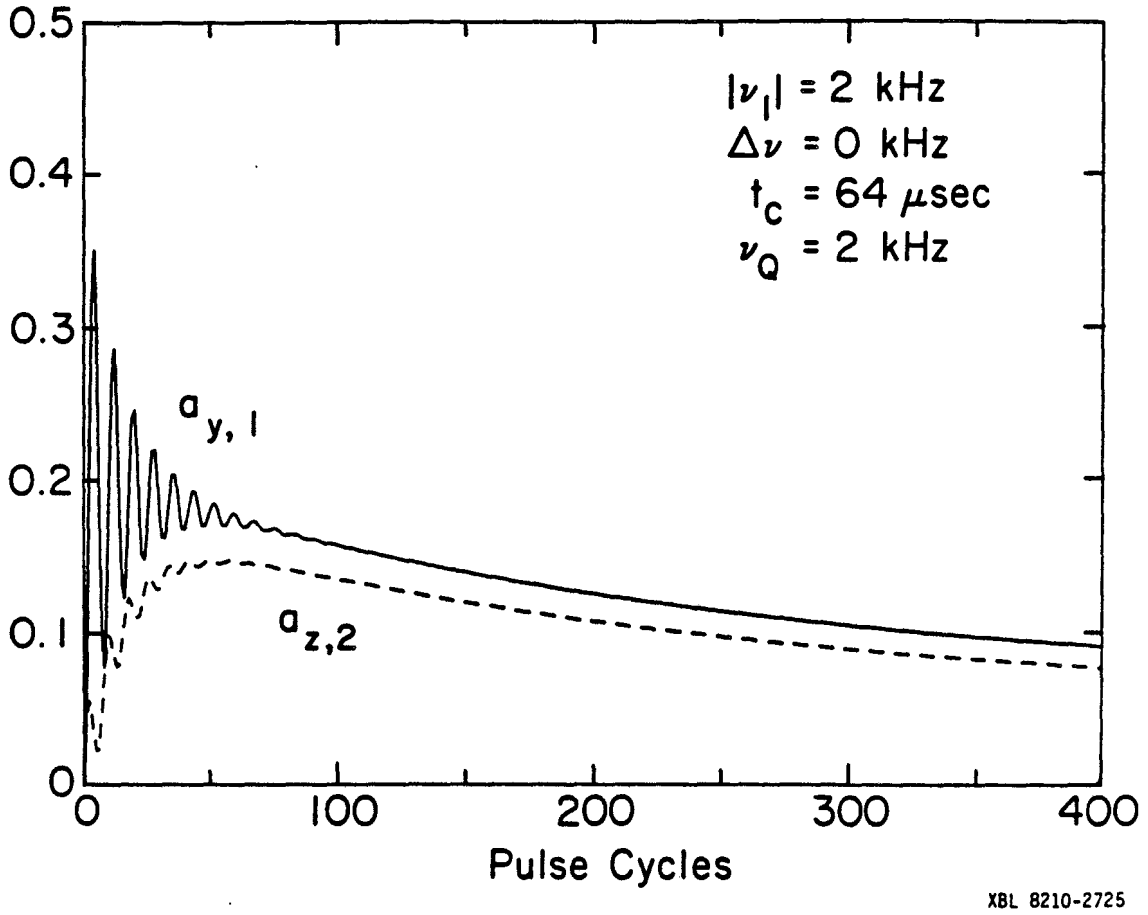

Figure III.7 Evolution of SQ and DQ coherence ($a_{y,1}$ and $a_{z,2}$ respectively) when a phase-cycled cw pulse is applied at the deuterium DQ transition frequency ($\Delta\nu = 0$). Two 32 μsec pulses, differing in phase by 180°, comprise each cycle. The initial density matrix is $I_{z,1}$, and relaxation times are as follows: $T_1 = 50$ msec, $T_{2SQ} = T_{2DQ} =$ 1 msec. The time increment over which evolution is assumed to be linear is 2 μsec.

For comparison, Fig. III.8 depicts coefficients $a_{y,1}(t)$ and $a_{z,2}(t)$ for single-quantum resonance: $\Delta\nu = \nu_Q = 2$ KHz with $|\nu_1| =$ 2 KHz and $t_c = 64$ μsec as before. The long-time value of $a_{z,2}$ is essentially zero, as we would expect, but the final value of $a_{y,1}$ is larger in magnitude than the corresponding $a_{y,1}$ value for $\Delta\nu = 0$. As this runs counter to our expectations for an alleged double-quantum selective sequence, the steady-state spectrum ($a_{y,1}$ vs. $\Delta\nu$) has also been computed and appears in Fig. III.9 along with a plot of $a_{z,2}$ vs. $\Delta\nu$. It can be seen that the spectrum is non-zero but essentially flat over the range of ±4 KHz, except for a dip at the double-quantum transition, $\Delta\nu = 0$. Nothing distinguishes the single-quantum transitions at $\Delta\nu = \pm\nu$, but matching the dip at $\Delta\nu = 0$ is a peak in the plot of $a_{z,2}$ vs. $\Delta\nu$. Apparently the creation of double-quantum coherence causes a reduction in the SQ "background" signal, a hole-burning that could be measured experimentally.

Three similar steady-state spectra have also been computed. Figure III.10 features the same system and the same pulse cycling as Fig. III.9; the only difference is the range of $\Delta\nu$ values shown: ±32 KHz instead of ±4 KHz. The spectrum looks considerably different, crossing zero at $\Delta\nu = \pm(1/t_c) = \pm 15.6$ KHz. This suggests that if ν^* is the width of a desired spectrum, the cycle time t_c should always be chosen such that $\nu^* t_c << 1.0$.

Figure III.11 displays the same limited range of $\Delta\nu$ values as does Fig. III.9 but with $|\nu_1|$ equal to 1.2 KHz instead of 2 KHz. For this less-than-optimal pulse strength, the amounts of SQ coherence created

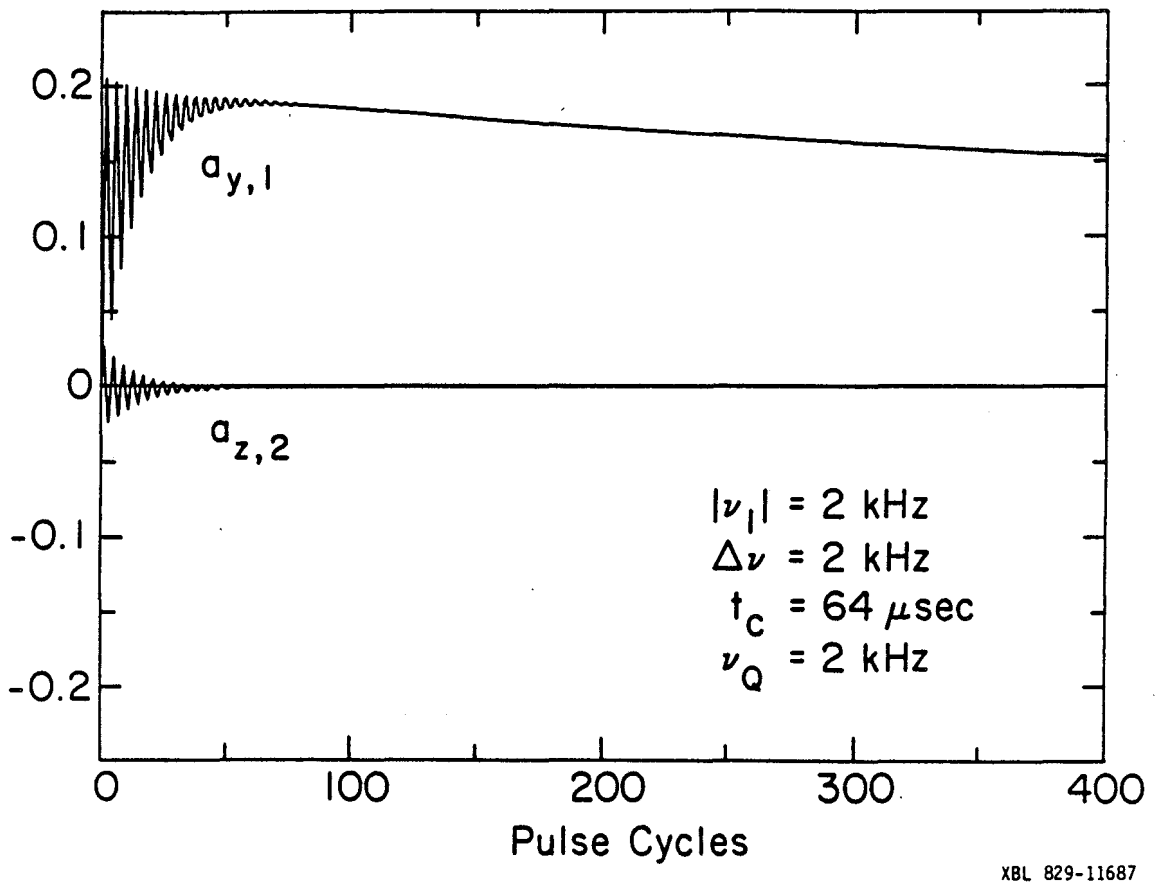

Figure III.8 Evolution of SQ coherence ($a_{y,1}$) and DQ coherence ($a_{z,2}$) when a 0° - 180° phase-cycled cw pulse is applied at a deuterium SQ transition frequency ($\Delta\nu = \nu_Q$). Pulse and system parameters as in Fig. III.7.

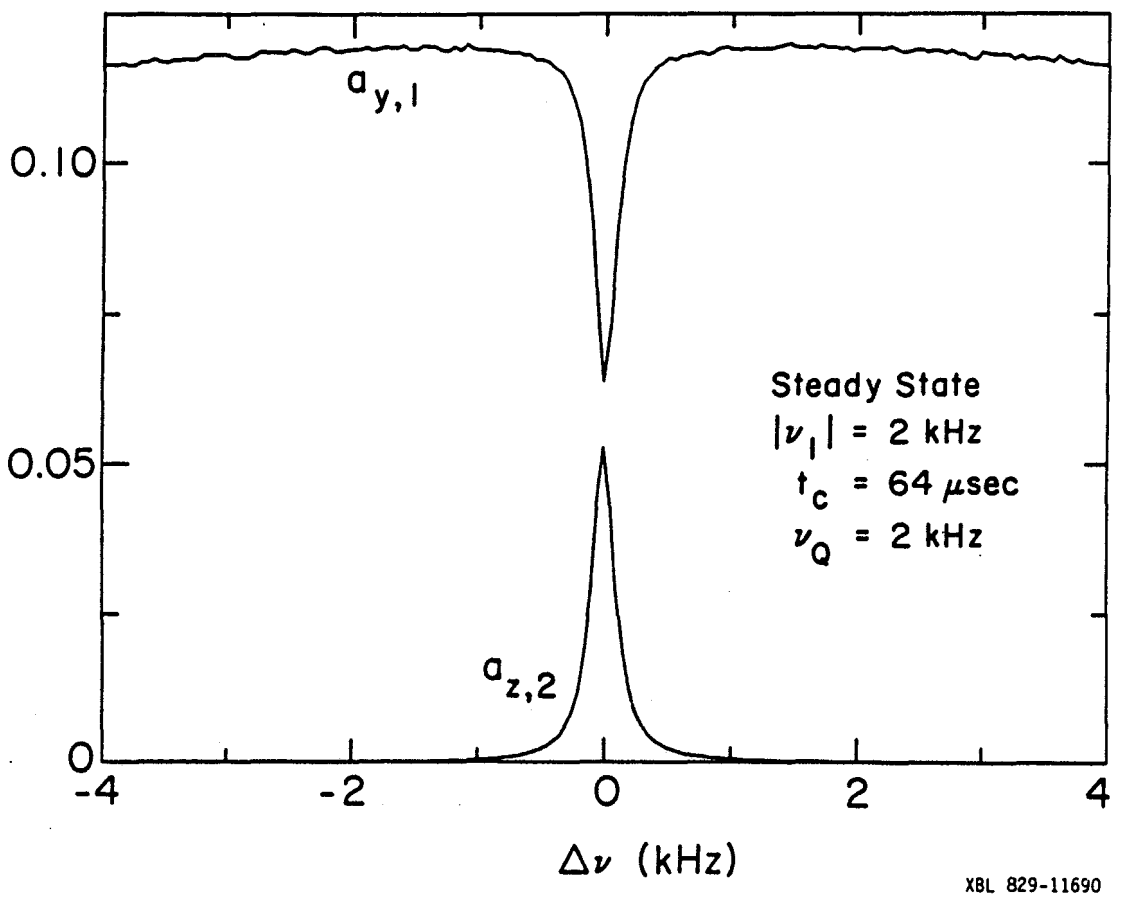

Figure III.9 Steady-state values of $a_{y,1}$ and $a_{z,2}$ as a function of rf frequency following 0° - 180° phase-cycled cw excitation. Pulse and system parameters are those of Fig. III.7. Note the dip in SQ intensity ($a_{y,1}$) at the double-quantum resonance frequency ($\Delta\nu = 0$) and the lack of an SQ intensity change at the single-quantum resonance frequencies ($\Delta\nu = \pm\nu_Q$). The spectral "noise" is a numerical artifact.

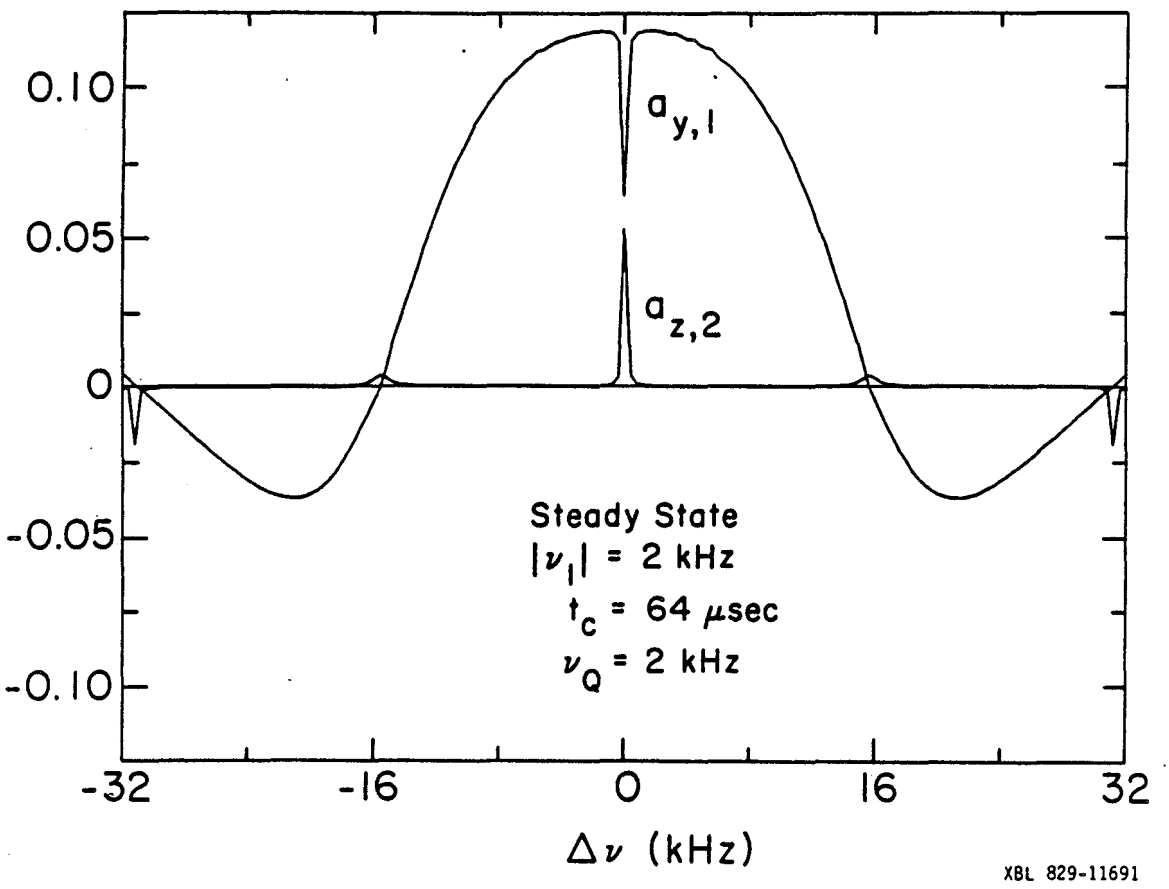

Figure III.10 Steady-state values of $a_{y,1}$ and $a_{z,2}$ as in Fig. III.9, but over a much wider range of frequencies. The value of $a_{y,1}$ is zero at $|\Delta\nu| = 1/t_c$ (15.625 KHz) and $|\Delta\nu| = 2/t_c$. In contrast, the value of $a_{z,2}$ is essentially zero except at $|\Delta\nu| = n/t_c$, n = 0,1,2.

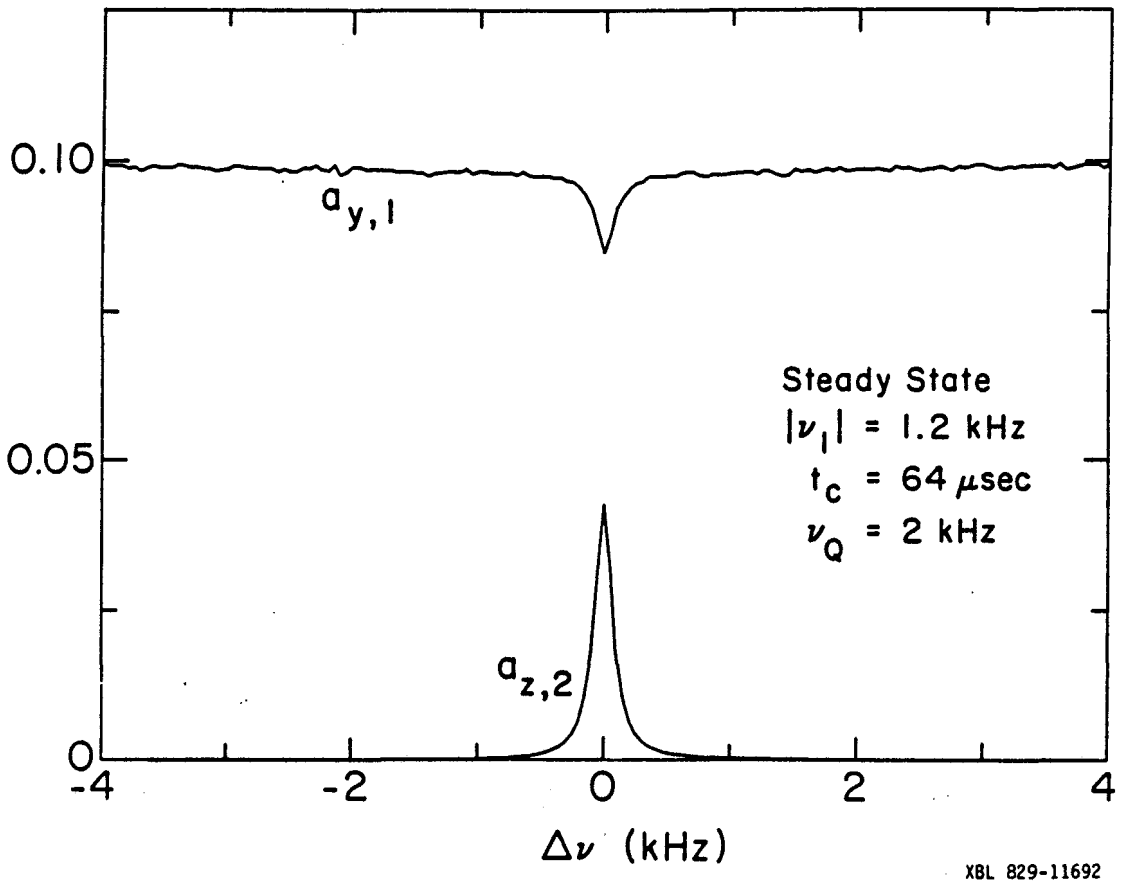

Figure III.11 Steady-state values of $a_{y,1}$ and $a_{z,2}$ following 0° - 180° phase-cycled cw excitation for a smaller value of $|\Delta\nu_1|$ than in Fig. III.9. The dip at $\Delta\nu = 0$ is much less pronounced.

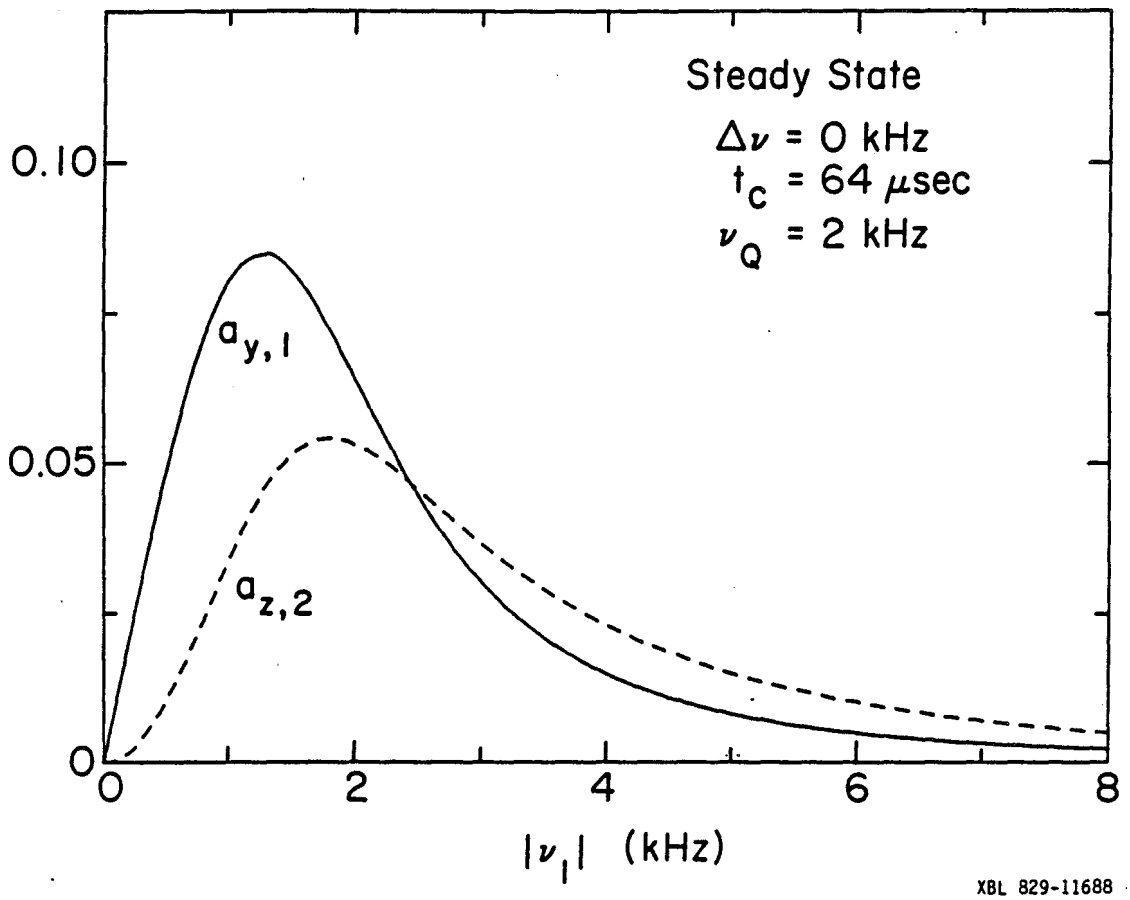

Figure III.12 Steady-state values for $a_{y,1}$ and $a_{z,2}$ at the double-quantum resonance frequency ($\Delta\nu = 0$) as a function of $|\nu_1|$ for 0° - 180° phase-cycled cw excitation. Relaxation times are as in Fig. III.7.

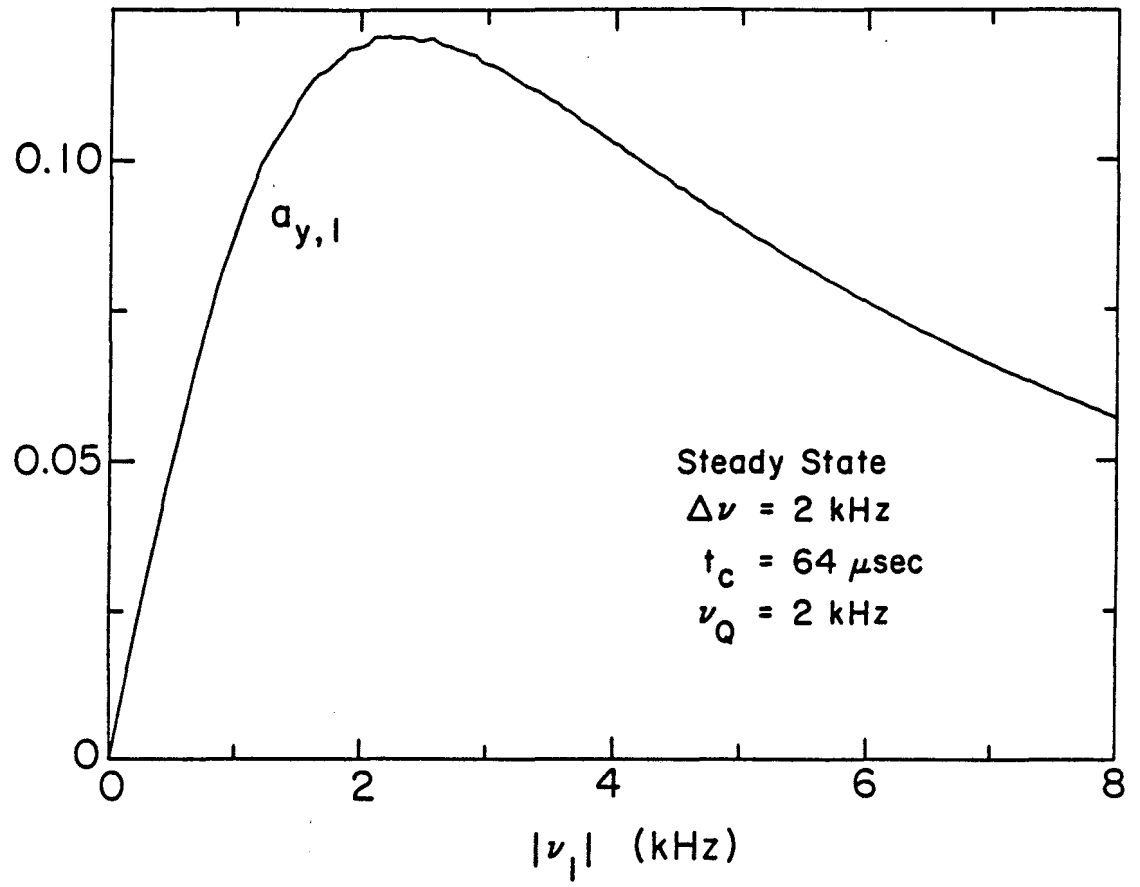

XBL 829-11689

Figure III.13 The steady-state value of $a_{y,1}$ at a single-quantum resonance frequency ($\Delta\nu = \nu_Q$) as a function of $|\nu_1|$; $a_{z,2}$ is essentially zero at this frequency and range of $|\nu_1|$ values and thus does not appear. Compare with Fig. III.12.

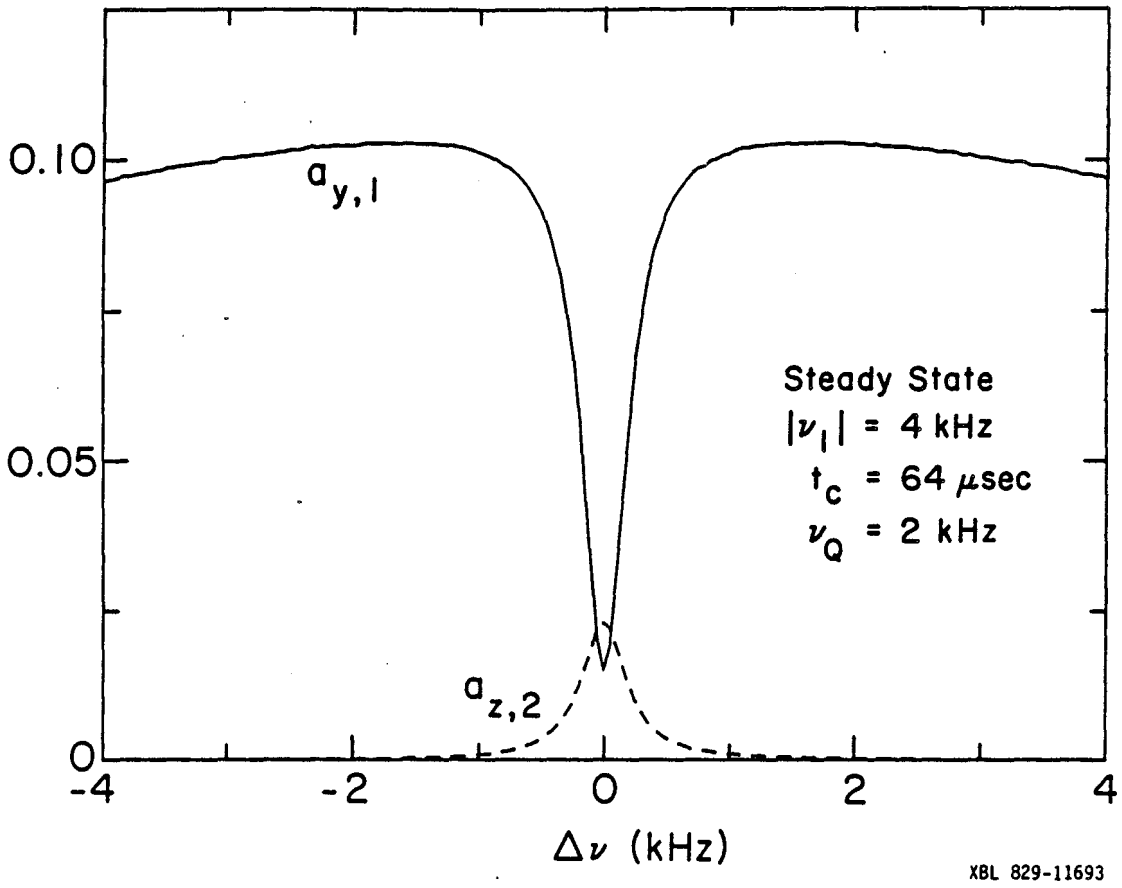

Figure III.14 Steady-state values of $a_{y,1}$ and $a_{z,2}$ following 0° - 180° phase-cycled cw excitation. The value of $|\nu_1|$ was chosen to maximize the dip in SQ coherence at $\Delta\nu = 0$. Notice, however, that the dip is broadened compared to those in Figs. III.9 and III.11.

at $\Delta\nu = 0$ and $\Delta\nu = \nu_Q$ are roughly equal, and the double-quantum dip is very small. Such ineffectual behavior could be predicted from plots of steady-state $a_{y,1}$ or $a_{z,2}$ values as a function of ν_1 for both $\Delta\nu = 0$ and $\Delta\nu = \nu_Q$. (See Figs. III.12 and III.13). These graphs suggest that $|\nu_1| \approx 4$ KHz is the best choice for selective depletion of the SQ signal at the double-quantum transition for the parameters chosen; a spectrum is shown in Fig. III.14.

3.6 Conclusions

As hoped, the preliminary simulations of phase-shifted spectra do exhibit two-quantum selectivity, although manifested as a dip in absorbance rather than a peak. Of course, only a few pulse parameter "knobs" have been turned in this study. A more detailed investigation using the mathematical framework developed in the chapter, perhaps on a system of three coupled protons and definitely making use of standard subroutines for the diagonalization and exponentiation of a general n x n matrix, should generate better insight and better selectivity.

IV. BEYOND THE THREE-LEVEL SYSTEM: FUNDAMENTALS OF MULTIPLE-QUANTUM NMR

4.1 Introduction

This chapter and the remaining one address a second area in which multiple-quantum techniques have proven useful: the proton NMR of molecules dissolved in nematic liquid crystal solvents and the NMR of liquid crystal molecules themselves. The advantage of multiple-quantum spectroscopy here is the spectral simplification it provides, allowing the determination of structural and conformational parameters.

Our focus will be on molecules with four to eight coupled protons (16 to 256 spin states, entailing 256 to 65536 density matrix elements). Such systems can formally be described in terms of fictitious spin-1/2 operators [65-67]:

$$I_x^{j-k} = \frac{1}{2}\left(|j\rangle\langle k| + |k\rangle\langle j|\right) \tag{IV.1a}$$

$$I_y^{j-k} = -\frac{i}{2}\left(|j\rangle\langle k| - |k\rangle\langle j|\right) \tag{IV.1b}$$

$$I_z^{j-k} = \frac{1}{2}\left(|j\rangle\langle j| - |k\rangle\langle k|\right) \quad . \tag{IV.1c}$$

However, the number of these operators required to span the density matrix quickly becomes enormous as N, the number of spins, increases: each pair of states gives rise to three operators, for a total of $(3)(\frac{1}{2})(2^N)(2^N-1)$. For N=4, there are 360 such operators; for N=8, there are 97920 of them. [The fictitious spin-1/2 operators are not all linearly independent, since

$I_z^{j-k} = I_z^{j-\ell} + I_z^{\ell-k}$. The minimum number of linearly independent operators needed to characterize an N spin-1/2 system is one for each density matrix element with the constraint that ρ be traceless, or 4^N-1. There are thus $(2^N-1)(2^{N-1}-1)$ "excess" I_p^{j-k} operators, roughly a third of the total.]

Clearly, an operator expansion of the density matrix as in Chapter II will not be possible; we never again will be able to know a system as intimately as we knew one single deuteron. Instead of keeping tabs on the entire density matrix, we will monitor expectation values, such as $Tr(\rho\ I_x)$ or the average six-quantum coherence magnitude. Even this limited knowledge of the exact dynamics will prove to be too much indigestable information, and we will eventually turn to statistical arguments in Chapter V.

In this chapter, the fundamentals of multiple-quantum NMR in coupled-proton systems are laid bare. We turn first to one motivation for the development of MQ techniques: the NMR of molecules in nematic liquid crystal solvents. Order tensors and the effect of anisotropic motion on the spin Hamiltonian are briefly presented, and the need for simplification of spectra becomes painfully apparent. An analysis of the Hamiltonian reveals that the use of multiple-quantum transitions can provide an elegant solution to this problem. Basic MQ pulse sequences and properties of the prepared density matrix are then described at some length, and three popular Pines group molecules--benzene, n-pentyl-d_{11}-cyanobiphenyl, and acetaldehyde--are discussed as examples. The chapter closes with a curious selection rule

demonstration.

4.2 NMR in Liquid Crystal Solvents

Liquid crystals are characterized on the molecular level by rapid translational diffusion but restricted molecular rotation. We will be interested in thermotropic liquid crystals, which as pure compounds form liquid crystalline mesophases over a temperature range between solid and isotropic liquid. The typically long, rod-like molecules align parallel to each other along local director axes, resulting in localized rotational order. When a static magnetic field is applied, the molecules respond cooperatively to reduce their free energy, given by [83]

$$\Delta G = -\Delta\chi\, H_0^2(3\cos^2\alpha-1)/6 \quad . \qquad \text{(IV.2)}$$

The result is long-range order characterized by a single director, $\Delta\chi$ is the difference in bulk diamagnetic susceptibility parallel and perpendicular to the director axis, and α is the angle between the director and the magnetic field. Usually $\Delta\chi = \chi_{\parallel} - \chi_{\perp}$ is positive, ΔG is minimized for $\alpha=0$, and the liquid crystal molecules align parallel to the magnetic field. Such is the case for the compounds used in experiments reported here. $\Delta\chi$ is negative for other liquid crystals, and molecules orient themselves perpendicular to the applied field.

Some thermotropic liquid crystals exhibit more than one liquid crystalline phase. The most disordered of these is the

nematic phase, for which there is no periodicity in molecular order along the director axis [Fig. IV.1(a)]. There are also a number of layered smectic phases that occur in some compounds at lower tempeatures [Fig. IV.1(b)]. We will only consider the nematic phase here.

4.2.1 The Order Tensor

A molecule dissolved in a nematic liquid crystal solvent will itself experience some degree of ordering, i.e., rotational anisotropy. The extent of this ordering for a rigid solute (or solvent) molecule can be described in terms of a symmetric and traceless second-rank Cartesian tensor (or 3x3 matrix), the Saupe order tensor $\underset{\approx}{S}$ [46,83,84]. In an arbitrary molecular axis system x,y,z,$\underset{\approx}{S}$ will in general have five independent elements, most conveniently chosen to be S_{zz}, $(S_{xx}-S_{yy})$, S_{xy}, S_{xz}, and S_{yz}. These elements of $\underset{\approx}{S}$ describe the average orientation of the molecule with respect to the magnetic field (and director). Alternately, they can be thought of as giving a probability distribution for the magnetic field direction in a molecule-fixed coordinate frame. This distribution involves an expansion in functions closely akin to zero-rank and second-rank spherical harmonics [46]:

$$P(\theta,\phi) = (4\pi)^{-1} \{1 + (\tfrac{5}{2})[(3\cos^2\theta-1)S_{zz} + (\sin^2\theta\cos 2\phi)(S_{xx}-S_{yy}) + (4\sin\theta\cos\theta\cos\phi)S_{xz} + (4\sin\theta\cos\theta\sin\phi)S_{yz} + (2\sin^2\theta\sin 2\phi)S_{xy}]\} \quad \text{(IV.3)}$$

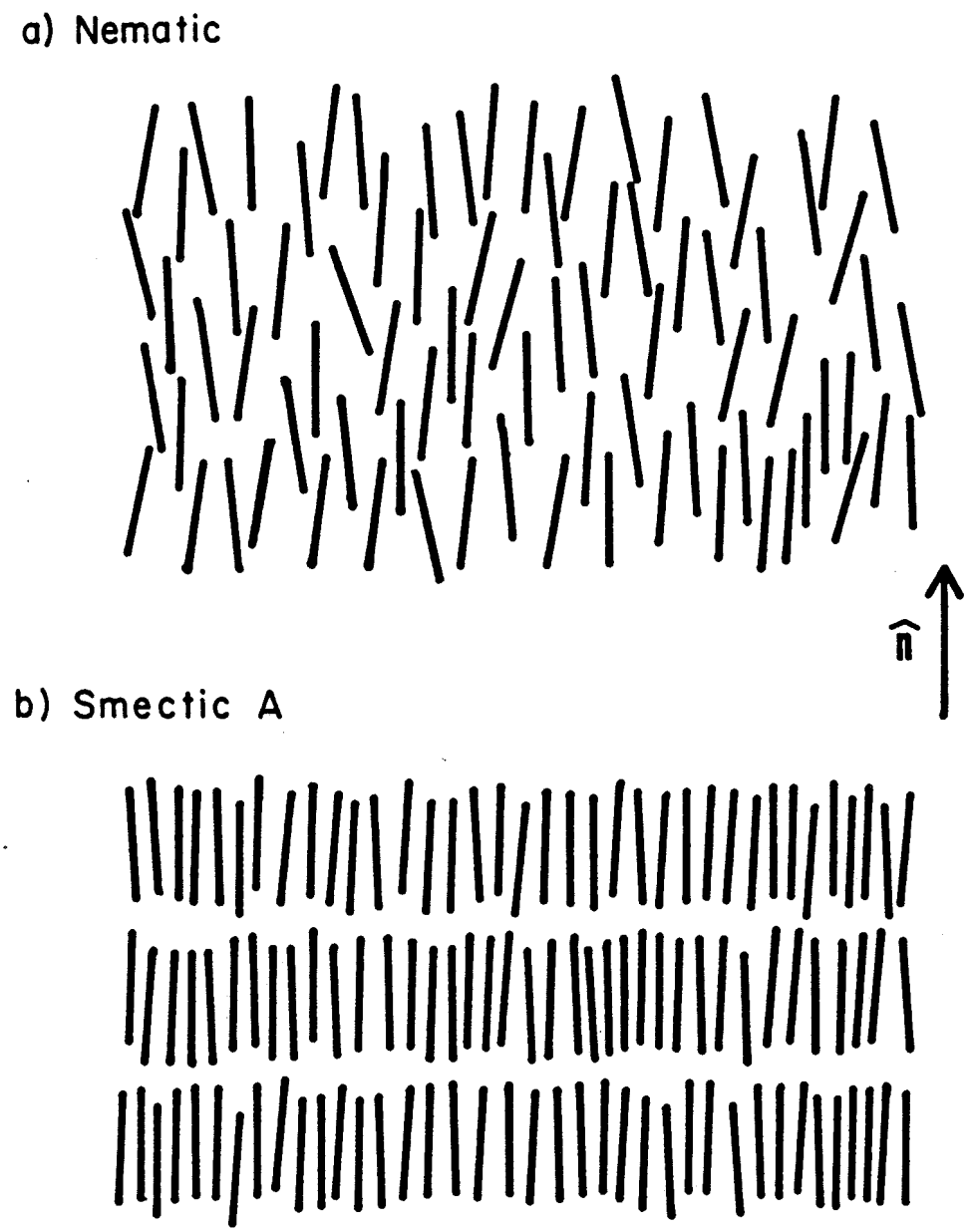

XBL 818-1765

Figure IV.1 An artist's conception of two common liquid crystal phases, as drafted by Steve Sinton. (a) In the nematic phase, the typically rod-like liquid crystal molecules tend to align parallel to the director axis $\hat{n}$, which in turn is parallel to the external magnetic field for most liquid crystals. (b) A lower-temperature smectic A phase features additional ordering: molecules are arranged in layers perpendicular to the director axis.

[Strictly speaking, $P(\theta,\phi)$, a probability per unit solid angle, should include terms proportional to all even-rank spherical harmonics. However, only the terms listed above can be analyzed using the second-rank tensor interactions of NMR.]

Tensor elements $S_{\alpha\beta}$ are defined as follows. Recall from section 1.4 that the expression for a symmetric second-rank tensor $\underset{\approx}{A}$ in the laboratory frame can be related to its form in some other axis system, specifically a molecule-fixed set of axes x,y,z, by a transformation matrix $\underset{\approx}{R}$:

$$\underset{\approx}{A}(\mathrm{LAB}) = \underset{\approx}{R}\,\underset{\approx}{A}\,\underset{\approx}{R}^{\dagger} \quad . \tag{IV.4}$$

In the high-field approximation, we are interested in $A_{ZZ}(\mathrm{LAB})$, given by

$$A_{ZZ}(\mathrm{LAB}) = (\underset{\approx}{R}\,\underset{\approx}{A}\,\underset{\approx}{R}^{\dagger})_{ZZ} = \sum_{\alpha,\beta}^{x,y,z} R_{Z\alpha}\, R_{Z\beta}\, A_{\alpha\beta} \quad . \tag{IV.5}$$

$R_{Z\alpha}$ is the cosine of the angle between the α-axis of the molecule and the lab Z-axis. Hence

$$A_{ZZ}(\mathrm{LAB}) = \sum_{\alpha,\beta}^{x,y,z} \cos\theta_{\alpha Z} \cos\theta_{\beta Z}\, A_{\alpha\beta} \tag{IV.6a}$$

$$= \frac{1}{3} \sum_{\alpha,\beta}^{x,y,z} (3 \cos\theta_{\alpha Z} \cos\theta_{\beta Z} - \delta_{\alpha\beta}) A_{\alpha\beta}$$

$$+ \frac{1}{3} (A_{xx} + A_{yy} + A_{zz}) \tag{IV.6b}$$

$$= \frac{2}{3} \sum_{\alpha,\beta}^{x,y,z} \frac{1}{2} (3 \cos\theta_{\alpha Z} \cos\theta_{\beta Z} - \delta_{\alpha\beta}) A_{\alpha\beta} + \bar{A} \quad . \qquad \text{(IV.6c)}$$

The angles in this expression must be averaged over molecular motion, yielding at last the definition of order elements $S_{\alpha\beta}$ [83,84]:

$$A_{ZZ}(\text{LAB}) = \frac{2}{3} \sum_{\alpha,\beta}^{x,y,z} \left\langle \frac{1}{2} (3 \cos\theta_{\alpha Z} \cos\theta_{\beta Z} - \delta_{\alpha\beta}) \right\rangle A_{\alpha\beta} + \bar{A} \qquad \text{(IV.7a)}$$

$$\equiv \frac{2}{3} \sum_{\alpha,\beta}^{x,y,z} S_{\alpha\beta} \; A_{\alpha\beta} + \bar{A} \quad . \qquad \text{(IV.7b)}$$

The range of each $S_{\alpha\beta}$ element is -0.5 to 1.0.

Like other symmetric second-rank tensors, $\underset{\approx}{S}$ can be diagonalized in a principal axis system x',y',z'. It can thus be characterized in terms of the three Euler angles relating frames x,y,z and x',y',z' and two independent principal values $S_{z'z'}$ and $S_{x'x'}-S_{y'y'}$ (only two since $\underset{\approx}{S}$ is traceless in any axis system). In a non-symmetric molecule, however, there is no obvious way to relate the orientation of the principal axis system to the molecular framework; hence diagonalizing $\underset{\approx}{S}$ provides no simplification.

In molecules with symmetry, on the other hand, one or more of the five independent elements of $\underset{\approx}{S}$ may equal zero if the molecular axis system x,y,z is chosen correctly [83]. For example, if the molecule has a plane of symmetry and the z-axis is oriented perpendicular to it, then S_{xz} and S_{yz} vanish. If the molecule possesses two perpendicular mirror planes, then the principal

axis system of $\underset{\approx}{S}$ is determined: the x-axis lies in one plane, the y-axis in the other, and the z-axis lies along the line of intersection. In this frame only S_{zz} and $S_{xx}-S_{yy}$ are non-zero. If the molecule is graced with a C_n axis, $n \geq 3$, and if this axis is chosen as the z-axis, then there is but one non-zero order parameter: S_{zz}. Finally, for molecules with tetrahedral or higher symmetry, no ordering is expected at all--the molecule should tumble freely and isotropically despite the aligning influence of the nematic solvent.

As it turns out, however, the NMR spectra of tetrahedral molecules like methane and tetramethylsilane show unmistakable dipolar splittings [85,86], a sure sign of some sort of anisotropic interaction. Common explanations for this anisotropy include coupling between the reorientation of a molecule and its asymmetric vibrational modes [87,88] and molecular distortion caused by interaction with the ordered solvent [86].

This leads us into an exceedingly brief consideration of ordering in molecules with large-amplitude internal motion. According to Burnell and de Lange [88,89], two extreme cases can be distinguished. When the rate of internal motion (typically rotation around a single bond) is much faster than the rate of molecular reorientation, then an averaged set of order parameters $\langle S_{zz}\rangle$, $\langle S_{xx}-S_{yy}\rangle$, etc., suffices to describe the ordering if a molecular axis system can be chosen to separate internal from reorientational motion. When the internal rotation is

characterized by jumps between conformations with a jump rate much lower than the rate of molecular reorientation, then each conformer is assigned its own set of order parameters, and the overall ordering is weighted by the amount of time the molecule spends in each conformation. For intermediate cases, analysis is even messier since an average over internal motion must be taken.

Emsley and Luckhurst [87], on the other hand, believe that "arguments based on time scales can be misleading and may be incorrect." They treat the order tensor as an equilibrium property and use statistical mechanics to calculate the average value of $A_{ZZ}(LAB)$, which for a molecule with discrete conformations again requires a separate set of order parameters for each conformer, weighted by its probability:

$$A_{ZZ}(LAB) = \bar{A} + \frac{2}{3} \sum_{n} P_n \sum_{\alpha,\beta}^{x,y,z} S^n_{\alpha\beta} A^n_{\alpha\beta} \quad . \qquad \text{(IV.8)}$$

Only when the intermolecular potential energy is independent of conformation, they claim, will a single set of order parameters suffice.

Clearly, the current understanding of internal motion as measured by nematic-phase NMR is undergoing some internal motion of its own. Multiple-quantum techniques can help resolve much of the ambiguity plaguing such measurements, as discussed in the Ph.D. theses of Gary Drobny [57], Steve Sinton [56], and Dan Weitekamp [58].

4.2.2 The Basics of NMR in Nematic Phase

Magnetic resonance spectroscopy of molecules dissolved in ordered liquid crystalline phases was introduced in the early 1960's by Saupe and Englert [90]. The spectra obtained are nearly ideal for detailed study of molecular conformation and internal motion. Due to rapid translational diffusion in the nematic phase, all intermolecular couplings average to zero; hence lines are narrow (on the order of a few Hz for solute molecules in the absence of exchange), free from the extensive dipolar broadening that generally characterizes solid-phase NMR. At the same time, rotational motion is anisotropic due to ordering imposed by the liquid crystal molecules. Non-scalar intramolecular couplings, in particular intramolecular direct dipole-dipole couplings, do not average to zero as in the NMR of isotropic liquids. These interactions give rise to a profusion of transitions, even for a small number of spins. The spectrum that results features a large number of sharp and hopefully resolvable lines; lines that are of interest because experimental dipolar couplings can be related to averaged internuclear distances. (The liquid crystal molecules themselves usually contain a large number of spins and order to a much greater extent than do the solute molecules. As such, they give rise to broad background features in the NMR spectrum which do not interfere with the sharp solute peaks.)

4.2.3 Effects of Molecular Motion on the Hamiltonian

For the details of proton NMR in liquid crystals, the reader must once again endure the ritualistic display of Hamiltonians.

First, however, the effect of anisotropic motion on the three terms of the internal Hamiltonian--those describing direct dipolar coupling, chemical shielding, and J-coupling--must be considered.

Of these, the largest and most interesting is the direct dipole-dipole term. Recall from section 1.5.5 that the Hamiltonian describing the direct interaction of pairs of protons is given in units of Hz by

$$\mathcal{H}_D(\mathrm{Hz}) = \sum_{j<k} \frac{\hbar \gamma^2}{2\pi r_{jk}^3} (1 - 3 \cos^2 \theta_{jk})$$

$$\cdot [I_{zj} I_{zk} - \frac{1}{2} (I_{xj} I_{xk} + I_{yj} I_{yk})] \quad . \qquad \text{(IV.9)}$$

where θ_{jk} is the angle between the internuclear vector and the magnetic field. When the nuclei are in motion, both r_{jk} and θ_{jk} may vary, and an average value of the spatial part of $\mathcal{H}_D$ must be calculated. $\langle D_{jk} \rangle$, the averaged dipolar coupling constant for spins j and k, can be expressed as

$$\langle D_{jk} \rangle (\mathrm{Hz}) = \frac{\hbar \gamma^2}{2\pi} \left\langle \frac{1}{r_{jk}^3} (1 - 3 \cos^2 \theta_{jk}) \right\rangle \quad . \qquad \text{(IV.10)}$$

In a rigid molecule (one without internal rotation), the internuclear separation r_{jk} is affected primarily by vibrations, which generally occur on a faster time scale than molecular reorientation, It is customary then to assume that r_{jk} and θ_{jk} can be averaged separately [85]:

$$\langle D_{jk}\rangle = \frac{\hbar\gamma^2}{2\pi\langle r_{jk}^{\,3}\rangle} \langle 1 - 3\cos^2\theta_{jk}\rangle \quad . \tag{IV.11}$$

In its own principal axis system a,b,c (with the c-axis aligned with the internuclear vector), the vibrationally averaged dipolar tensor for protons j and k is given by

$$\underset{\approx}{D}_{jk}(\mathrm{PAS}) = \frac{\hbar\gamma^2}{2\pi\langle r_{jk}^{\,3}\rangle} \begin{pmatrix} 1 & 0 & 0 \\ 0 & 1 & 0 \\ 0 & 0 & -2 \end{pmatrix} \tag{IV.12}$$

Equation I.4 can be used to transform $\underset{\approx}{D}_{jk}$ to the molecule-fixed axis system x,y,z chosen to describe the order parameters. In this reference frame,

$$(D_{jk})_{\alpha\beta} = [\underset{\approx}{R}\, \underset{\approx}{D}_{jk}(\mathrm{PAS})\underset{\approx}{R}^{\dagger}]_{\alpha\beta} \tag{IV.13a}$$

$$= -\frac{\hbar\gamma^2}{2\pi\langle r_{jk}^{\,3}\rangle} (3\cos\theta_{\alpha c}\cos\theta_{\beta c} - \delta_{\alpha\beta}) \quad , \tag{IV.13b}$$

where $\theta_{\alpha c}$ is the angle between the α-axis of the molecule-fixed system (α=x,y,z) and the principal axis c. The average value of $D_{jk} \equiv (\underset{\approx}{D}_{jk})_{ZZ}$ is given by Eq. IV.8:

$$\langle D_{jk}\rangle = \frac{2}{3} \sum_{\alpha,\beta}^{x,y,z} S_{\alpha\beta}\, D_{\alpha\beta} \quad . \tag{IV.14}$$

(There is no isotropic component.) A little manipulation yields finally [47]

$$\langle D_{jk}\rangle = \left(-\frac{\hbar\gamma^2}{2\pi\langle r_{jk}^3\rangle}\right) [(3\cos^2\theta_{zc} - 1)S_{zz}$$

$$+ (\cos^2\theta_{xc}-\cos^2\theta_{yc})(S_{xx}-S_{yy})$$

$$+ 4\,(\cos\theta_{xc}\,\cos\theta_{yc})S_{xy} + 4(\cos\theta_{xc}\,\cos\theta_{zc})S_{xz}$$

$$+ 4\,(\cos\theta_{yc}\,\cos\theta_{zc})S_{yz}] \quad . \qquad \text{(IV.15)}$$

For simplicity, we will drop the averaging brackets on D_{jk} from now on.

Each term in this expression for D_{jk} involves the product of an order parameter and $\langle r_{jk}^3\rangle^{-1}$. Hence, unless the order parameters are determined by some other experiment, measurement of D_{jk} values can never yield absolute internuclear distances; one such separation r_{jk} must be assumed from another technique. Nonetheless, Eq. IV.15 is exceedingly useful: it can provide information not only on molecular dimensions, but also on the nature and timescale of internal motion.

The effect of partial molecular ordering on the other terms of the internal Hamiltonian is easier to deal with. Recall from section 1.5.3 that the chemical shielding experienced by a nucleus j can be expressed as a second-rank tensor $\underset{\approx}{\sigma}_j$. In the high-field

approximation, the chemical shielding Hamiltonian is

$$\mathcal{H}_{cs} = - \sum_j (\sigma_j)_{ZZ} I_{zj} \quad . \tag{IV.16}$$

Using Eq. IV.7b, $(\sigma_j)_{ZZ}$ can be related to the components of $\underset{\approx}{\sigma}_j$ in a molecule-fixed axis system as follows:

$$(\sigma_j)_{ZZ}(\mathrm{LAB}) = \overline{\sigma_j} + \frac{2}{3} \sum_{\alpha,\beta}^{x,y,z} S_{\alpha\beta}(\sigma_j)_{\alpha\beta} \tag{IV.17a}$$

$$\equiv \overline{\sigma_j} + \sigma_j^{\mathrm{aniso}} \quad . \tag{IV.17b}$$

A chemical shift $(\sigma_j)_{ZZ}$ (or σ_j for short) measured in nematic phase is therefore likely to differ from the corresponding isotropic-phase value, and a determination of this difference can provide information on the anisotropy of chemical shielding [91]. However, the difficulty in distinguishing order parameter effects from chemical shielding effects and in separating intramolecular and intermolecular contributions to shielding make detailed analysis often difficult and unreliable.

Anisotropic terms in the indirect spin-spin coupling Hamiltonian were cast to the wind in Chapter I, since calculations indicate that such terms are likely to be negligible for interaction between protons. The remaining scalar coupling is impervious to any sort of rotation or motion; hence no modification of Eq. I.36 is necessary:

$$\mathcal{H}_J = \sum_{j<k} J_{jk} \underset{\sim}{I}_j \cdot \underset{\sim}{I}_k \quad . \tag{IV.18}$$

With the inclusion of an rf offset term, the overall Hamiltonian for a coupled-proton system in nematic phase is (at last) given as follows:

$$\mathcal{H} = \mathcal{H}_D + \mathcal{H}_{cs} + \mathcal{H}_J + \mathcal{H}_{off} \quad , \tag{IV.19}$$

where

$$\mathcal{H}_D = \sum_{j<k} D_{jk}[I_{zj}I_{zk} - \frac{1}{2}(I_{xj}I_{xk} + I_{yj}I_{yk})] \tag{IV.20a}$$

$$\mathcal{H}_{cs} = - \sum_j \sigma_j I_{zj} \tag{IV.20b}$$

$$\mathcal{H}_J = \sum_{j<k} J_{jk} \underset{\sim}{I}_j \cdot \underset{\sim}{I}_k \tag{IV.20c}$$

$$\mathcal{H}_{off} = - \Delta\omega I_z \quad . \tag{IV.20d}$$

Again it should be noted that D_{jk} and σ_j are partially averaged quantities that depend on the degree of molecular ordering.

4.2.4 The Case for Multiple-Quantum NMR

A large number of rigid and flexible molecules have been successfully analyzed in nematic phase [25,45,46,92] by use of conventional single-quantum (SQ) NMR and various computer lineshape-fitting programs [51]. For small molecules, the lush

profusion of resolvable transitions in the SQ spectrum can be harvested to yield information on the nature of conformer geometries and probabilities, rotational barrier heights, exchange rates, chemical shielding anisotropies, etc. The technique is limited, however, by a gross overabundance of spectral lines as the number of spins increases beyond six or so. An example is the calculated and slightly broadened single-quantum spectrum of a 4,4'-disubstituted biphenyl in Figure IV.2. For this eight-spin molecule (discussed further in section 4.8.2), there are 1580 distinct single-quantum transition frequencies, even when D_4 symmetry is assumed [56,93]. The resulting tangle of transitions is extremely difficult to analyze (although Diehl et al. [94] were able to simulate a 16384-point spectrum of 4,4'-dichlorobiphenyl dissolved in nematic phase). Moreover, even if individual lines can be resolved and identified, most of the spectral information is redundant: for D_4 symmetry there are at most sixteen independent parameters to be determined--seven unique dipolar couplings, seven J-couplings, and two chemical shifts.

Deuterium substitution is certainly one remedy, since replacing all but two or three protons with deuterons would result in a well-resolved deuterium-decoupled proton spectrum. Unfortunately, selective deuteration is time-consuming and expensive, even with an experienced chemist on hand, since an entire series of deuterated compounds would need to be synthesized in order to map out all the proton-proton couplings. To make matters worse, deuteration may

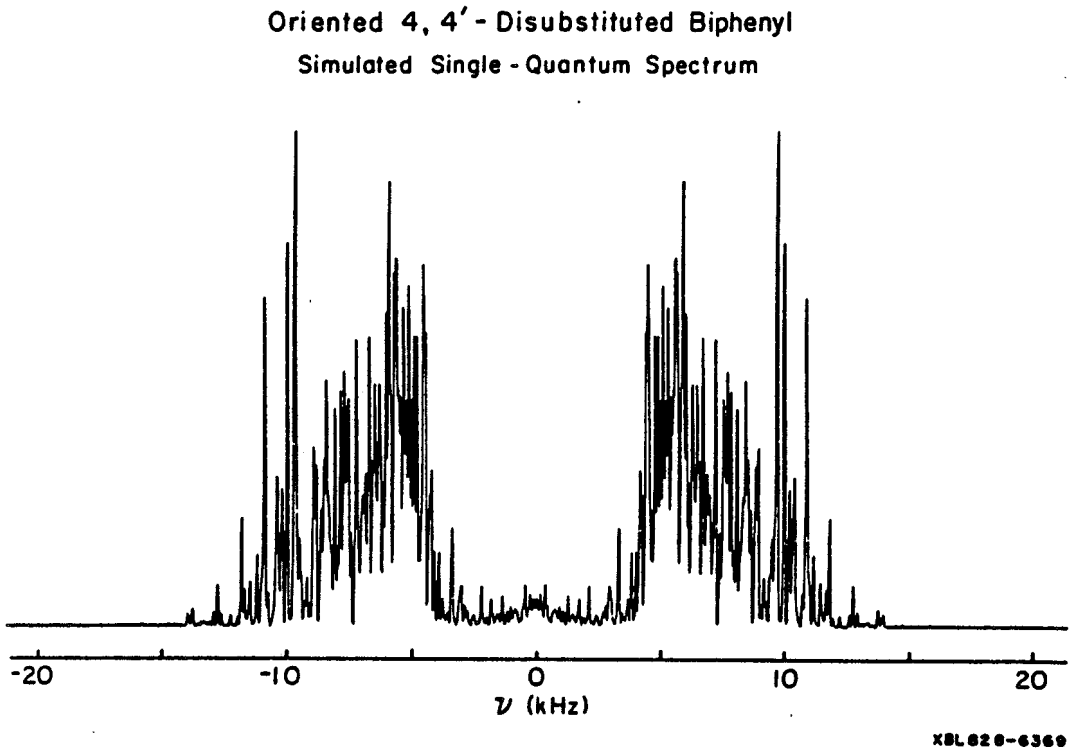

Figure IV.2 A simulated nematic-phase single-quantum spectrum (with some artificial broadening) for a 4,4'-disubstituted biphenyl with D_4 spin symmetry. Steve Sinton's coupling constants for 4-cyano-4'-n-pentyl-d_{11}-biphenyl were used, although that particular molecule is itself a liquid crystal and would be expected to have broader lines than those here [56]. There are 2220 symmetry-allowed SQ transitions, of which 640 pairs are doubly degenerate. The result is 1580 unique transition frequencies, making analysis a formidable task.

change the conformational geometry, the rate of internal motion, or the order parameters [95]. What is needed instead is a general spectroscopic technique for isolating a reduced number of resolvable transitions. As the reader no doubt has guessed, multiple-quantum FT NMR is "the answer".

4.3 Up Close and Personal with the Multiple-Quantum Hamiltonian

"By their Hamiltonians ye shall know them ..."

As stated earlier, the Hamiltonian for a collection of N coupled protons adrift in nematic phase consists of four terms describing direct dipole-dipole coupling, indirect J-coupling, chemical shifts, and the rf frequency offset. It commutes with I_z in high field and thus shares a common set of 2^N eigenfunctions. When written in the convenient spin-product basis set (e.g., $|++-+ \ldots \rangle$ or $|\alpha\alpha\beta\alpha\ldots\beta\rangle$), the Hamiltonian is block-diagonal, each block characterized by a value of M, the eigenvalue of I_z. (Because it only connects states with the same value of M, $\mathcal{H}$ is in effect a zero-quantum operator.) Its simplified form in the spin-product basis makes numerical diagonalization much easier, since each block can be treated separately. As an example, an eight-spin system has 256 eigenstates, but the largest block with M=0 contains only 70 states.

The energy levels of $\mathcal{H}$ are shown schematically in the much-reproduced Fig. IV.3. They are divided into N+1 Zeeman manifolds, each corresponding to a different value of M. If $n = N/2 + M$ is defined as the number of spins "up", then each manifold contains

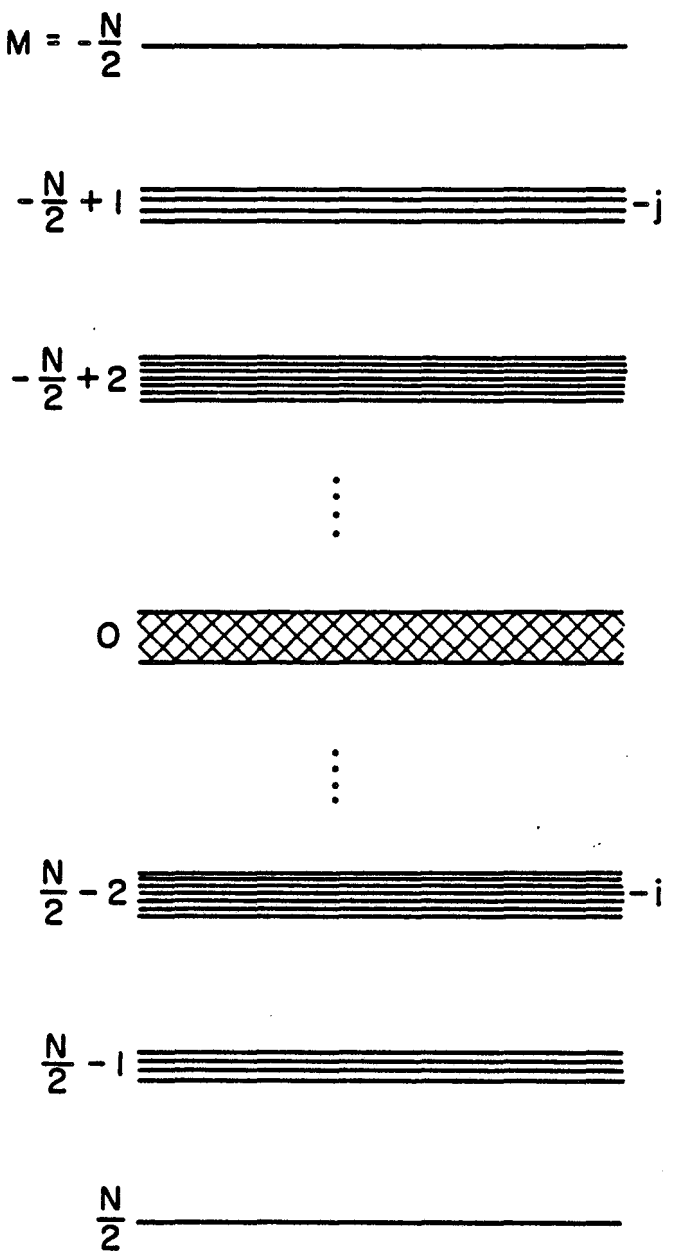

XBL 7710-10022

Figure IV.3 A schematic energy level diagram for N coupled spin-$\frac{1}{2}$ nuclei. Eigenstates are divided into Zeeman manifolds characterized by the value of M. The number of states in each manifold follows a binomial distribution: the ways of choosing n out of N spins to be "up" instead of "down", where n = M + N/2. It can be seen from this figure that there can be many single-quantum transitions ($\Delta M = \pm 1$) but only one N-quantum transition.

$\binom{N}{n} = N!/[(N/2+M)!(N/2-M)!]$ states, the number of ways of choosing N spins n at a time. Splittings within all but the extreme Zeeman manifolds are due to the coupling and chemical shift terms in $\mathcal{H}$.

The key to the usefulness of multiple-quantum NMR is that the number of possible transitions drops sharply as ΔM increases. The total number of transitions in a non-symmetric N-spin system is the number of density matrix elements above the diagonal, or $\frac{1}{2}(4^N-2^N)$. The number of ΔM-quantum transitions is given by a sum over products of appropriate Zeeman manifold dimensions:

$$\sum_{n=0}^{N-\Delta M} \binom{N}{n} \binom{N}{n+\Delta M} \text{ for } \Delta M \neq 0 \quad ,$$

$$\frac{1}{2} \sum_{n=1}^{N-1} \binom{N}{n} \left[\binom{N}{n} - 1\right] \text{ for } \Delta M = 0 \quad .$$

Wokann and Ernst [13] noted that these sums could be reduced to simpler expressions:

$$\binom{2N}{N-\Delta M} \text{ for } \Delta M \neq 0 \quad ,$$

$$\frac{1}{2}\left[\binom{2N}{N} - 2^N\right] \text{ for } \Delta M = 0 \quad .$$

Making use of the Stirling approximation ($\ln p! \approx (n+\frac{1}{2}) \ln p - p + \ln \sqrt{2\pi}$), one obtains the following useful relationship for large

N and small ΔM:

$$\text{Number of } \Delta M\text{-quantum transitions} \approx \frac{4^N}{\sqrt{N\pi}} \; e^{-(\Delta M)^2/N} \text{ for } \Delta M \neq 0$$

$$\approx \frac{1}{2}\left(\frac{4^N}{\sqrt{N\pi}} - 2^N\right) \text{ for } \Delta M = 0 \; .$$

The number of ΔM-quantum transitions is seen to drop off in a Gaussian manner. [The overall spectral intensity of each multiple-quantum order (ΔM = 1,2,3, etc.) will decrease in much the same way, although much of Chapter V is devoted to showing that an accurate treatment of high-quantum intensity predicts a less drastic rate of decline.] For some actual numbers, a non-symmetric eight-spin system has (using the exact formula) a whopping 11440 single-quantum transitions, but only 1 eight-quantum transition, 16 seven-quantum transitions, and 120 six-quantum transitions. The N,N-1, and N-2 quantum regions of the MQ spectrum are thus expected to contain resolvable transitions. (Techniques for separating different multiple-quantum orders will be discussed in section 4.7.) But will an analysis of these high-quantum lines enable us to determine all molecular parameters of interest? The answer, at least in principle, is yes. For a non-symmetric N-spin system we expect $2N^2$-N (N-2)-quantum lines and 2N (N-1)-quantum lines, plus one N-quantum transition (which, however, is uninformative--see section 4.6.3). In comparison, there are at most N^2 molecular parameters: $\frac{1}{2}$ N (N-1) dipolar couplings, the

same number of J-couplings, and N chemical shifts. Because there are more frequencies for input than molecular unknowns, the problem of fitting the experimental spectrum using an iterative computer program is not underdetermined.

4.4 The Effect of Symmetry

Benzene, benzene (ordered phase),
On your spectra still we gaze;
What a tangled mess they'd be
Without your six-fold symmetry ...

The existence of spin-system symmetry often leads to substantial simplification of both experimental spectra and computer analysis. When the eigenstates of $\mathcal{H}$ can be divided into different irreducible representations [96,97], the original $2^N \times 2^N$ density matrix can be split up into smaller units, spawning what are effectively new and independent systems. This division is possible because pulses do not mix symmetries. I_x and I_y, the operators involved in the rf Hamiltonian, belong to the totally symmetric A_1 representation [98] and hence cannot connect states in different representations.

There are several ways to determine the symmetry of a spin system. For a rigid collection of spins, one can assign a point group (C_{3v}, D_4, O_h, etc.) from the spatial relationship of the nuclei, omitting those symmetry operations (other than the identity) which do not exchange the spins. More generally, the permutation group [99] of the system is determined by noting which nuclear

labels in the Hamiltonian can be interchanged without altering its form. The spin system is then characterized by the point group isomorphic to this permutation group. Once the group is known, symmetry-adapted states for the various irreducible representations can be constructed using projection operators [97].

An alternate procedure (to be discussed more fully in Appendix D) is to let the computer do the symmetry sorting. The essence of this method is as follows. After $\mathcal{H}$ is diagonalized and its eigenstates determined numerically, appropriate matrix elements of I_x are calculated. Assume ψ_a and ψ_b are eigenstates of $\mathcal{H}$, differing in $\dot{M}$ value by ± 1. If $\langle\psi_a|I_x|\psi_b\rangle \neq 0$, then ψ_a and ψ_b must belong to the same representation. In contrast, if there are no other eigenstates ψ_c and ψ_d such that $\langle\psi_a|I_x|\psi_c\rangle \neq 0$, $\langle\psi_c|I_x|\psi_d\rangle \neq 0$, and $\langle\psi_d|I_x|\psi_b\rangle \neq 0$, then ψ_a and ψ_b are in different representations. This sorting technique has two disadvantages--the diagonalization of $\mathcal{H}$ must take place prior to symmetry-labeling and the resulting representations are not properly identified (e.g., A_1,B_1, etc.)--but its speed and generality make it extremely useful.

An example of the spectral simplification provided by spin-system symmetry can be found in Table IV.1, a comparison of 8-spin molecules. The number of allowed transitions is seen to decrease greatly when transitions can occur only between states of the same representation. The computer simulation of intensities is also simplified by the reduced size of the symmetry species. The lengthiest part of such simulation involves matrix multiplication,

Table IV.1

Effects of Symmetry in 8-spin Systems

	non-symmetric molecule	4,4'-disubstituted biphenyl	cyclooctatetraene	$Cd_3(CH_2)_4CD_3$ chain
Symmetry	C_1	D_4	D_{2d}[a]	D_2
Eigenstate breakdown into irredubile reps.	256 A_1	55 A_1 15 A_2 21 B_1 45 B_2 120 E	43 A_1 27 A_2 33 B_1 33 B_2 120 E	76 A_1 60 B_1 60 B_2 60 B_3
Relative simulation time	1.0	0.119	0.113	0.065
Number of transitions				
8Q	1	1	1	1
7Q	16	4	2	4
6Q	120	30	24	36
5Q	560	116	94	140
4Q	1820	378	338	476
3Q	4368	860	778	1092
2Q	8008	1586	1480	2044
1Q	11440	2220	2070	2860
0Q	6307	1135	1063	1506
Reference		56	55	57

[a] slow exchange limit

which obviously takes longer when the matrices are bigger: specifically, if A and B are nxn matrices, then the calculation of $A \cdot B$ involves n^3 individual products. The computation times required for a general 8-spin system and for the 8-spin methylene chain are thus approximately in the following ratio:

$$\frac{\text{chain computation time}}{\text{general system computation time}} \propto \frac{(76)^3+3\cdot(60)^3}{(256)^3} = 0.065 \quad . \qquad \text{(IV.21)}$$

(Another curious comparison--the number of allowed transitions for each odd-quantum order in the 8-spin chain is exactly one-fourth the corresponding general system value.)

The extreme "top" and "bottom" states with $M = \pm N/2$ always belong to the totally symmetric A_1 representation. Hence the N-quantum line and all (N-1)-quantum lines in the MQ spectrum are A_1 transitions. Transitions between states of other symmetry occur in lower orders.

It was earlier demonstrated that the number of (N-1)-quantum and (N-2)-quantum lines in the spectrum of a general non-symmetric system is sufficient to determine all relevant molecular parameters. Warren and Pines [95] have shown, by means of the analogy between high-quantum spectroscopy and isotopic spin-labeling, that the same sufficiency relation holds when both the number of lines and the number of independent couplings and shifts are reduced by symmetry.

4.5 Your Basic Multiple-Quantum Pulse Sequence

Conventional single-quantum pulsed NMR is singularly straightforward. A pulse applied to the system creates single-quantum coherence, which manifests itself macroscopically as a rotating magnetization. The magnetization is monitored as a function of time by the current it induces in a coil. This free induction decay (FID) signal is then Fourier transformed to obtain the NMR spectrum, which is equivalent to that found in a slow-passage low-power cw experiment.

In contrast, the simplest multiple-quantum pulse sequence contains three pulses [40,100,101] [Fig. IV.4(a)]. Two pulses separated by a time τ are necessary to create multiple-quantum coherences, which then evolve for a time t_1. Because these coherences do not generate a rotating magnetization, they are not directly measurable. Hence a third pulse is needed to transform multiple-quantum coherence back to single-quantum coherence, which is detected after an additional delay t_2. One point is taken for each incremented value of t_1; the resulting MQ free induction decay is then Fourier transformed to yield the multiple-quantum spectrum. Different multiple-quantum orders (ΔM = 1,2,3, etc.) can be separated by a variety of techniques to be discussed in section 4.7.

Schematically, the experiment can be divided into a <u>preparation</u> phase, an <u>evolution</u> phase, and a <u>detection</u> phase [100]. (For some experiments, it is convenient to separate the third

Typical Multiple Quantum Pulse Sequences

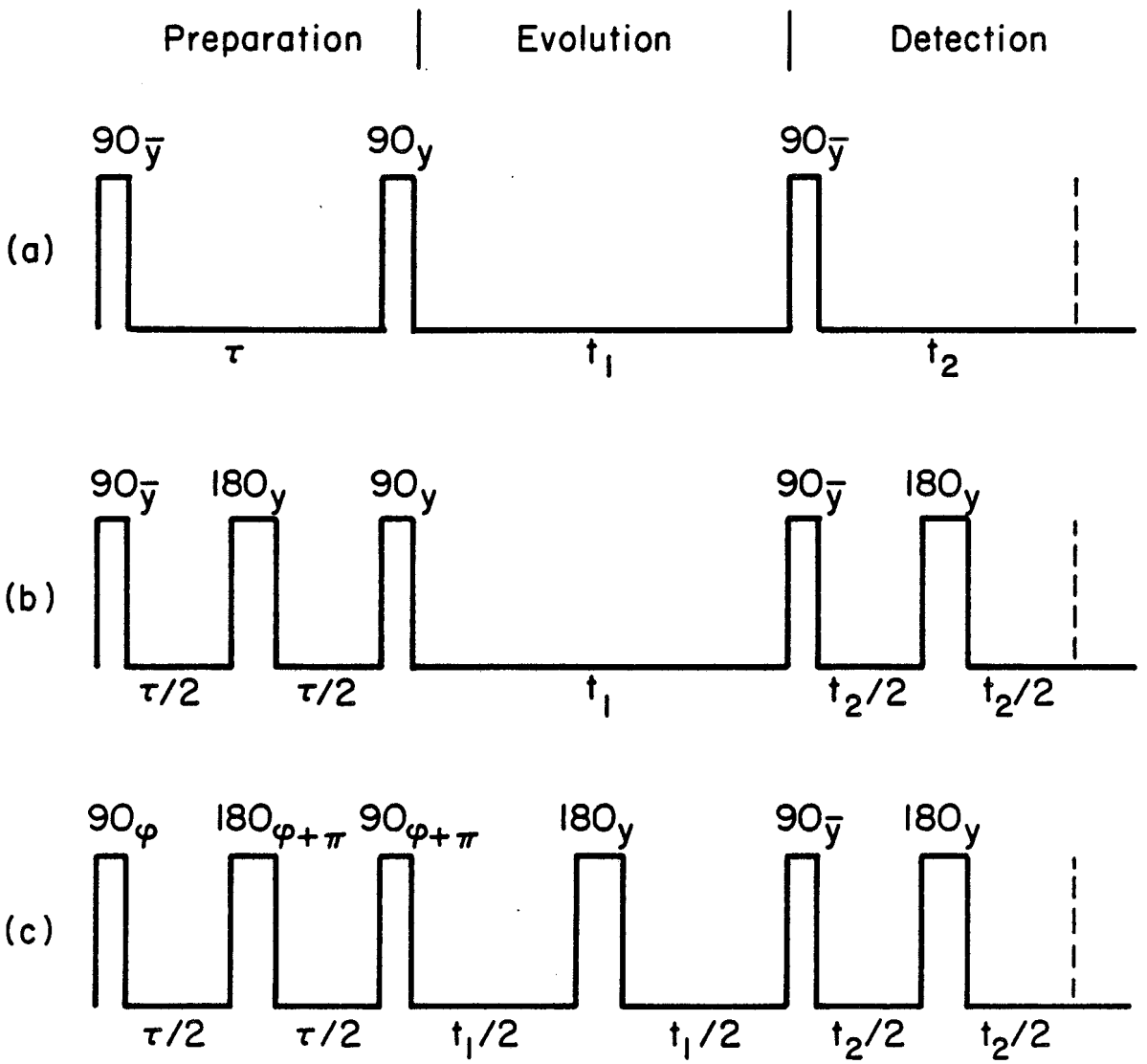

XBL 821-7589

Figure IV.4 (a) The simple three-pulse multiple-quantum sequence. (b) π pulses during the preparation and detection periods remove effects of the offset Hamiltonian, permitting even-odd selectivity for systems without chemical shift differences. (c) In this TPPI sequence, the incrementation of preparation pulse phase as t_1 is increased separates different MQ orders. No rf frequency offset is then needed during evolution; hence a π pulse can be added to eliminate inhomogeneous line broadening.

phase into a mixing period wherein MQ coherence is rotated back to SQ coherence and a subsequent detection period for the SQ signal. We won't make the distinction here.)

A few assumptions will simplify the analysis of this sequence. Unlike Chapter II, we will assume here that $\|\mathcal{H}_{rf}\| >> \|\mathcal{H}\|$, so that the internal Hamiltonian can be neglected during pulses. Each pulse can thereby be described in terms of a flip angle θ and an rf phase ϕ. We will deal almost exclusively with 90° flip angles. The first pulse will generally be chosen to be a $90\bar{y}$ pulse (ϕ = -90°), rotating βI_z, the initial equilibrium density matrix [$\beta = (\omega_0/kT)(2^{-N})$] to βI_x. Additionally, the rf detector in the rotating frame will be assumed to measure magnetization proportional to I_x. We will ignore relaxation effects since τ and t_2 are generally less than T_2 for the proton systems of interest. Finally, for simplicity we will often assume a perfectly homogeneous magnetic field.

Although three pulses are sufficient for the creation, evolution, and eventual detection of multiple-quantum coherence, more are often desirable. Indeed, the complexity of an MQ experiment is limited only by the imagination and obsession of the experimenter, the capabilities of his pulse programmer, the T_2 relaxation time of his molecule, and the susceptibility of his sample to rf heating. The most common modification, to be discussed in the next section, is the addition of two or three pi pulses to eliminate or reduce the effect of the offset Hamiltonian.

At the other extreme, selective excitation of a particular order of coherence may require thousands of pulses [55,102-104].

Before moving onward, it should be noted that the preparation and detection periods of the three-pulse experiment are closely related. This similarity is heightened by including an additional 90y pulse after the t_2 delay in Fig. IV.4(a) [40]. Detecting the signal proportional to I_x in the absence of this extra pulse is equivalent to monitoring $\langle I_z \rangle$ just after the pulse when it is present. In this scheme, the preparation sequence evolves I_z forward in time to MQ coherence; the modified detection sequence devolves I_z backward in time, also resulting in MQ coherence. Due to this preparation/detection symmetry, all the characteristics of "prepared density matrices" described in the next section apply equally well to "devolved detection matrices".

4.6 Properties of the Prepared Density Matrix

In analyzing the effect of pulses and delays on the density matrix of a spin system, there are two paths one can follow. The first is to consider the transformation caused by each pulse or delay in a step-by-step manner. This procedure has several computational advantages, especially when hard pulses are used: the only Hamiltonian which must be diagonalized is $\mathcal{H}_{int}$, which is easy to construct and (more importantly) block-diagonal in the spin-product basis.

A second technique, more convenient for manipulation of operators, is to work in terms of effective Hamiltonians.

Consider, for example, the preparation pulse sequence $90\bar{y}$-τ-$90y$ applied to a density matrix proportional to I_z. The propagator for this sequence is

$$U = \exp(i \frac{\pi}{2} I_y) \exp(-i\mathcal{H}\tau) \exp(-i \frac{\pi}{2} I_y) \quad . \tag{IV.22}$$

Rather than having the pulse propagators $\exp(\pm i \frac{\pi}{2} I_y)$ act on the density matrix, we can let them act on $\mathcal{H}$ instead to create an effective preparation Hamiltonian (see Appendix A):

$$\mathcal{H}_x \equiv \exp(i \frac{\pi}{2} I_y)\mathcal{H} \exp(-i \frac{\pi}{2} I_y) \tag{IV.23}$$

$$U = \exp(-i \mathcal{H}_x \tau) \quad . \tag{IV.24}$$

Rotation of $\mathcal{H}$ by 90 degrees about the y-axis, as in Eq. IV.23, converts I_{zj} to $-I_{xj}$ and I_{xj} to I_{zj}. Hence

$$\mathcal{H}_x = \sum_{j<k}^{N} D_{jk}[I_{xj}I_{xk} - \frac{1}{2}(I_{yj}I_{yk} + I_{zj}I_{zk})]$$

$$+ \sum_{j<k}^{N} J_{jk} \underset{\sim}{I}_j \cdot \underset{\sim}{I}_k + \sum_{j}^{N} \sigma_j I_{xj} + \Delta\omega I_x \quad . \tag{IV.25}$$

(The "x" subscript signifies that $\mathcal{H}_x$ is quantized along the x-axis and that $[\mathcal{H}_x, I_x] = 0$. Note that the scalar J-coupling term is unaffected by the rotation.) It is also convenient to lump all the bilinear operators of $\mathcal{H}_x$ into yet another Hamiltonian $\mathcal{H}_{xx}$:

$$\mathcal{H}_x = \mathcal{H}_{xx} + \sum_j^N \sigma_j \, I_{xj} + \Delta\omega \, I_x \tag{IV.26}$$

$$\mathcal{H}_{xx} = \sum_{j<k}^N D_{jk} \, [I_{xj} I_{xk} - \frac{1}{2} (I_{yj} I_{yk} + I_{zj} I_{zk})] + \mathcal{H}_J \tag{IV.27a}$$

$$= -\frac{1}{2} \mathcal{H}_{zz} + \sum_{j<k}^N \frac{3}{8} D_{jk} (I_{+j} I_{+k} + I_{-j} I_{-k}) + \mathcal{H}_J \quad , \tag{IV.27b}$$

where $\mathcal{H}_{zz}$ is the bilinear portion of the unrotated Hamiltonian.

The prepared density matrix P immediately following the sequence is given by

$$\beta P = U \, \beta \, I_z \, U^\dagger = \exp(-i \, \mathcal{H}_x \tau) \, \beta \, I_z \, \exp(i \, \mathcal{H}_x \tau) \quad . \tag{IV.28}$$

In general, $\mathcal{H}_x$ contains zero-quantum operators $(-\frac{1}{2} \mathcal{H}_{zz}, \mathcal{H}_J)$, one-quantum operators $(\Sigma_j \, \sigma_j \, I_{xj} + \Delta\omega \, I_x)$, and two-quantum operators $[\frac{3}{8} \Sigma_{j<k} \, D_{jk} \, (I_{+j} I_{+k} + I_{-j} I_{-k})]$. The complex exponential of $\mathcal{H}_x$ in Eq. IV.28 can therefore generate non-zero matrix elements P_{jk} corresponding to all multiple-quantum orders.

4.6.1 Even-Odd Selection

Consider now a system with no chemical shift differences. If $\Delta\omega = 0$, then

$$\beta P = \exp(-i \, \mathcal{H}_{xx} \tau) \beta \, I_z \, \exp(i \, \mathcal{H}_{xx} \tau) \quad . \tag{IV.29}$$

$\mathcal{H}_{xx}$ contains only zero- and two-quantum operators; thus the expansion of $\exp(-i\,\mathcal{H}_{xx}\tau) = \underset{\approx}{1} - i\,\mathcal{H}_{xx}\tau - \frac{1}{2}\mathcal{H}_{xx}^2\,\tau^2 + \ldots$ gives rise to only even-quantum terms. Since I_z itself is a zero-quantum operator, no odd-quantum coherence can ever be created in the prepared density matrix. Hence the sequence $90\bar{y}$-τ-90y is <u>even-quantum selective</u> when $\mathcal{H}_x = \mathcal{H}_{xx}$ [40].

Similarly, the sequence 90x-τ-90y will be <u>odd-quantum selective</u>. Note that this sequence applied to βI_z is equivalent to a $90\bar{y}$-τ-90y sequence acting on βI_y [40]. (In each case, the density matrix at τ=0 is βI_y.) The prepared density matrix can thus be written as follows:

$$P = \exp(-i\,\mathcal{H}_{xx}\tau)\beta\, I_y \exp(i\,\mathcal{H}_{xx}\tau)$$

$$= \beta\{\underset{\approx}{1} + i\tau[I_y,\mathcal{H}_{xx}] - \frac{1}{2}\tau^2[[I_y,\mathcal{H}_{xx}],\mathcal{H}_{xx}] + \ldots\} \quad . \qquad \text{(IV.30)}$$

Since the product of an odd-quantum operator (I_y) and an even-quantum operator ($\mathcal{H}_{xx}$) is an odd-quantum operator, only odd-quantum coherence will be created in P.

The requirement that $\Delta\omega$ be zero can be met by adding a pi pulse (θ = 180°) of any phase to the middle of the preparation period [40], as in Fig. IV.4(b). (This is entirely analogous to the use of the familiar Hahn spin echo [105] for removing the effect of magnet inhomogeneity in conventional FT NMR.) Consider, for

example, the even-selective experiment. If the phase of the pi pulse is chosen to be zero, then the augmented preparation sequence is $90\bar{y} - \tau/2 - 180x - \tau/2 - 90y$. Since the first pulse rotates I_z to I_x, this sequence is equivalent to $90\bar{y} - \{180\bar{x} - \tau/2 - 180x\} - \tau/2 - 90y$. (The extra $180\bar{x}$ pulse does nothing to I_x.) Within the brackets, the pi pulses have no effect on $\mathcal{H}_{zz}$, the bilinear part of the Hamiltonian, but reverse the sign of $\mathcal{H}_{off}$. The preparation propagator is therefore

$$U = \exp(i \frac{\pi}{2} I_y) \exp[- \frac{i}{2} (\mathcal{H}_{zz} - \mathcal{H}_{off})\tau] \exp[- \frac{i}{2} (\mathcal{H}_{zz} + \mathcal{H}_{off})\tau] \cdot \exp(-i \frac{\pi}{2} I_y) \quad . \qquad \text{(IV.31)}$$

Since $[\mathcal{H}_{zz}, \mathcal{H}_{off}] = 0$, exponentials involving these operators can be separated and

$$U = \exp(i \frac{\pi}{2} I_y) \exp(-i \mathcal{H}_{zz} \tau) \exp(-i \frac{\pi}{2} I_y) = \exp(-i \mathcal{H}_{xx} \tau) \quad . \qquad \text{(IV.32)}$$

Changing the phase of the pi pulse merely adds a phase factor to U.

When $\Delta\omega \neq 0$, the prepared density matrix of a "shiftless" system oscillates between even- and odd-quantum selectivity. The propagator U can be divided into bilinear and offset exponentials because $[\mathcal{H}_{xx}, I_x] = 0$. Hence

$$\beta P = \exp(-i\,\mathcal{H}_x\tau)\beta\, I_z \exp(i\,\mathcal{H}_x\,\tau) \tag{IV.33a}$$

$$= \exp(-i\,\mathcal{H}_{xx}\tau)\,\exp(-i\Delta\omega\, I_x\tau)\beta\, I_z \exp(i\Delta\omega\, I_x\tau)\,\exp(i\,\mathcal{H}_{xx}\tau) \tag{IV.33b}$$

$$= \cos\Delta\omega\tau\,\exp(-i\,\mathcal{H}_{xx}\tau)\beta\, I_z \exp(i\,\mathcal{H}_{xx}\tau)$$

$$- \sin\Delta\omega\tau\,\exp(-i\,\mathcal{H}_{xx}\tau)\beta\, I_y \exp(i\,\mathcal{H}_{xx}\tau) \quad , \tag{IV.33c}$$

where the first term in Eq. IV.33c is even-selective and the second is odd-selective. Ideally, the value of τ could be adjusted to select one or the other. However, magnet homogeneity is usually not good enough to make this a practical technique--different regions of the sample experience different $\Delta\omega$ values, destroying the even/odd separation [106].

The even-odd effect is the simplest example of selective excitation, the funneling of spectral intensity into a certain MQ order or orders [55,102-104]. For success, the pulses at the beginning and the end of the preparation period must have a flip angle θ=90° and the appropriate relative phase. Moreover, the Hamiltonian must be made purely bilinear. When there are no chemical shift differences, this condition is easily met by adding an echoing pi pulse; when $\mathcal{H}_{cs} \neq 0$, a Carr-Purcell [107] train of closely and evenly spaced pi pulses will yield a purely bilinear zero-order <u>average</u> Hamiltonian $\bar{\mathcal{H}}^{(0)}$ [24]. Unwanted correction terms $\bar{\mathcal{H}}^{(2)}$,

$\bar{\mathcal{H}}^{(4)}$, etc., are smallest when the time between pulses shrinks toward zero.

4.6.2 Rotation About I_z: The Ways of Phase

Consider changing the rf phase of all pulses in the preparation sequence by an angle ϕ. This corresponds to rotation about the z-axis of the associated pulse propagators; for example, if a $90_{\bar{y}}$ pulse is converted to a $90_{-y+\phi}$ pulse, then $\exp(-i\,\frac{\pi}{2}\,I_y)$ becomes $\exp[-i\,\frac{\pi}{2}\,(\cos\phi\,I_y - \sin\phi\,I_x)]$ or $\exp(-i\,\phi\,I_z)\,\exp(-i\,\frac{\pi}{2}\,I_y)\,\exp(i\,\phi\,I_z)$. In contrast, a term like $\exp(-i\,\mathcal{H}\,\tau)$ is unaltered by a z-axis rotation, since $[\mathcal{H},I_z] = 0$. A change in phase of all preparation pulses is therefore equivalent to a rotation about $\hat{z}$ of every exponential factor in the preparation propagator, which in turn is equivalent to a rotation of the propagator itself:

$$U'\ (\text{new phases}) = \exp(-i\,\phi\,I_z)\,U\,\exp(i\,\phi\,I_z) \quad . \qquad \text{(IV.34a)}$$

The effect on the density matrix is also a rotation:

$$\begin{aligned}\beta P'\ (\text{new phases}) &= (e^{-i\phi I_z}\,U\,e^{i\phi I_z})\beta\,I_z(e^{-i\phi I_z}\,U^{\dagger}\,e^{i\phi I_z}) \\ &= e^{-i\phi I_z}\,U\,\beta\,I_z\,U^{\dagger}\,e^{i\phi I_z} \\ &= e^{-i\phi I_z}\,\beta P\,e^{i\phi I_z} \quad . \qquad \text{(IV.34b)}\end{aligned}$$

In terms of a single element,

$$P'_{jk} = (e^{-i\phi I_z} P e^{i\phi I_z})_{jk}$$

$$= e^{-iM_j\phi} P_{jk} e^{iM_k\phi}$$

$$= e^{-i\Delta M\phi} P_{jk} \quad . \qquad \text{(IV.35)}$$

Thus a change in pulse phases by an angle ϕ produces a change in the phase of prepared ΔM-quantum coherence by an angle $\Delta M\phi$ [40,108,109]. This simple relationship is fraught with useful consequences for the separation or selective excitation of multiple-quantum orders.

4.6.3 Spin-Inversion States

It is of interest to investigate the effect of a spin-inversion operator [110] on the prepared density matrix βP. Define Π as $\exp(-i\ \pi\ I_x)$, the propagator for a 180x pulse. I_x commutes with $\mathcal{H}_x$, so

$$\Pi^\dagger P \Pi = e^{-i\mathcal{H}_x\tau} \Pi^\dagger I_z \Pi e^{i\mathcal{H}_x\tau}$$

$$= e^{-i\mathcal{H}_x\tau} (-I_z) e^{i\mathcal{H}_x\tau}$$

$$= -P \quad . \qquad \text{(IV.36)}$$

In terms of a single matrix element,

$$P_{jk} = \langle\psi_j|P|\psi_k\rangle = -\langle\psi_j|\ \Pi^\dagger P\Pi|\psi_k\rangle = -\langle\Pi\psi_j|P|\Pi\psi_k\rangle \qquad \text{(IV.37)}$$

In certain cases, $|\Pi\ \psi_k\rangle$ will itself be an eigenstate $|\psi_{\bar{k}}\rangle$ of $\mathcal{H}$. Three such cases are as follows:

1) When the internal Hamiltonian is purely bilinear ($\mathcal{H} = \mathcal{H}_D + \mathcal{H}_J$), it commutes with Π. For all ψ_k,

$$\mathcal{H}(\Pi\ \psi_k) = E_k(\Pi\ \psi_k) \quad . \tag{IV.38}$$

2) For <u>any</u> Hamiltonian, the effect of Π on the lone $M = N/2$ eigenstate $|+ + + \ldots +\rangle$ is to flip all the spins, creating the lone $M = -N/2$ eigenstate $|- - - \ldots -\rangle$.

3) Computer calculations suggest that if the highest possible MQ coherence order attainable in any given representation is composed of only one transition or one set of degenerate transitions, then that transition (or set of transitions) connects spin-inversion states.

Some examples will make this third statement clearer. In Table IV.2, two 6-spin systems are compared as to the separation of eigenstates by M value and representation. In the A_3B_2C system with D_{3h} permutation symmetry, there are four types of spin-inversion states: two A_1' states with $M = \pm 3$, two A_2'' states with $M = \pm 2$, four E' states with $M = \pm 2$, and four E'' states with $M = \pm 1$. In contrast, for the $AA'A''A'''BB'$ system with D_2 symmetry, there are only three spin-inversion pairs: two A_1 states with $M = \pm 3$, two B_2 states with $M = \pm 2$, and two B_3 states with $M = \pm 2$. The non-degenerate pair of $M = 2$ B_1 states are not related by spin inversion to the corresponding $M = -2$ states.

Table IV.2

Symmetry States for 6-Spin Systems

a) An A_3B_2C system with D_{3h} permutation symmetry (e.g., CH_3CH_2OH)

	Number of states in each representation			
M	A_1'	A_2''	E'	E''
3	1			
2	3	1	2x1	
1	5	2	2x3	2x1
0	6	2	2x4	2x2
-1	5	2	2x3	2x1
-2	3	1	2x1	
-3	1			
total:	24	8	24	8

b) An AA'A"A"'BB' system with D_2 symmetry (e.g., $CBr_3CH_2CH_2CH_2CBr_3$)

	Number of states in each representation			
M	A_1	B_1	B_2	B_3
3	1			
2	2	2	1	1
1	6	3	3	3
0	6	6	4	4
-1	6	3	3	3
-2	2	2	1	1
-3	1			
total:	24	16	12	12

Spin-inversion transitions have a number of interesting properties. First of all, the frequency of such a transition is independent of any bilinear term in the Hamiltonian. This can be readily shown if we first note that

$$\Pi^{\dagger} \mathcal{H}_D \Pi = \mathcal{H}_D \tag{IV.39a}$$

$$\Pi^{\dagger} \mathcal{H}_J \Pi = \mathcal{H}_J \tag{IV.39b}$$

but

$$\Pi^{\dagger} \mathcal{H}_{cs} \Pi = -\mathcal{H}_{cs} \tag{IV.39c}$$

$$\Pi^{\dagger} \mathcal{H}_{off} \Pi = -\mathcal{H}_{off} \quad . \tag{IV.39d}$$

Hence

$$\begin{aligned}
\omega_{\bar{k}k} = E_{\bar{k}} - E_k &= \langle\bar{k}|\mathcal{H}|\bar{k}\rangle - \langle k|\mathcal{H}|k\rangle \\
&= \langle\Pi k|\mathcal{H}|\Pi k\rangle - \langle k|\mathcal{H}|k\rangle \\
&= \langle k|\Pi^{\dagger}\mathcal{H}\Pi|k\rangle - \langle k|\mathcal{H}|k\rangle \\
&= \langle k|\Pi^{\dagger}\mathcal{H}\Pi - \mathcal{H}|k\rangle \\
&= -2\langle k|\mathcal{H}_{cs}+\mathcal{H}_{off}|k\rangle \quad .
\end{aligned} \tag{IV.40}$$

If $|k\rangle$ and $|\bar{k}\rangle$ refer to extreme states $|+++..,+\rangle$ and $|---,..-\rangle$, and if $\mathcal{H}_{cs}$ is chosen such that the sum of all shifts is zero, then $\omega_{\bar{k}k}$ is merely N $\Delta\omega$. For any nematic-phase system, therefore, the N-quantum transition frequency provides no information on the internal Hamiltonian. (The N-quantum line from a powdered solid sample will broaden into a chemical shielding tensor lineshape, however [111].)

In a system with no chemical shift differences, each transition $|k\rangle$ to $|\bar{k}\rangle$ occurs with frequency $(M_k - M_{\bar{k}})\Delta\omega$, simply a multiple of the effective rf offset. For N spins, these spin-inversion transitions lie at the center of the (N-2n)-quantum spectra (n = 0,1,2...) and again provide no information on $\mathcal{H}_{int}$. For "shiftless" systems, the spectrum of each MQ order is symmetric about its center at $\Delta M\Delta\omega$, since $(\omega_{jk} - \Delta M\Delta\omega) = -(\omega_{\bar{k}\bar{j}} - \Delta M\Delta\omega)$.

A second property of spin-inversion transitions concerns the phase of the prepared density matrix element $P_{k\bar{k}}$ following a $90\bar{y} - \tau - 90y$ or $90x - \tau - 90y$ sequence. From Eq. IV.37, if spin-inversion pairs exist, then $P_{jk} = -P_{\bar{j}\bar{k}}$. In particular, for a spin-inversion transition $|k\rangle$ to $|\bar{k}\rangle$, $P_{k\bar{k}} = -P_{\bar{k}k}$. Since P is Hermitian, $P_{k\bar{k}}$ must always be purely imaginary, no matter what the value of τ. In any system, therefore, statement (2) above implies that the highest-quantum coherence is quantized along one axis of the complex plane. In systems without chemical shift differences, each eigenstate with $M \neq 0$ belongs to a spin-inversion pair, so the number of coherences restricted to one axis is

$\frac{1}{2}\,[2^N]$ for N odd,

$\frac{1}{2}\,[2^N - \binom{N}{N/2}]$ for N even.

It will be shown in the next chapter that the intensity and phase of a transition $|j\rangle$ to $|k\rangle$ in a three-pulse $t_2=\tau$ experiment are given by $[P_{jk}(\tau)]^2$. P_{jk} is in general a complex number, so as τ varies, the phase of P_{jk} varies also. In contrast, $[P_{k\bar{k}}(\tau)]^2$ is <u>always</u> a real negative number for any value of τ. The transition $|k\rangle$ to $|\bar{k}\rangle$ is, in the words of Dan Weitekamp, a "line of resolute phase." [106].

Such resolute behavior is useful in the determination of chemical shielding tensors from N-quantum transitions in powdered samples. For a molecule of solid benzene, at a temperature characterized by rapid rotation about its six-fold axis, both the intramolecular dipolar couplings and the chemical shift relative to its isotropic value are proportional to $\xi = (3\cos^2\theta - 1)$, where θ is the angle between the six-fold axis and the magnetic field (see sections 1.5.3 and 1.5.5). If the small J-couplings are ignored, then for any value of θ,

$$\mathcal{H}(\theta) = \xi(\theta)\,\mathcal{H}_c \quad , \tag{IV.41}$$

where $\mathcal{H}_c$ is a "characteristic" Hamiltonian. Each propagator $U = \exp[-i\,\mathcal{H}(\theta)t]$ can thus be written as $U = \exp\{-i\,\mathcal{H}_c[\xi(\theta)t]\}$.

That is, changing the orientation of a benzene molecule is equivalent to scaling the preparation (or evolution or detection) time, but because the six-quantum benzene transition entails spin inversion, its phase is unaffected by this time scaling. Hence the entire six-quantum chemical shielding lineshape will appear with the same phase--no cancellation of intensity occurs.

Spin-inversion properties also give rise to additional selection rules for zero-quantum transitions between M = 0 states when N is even and $\mathcal{H}$ contains no chemical shift differences. Then eigenstates of $\mathcal{H}$ and I_z can be chosen to be eigenstates of Π as well, with eigenvalues of +1 (gerade) or -1 (ungerade) [112]. Since $\langle\psi_j|P|\psi_k\rangle = -\langle\Pi\,\psi_j|P|\Pi\,\psi_k\rangle$, transitions between M = 0 states with the same eigenvalue of Π are forbidden.

4.6.4 A Note on Degeneracy

Degeneracy is claimed to have caused the downfall of the Roman empire, and it is somewhat of a problem here too in the analysis of multiple-quantum experiments. Consider a doubly-degenerate E representation. The computer has no difficulty generating the requisite eigenstates, but their specific form is arbitrary within the constraint of orthonormality. (If ψ_{a1} and ψ_{a2} are degenerate eigenstates, then for any value of χ, $\psi_{a3} = \cos\chi\ \psi_{a1} + \sin\chi\ \psi_{a2}$ and $\psi_{a4} = -\sin\chi\ \psi_{a1} + \cos\chi\ \psi_{a2}$ are also eigenstates.) If ψ_{a1}, ψ_{a2} and ψ_{b1}, ψ_{b2} are two different sets of degenerate states, then in general all prepared density matrix elements $P_{a1,b1}$, $P_{a1,b2}$, $P_{a2,b1}$, and $P_{a2,b2}$ will be non-zero. However, using appropriate

linear combinations, these states can be chosen such that $P_{a1,b2} = P_{a2,b1} = 0$ [98]. (This separation generally entails the use of complex numbers in the eigenfunction expansions, and so is not actually attempted in subsequent calculations.) Nonetheless, we will count two (not one or four) distinct though degenerate transitions between the pairs of states, as if an E manifold of 2n states were in fact two separate, identical, non-degenerate manifolds of n states each. (Analogous relationships hold in the case of a triply-degenerate representation.)

It is not immediately apparent whether the combined intensity for the two transitions mentioned above in a $t_2=\tau$ three-pulse experiment should be $|(P_{a1,b1})^2 + (P_{a1,b2})^2 + (P_{a2,b1})^2 + (P_{a2,b2})^2|$ or $|P_{a1'b1}|^2 + |P_{a1,b2}|^2 + |P_{a2,b1}|^2 + |P_{a2,b2}|^2$. Fortunately, each $(P_{ai,bj})^2$ term has the same complex phase, so the sums are equal.

4.7 Separation of Multiple-Quantum Orders

The spectral simplicity resulting from excitation of high-quantum coherences is for naught if these lines appear amidst a tangled thicket of single-quantum transitions (one of the unavoidable drawbacks of cw multiple-quantum experiments). Fortunately, there exist a variety of techniques for cleanly separating different orders in pulsed MQ spectra. Each in some way depends on the fundamental relationship between the phase of MQ coherence and rotation about the z-axis:

$$[e^{-i\phi I_z} P e^{i\phi I_z}]_{jk} = e^{i(M_k-M_j)\phi} P_{jk} \quad . \qquad \text{(IV.42)}$$

4.7.1 A Frequency Offset

The easiest way to separate MQ orders is merely to go off-resonance with the rf irradiation. Recall that our Hamiltonian is the sum of two commuting terms, $\mathcal{H}_{int}$ and $\mathcal{H}_{off}$. The eigenfunctions of $\mathcal{H}$ are determined entirely by the internal Hamiltonian; the effect of $\mathcal{H}_{off}$ is merely to shift the energy of each state $|j\rangle$ by an amount $-M_j\Delta\omega$. The frequency of each transition $|j\rangle$ to $|k\rangle$ is thus augmented by $(M_j-M_k)\Delta\omega = (\Delta M)(\Delta\omega)$. When $\Delta\omega$ is greater than the splittings due to $\mathcal{H}_{int}$, different multiple-quantum orders will not overlap.

Unfortunately, the effects of magnet inhomogeneity also scale with the value of ΔM. This can be seen by rewriting $\mathcal{H}_{off}$ to take account of the variation in $\omega-\omega_0$ from region to region in the sample:

$$\mathcal{H}_{off} = -\sum_i \Delta\omega_i(\underset{\sim}{r})\, I_z \quad . \tag{IV.43}$$

If the spread in frequencies is characterized by some full width at half-height ω^*, then the inhomogeneous contribution to the linewidth of a ΔM-quantum transition is $(\Delta M)(\omega^*)$. The resolution and effective intensity of high-quantum transitions are of course reduced by this broadening. Zero-quantum lines, however, are unaffected and remain sharp in even the worst of magnets [108].

To eliminate inhomogeneous broadening of MQ transitions in systems without chemical shifts, an echoing pi pulse can be added to the middle of the <u>evolution</u> period to reverse the sign of $\mathcal{H}_{off}$ but leave $\mathcal{H}_J$ and $\mathcal{H}_D$ unaffected. (Compare with section 4.6.1.

For systems with chemical shifts, a Carr-Purcell train of pi pulses can be used to remove $\mathcal{H}_{cs}$ and $\mathcal{H}_{off}$ from the zero-order average evolution Hamiltonian.) Alas, the added pulse or pulse train gets rid of not only the spread in offset frequencies but the average value as well--hence, no separation of orders. With the following more involved techniques, however, one can retain the Hahn echo during evolution and still avoid the painful swelling of spectral overlap.

4.7.2 Phase Fourier Transforms

As stated in section 4.6.2, changing all the pulse phases in the preparation sequence has a characteristic effect on the phase of multiple-quantum coherence: pulse phase shifts are multiplied by the value of ΔM. A particular multiple-quantum order or orders can be selected, therefore, by taking linear combinations of the appropriate phase-shifted spectra [40,108]. As an example, consider these four MQ spectra of a 4-spin system:

		Relative coherence phases				
Spectrum	Pulse phase shift	0Q	1Q	2Q	3Q	4Q
A	0°	0°	0°	0°	0°	0°
B	90°	0°	90°	180°	270°	0°
C	180°	0°	180°	0°	180°	0°
D	270°	0°	270°	180°	90°	0°

The prescription for generating only three-quantum transitions is to combine spectra A through D as follows: A-C + i(B-D). For two

quantum transitions, one can add spectra A and C, then subtract the sum of B and D.

4.7.3 Frequency Adjustment to Separate Orders

With a pi pulse added to the evolution period, the offset Hamiltonian is effectively $\mathcal{H}_{off} = -\sum \Delta\omega_i(\underset{\sim}{r})\ I_z$ before the pulse and $-\mathcal{H}_{off}$ afterwards. When the evolution propagator U_E is calculated, these terms cancel--no broadening, but also no separation. If, however, $\mathcal{H}_{off}$ were augmented by an additional spatially homogeneous term $-2\Delta\omega'\ I_z$ for the first half of the evolution period, then the propagator would be

$$U_E = \exp[-\tfrac{i}{2}\ (\mathcal{H}_{int}-\mathcal{H}_{off})t_1]\ \exp[-\tfrac{i}{2}\ (\mathcal{H}_{int}+\mathcal{H}_{off} - 2\Delta\omega' I_z)t_1]$$

$$= \exp[-i(\mathcal{H}_{int}-\Delta\omega' I_z)t_1] \quad . \qquad \text{(IV.44)}$$

If large enough, the additional offset would provide the necessary separation of orders.

One means of changing the offset Hamiltonian in this manner is to change the rf frequency. Specifically, switch the frequency from ω to $\omega + 2\Delta\omega'$ immediately after the preparation period, then switch it back before the pi pulse in evolution. This Frequency Adjustment to Separate Orders (FATSO) technique is illustrated schematically in Fig. IV.5. In (a), at the start of the evolution period, multiple-quantum coherences have not yet been affected by inhomogeneities in H_0. In (b) and (c), the prepared coherences then evolve under the influence of $\mathcal{H}_{int}$ (not depicted) and $\mathcal{H}_{off}$,

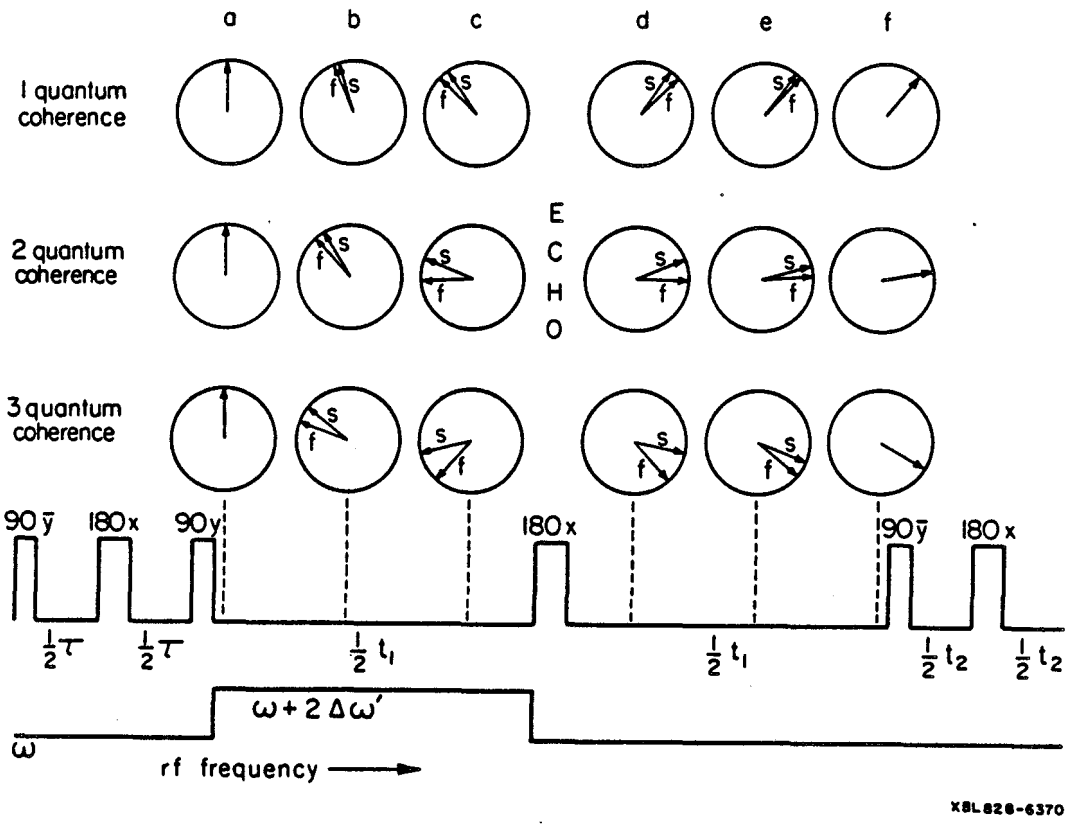

Figure IV.5 A spin-vector dramatization of the FATSO technique. For each MQ order, the pi pulse during the evolution period removes the spread in slow (s) and fast (f) frequencies resulting from inhomogeneity in the magnetic field H_o. The shift in rf frequency, however, enables each order to evolve with an effective offset (ΔM) ($\Delta\omega'$). See the text for more details.

the sum of inhomogeneous terms and the additional quantity $-2\Delta\omega' I_z$ due to the rf offset. Vectors marked "s" and "f" are meant to suggest "slow" and "fast" rotation in the x-y plane caused by spatial variation in the static field; the spread of these vectors is proportional to both ΔM and the evolution time. The pi pulse then flips the spin "pancake" [20], reversing the relative positions of vectors "s" and "f". In (d) and (e), the special frequency offset is removed, but the H_0 inhomogeneity remains, now refocusing spin vectors. Finally in (f), at the end of the evolution period, each order of MQ coherence has echoed, but at a different relative phase that depends on the value of t_1. As t_1 is varied, each echoed coherence rotates in the x-y plane at a frequency $(\Delta M)(\Delta\omega')$.

The reader may wonder how the spin system "knows" what the rf frequency is when pulses are not being applied. How can each MQ order march to the beat of its own drummer if the music isn't playing? For the answer, we must realize that the spectrometer's frequency synthesizer (with accompanying mixers, doublers, etc.) is more than just a source of megahertz radiation; the phase of its rf output, whether amplified into a pulse or left alone, defines the x and y axes of the rotating frame. To see the effect of a frequency shift (and to avoid getting dizzy), let's observe from a reference system spinning at frequency ω. From this vantage point, the rf-defined x and y axes are motionless during the preparation period, but are seen to rotate when the

rf frequency is changed. When the frequency returns to its original value of ω after a time $\frac{1}{2}t_1$, the axes once more stand still; how far they have traveled depends on the product of $\frac{1}{2}t_1$ and the frequency jump $2\Delta\omega'$. The spins learn of this axis rotation when subsequent pulses are applied: the x-axis defined for evolution and detection pulses is not the same as the x-axis defined during the preparation period. The change in rf frequency is thus manifested as a change in relative pulse phase.

Clearly, this procedure requires a synthesizer which can be externally triggered to switch frequencies in a phase-coherent manner; i.e., the rf phase must remain continuous when the frequency is shifted. Otherwise, the rotating frame axes would jump unpredictably each time ω is changed, totally scrambling the evolution.

4.7.4 Time-Proportional Phase Incrementation

FATSO was never tried in the Pines lab for two reasons: (1) We lacked the necessary frequency-jump synthesizer and (2) an equivalent technique which was somewhat more general and easier to implement was soon developed. As noted above, the effect of shifting the rf frequency is to change the phase of the preparation pulses relative to the rest of the pulse sequence by an amount proportional to the value of t_1. (As t_1 increases, the two frequencies grow more and more out of phase.) Thus we can adjust the pulse phases directly instead of playing with the frequency. In the Time-Proportional Phase Incrementation (TPPI) technique

[109] (discovered independently by Bodenhausen, et al. [16]), a digital phase-shifter is used to increment the preparation pulse phases by an angle ϕ for each value of t_1 in the multiple-quantum experiment. This sequence is displayed in Fig. IV.4(c).

The angle ϕ equals $(\Delta\omega)(\Delta t_1)$, where $\Delta\omega$ is the effective TPPI offset frequency and Δt_1 is the increment in the evolution time. The evolved density matrix at a time $t_{1n} = n\,\Delta t_1$ (i.e., the density matrix for the nth point in the MQ FID) is given by

$$\begin{aligned}\rho(t_{1n}) &= \exp(-i\mathcal{H}_{int}\, t_{1n})\, \exp(-in\phi I_z)\beta P \\ &\qquad \cdot \exp(in\phi I_z)\, \exp(i\mathcal{H}_{int}\, t_{1n}) \\ &= \exp(-i\mathcal{H}_{int}\, t_{1n})\, \exp(-in\Delta\omega\Delta t_1\, I_z)\beta P \\ &\qquad \cdot \exp(in\Delta\omega\Delta t_1\, I_z)\, \exp(i\mathcal{H}_{int}\, t_{1n}) \\ &= \exp[-i(\mathcal{H}_{int}+\Delta\omega I_z)t_{1n}]\beta P\, \exp[i(\mathcal{H}_{int}+\Delta\omega I_z)t_{1n}]. \qquad \text{(IV.45)}\end{aligned}$$

demonstrating the equivalence of a time-proportional phase shift to an artificial offset frequency. A useful relationship for an N-spin system: if ϕ is chosen to be 180/N degrees, then the N-quantum line will sit at the Nyquist frequency [11,113] $\nu_{Nyq} = (2\,\Delta\, t_1)^{-1}$.

4.7.5 Coherence Transfer Echoes

For the most useful version of this technique [58,114,115], the pulse sequence can be written as follows:

Preparation: $90\bar{y} - \frac{1}{2}\tau - 180x - \frac{1}{2}\tau - 90y$

Evolution: $\frac{1}{2}t_1 - 180x - \frac{1}{2}t_1$

Detection: $T - 90y - t_2$.

By the start of the detection period, multiple-quantum coherences have been excited and allowed to evolve in what is effectively a homogeneous magnetic field. They then dephase for a fixed time T without benefit of pi pulses; the rate of dephasing is once again proportional to ΔM. Next the detection pulse rotates these MQ coherences back to single-quantum coherences, which can rephase in the same inhomogeneous field at a rate proportional to $\Delta M=1$. A coherence transfer echo thus occurs for each non-zero order at $t_2 = \Delta MT$. By sampling at $t_2 = \Delta MT$, only that signal transferred from ΔM-quantum coherence will be appreciably detected. Coherence transfer echoes can be combined with TPPI to eliminate the dynamic range problem associated with detecting all MQ orders at the same point [58,106].

4.8 Meet the Molecules

As a breather from the numbing details of density matrix manipulation, a whiff of chemistry seems in order--specifically, an introduction to three molecules which have served as model systems in the Pines lab for both experimental and computational studies of MQ NMR. Each will be used illustratively in the next chapter on intensity calculations.

4.8.1 Benzene

Benzene was the very first solute molecule to be analyzed in nematic phase using conventional NMR, by Saupe and Englert in 1963 [90]. It is only fitting that benzene has since become the archetype, the consummate model system, for multiple-quantum studies as well [40,101,102,116].

The benzene molecule itself can be described in terms of D_{6h} symmetry, but since reflection in the horizontal mirror plane σ_h has no effect on the position of nuclei, the spin permutation group is D_6 or C_{6v}. (The g and u subscripts associated with the irreducible representations of D_{6h} are useful in labeling the spin-inversion properties of the M=0 eigenstates, however.) In isotropic phase, benzene is an A_6 system; all protons have the same chemical shift, and J-couplings between these magnetically-equivalent nuclei do not perturb the one-line SQ spectrum [117]. In nematic phase, however, the three different dipolar couplings--D_{ortho}, D_{meta}, and D_{para}--make benzene an AA'A"A"'A""A""' spin system with 38 distinct pairs of lines in its single-quantum spectrum [112].

The breakdown of eigenstates by magnetic quantum number and symmetry manifold is displayed in Fig. IV.6--there are 13 A_1 states, 1 A_2 state, 7 B_1 states, 3 B_2 states, 2x9 E_1 states, and 2x11 E_2 states. Because there are no chemical shift differences, each state with $M \neq 0$ belongs to a spin-inversion pair, and M=0 states are g or u eigenfunctions of the spin-inversion operator Π. A typical benzene multiple-quantum spectrum is shown in

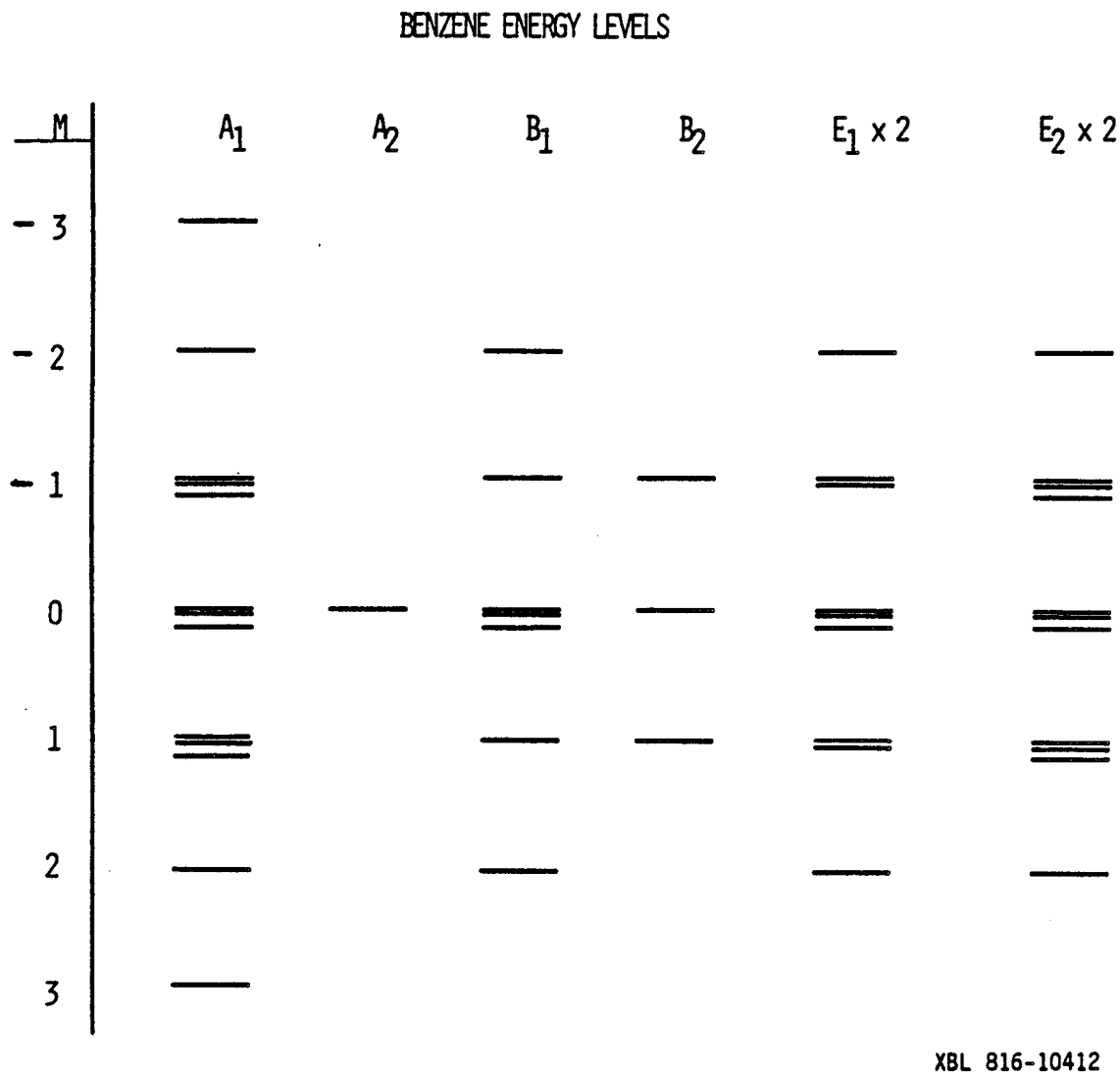

Figure IV.6 The eigenstates of oriented benzene, divided according to M value and irreducible representation. The E_1 and E_2 representations are two-dimensional: each energy level is doubly degenerate.

Fig. IV.7, courtesy of Warren Warren. Because chemical shifts are absent, each MQ order is symmetric about a central frequency $(\Delta M)(\Delta\omega)$.

Saupe [112] long ago worked out all the symmetrized basis functions for benzene and also calculated the conventional single-quantum transition frequencies and intensities. For 11 states (or pairs of states) with $M \geq 0$, the symmetrized functions are themselves eigenfunctions of $\mathcal{H}$; their energies can thus be given exactly as multiples of the coupling constants J_{12}, J_{13}, J_{14}, D_{12}, D_{13}, and D_{14}. To treat the remaining states, Saupe assumed a ratio of dipolar couplings appropriate for a hexagonal molecule and included the small J-couplings only to first order in a perturbation expansion.

Four of the "exact" transition frequencies, $|A_1(M=3)\rangle \leftrightarrow |A_1(M=\pm 2)\rangle$, $|B_1(M=2)\rangle \leftrightarrow |B_1(M=\pm 1)\rangle$, $|B_2(M=1)\rangle \leftrightarrow |B_2(M=0)\rangle$, and $|E_{2u}(M=2)\rangle \leftrightarrow |E_{2u}(M=0)\rangle$, are independent of J_{jk} values and can be used to solve for the three unique dipolar couplings. Using linear combinations of these frequencies from his experimental spectrum, Saupe found D_{12}, D_{13}, and D_{14} to be very nearly in the ratio expected for a perfect hexagon of protons:

$$D_{12} : D_{13} : D_{14} = 1 : \frac{1}{3\sqrt{3}} : \frac{1}{8} \quad . \qquad \text{(IV.46)}$$

More recently, Diehl <u>et al.</u> [118] have analyzed benzene in a number of nematic solvents to prodigious lengths with SQ NMR. Correcting for the small difference between $\langle r_{jk}^3 \rangle$ and $\langle r_{jk} \rangle^3$, they find deviations in coupling constant ratios from "hexagonality"

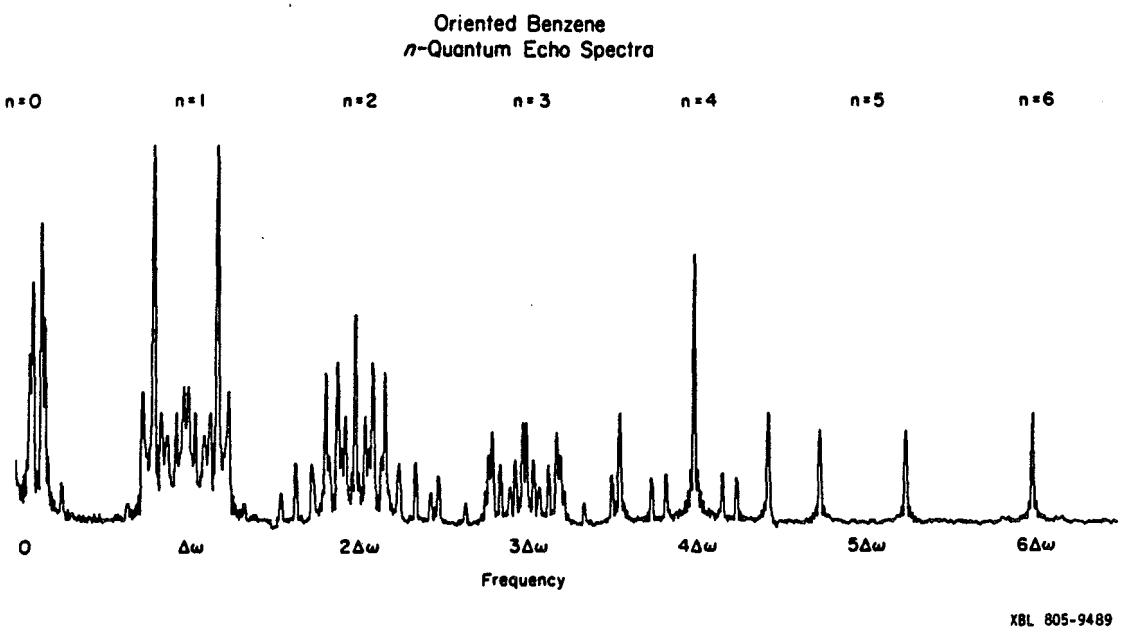

Figure IV.7 The TPPI multiple-quantum spectrum of benzene, oriented in Eastman nematic liquid crystal #15320. This spectrum, obtained by Warren Warren, is an average over four values of $\tau = t_2$ (4, 6, 8 and 10 msec).

of ∿ 0.05% to ∿ 0.45%, depending on the coupling constant and the solvent in use. This slight distortion apparently results from solute-solvent interaction.

The existence of a C_6 axis of symmetry in benzene implies that only one order parameter, S_{zz}, is needed to characterize the degree of orientational anisotropy. The three dipolar couplings are thus proportional to S_{zz}; from Eq. IV.15 with $\theta_{zc} = 90°$,

$$D_{jk}(\mathrm{Hz}) = \frac{\hbar\,\gamma^2}{2\pi\langle r_{jk}^3\rangle}\; S_{zz} \quad . \tag{IV.47}$$

S_{zz} itself is a function of the liquid crystal in use, the concentration of benzene, and the temperature. For some typical numbers, I found D_{12} to be -817.06 Hz in Eastman nematic solvent #15320 at 25°C, measured using the J-free A_1 single-quantum transition frequency mentioned above. "Hexagon" values of D_{13} and D_{14} (-157.25 Hz and -102.13 Hz respectively) were sufficient to simulate the spectrum. With $\langle r_{12}^3\rangle^{1/3} \approx \langle r_{12}\rangle = 2.477$ Å [118], the corresponding value of S_{zz} is -0.103. The negative sign implies that the benzene C_6 axis is much more likely to be pointing perpendicular to the magnetic field than parallel with it.

The indirect spin-spin coupling constants that have been used in benzene spectral simulations are the isotropic values [112,118]. Different authors report slightly different numbers;

from these I chose J_{12} = 7.5 Hz, J_{13} = 1.4 Hz, and J_{14} = 0.65 Hz. These are small in comparison to the direct dipolar couplings, but nonetheless must be included to correctly simulate the spectrum. Moreover, the presence or absence of J-couplings has a curious effect on the number of allowed transitions. When all J_{jk} values are zero for benzene, it can be shown that one of the three M=0 eigenfunctions in the B_1 representation no longer connects to other B_1 states--matrix elements of I_x involving this eigenfunction are identically zero. (For an outline of the proof, see Appendix B.) Eliminated are two zero-quantum transitions, one single-quantum transition, and one double-quantum transition. When small J-couplings are present, the wayward state reestablishes tenuous links to its B_1 brethren and these transitions reappear, but with miniscule intensities.

The same phenomenon of an uncoupled M=0 state occurs in random 4-spin systems with $\mathcal{H} = \mathcal{H}_D$--see Appendix C. I have not been able to determine if this uncoupling in the absence of indirect spin-spin interaction is a consequence of some more general selection rule.

4.8.2 4-cyano-4'-n-pentyl-d_{11}-biphenyl

This eight-proton liquid crystal was manfully analyzed by my colleague, Steve Sinton [56,93], and his efforts inspired some intensity computations of my own. A rather heroic molecular diagram can be found in Fig. IV.8. Rapid reorientation on the NMR timescale occurs about the central single bond, with potential wells at dihedral angles of ± 32°. Inter-ring couplings are thus

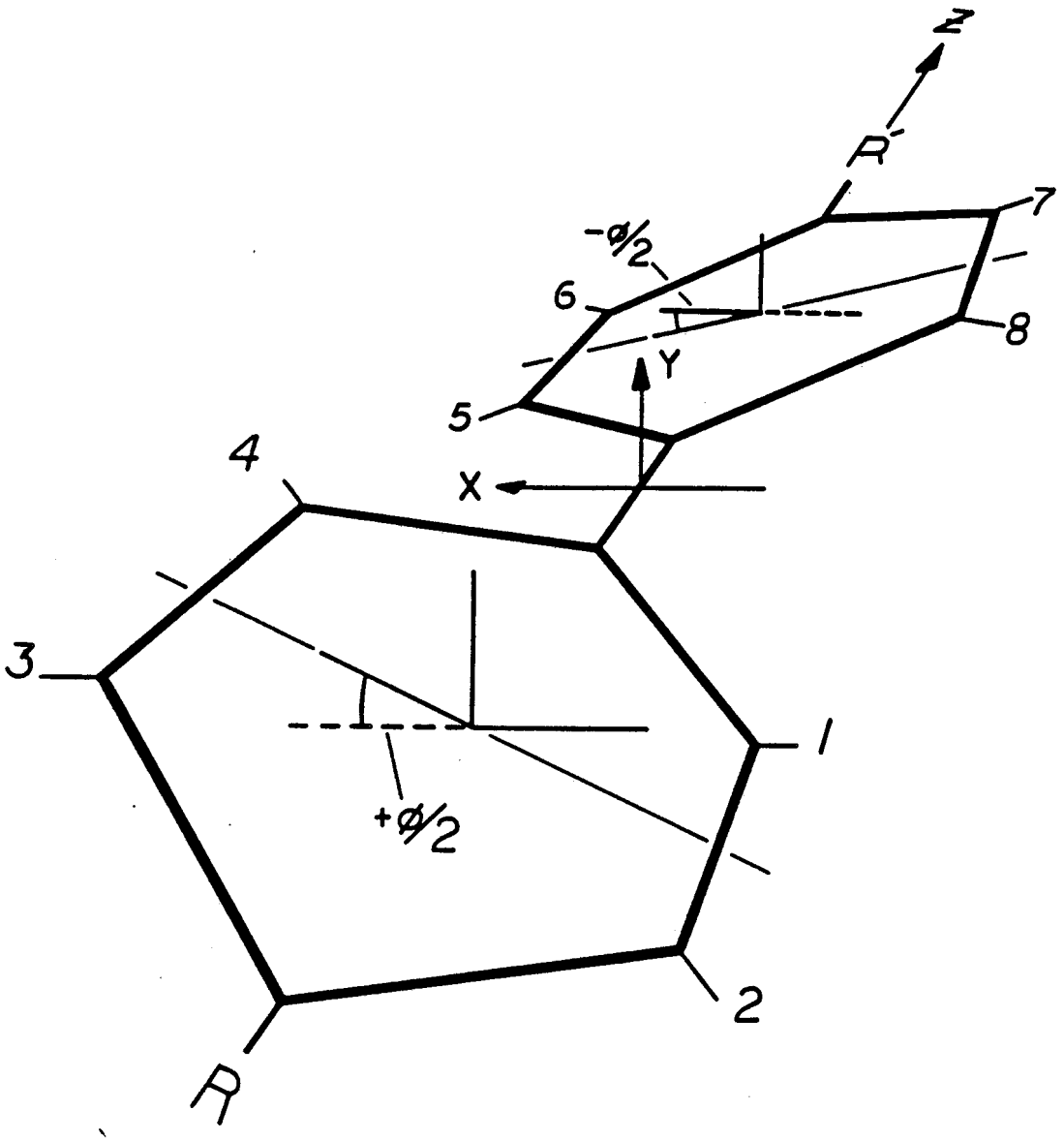

XBL 808-10942

Figure IV.8 A dramatic rendering of the biphenyl moiety, complete with the molecular axis system used to define the order parameters. For the molecule discussed in section 4.8.2, R≡-CN, R'≡-$(CD_2)_4CD_3$, and the favored dihedral angle Ø between the phenyl planes is measured to be ±32°. Rapid rotation about the single bond results in only three unique inter-ring couplings, D_{15}, D_{16}, and D_{26}.

characteristic of an average over four equivalent orientations of one ring relative to the other. Moreover, Steve found that couplings between protons on one ring were essentially the same as those between protons on the other, in spite of the difference in para-substituents. The spin-system permutation group is therefore isomorphic to the D_4 point group, and there are only seven unique dipolar couplings: D_{12}, D_{13}, D_{14}, D_{15}, D_{16}, D_{23}, and D_{26}. Steve determined the values of these using MQITER, his least-squares iterative computer program for fitting MQ spectra. Small isotropic J-coupling constants were included in the simulation, but no chemical shift difference between "outer" and "inner" protons was needed. (Actually, a small but real difference in chemical shifts exists, but as detailed in section 5.9.2, the effect of this difference is removed by the pi pulse in the TPPI evolution period.)

Two order parameters are necessary to characterize the orientation of this molecule. Steve found $S_{zz} = 0.568 \pm .001$ and $(S_{xx}-S_{yy}) = 0.057 \pm .002$. The rather large S_{zz} value reflects the fact that a liquid crystal molecule is reasonably well-ordered along its director axis in nematic phase. The resulting dipolar couplings are roughly an order of magnitude larger than those found in partially oriented benzene.

A tableau of the 256 eigenstates separated by M value and symmetry species is displayed in Fig. IV.9. Due to the lack of chemical shift differences, each state with $M \neq 0$ belongs to a

Symmetrically Para-substituted Biphenyl

D_4 Point Group Energy Level Diagram

M	A_1	A_2	B_1	B_2	E
-4	1				
-3	2			2	2X2
-2	7	1	3	5	2X6
-1	10	4	4	10	2X14
0	15	5	7	11	2X16
1	10	4	4	10	2X14
2	7	1	3	5	2X6
3	2			2	2X2
4	1				

XBL 8110-7191

Figure IV.9 A schematic energy level diagram for a 4,4'-disubstituted biphenyl, assuming a permutation group for the eight protons isomorphic to the D_4 point group. Each energy level in the E representation is doubly degenerate.

spin-inversion pair, and M=0 states are gerade or ungerade with respect to spin inversion.

4.8.3 Acetaldehyde

At last a chemical shift! This AB_3 system (CH_3CHO) was analyzed as part of an experiment involving total spin coherence transfer echoes [119] (see section 6.2). Because of the rapid methyl rotation, only four molecular parameters affect the spectrum: D_{AB}, D_{BB}, J_{AB} and $\sigma_{AB} = \sigma_A - \sigma_B$. The separation of eigenstates into A_1 and E representations can be found in Table IV.3; the highest-quantum transition in each representation connects spin-inversion states.

Exact expressions for all single-quantum frequencies of an AB_3 system can be found in Emsley and Lindon [120]. My task of assigning these frequencies to the proper experimental lines was made easier by calculating trial spectra as a function of each of the three adjustable parameters D_{AB}, D_{BB}, and σ_{AB}. (J_{AB} was fixed at its isotropic value of 2.8 Hz.) For the expected range of coupling constant and chemical shift values, the separation between certain pairs of lines was found to depend almost entirely on D_{AB}. A knowledge of this coupling constant then enabled the correct matching of tabled frequency expressions to experimental line positions. The fitted molecular parameters are as follows: D_{AB} = -358.0 Hz, D_{BB} = 917.2 Hz, σ_{AB} = 1361 Hz, and J_{AB} = 2.8 Hz. (The dipolar couplings here are a factor of two larger than those reported in Ref. 119.) In a different nematic

Table IV.3

Symmetry States for Oriented Acetaldehyde

	Number of states in each representation	
M	A_1	E
2	1	
1	2	2x1
0	2	2x2
-1	2	2x1
-2	1	
total:	8	8

solvent and at 100 MHz proton resonance, Emsley et al. [121] found D_{AB} = -555.2 Hz (155% of our value), D_{BB} = 1575.2 Hz (172% of our value), and σ_{AB} = 742.7 Hz (which corresponds to 1359 Hz at our Larmor frequency of 183 MHz). Because three order parameters--S_{zz}, S_{xx}-S_{yy}, and S_{xy}--are needed to describe the orientation of acetaldehyde, Emsley's dipolar couplings are not scaled by a single factor relative to ours.

The twelve A_1 single-quantum transition frequencies of acetaldehyde are displayed as a function of D_{AB}, D_{BB}, and σ_{AB} in Figs. IV.10-IV.12.

4.9 Gerade-Ungerade Selectivity

(This experiment was suggested by Dan Weitekamp and involved a sample prepared by George Wolf.)

The spin-inversion selection rules discussed in section 4.6.3 depend on the flip angle θ of the second preparation pulse. There we focused on $\theta = 90°$. When $\theta = 45°$, however, it is possible in systems with no chemical shift differences to select either the $g \leftrightarrow u$ or the $g \leftrightarrow g$, $u \leftrightarrow u$ M = 0 zero-quantum transitions merely by adjusting the rf phases.

Consider first the preparation pulse sequence $45x - \tau - 45\bar{x}$ applied on resonance to such systems. (The flip angle of the first pulse is set here at 45° to simplify the analysis; experimentally, a 90° pulse would be used to maximize the MQ signal.) The effective preparation Hamiltonian for this sequence is

Figures IV.10-IV.12. The single-quantum spectrum of oriented acetaldehyde calculated as a function of various molecular parameters. Only the A_1 transitions are shown, and the intensities are those for a conventional one-pulse experiment. Each figure consists of a series of horizontal spectra, wherein each symbol represents a line position. Relative intensities are denoted by the choice of symbol. The squares are for manly transitions at least two thirds as intense as the strongest line. Weak transitions, with less than one sixth of the intensity of the strongest line, are indicated with dots. Intermediate transitions are marked with x's.

In all three figures, the bottom-most spectrum corresponds to the experimental parameters: D_{AB} = -358.0 Hz, D_{BB} = 917.2 Hz, σ_{AB} = 1361 Hz, and J_{AB} = 2.8 Hz.

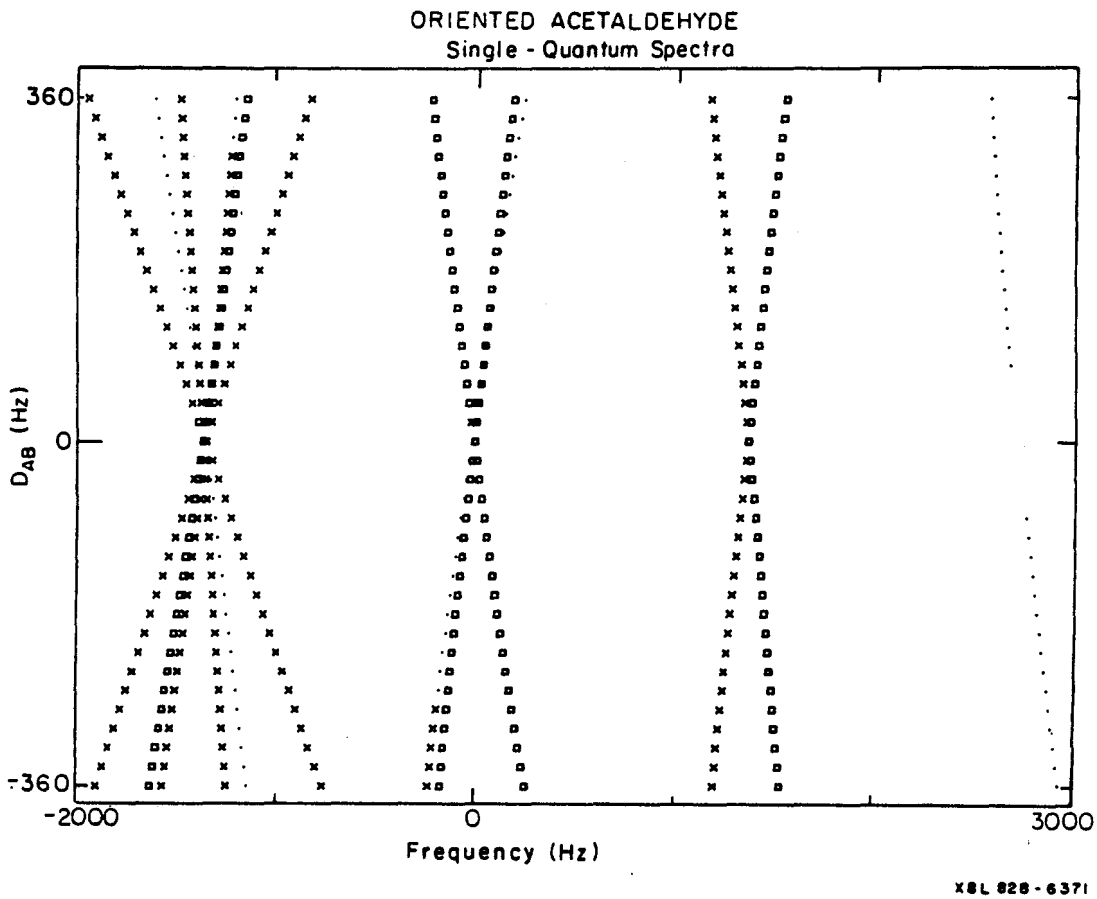

Figure IV.10 A_1 single-quantum frequencies of oriented acetaldehyde as a function of D_{AB}, the methyl proton-aldehyde proton dipolar coupling constant.

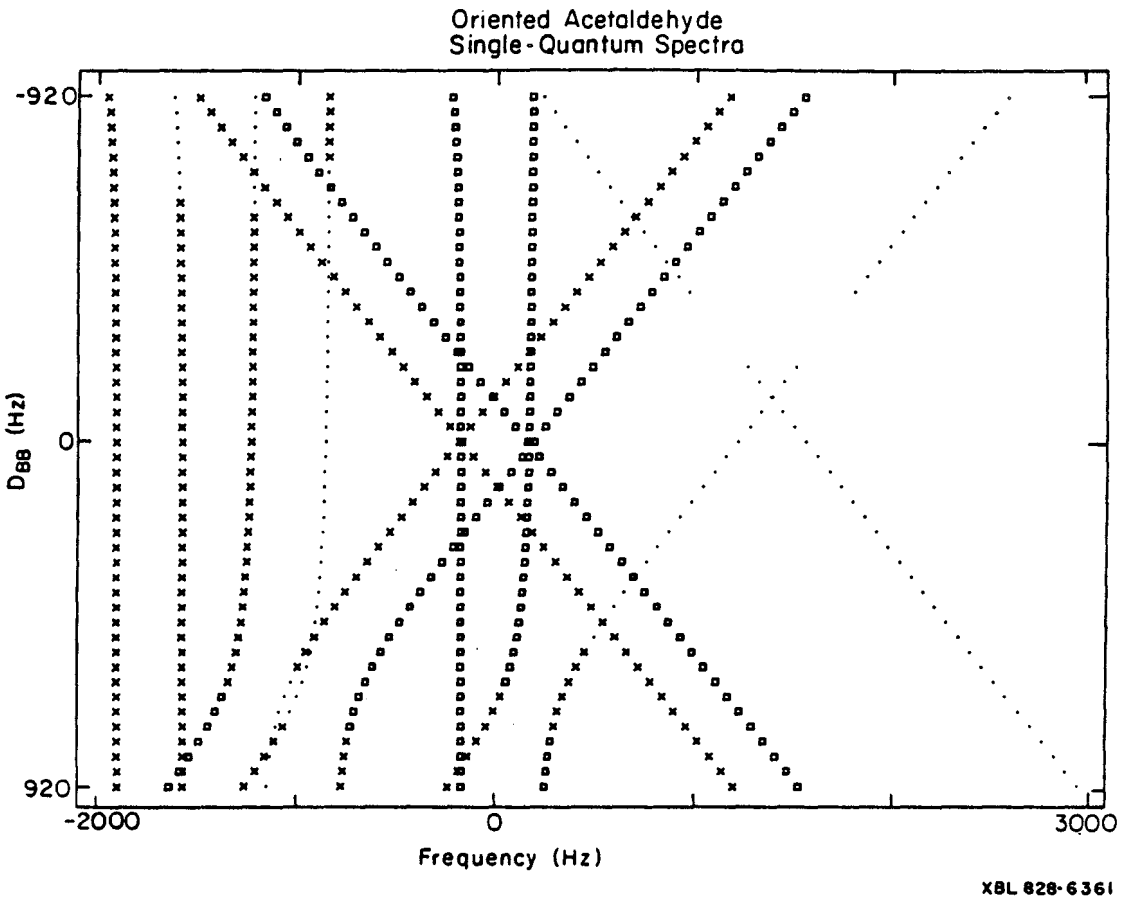

Figure IV.11 A_1 single-quantum frequencies of oriented acetaldehyde as a function of D_{BB}, the intramethyl dipolar coupling constant.

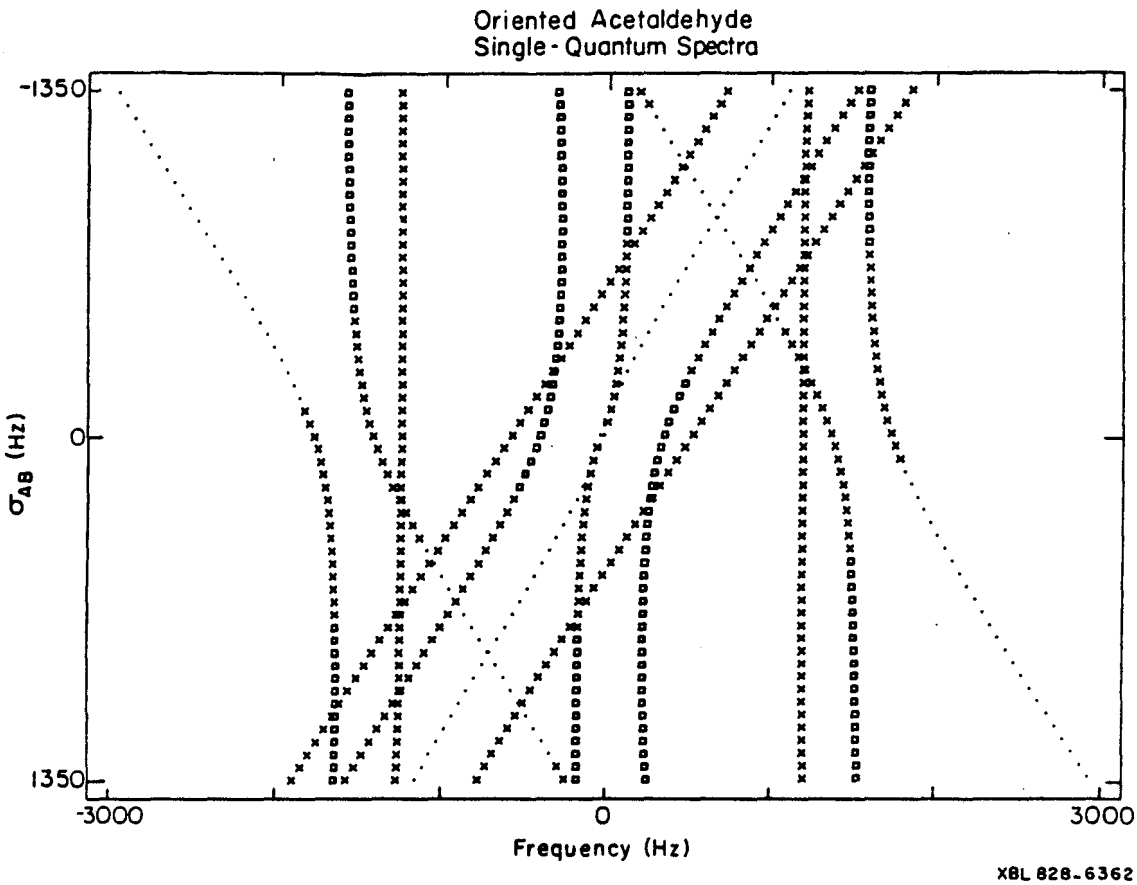

Figure IV.12 A_1 single-quantum frequencies of oriented acetaldehyde as a function of σ_{AB}, the chemical shift difference between aldehyde and methyl protons.

$$\mathcal{H}_{45} = e^{-i\,\pi/4\,I_x}\,\mathcal{H}e^{i\,\pi/4\,I_x} \tag{IV.48a}$$

$$= -\frac{1}{2}\mathcal{H}_{xx} - \frac{3}{4}\sum_{j<k}\sum D_{jk}\,(I_{yj}I_{zk}+I_{zj}I_{yk}) + \mathcal{H}_J\ . \tag{IV.48b}$$

$\mathcal{H}_{45}$ commutes with Π; if

$$\beta P = e^{-i\,\mathcal{H}_{45}\,\tau}\,\beta I_z\,e^{i\,\mathcal{H}_{45}\,\tau}\quad , \tag{IV.49}$$

then $\Pi^{\dagger}\,P\,\Pi = -P$, as in Eq. IV.36.

In comparison, the pulse sequence $45\bar{y} - \tau - 45\bar{x}$ is equivalent to the previous $x,\bar{x}$ sequence acting on an initial density matrix proportional to I_x. In this case,

$$\beta P = e^{-i\,\mathcal{H}_{45}\,\tau}\,\beta I_x\,e^{i\,\mathcal{H}_{45}\,\tau} \tag{IV.50}$$

and

$$\Pi^{\dagger}\,P\,\Pi = e^{-i\,\mathcal{H}_{45}\,\tau}\,\Pi^{\dagger}\,I_x\,\Pi\,e^{i\,\mathcal{H}_{45}\,\tau} = P\quad . \tag{IV.51}$$

Thus the first sequence prepares transitions between M = 0 states with different eigenvalues of Π, whereas the second sequence prepares transitions between M = 0 states with the same eigenvalue of Π. Note that because $\mathcal{H}_{45}$ contains both even-quantum and odd-quantum operators, neither sequence results in the even-odd selection described earlier for 90° pulses.

Figure IV.13 displays the gerade-ungerade selectivity in the zero-quantum spectrum of oriented benzene (D_{12} = -817.06 Hz). For the spectrum in (a), the pulse sequence used was

$$90x - \frac{1}{2}\tau - 180x - \frac{1}{2}\tau - 45x - t_1 - 45x - \frac{1}{2}\tau - 180x - \frac{1}{2}\tau ,$$

where the pi pulses simply remove any $\Delta\omega$ offset. For the spectrum in (b), the 45x pulses were changed to 45y pulses. In each case, magnitude spectra corresponding to seven different values of τ between 4 and 16 msec were averaged together. The magnet homogeneity was sufficiently poor that only zero-quantum transitions appeared as sharp lines; hence, no special techniques were needed to separate MQ orders.

Lines present in both spectra are due to zero-quantum transitions between states with $M \neq 0$. Lines which appear solely in the first spectrum are due to $g \leftrightarrow u$ $M = 0$ transitions; the $g \leftrightarrow g$ and $u \leftrightarrow u$ transitions show up in the second spectrum. Two of these $u \leftrightarrow u$ transitions, however, involve the weakly-coupled B_1 state described earlier and thus have vanishing intensity.

The simulations accompanying the experimental spectra are exact calculations for the actual values of τ that were used. A list of computed frequencies and symmetry properties for all the zero-quantum transitions of benzene can be found in Table IV.4.

4.10 Summary

NMR spectroscopy of small molecules dissolved in nematic

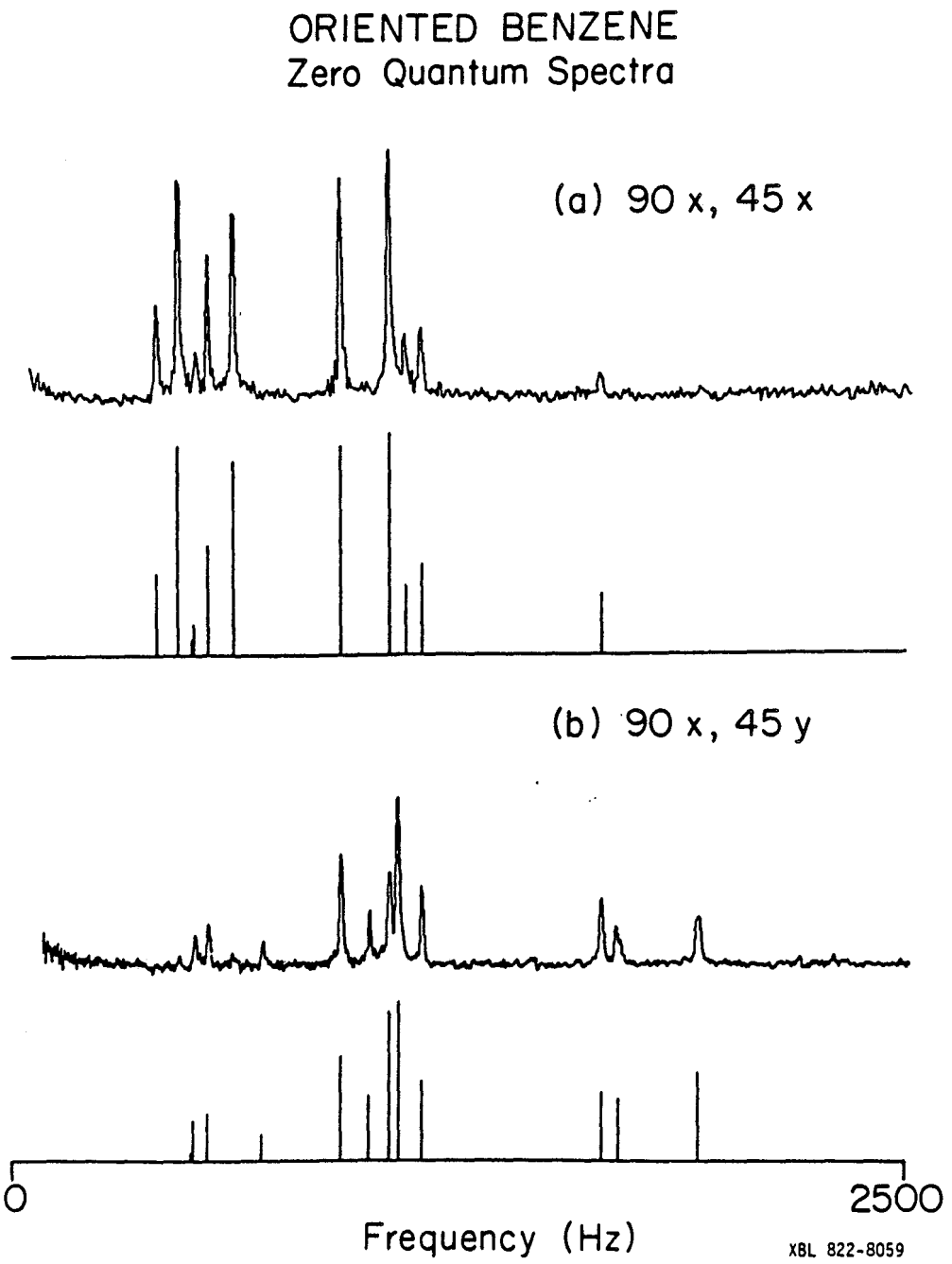

Figure IV.13 Gerade-ungerade selectivity in the zero-quantum spectrum of oriented benzene. Each spectrum and its accompanying simulation are an average over seven τ values. (a) An on-resonance 90x-τ-45x preparation sequence excites g↔u M=0 transitions. (b) In contrast, an on-resonance 90x-τ-45y sequence prepares g↔g and u↔u transitions. Zero-quantum lines involving states with M≠0 appear in both spectra.

Table IV.4

Zero-Quantum Transitions of Oriented Benzene

D_{12} = -817.06 Hz J_{12} = 7.5 Hz

D_{13} = -157.25 Hz J_{13} = 1.4 Hz

D_{14} = -102.13 Hz J_{14} = 0.65 Hz

	Frequency (Hz)	Symmetry	|M|	Type	where the transition appears: 90x-τ-45x sequence	where the transition appears: 90x-τ-45y sequence
1.	402.76	E_2	0	g↔u	x	
2.	408.93	B_1	0	u↔u		(x)[a]
3.	465.06	E_1	0	g↔u	x	
4.	501.71	A_1	1		x	x
5.	511.47	E_2	1		x	x
6.	546.95	E_2	1		x	x
7.	617.42	E_1	0	g↔u	x	
8.	698.38	E_2	0	g↔g		x
9.	921.09	E_1	1		x	x
10.	923.85	A_1	0	g↔g		x
11.	996.92	A_1	0	g↔g		x
12.	1058.41	E_2	1		x	x
13.	1082.48	E_1	0	u↔u		x
14.	1101.14	E_2	0	g↔u	x	
15.	1147.64	A_1	1		x	x
16.	1286.39	B_1	0	u↔u		(x)[a]
17.	1649.35	A_1	1		x	x
18.	1695.32	B_1	0	u↔u		x
19.	1920.77	A_1	0	g↔g		x

[a] extremely weak transition.

phase is a powerful tool in the investigation of structure and internal motion. Unfortunately, the conventional SQ experiment cannot be extended to larger molecules without an explosive growth in the number of transitions to the point of unresolvable blobs. Multiple-quantum techniques, however, can provide the same information on molecular parameters from a greatly reduced set of lines.

In this chapter, the basic three-pulse sequence for the excitation, evolution, and detection of MQ coherence has been analyzed using an effective Hamiltonian formalism. More complicated sequences to provide even-odd selectivity or to separate different MQ orders have also been considered, as well as the effect of molecular symmetry on the resulting spectra. Three molecules--benzene, a 4,4'-disubstituted biphenyl, and acetaldehyde--have been examined at length in preparation for the fevered computational excesses featured in the next chapter.

V. COMPUTER SIMULATION OF MULTIPLE-QUANTUM INTENSITIES

5.1 Introduction

Multiple-quantum intensities are of interest for several reasons. One is a practical consideration: can the higher-order transitions of use in the analysis of molecular structure and motion be excited with reasonable or at least detectable intensity; i.e., is non-selective MQ NMR a viable technique for systems with more than five or six spins. A second reason is the importance of intensities in computer simulations of experimental MQ spectra to determine dipolar couplings and chemical shifts. An iterative least-squares fitting program like Steve Sinton's MQITER [56] will generate multiple-quantum frequencies; a complementary calculation of the corresponding intensities can confirm or throw doubt on the simulation. Finally, a third reason for studying MQ intensities is to probe the curious relationship between exact quantum-mechanical dynamics and statistical "random walk" behavior in multi-spin systems.

In this chapter, most of the analysis concerns multiple-quantum coherences generated by the basic three-pulse sequence, although the effects of a pi pulse in the evolution period will be examined briefly. (Because a simulated magnetic field is easy to make homogeneous, a simple rf offset will be used to separate MQ orders if necessary--no explicit calculation of TPPI, phase Fourier transforms, FATSO, etc., is included.) A discussion of computer-simulated spectra for more complicated selective excitation sequences can be found elsewhere [122].

5.2 An Expression for Multiple-Quantum Intensity

Before discussing the computer results, we will first rewrite the prepared density matrix in a form more convenient for computation. The pulse sequence to be considered is

$$90\bar{y} - \tau - 90y - t_1 - 90\bar{y} - t_2$$

The density matrix at the moment of detection may be written as

$$\rho(t_1;\tau,t_2) = e^{-i\mathcal{H}t_2} e^{-i\pi/2 I_y} e^{-i\mathcal{H}t_1} e^{i\pi/2 I_y} e^{-i\mathcal{H}\tau} \beta I_x e^{i\mathcal{H}\tau} e^{-i\pi/2 I_y} e^{i\mathcal{H}t_1} e^{i\pi/2 I_y} e^{i\mathcal{H}t_2} \quad . \quad \text{(V.1)}$$

If S is the orthogonal transformation (or matrix of eigenvectors) which diagonalizes $\mathcal{H}$,

$$\mathcal{H} = S\ E\ S^{\dagger} \quad , \quad \text{(E diagonal)} \qquad \text{(V.2)}$$

we may define

$X = S^{\dagger}\ I_x\ S$ -- I_x expressed in the basis set of $\mathcal{H}$

and

$A = S^{\dagger}\ e^{-i\ \pi/2\ I_y}\ S$ -- the pulse propagator in the basis set of $\mathcal{H}$. X and A are both real matrices and X is symmetric.

With these definitions,

$$\rho(t_1;\tau,t_2) = \beta\, S\, e^{-iEt_2} A\, e^{-iEt_1} A^\dagger\, e^{-iE\tau}\, X\, e^{iE\tau}\, A\, e^{iEt_1} A^\dagger\, e^{iEt_2}\, S^\dagger \quad . \tag{V.3}$$

The signal $s(t_1;\tau,t_2)$ equals $\mathrm{Tr}\{\rho\, I_x\}$. In a flurry of symbols, we introduce $P(\tau)$ as the prepared density matrix and $Q(t_2)$ as the "devolved detection matrix"--I_x taken backwards in time to the start of the detection period. We write both in the basis set of $\mathcal{H}$:

$$P = A^\dagger\, e^{-iE\tau}\, X\, e^{iE\tau}\, A \tag{V.4a}$$

$$Q = A^\dagger\, e^{iEt_2}\, X\, e^{-iEt_2}\, A \quad . \tag{V.4b}$$

In terms of these matrices,

$$s(t_1;\tau,t_2) = \beta\, \mathrm{Tr}\{e^{-iEt_1} P e^{iEt_1} Q\} = \beta \sum_j \sum_k P_{jk} Q_{kj}\, e^{i(E_k - E_j)t_1} \quad . \tag{V.5}$$

Fourier-transforming with respect to the evolution time t_1 yields the multiple-quantum spectrum:

$$\underline{S}(\omega,\tau,t_2) = \beta \sum_j \sum_k P_{jk} Q_{kj}\, \delta(\omega - \omega_{kj}) \quad . \tag{V.6}$$

The intensity of each multiple-quantum line is thus determined by the product of two complex matrix elements, with

$$P_{jk} = \sum_a \sum_b A^{\dagger}_{ja} X_{ab} A_{bk} e^{i\omega_{ba}\tau}$$

$$= \sum_a \sum_b A_{aj} X_{ab} A_{bk} e^{i\omega_{ba}\tau}$$

$$= \sum_a \sum_b B_{ab} e^{i\omega_{ba}\tau} \qquad \text{(V.7)}$$

and

$$Q_{kj} = \sum_a \sum_b A^{\dagger}_{kb} X_{ba} A_{aj} e^{i\omega_{ba}t_2}$$

$$= \sum_a \sum_b A_{aj} X_{ab} A_{bk} e^{i\omega_{ba}t_2}$$

$$= \sum_a \sum_b B_{ab} e^{i\omega_{ba}t_2} \quad . \qquad \text{(V.8)}$$

(B, a real matrix, is different for each transition $|j\rangle$ to $|k\rangle$. For convenience though, we will not include an explicit j,k label.) Because X is a single-quantum operator, $|M_a - M_b| = 1$ and the frequencies ω_{ba} correspond to symmetry-allowed single-quantum transitions. These dephase during the preparation period and rephase during the detection period.

When $\tau = t_2$, $P_{jk}(\tau) = Q_{kj}(t_2)$ and the intensity and phase of a transition $|j\rangle$ to $|k\rangle$ are given by

$$\underline{S}_{jk} = \beta\ P_{jk}^2 = \beta\{\sum_a \sum_b\ B_{ab}\ e^{i\omega_{ba}\tau}\}^2 \quad . \qquad (V.9)$$

This quantity is in general a complex number (except for spin-inversion transitions, for which $\underline{S}_{k\bar{k}}$ is always real and negative); thus the multiple-quantum spectrum contains lines with many different phases (Fig. V.1a). In comparison, the intensity of a single-quantum transition in the usual FT experiment is βX_{jk}^2; barring experimental misadjustments, all lines have the same phase.

With a more complicated pulse sequence, it is possible, at least in theory, to generate a multiple-quantum spectrum with all lines in phase. If τ were made equal to $-t_2$ by some time-reversal sequence [123] applied during preparation, then P_{jk} would equal Q_{kj}^* and for all transitions $|j\rangle$ to $|k\rangle$,

$$\underline{S}_{jk} = \beta\ |P_{jk}|^2 \quad . \qquad (V.10)$$

Time reversal (which may involve literally hundreds of pulses) is fortunately not necessary in many cases. Lines in the proton spectra of molecules dissolved in liquid crystals are narrow (3-10 Hz) in the absence of exchange and do not overlap in the "interesting" higher-quantum regions. A magnitude spectrum can therefore be calculated as in Fig. V.1b (creating some line broadening due to dispersive tails) or each line can be phased individually. For $t_2=\tau$, the resulting intensity of each transition $|j\rangle$ to $|k\rangle$ is again $\beta|P_{jk}|^2$.

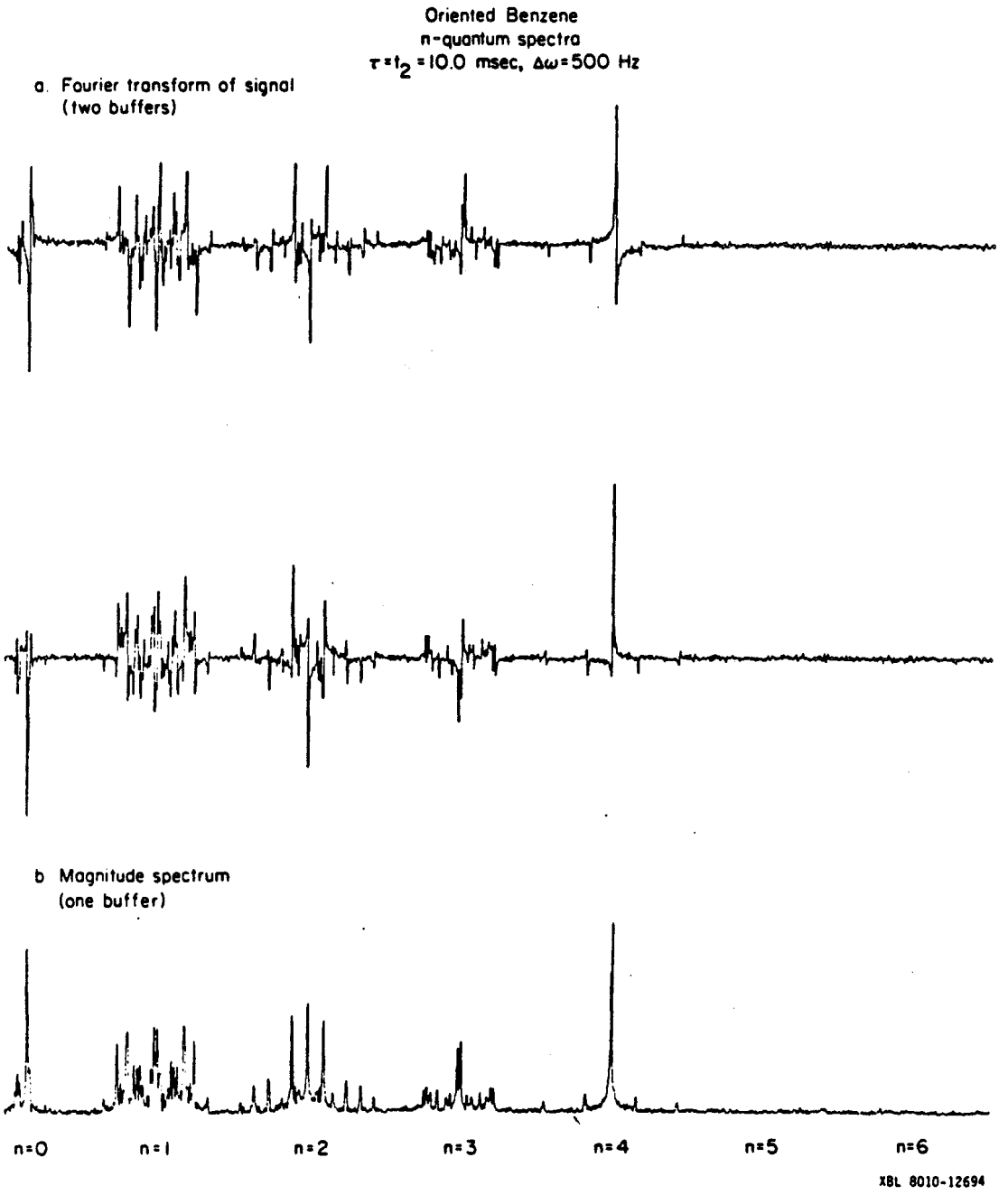

Figure V.1 The multiple-quantum spectrum of oriented benzene (14 wt % in Eastman nematic liquid crystal #15320 at 24.0°), obtained by Warren Warren. The wide range of MQ phases apparent in (a) makes analysis difficult. The magnitude spectrum in (b) shows only slight broadening and is much more informative.

In solids, however, the existence of intermolecular dipolar couplings gives rise to a continuum of transitions. Significant cancellation of intensity will thus occur if time-reversal sequences are not used [124]. The extent of this cancellation can be roughly estimated as follows. If L transitions of equal magnitude p but random phase overlap, then the intensity in the absence of time reversal is, by analogy to a random walk in the complex plane, given by

$$\frac{\sqrt{\pi}}{2} (L\ p^2)^{1/2} = \frac{1}{2} (\pi\ L)^{1/2}\ p \qquad \text{(V.11)}$$

for L >> 1. (See section 5.7 for the details of a similar calculation.) In contrast, when a time-reversal sequence is used to generate all lines in phase, the overall intensity is merely Lp. The gain in signal to noise associated with time reversal is therefore

$$\frac{Lp}{\frac{1}{2} (\pi\ L)^{1/2} p} = \frac{2}{\sqrt{\pi}} L^{1/2} \approx 1.128\ L^{1/2}\ . \qquad \text{(V.12)}$$

A more complete discussion of MQ intensities in solids will be presented elsewhere [125]. In this chapter, we will focus on magnitude spectra for molecules in liquid crystalline phase.

5.3 Coherence Magnitude as a Function of Preparation Time

From Eq. V.6 it is apparent that the intensity of multiple-quantum lines depends on the values of τ and t_2. For example, the calculated multiple-quantum magnitude spectra of oriented benzene for $\tau = t_2 = .25$ msec, 5 msec, and 100 msec are displayed in Fig. V.2. Lines appear and disappear as the preparation and detection times are varied. To avoid missing a line due to an unfortunate choice of τ and t_2, magnitude spectra for different values of τ and t_2 can be averaged together, as in Fig. V.3.

We have also computed, again for oriented benzene, the average prepared coherence magnitude $\beta|P_{jk}|$ for each multiple-quantum order as a function of τ. To avoid even-odd selectivity, the two preparation pulses were chosen to differ in phase by 45° [40]. Three such plots are displayed in Fig. V.4. For the lower-quantum orders with many allowed transitions, the averaged coherence magnitude per transition is largely independent of τ after an initial "incubation" period [given roughly by $(2\pi\tau)$ (average dipolar coupling $\bar{D}$ in Hz) $\approx \pi/2$ or $\tau \approx (4\bar{D})^{-1} \approx 570$ μsec in this case]. The single six-quantum coherence naturally shows greater oscillation but is also more intense on the average than a lower-order transition, as will be discussed later.

Let's examine this six-quantum spin-inversion transition further. The prepared coherence $P_{k\bar{k}}$ is purely imaginary for all values of τ (see section 4.6.3); specifically

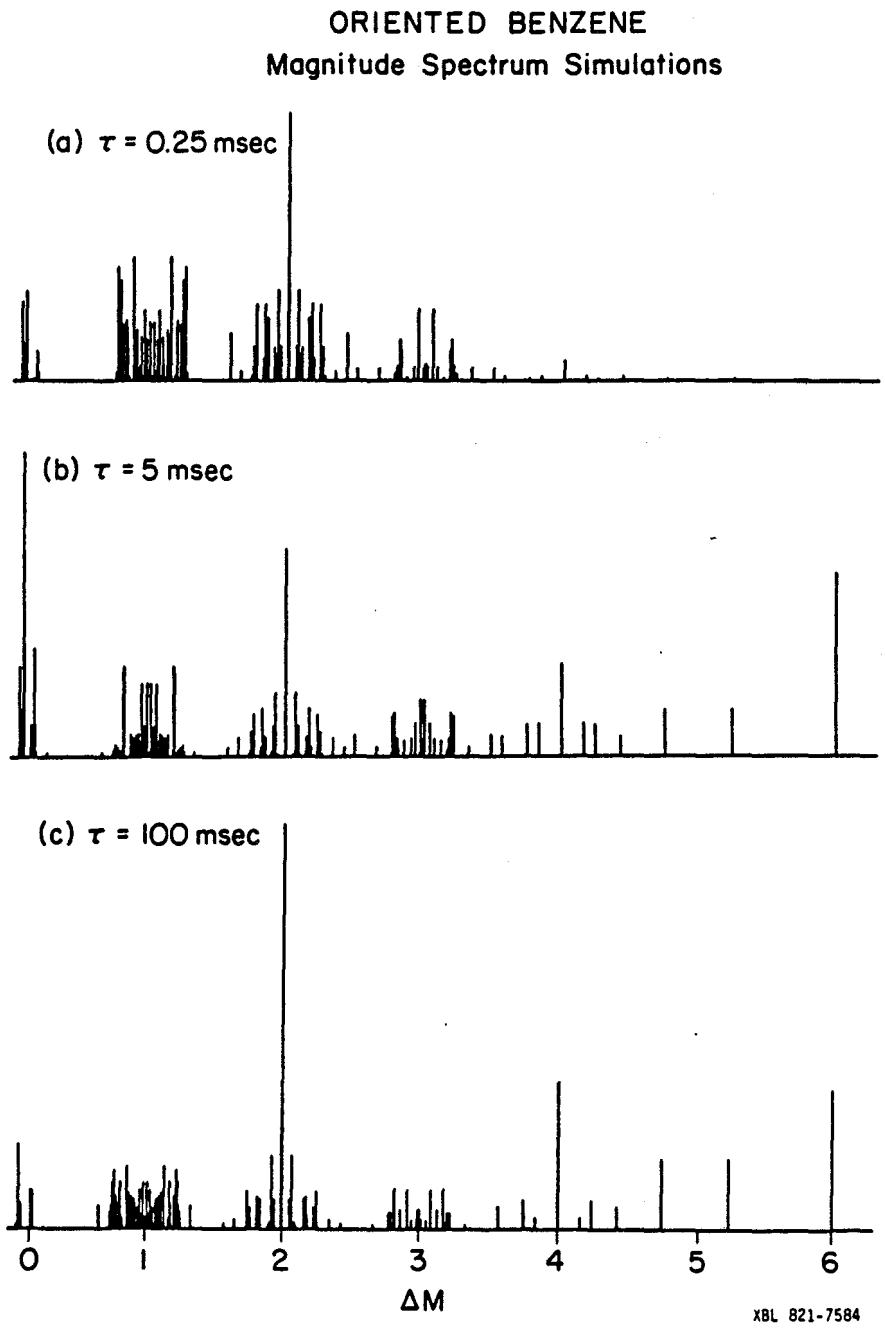

Figure V.2 Three calculated magnitude spectra for oriented benzene. The molecule was assumed to be hexagonal, with rapid reorientation about the C_6 axis. D_{12} was chosen to be -817.08 Hz, and isotropic J-coupling values were used. In the top spectrum, τ and t_2 are too short for higher-order transitions to be prepared or detected.

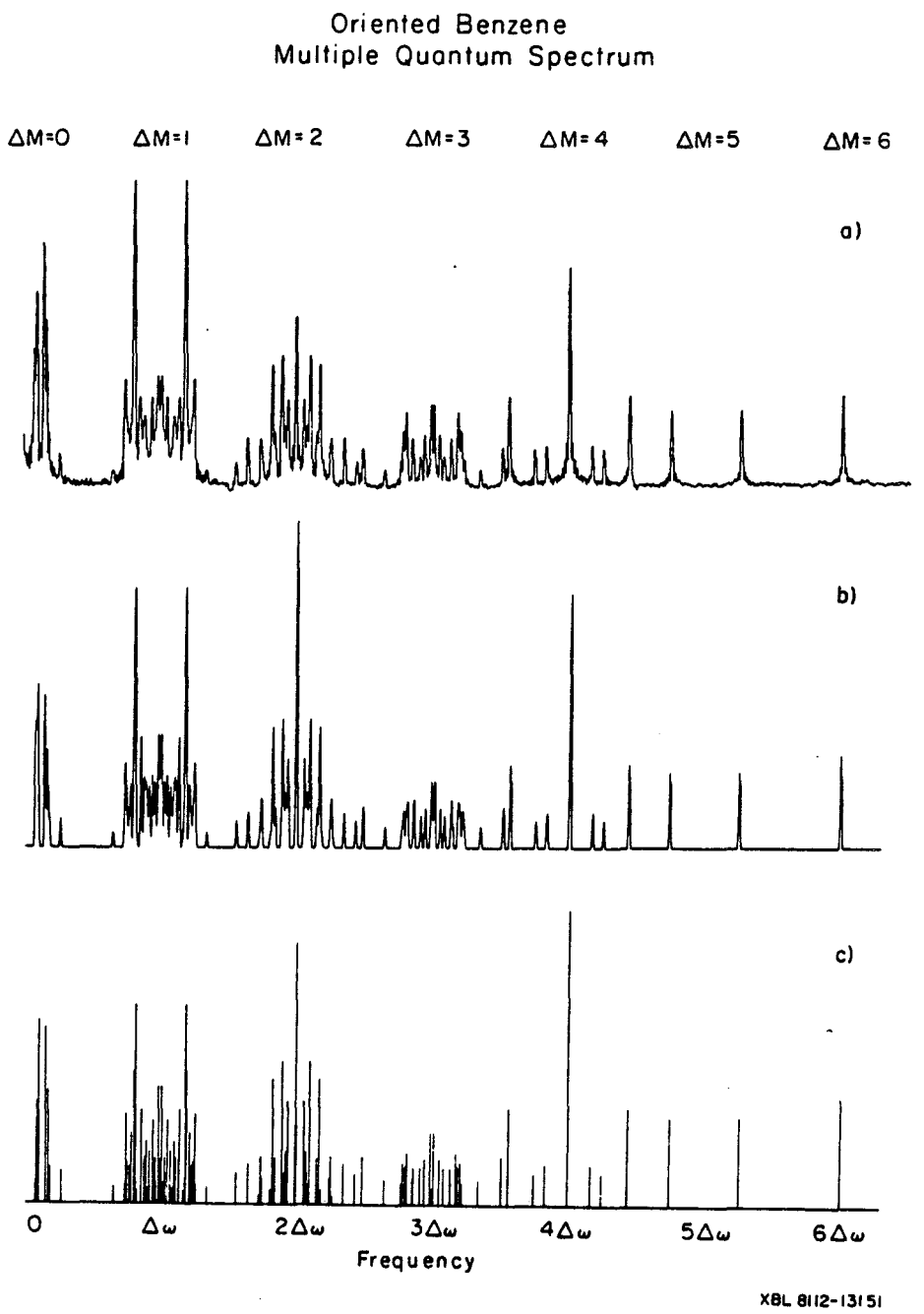

Figure V.3 The multiple-quantum spectrum of oriented benzene, averaged over four values of $\tau=t_2$ (4, 6, 8, and 10 msec). (a) Experiment (a duplicate of Figure IV.7), (b) simulation with broadening, (c) stick simulation.

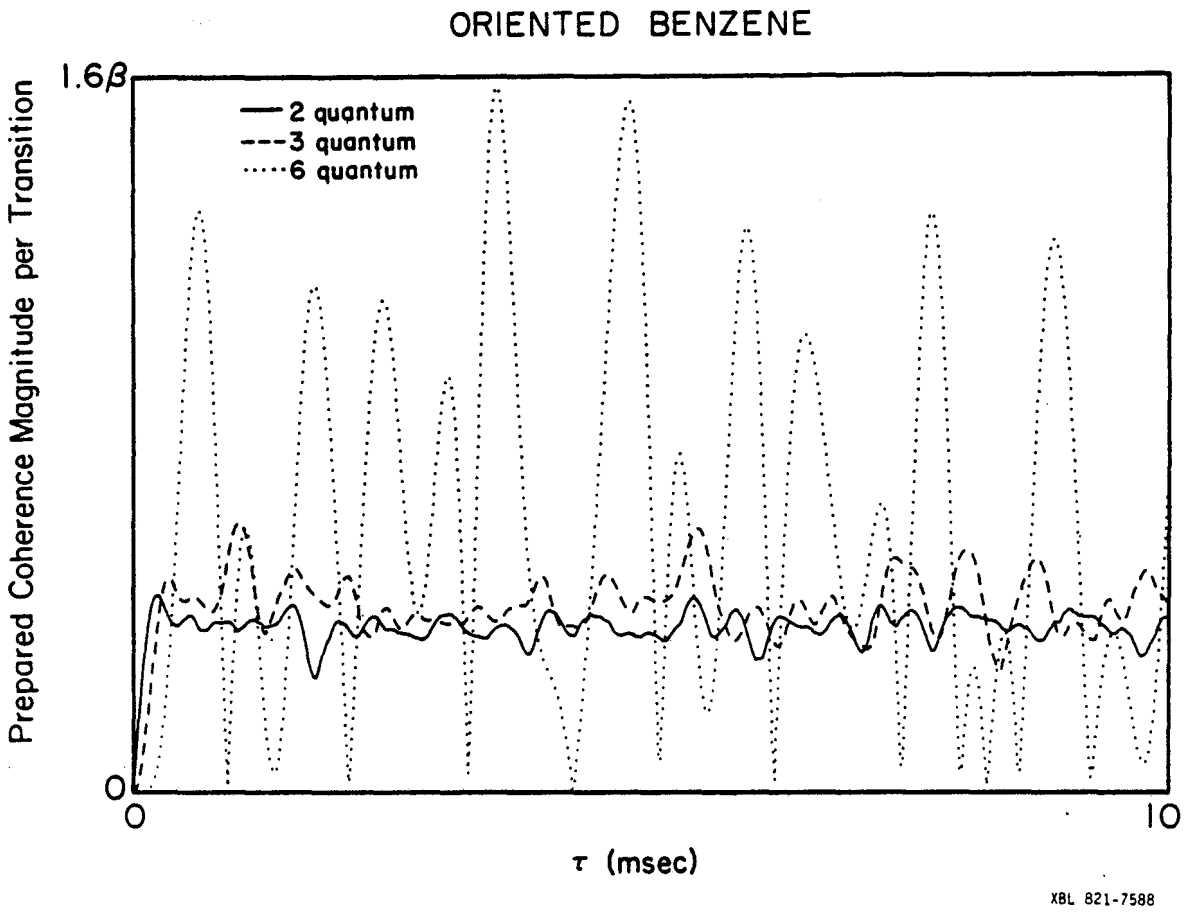

Figure V.4 Average prepared coherence magnitude $\beta|P_{jk}|$ as a function of τ for oriented benzene. The preparation sequence contained two $\pi/2$ pulses with a relative phase of 45°, and $\Delta\omega$ was assumed to be zero.

$$B_{ba} = -B_{ab} \quad \text{and}$$

$$P_{k\bar{k}} = 2i \sum_{a<b} B_{ab} \sin\omega_{ba}\tau \quad . \qquad (V.13)$$

With its i removed, $P_{k\bar{k}}$ is plotted in Fig. V.5a for values of τ up to 20 msec. Of more practical relevance is the six-quantum intensity $|P_{k\bar{k}}|^2$ plotted versus $\tau = t_2$ in Fig. V.5b. It can be seen that over the range of a few hundred microseconds, the intensity can vary markedly. Thus to make certain of appreciably pumping the transition, it is necessary to combine magnitude spectra for different values of τ or use the parameter-proportional phase incrementation (PPPI) technique [126] to select an optimal τ or a set thereof.

To check for the possibility of long-term drift, the intensity has also been calculated out to $\tau = 5$ seconds (again it should be stressed that relaxation is <u>not</u> considered here). 250 000 τ values were examined at 20 μsec intervals. Intensities in groups of 500 were then combined to give average intensities over 10 msec periods. The resulting 500 points are displayed in Fig. V.6; no drift in the "noise" is apparent. The dotted line represents the soon-to-be-discussed ultimate τ average intensity for an even-selective sequence.

The normalized <u>short</u> τ behavior of prepared benzene coherence is presented in Fig. V.7. (Again the two preparation pulses differ in phase by 45° to avoid even-odd selectivity.) For $\tau = 0$, only

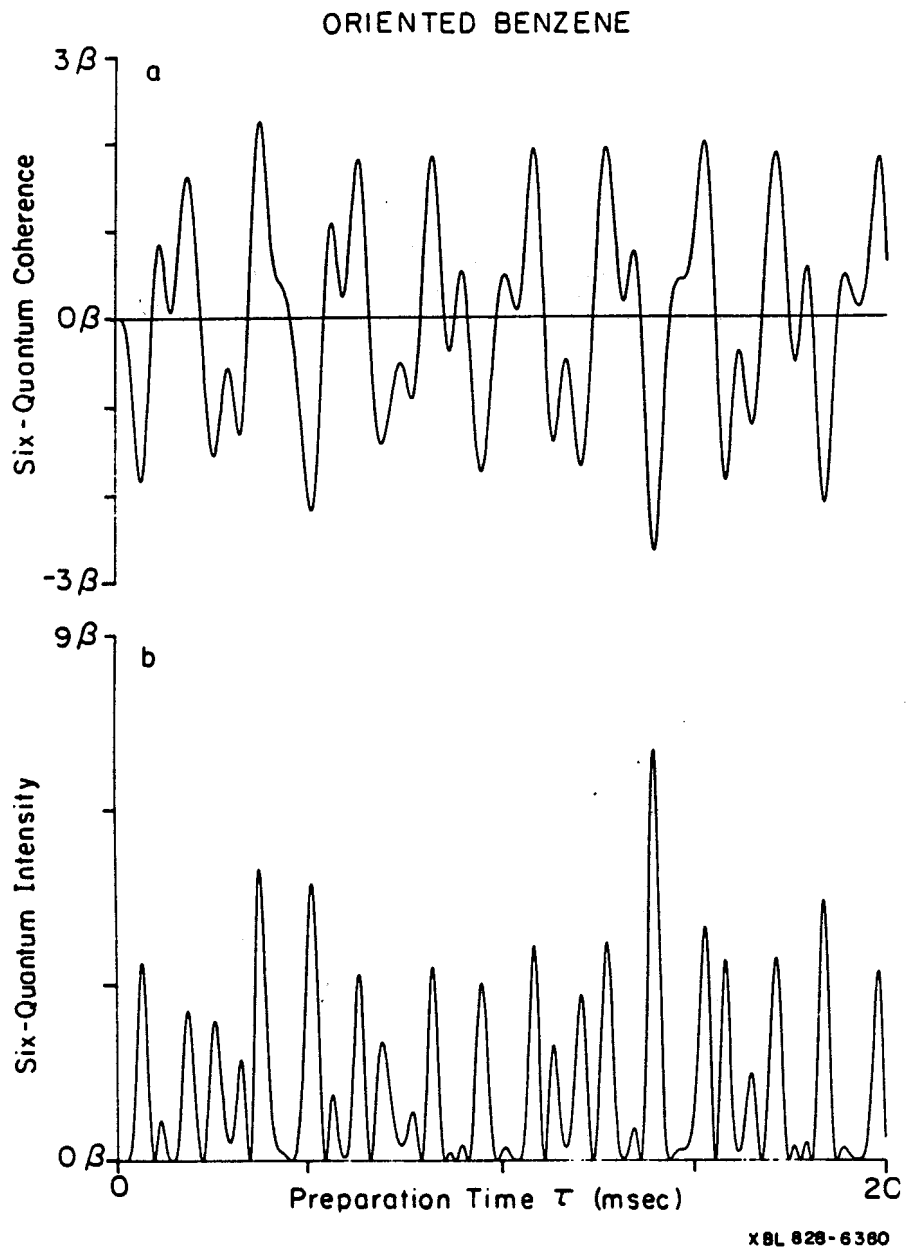

Figure V.5 (a) Six-quantum coherence as a function of preparation time τ for oriented benzene and an even-quantum-selective $90\bar{y} - \tau - 90y$ sequence with $\Delta\omega = 0$. The maximum magnitude of this N-quantum coherence is $N\beta/2 = 3\beta$. (b) The corresponding intensity for a three-pulse even-quantum-selective sequence with $t_2 = \tau$.

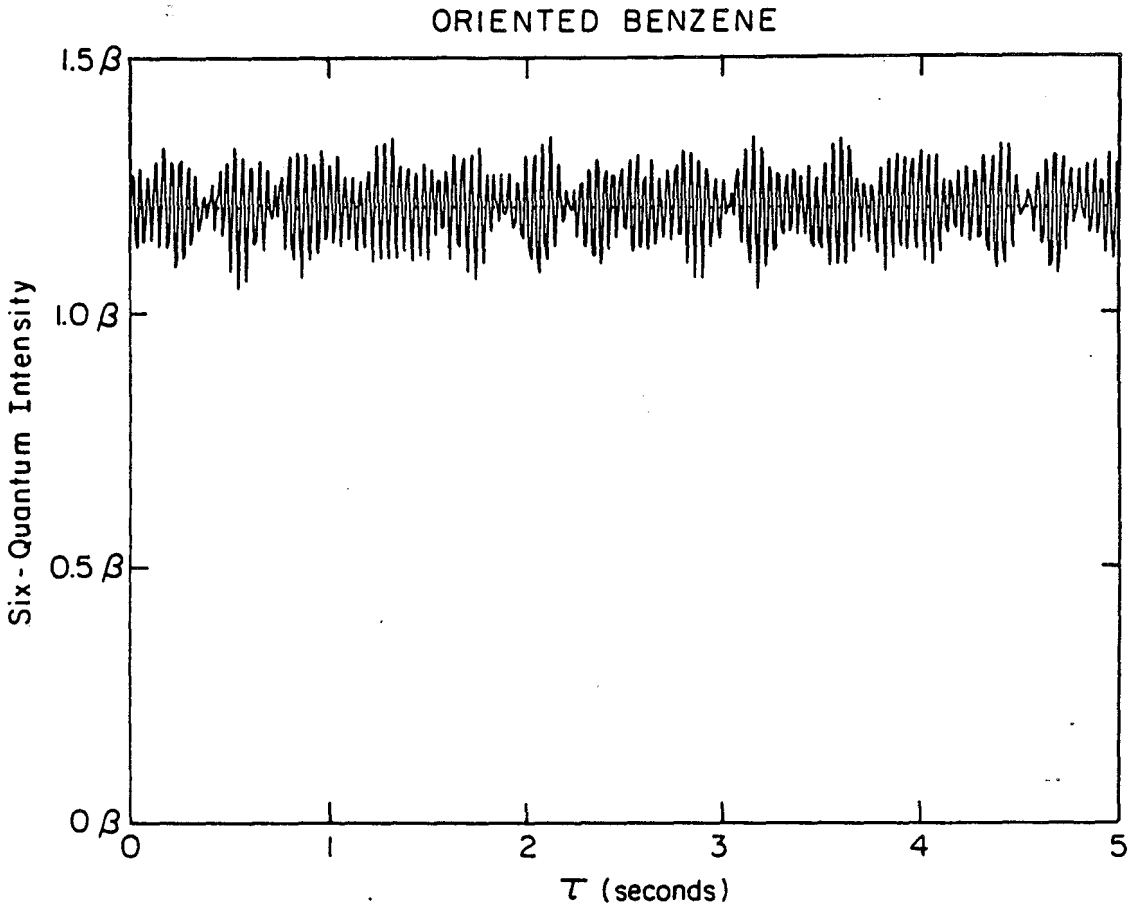

XBL 828-6374

Figure V.6 Benzene six-quantum intensity for a three-pulse even-quantum-selective sequence examined at great lengths -- out to $t_2 = \tau = 5$ sec. Each of the 500 points is an average over 500 intensity values at 20 μsec intervals. The averaged intensity varies by ∿10% from one 10 msec "bin" to another, but there is no long-term drift. The dotted line marks the even-quantum-selective ultimate τ average intensity.

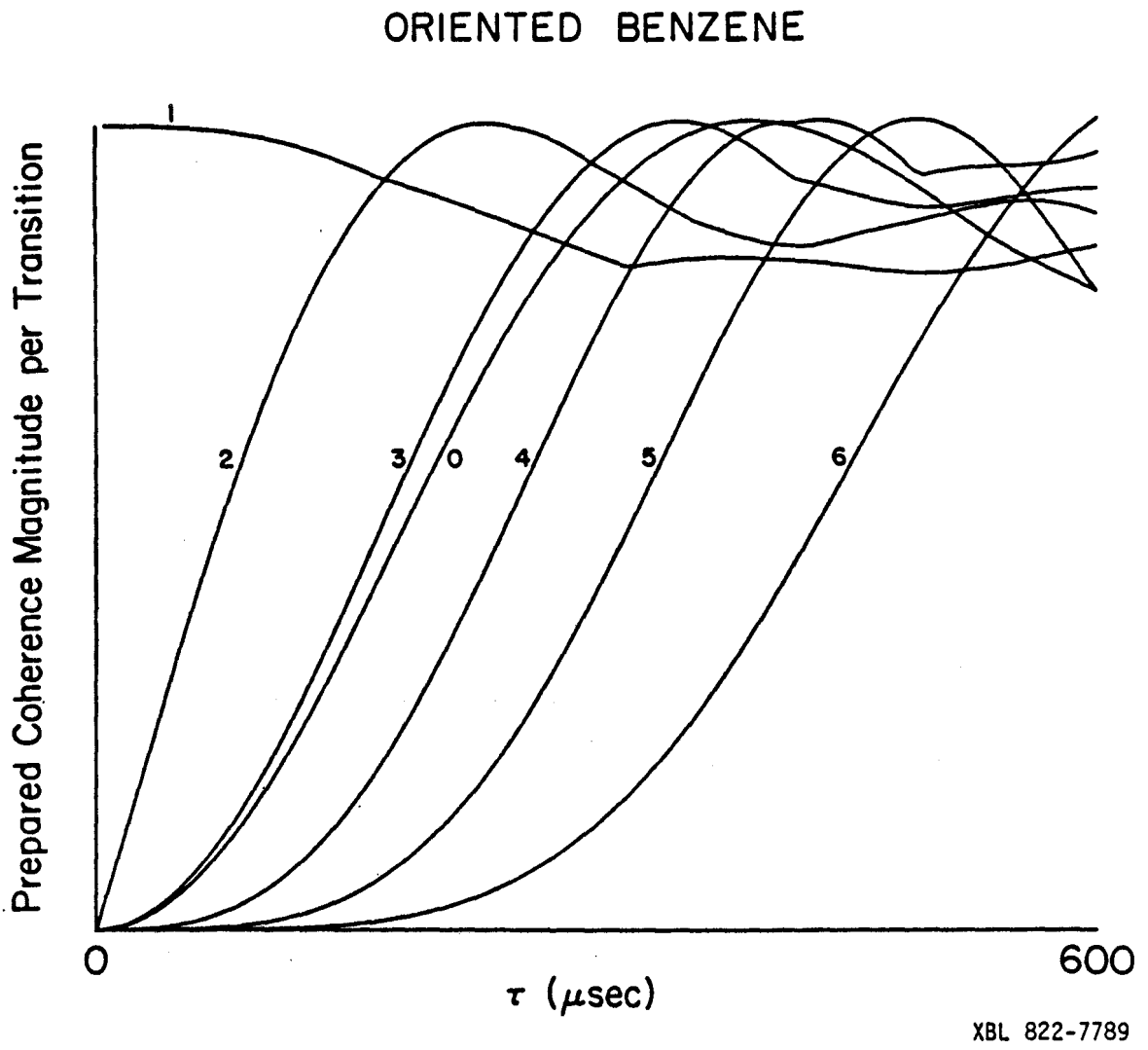

Figure V.7 Average prepared coherence magnitude at short values of τ for oriented benzene, with the same type of pulse sequence as in Figure V.4. The height of each curve has been normalized, and the τ power dependences calculated for the coherences match the values in the last column of Table V.1. All orders of coherence are present when $2\pi|\bar{D}|\tau \approx \pi/2$ or $\tau \approx 570$ μsec.

single-quantum coherence can be created; as τ increases, other orders of coherence appear. Higher-quantum transitions, in a sense more forbidden, require more time to be pumped. This dependence on τ can be quantified by expanding the prepared density matrix in a power series and evaluating commutators, as detailed in Ref. 55:

$$\beta P = e^{-i\mathcal{H}_x \tau} \rho_0 e^{i\mathcal{H}_x \tau}$$

$$= \rho_0 + i\tau [\rho_0, \mathcal{H}_x] - \frac{\tau^2}{2} [[\rho_0, \mathcal{H}_x], \mathcal{H}_x] + \ldots \quad \text{(V.14)}$$

(ρ_0 can be βI_z or βI_x, depending on the phase of the preparation pulses.) Alternately, one can expand Eq. V.7 and use the computer to calculate the $(P_{jk})_n$ terms:

$$P_{jk} = (P_{jk})_0 + i(P_{jk})_1 \tau - \frac{1}{2} (P_{jk})_2 \tau^2 + \ldots \quad \text{(V.15a)}$$

$$(P_{jk})_n = \sum_a \sum_b B_{ab} (\omega_{ba})^n \quad . \quad \text{(V.15b)}$$

The first non-zero commutator or $(P_{jk})_n$ term in the expansion determines the growth of coherence magnitude for short τ values. The exponents describing the τ power dependence of prepared coherence magnitude for different values of ΔM are listed in Table V.1. The τ power exponents for MQ spectral <u>intensity</u> in a $t_2 = \tau$ experiment would be double these numbers, since the effects

Table V.1

Dependence on τ of Multiple-Quantum Coherences Produced by the Sequence $90\phi - \tau - 90y$

		Initial τ power dependence		
	ΔM	$\phi=-90°$ [a]	$\phi=0°$ [a]	$\phi=-45°$ [b]
Anisotropic systems	0	2	1	1 [c]
	1	1	0	0
	2	1	2	1
	3	3	2	2
	4	3	4	3
	n(even)	n-1	n	n-1
	n(odd)	n	n-1	n-1
Isotropic systems	0	2	1	1
	1	1	0	0
	2	3	4	3
	3	5	6	5
	4	7	8	7
	n(even)	2n-1	2n	2n-1
	n(odd)	2n-1	2n	2n-1

[a] For systems without chemical shift differences, $\phi=-90°$ is even-selective and $\phi=0°$ is odd-selective when $\Delta\omega=0$.

[b] $\phi=-45°$ is equivalent to a superposition of $\phi=-90°$ and $\phi=0°$ results.

[c] In systems without chemical shift differences, only even-selective terms can prepare zero-quantum coherence. For these systems, the appearance of zero-quantum coherence is therefore proportional to τ^2.

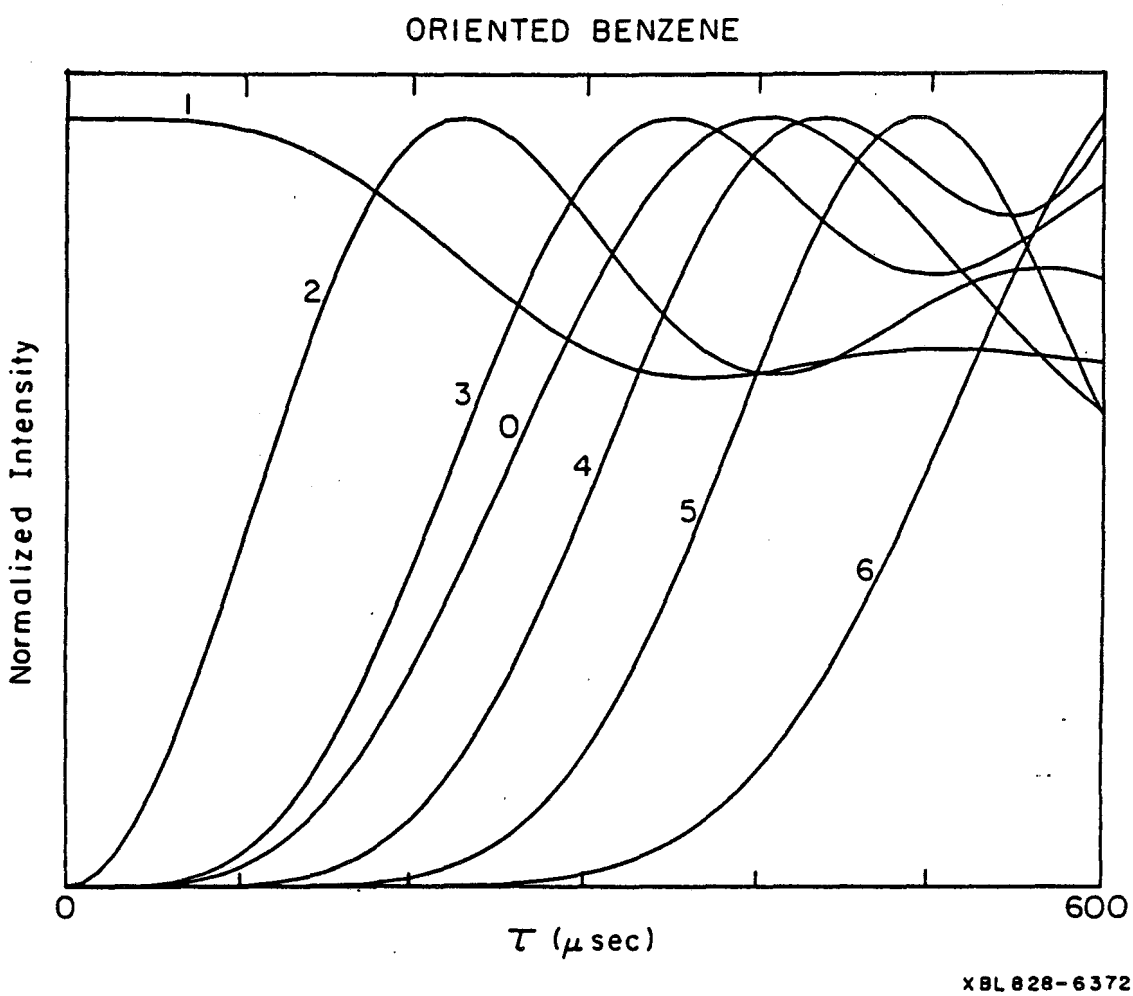

Figure V.8 Intensity per transition for each MQ order of oriented benzene as a function of $t_2 = \tau$. (All seven curves are normalized to the same height.) The growth of n-quantum intensity ($n > 0$) is proportional to τ^{2n-2}; the growth of zero-quantum intensity is proportional to τ^4.

of both preparation and detection must be included. The growth of normalized intensities as a function of $t_2=\tau$ for oriented benzene is shown in Fig. V.8.

As an added feature of Table V.1, the anisotropic spin systems we have been considering are compared with isotropic liquid systems. The fundamental difference between the two is the existence of non-scalar dipolar couplings in anisotropic systems. These couplings greatly facilitate the creation of multiple-quantum coherence; not only are they roughly 100 times larger than the J-couplings present in liquids, but their very form is such that lower powers of τ are sufficient to produce coherence [55].

5.4 τ-Independent Spectra

We turn now to the question of line intensities in the limit of a spectrum averaged over all possible values of τ. Such a spectrum should contain the "intrinsic" intensity for each line, free from the distortions due to a limited range of τ values.

5.4.1 The Statistical Limit Model

The simplest estimate of τ-independent intensities is to assume that in the limit of long preparation times each symmetry-allowed coherence in the prepared density matrix will have the same magnitude but random phase. In this statistical limit, all symmetry-allowed transitions are excited equally [40]. Figure V.9a displays the statistical-limit multiple-quantum magnitude spectrum for benzene. Such spectra are relatively easy to calculate but ignore the fact that some transitions are inherently stronger than others. In particular, these spectra often underestimate the intensity of higher-quantum lines, as will be discussed later.

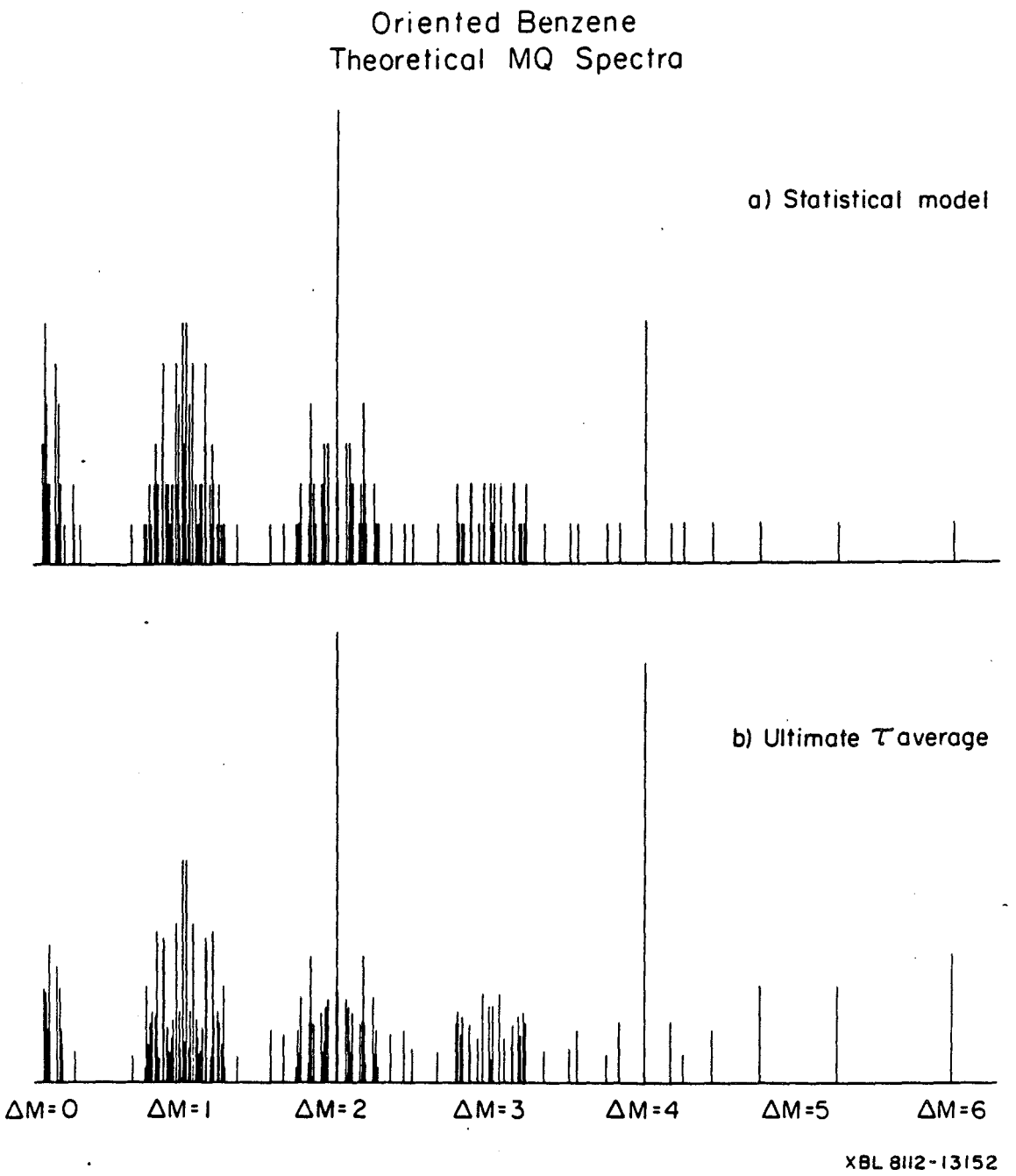

Figure V.9 Two τ-independent spectra calculated for oriented benzene. (a) The statistical-limit spectrum, in which every allowed transition is weighted equally. (b) The "ultimate" τ average spectrum.

For the $\tau=t_2$ MQ experiment, the total magnitude spectrum intensity plus the sum of the squares of the associated populations is given by

$$\beta \sum_j \sum_k |P_{jk}^2| = \beta \, \mathrm{Tr}\{P^2\} \quad . \tag{V.16}$$

Since the trace is invariant to unitary transformations,

$$\mathrm{Tr}\{P^2\} = \mathrm{Tr}\{I_z^2\} = N \, 2^{(N-2)} \quad . \tag{V.17}$$

The number of density matrix elements is 2^{2N} (coherences plus populations). The statistical-limit intensity per transition in multiples of β is thus $N \, 2^{-(N+2)}$ and the statistical-limit value for coherence magnitude $|P_{jk}|$ is just the square root of this number.

The integrated spectral intensity per order is merely the intensity per transition times the number of allowed transitions. For non-symmetric systems, recall (from section 4.3) that the number of ΔM-quantum transitions is given by the following expressions:

$$\binom{2N}{N-\Delta M} \qquad \text{for } \Delta M \neq 0 \quad ,$$

$$\frac{1}{2}\left[\binom{2N}{N} - 2^N\right] \qquad \text{for } \Delta M = 0 \quad ,$$

or roughly

$$\frac{4^N}{\sqrt{N\pi}} \, e^{-(\Delta M)^2/N} \qquad \text{for } \Delta M \neq 0 \quad .$$

The integrated statistical-limit intensities per order in non-symmetric four, six, and eight-spin systems are listed in Table V.2. It can be seen that the statistical model suggests that simple non-selective excitation of high-quantum transitions will be very difficult to achieve.

5.4.2 Symmetry-Adjusted Statistical-Limit Intensities

A somewhat more accurate model for systems with symmetry is to calculate the statistical-limit intensity for each representation, equal to the initial magnetization $\beta\ \mathrm{Tr}(I_z^2)$ available to the representation divided by the number of elements in its reduced density matrix. This procedure is appropriate because each representation is in essence a separate system and evolves independently.

As an example, the A_1 representation of benzene contains thirteen states--one with M=3, one with M=2, three with M=1, and three with M=0, plus equivalent totals for M<0. Hence

$$\mathrm{Tr}(I_z^2) = 2[1\cdot(3)^2 + 1\cdot(2)^2 + 3\cdot(1)^2] = 32 \quad , \qquad (V.18)$$

and the symmetry-adjusted intensity per A_1 transition is

$$\frac{32}{(13)^2}\,\beta = 0.189\ \beta \quad , \qquad (V.19)$$

8.08 times the simple statistical-limit value of 0.0235 β for a six-spin system.

Table V.2

Integrated Statistical-Limit Intensities Vs. Multiple-Quantum Order for Systems Without Symmetry

in multiples of $\beta = (\omega_0/kT)(2^{-N})$

ΔM	8 spins	6 spins	4 spins
0	49.27	10.08	1.688
1	89.38	18.56	3.500
2	62.56	11.60	1.750
3	34.13	5.156	0.500
4	14.22	1.547	0.063
5	4.375	0.281	
6	0.938	0.023	
7	0.125		
8	0.008		

Table V.3 gives the symmetry-adjusted statistical-limit intensity per transition for the various representations of several by-now-familiar molecules. A number of conclusions can be drawn from the data: (1) When the overall density matrix is partitioned according to representation, the number of allowed coherences drops considerably. As a result, the intensities of all remaining transitions are several times greater than the simple statistical-limit value of $\beta N 2^{-(N+2)}$. (2) Different representations in general have different average intensities, although for a given molecule these intensities vary by less than a factor of two or three. (3) For a given number of spins, smaller representations tend to have higher average intensities.

In Table V.4, symmetry-adjusted statistical-limit intensities are given as a function of ΔM. In each case the N-quantum and (N+1)-quantum lines, which are always A_1 transitions, have the same intensity. Beyond that it is difficult to say anything profound: in acetaldehyde, benzene, and disubstituted biphenyl, the intensity per transition increases modestly from $\Delta M=0$ to $\Delta M=8$, but hexane-d6 shows a slight decline over the same range.

The simple and symmetry-adjusted statistical-limit spectra for oriented benzene are comparable in appearance. The major difference between the two spectra when plotted to the same height is that the E-representation lines are smaller in the symmetry-adjusted spectrum, especially the E_2 lines.

The calculation of symmetry-adjusted intensities is eminently straightforward and naturally more accurate than the

Table V.3

Symmetry-Adjusted Statistical-Limit Intensities per Transition

Molecule	Representation	Number of states	$Tr\{I_z^2\}$	Intensity per transition (multiples of β)	Intensity per transition: Relative to simple statistical model
acetaldehyde	A_1	8	12.0	0.1875	3.0
	E	8	4.0	0.1250	2.0
benzene	A_1	13	32.0	0.1893	8.079
	B_1	7	10.0	0.2041	8.708
	B_2	3	2.0	0.2222	9.482
	E_1	2x9	2x12.0	0.1481	6.321
	E_2	2x11	2x14.0	0.1157	4.937
4,4'-disubstituted biphenyl	A_1	55	144.0	0.0476	6.093
	A_2	15	16.0	0.0711	9.102
	B_1	21	32.0	0.0726	9.288
	B_2	45	96.0	0.0474	6.068
	E	2x60	2x112.0	0.0311	3.982
$CD_3(CH_2)_4CD_3$ chain	A_1	76	176.0	0.0305	3.900
	B_1	60	112.0	0.0311	3.982
	B_2	60	112.0	0.0311	3.982
	B_3	60	112.0	0.0311	3.982

Table V.4

Symmetry-Adjusted Statistical-Limit Intensities per Transition

in multiples of $\beta = (\omega_0/kT)(2^{-N})$

ΔM	Acetaldehyde	Benzene	4,4'-disubstituted biphenyl	$CD_3(CH_2)_4CD_3$ chain
0	0.1625	0.1470	0.0392	0.0309
1	0.1625	0.1491	0.0395	0.0309
2	0.1750	0.1527	0.0396	0.0309
3	0.1875	0.1545	0.0396	0.0309
4	0.1875	0.1714	0.0402	0.0308
5		0.1893	0.0407	0.0308
6		0.1893	0.0432	0.0307
7			0.0476	0.0305
8			0.0476	0.0305

simple statistical approach. If the couplings and chemical shifts are known however, a little computation yields a far more realistic set of τ-independent intensities, as presented in the next section.

5.4.3 Ultimate τ Average Intensities

This alternate approach, for $t_2 = \tau$, is to actually average the τ-dependence contained in the expression for the magnitude of a given line. An expression for this "ultimate" τ average can be derived as follows. From Eq. V.9,

$$<|\underline{S}_{jk}|>_\tau = \beta<|P_{jk}|^2>_\tau = \beta<\mathrm{Re}(P_{jk})^2 + \mathrm{Im}(P_{jk})^2>_\tau \quad . \qquad (V.20)$$

Using Eq. V.7,

$$\mathrm{Re}(P_{jk}) = \sum_a \sum_b B_{ab} \cos\omega_{ba}\tau \quad . \qquad (V.21a)$$

and

$$\mathrm{Im}(P_{jk}) = \sum_a \sum_b B_{ab} \sin\omega_{ba}\tau \quad . \qquad (V.21b)$$

$$<|\underline{S}_{jk}|>_\tau = \beta < \sum_a \sum_b \sum_{a'} \sum_{b'} B_{ab}B_{a'b'} \cos(\omega_{ba}-\omega_{b'a'})\tau>_\tau$$

$$= \beta \sum_a \sum_b B_{ab}^2 + \beta \sum_a{}' \sum_b{}' \sum_{a'}{}' \sum_{b'}{}' B_{ab}B_{a'b'} \ , \qquad (V.22)$$

where the second set of summations is restricted: ω_{ba} must equal $\omega_{b'a'}$ and B_{ab}^2 terms are excluded.

Except for accidental degeneracies, there are only three circumstances for which single-quantum frequencies ω_{ba} and $\omega_{b'a'}$ would be expected to be equal. The first is the case of degenerate eigenstates in multi-dimensional irreducible representations, such as the doubly-degenerate E_1 or E_2 states of benzene. Calculations indicate, however, that the sum over all $B_{ab}B_{a'b'}$ terms associated with the transitions between two sets of degenerate states is always zero.

The second cause for overlap of single-quantum frequencies is the existence of spin-inversion states. In this case $\omega_{\bar{b}\bar{a}} = \omega_{ba}$ and

$$<|\underline{S}_{jk}|>_\tau = \beta \sum_a \sum_b B_{ab}^2 + \beta \sum_a \sum_b B_{ab} B_{\bar{a}\bar{b}} \quad . \qquad \text{(V.23)}$$

$B_{\bar{a}\bar{b}}$ can be shown to equal B_{ab} for ΔM even and $-B_{ab}$ for ΔM odd; hence

for even-quantum transitions, $<|\underline{S}_{jk}|>_\tau = 2\beta \sum_a \sum_b B_{ab}^2$,

(V.24a)

for odd-quantum transitions, $<|\underline{S}_{jk}|>_\tau = 0$. (V.24b)

This result is merely a manifestation of the even-quantum selectivity of the $90\bar{y} - \tau - 90y$ preparation sequence applied to systems with purely bilinear Hamiltonians. With the more general sequence

$$90\bar{y} - \tau - 90\phi - t_1 - 90\bar{\phi} - \tau \qquad (\bar{\phi} = \pi+\phi) \qquad ,$$

the dependence of the ultimate τ average on the phase of the second and third pulses for these systems is as follows:

for even-quantum transitions, $\langle|\underline{S}_{jk}|\rangle_\tau = 2\beta \cos^2\phi \sum_a \sum_b B_{ab}^2$,

(V.25a)

for odd-quantum transitions, $\langle|\underline{S}_{jk}|\rangle_\tau = 2\beta \sin^2\phi \sum_a \sum_b B_{ab}^2$.

(V.25b)

To avoid the effect of even-odd selectivity when analyzing systems with no chemical shift differences, we will choose $\phi = 45°$, for which $\langle|\underline{S}_{jk}|\rangle_\tau$ is simply $\beta\sum_a\sum_b B_{ab}^2$. This intensity is half that of the corresponding purely even-selective or odd-selective value.

(An additional curious and useful relationship for spin-inversion states: the ultimate τ average intensities of transitions $|j\rangle$ to $|k\rangle$, $|j\rangle$ to $|\bar{k}\rangle$, $|\bar{j}\rangle$ to $|k\rangle$, and $|\bar{j}\rangle$ to $|\bar{k}\rangle$ are equal.)

The third cause for overlap of frequencies ω_{ba} and $\omega_{b'a'}$ is the extra single-quantum degeneracy in certain highly symmetric systems, such as D_2 or C_{4v} four-spin systems with $\bar{D}=0$ or with no J-coupling. Only for these special cases must the sum over

$B_{ab}B_{a'b'}$ terms be actually calculated to obtain the correct intensity. Of course, the inclusion of $B_{ab}B_{a'b'}$ terms re-introduces even-quantum selectivity for "shiftless" systems when $\Delta\omega=0$. To eliminate this effect yet retain the corrected intensity values, the search for overlapping single-quantum frequencies should be restricted to either the upper or the lower triangular portion of the density matrix.

5.4.3.1 Simplifying the Calculation

When the $B_{ab}B_{a'b'}$ terms can be ignored, the computation of ultimate τ average intensities is greatly simplified. If we let $\mathcal{A}_{\ell m} = A^2_{\ell m}$ and $\mathcal{X}_{\ell m} = X^2_{\ell m}$, the τ-averaged intensity of any transition $|j\rangle$ to $|k\rangle$ is just $\beta(\mathcal{A}^{\dagger}\mathcal{X}\mathcal{A})_{jk}$. This calculation requires no more multiplication than the calculation of $\mathcal{S}_{jk}$ for a single value of τ: roughly $2\cdot 2^{2N} + 2\cdot 2^{3N}$ real-number multiplications for a general N-spin system once A and X have been computed. {As a comparison, the use of Eq. V.24a for every transition would entail $[(2^{2N}-2^N)/2]\cdot[2\cdot 2^{3N}]$ or approximately 2^{5N} multiplications.} The ultimate τ average spectrum for most systems can thus be generated much more quickly than an average over a number of discrete τ values.

Even greater computational speed is possible if only the average or integrated intensity <u>per MQ order</u> is desired. We first define $\mathcal{A}'$, a 2^N x (N+1) matrix, as follows:

$$\mathcal{A}'_{iJ} = \sum_j \mathcal{A}_{ij}\ \delta\ (J,M_j) \quad , \qquad \text{(V.26)}$$

where $\delta(J,M_j)$ is unity when $J=M_j$ and zero otherwise. The integrated ultimate τ average intensity $\langle \underline{S}_{JK} \rangle$ for transitions between the M=J and M=K manifolds is in turn given by

$$\begin{aligned}
\langle \underline{S}_{JK} \rangle &= \beta \sum_j \sum_k |P_{jk}|^2 \, \delta(J,M_j) \, \delta(K,M_k) \\
&= \beta \sum_j \sum_k (A^{\dagger} X A)_{jk} \, \delta(J,M_j) \, \delta(K,M_k) \\
&= \beta \sum_j \sum_k \sum_a \sum_b A_{aj} \, X_{ab} \, A_{bk} \, \delta(J,M_j) \, \delta(K,M_k) \\
&= \beta \sum_a \sum_b [\sum_j A_{aj} \, \delta(J,M_j)] \, X_{ab} [\sum_k A_{bk} \, \delta(K,M_k)] \\
&= \beta \sum_a \sum_b A'_{aJ} \, X_{ab} \, A'_{bK} \\
&= \beta \, [(A')^{\dagger} X \, A']_{JK} \quad .
\end{aligned} \tag{V.27}$$

The integrated intensity between manifolds J and K is thus given by one element of an (N+1)x(N+1) matrix. The integrated n-quantum intensity is then

$$\langle \underline{S}_n \rangle = \sum_{J=0}^{N-n} \langle \underline{S}_{J,J+n} \rangle \quad . \tag{V.28}$$

Only on the order of $2 \cdot 2^{2N} + 2 \cdot (N+1) \cdot 2^{2N}$ multiplications are required once A and X are computed, a substantial savings over the previous total of $2 \cdot 2^{2N} + 2 \cdot 2^{3N}$ for large N.

In the pursuit of still more rapid evaluation of intensities as a function of MQ order, one is tempted to reduce the problem even further. For an <u>approximate</u> integrated intensity, the following (N+1)x(N+1) matrices could be defined:

$$A''_{JK} = \sum_j \sum_k A_{jk}\, \delta(J,M_j)\, \delta(K,M_k)$$

$$= \sum_j A'_{jK}\, \delta(J,M_j) \quad , \qquad \text{(V.29)}$$

$$X''_{JK} = \frac{1}{n_{JK}} \sum_j \sum_k X_{jk}\, \delta(J,M_j)\, \delta(K,M_k) \quad . \qquad \text{(V.30)}$$

where n_{JK} is the number of matrix elements X_{jk} with M_j=J and M_k=K. (Because X is a single-quantum operator, X''_{JK}=0 unless |J-K|=1.) One would expect by analogy to Eq. V.27 that

$$\langle \underline{S}_{JK} \rangle \approx \beta[(A'')^{\dagger}\, X''\, A'']_{JK} \quad . \qquad \text{(V.31)}$$

However, this is going too far: $\langle S_{JK} \rangle$ by this formula turns out to be exactly the statistical-limit integrated intensity for transitions between the M=J and M=K manifolds. That is,

$$[(A'')^{\dagger}\, X''\, A'']_{JK} = (n_{JK}) \cdot [N\, 2^{-(N+2)}] \quad . \qquad \text{(V.32)}$$

<u>5.4.3.2 Some Ultimate τ Average Spectra</u>

Figure V.9b displays the ultimate τ average spectrum of benzene. Although both this spectrum and the statistical-limit

spectrum simulate the general features of the experimental results, the ultimate τ average approach more correctly predicts the intensity of individual lines. All transitions are not pumped equally; in particular, the lone six-quantum transition is appreciably stronger than an average isolated lower-quantum transition.

Figure V.10 compares the experimental MQ spectrum of an eight-proton cyanobiphenyl liquid crystal (kindly supplied by Steven Sinton) with statistical-limit and ultimate τ average simulations. Of the two, clearly the ultimate τ average spectrum more accurately models such experimental features as the bimodality of the one-quantum region, the side peaks of the two-quantum region, and the enhanced intensity of the higher-quantum lines. That these latter transitions are in fact more intense than the ultimate τ average calculation would predict reflects a choice of experimental τ values fortuitous for the creation of high-quantum coherence.

5.5 Higher-Quantum Selectivity in the Ultimate τ Average

It is worthwhile to study the ultimate τ average intensity per transition as a function of multiple-quantum order. Results for a number of molecules are listed in Table V.5. In each case, the integrated intensity per MQ order decreases as ΔM increases, but the average intensity per transition is greater for larger ΔM. This increase in intensity per transition is most pronounced for systems possessing a high degree of symmetry or for systems

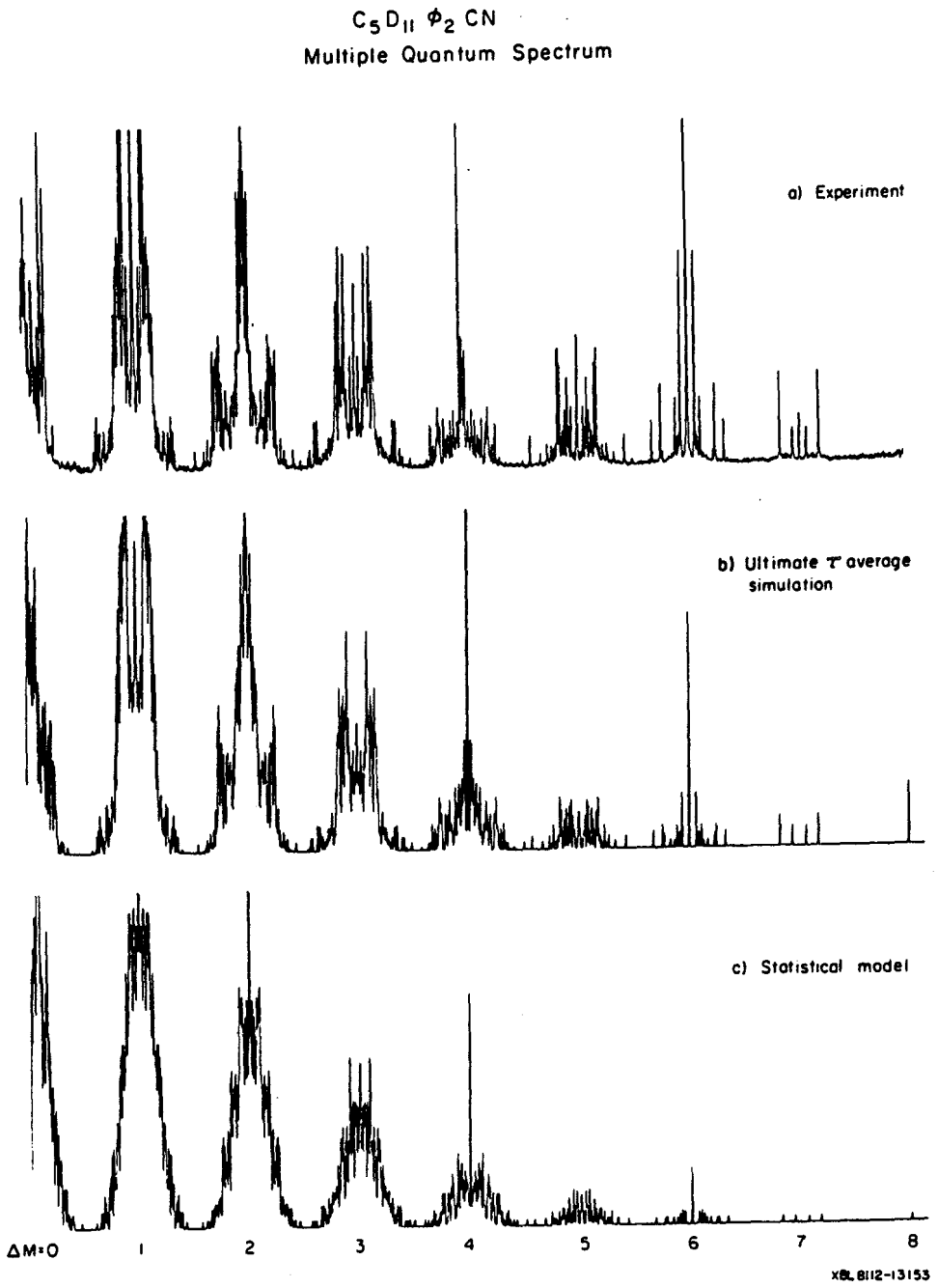

Figure V.10 (a) The proton TPPI MQ spectrum of a nematic n-pentyl-d_{11}-cyanobiphenyl liquid crystal, obtained by Steven Sinton. Six individual spectra with τ values ranging from 4 to 14 msec were averaged together. The 8Q line does not appear due to the choice of TPPI parameters, and the center line in the 7Q region is a TPPI artifact. (b) and (c) Two τ-independent simulations assuming D_4 spin symmetry. In all three spectra, the strongest 0Q,1Q,2Q, and 4Q lines have been clipped to better emphasize the overall lineshape.

Table V.5

Ultimate τ Average Intensity Vs. Multiple-Quantum Order for Various Molecules

in multiples of $\beta = (\omega_0/kT)(2^{-N})$

	Benzene	Cyclopropane[a]	Cyclo-pentadiene[a]	2,5-Dichloro-acetophenone[a]	4,4'-Disubstituted biphenyl[b]	$CD_3(CH_2)_4CD_3$
$\overline{D_{ij}}/(\overline{D_{ij}^2})^{1/2}$	0.777	0.567	0.028	0.225	0.519	0.080
Integrated intensity:						
ΔM = 0	4.354	5.006	6.632	6.917	33.06	29.69
1	17.08	17.36	17.56	17.32	83.89	83.92
2	11.72	12.19	11.83	11.58	62.62	63.16
3	6.007	6.002	5.820	6.039	36.59	36.87
4	3.289	3.020	2.602	2.388	20.09	20.49
5	0.909	0.642	0.625	0.640	6.920	6.782
6	0.605	0.379	0.164	0.126	3.251	3.083
7					0.594	0.432
8					0.354	0.223
Intensity per transition:						
ΔM = 0	0.109	0.132	0.060	0.051	0.029	0.020
1	0.147	0.152	0.072	0.060	0.038	0.029
2	0.148	0.158	0.073	0.063	0.040	0.031
3	0.177	0.177	0.075	0.069	0.043	0.034
4	0.274	0.252	0.093	0.075	0.053	0.043
5	0.455	0.321	0.104	0.080	0.060	0.048
6	0.605	0.379	0.164	0.126	0.108	0.086
7					0.148	0.108
8					0.354	0.223

[a]Coupling constants from Ref. 25.

[b]Coupling constants from Ref. 56.

[c]Coupling constants courtesy of G. Drobny, private communication, for the all-trans configuration.

whose dipolar couplings are similar in value, for which the quantity

$$d = \frac{\overline{D_{ij}}}{(\overline{D_{ij}^2})^{1/2}} \tag{V.33}$$

is close to 1.0. We now shall explore the relationship between the value of d and the enhancement of higher-quantum coherence.

5.5.1 Equivalent-Spin Systems

Consider the case of N magnetically fully equivalent spins in an anisotropic medium--an example would be the fluxional ten-spin molecule bullvalene dissolved in a liquid crystal [127]. For such a system with unique dipolar coupling constant D and indirect spin-spin coupling constant J, d = 1.0 and

$$\mathcal{H} = \frac{3}{2} D \sum_{j<}^{N} \sum_{k}^{N} I_{zj} I_{zk} + (J - \frac{1}{2} D) \sum_{j<}^{N} \sum_{k}^{N} \underset{\sim}{I}_j \cdot \underset{\sim}{I}_k - \Delta\omega \, I_z \quad . \tag{V.34}$$

The second term describes scalar coupling between equivalent spins and has no effect on the spectrum [117]. The remaining terms commute with $\underset{\sim}{I}^2$; hence the eigenstates can be separated into representations labeled by the value of I(I+1). As an example, the states of a four spin system of this type divide into one quintet, three triplets, and two singlets. The number of allowed transitions is thus greatly reduced. In particular, there can be no zero-quantum transitions.

Warren Warren [55] has calculated the resulting line intensities using the effective preparation Hamiltonian

$$\mathcal{H}_x = \frac{3}{2} D \sum_{j<}^{N} \sum_{k}^{N} I_{xj} I_{xk} - \Delta\omega\, I_x \quad . \tag{V.35}$$

The two terms of $\mathcal{H}_x$ commute, so

$$\beta P = \beta\{\exp(-i\,\frac{3}{2} D\tau \sum_{j<}^{N} \sum_{k}^{N} I_{xj} I_{xk})\}(\cos\Delta\omega\tau\; I_z + \sin\Delta\omega\tau\; I_y)$$

$$\{\exp(i\,\frac{3}{2} D\tau \sum_{j<}^{N} \sum_{k}^{N} I_{xj} I_{xk})\}. \tag{V.36}$$

This expression can be evaluated using the relationships

$$\exp(-i\,\frac{3}{2} D\tau\; I_{xj} I_{xk}) I_{zj}\; \exp(i\,\frac{3}{2} D\tau\; I_{xj} I_{xk})$$

$$= \cos\,(\frac{3D\tau}{4}) I_{zj} - 2\,\sin\,(\frac{3D\tau}{4}) I_{yj} I_{xk} \tag{V.37a}$$

and

$$\exp(-i\,\frac{3}{2} D\tau\; I_{xj} I_{xk}) I_{yj}\; \exp(i\,\frac{3}{2} D\tau\; I_{xj} I_{xk})$$

$$= \cos\,(\frac{3D\tau}{4}) I_{yj} + 2\,\sin\,(\frac{3D\tau}{4}) I_{zj} I_{xk} \quad . \tag{V.37b}$$

The prepared N-quantum coherence, given by the coefficient of $\prod_{i=1}^{N} I_{+i}$, is

$$(-\frac{i\beta N}{2})\ (\cos\Delta\omega\tau)\ [\sin\ (\frac{3D\tau}{4})]^{(N-1)} \qquad \text{for N even,} \qquad (V.38a)$$

$$(\frac{i\beta N}{2})\ (\sin\Delta\omega\tau)\ [\sin\ (\frac{3D\tau}{4})]^{(N-1)} \qquad \text{for N odd.} \qquad (V.38b)$$

The τ-averaged intensity for the N-quantum transition is

$$\beta\ N^2\ (\frac{1}{2})^{2N+1}\ \frac{(2N-2)!}{(N-1)!(N-1)!} \quad . \qquad (V.39)$$

Table V.6 presents these τ-averaged N-quantum intensities for several different values of N. Also included are computer-calculated values of τ-averaged integrated intensity for lower multiple-quantum orders of these equivalent-spin systems. When N=8, note that the integrated one-quantum and N-quantum intensities differ only by a factor of roughly 46; for a general 8-spin molecule, the difference would be a factor of 11440 in the statistical limit.

5.5.2 General Spin Systems

Now return to the problem of a general N-spin system with arbitrary D_{ij}'s. Let $\bar{D}$ be the average value of the N(N-1)/2 dipolar couplings. The dipolar Hamiltonian can be written as

$$\mathcal{H}_D = \sum_{j<}^{N}\sum_{k}^{N} (D_{jk}-\bar{D})(\frac{3}{2}\ I_{zj}I_{zk} - \frac{1}{2}\ \underset{\sim}{I}_j\cdot\underset{\sim}{I}_k) + \bar{D}\ \sum_{j<}^{N}\sum_{k}^{N} (\frac{3}{2}\ I_{zj}I_{zk} - \frac{1}{2}\ \underset{\sim}{I}_j\cdot\underset{\sim}{I}_k)\ ,$$

(V.40)

Table V.6

Integrated Ultimate τ Average Intensities Vs. Multiple-Quantum Order for Equivalent-Spin Systems in multiples of $\beta = (\omega_0/kT)(2^{-N})$

ΔM	8 spins	6 spins	4 spins
0	0	0	0
1	76.95	16.10	3.125
2	47.61	9.580	1.750
3	36.33	6.504	0.875
4	27.18	4.770	0.625
5	12.73	1.395	
6	10.21	1.107	
7	1.998		
8	1.676		

where the second term preferentially pumps higher-quantum transitions. In going from a symmetric to a nonsymmetric system, this term will become less important and the integrated intensities of these higher-quantum spectral regions will drop. However, the number of allowed lower-quantum transitions increases rapidly as the symmetry is reduced, especially in the one- and two-quantum orders. Thus the τ-averaged intensity per transition is greater for large ΔM, even in completely general systems.

To illustrate this, we have calculated ultimate τ average intensities for non-symmetric four-spin systems as a function of $\bar{D}$, the average value of the dipolar coupling. For each system, six dipolar couplings were generated randomly between ± 1000 Hz, and a constant value was added to each to fix the proper $\bar{D}$. Small random J-couplings were included, but no chemical shifts. Intensities from fifty different random systems were then averaged for each value of $\bar{D}$. Figure V.11 displays the resulting intensity per transition for each MQ order as the contribution of the average dipolar operator is varied. When $\bar{D}$ grows large compared to the range of dipolar couplings, the average four-quantum intensity naturally approaches its equivalent-spin value of 0.625 β, or ten times the statistical-limit prediction. The average zero-quantum intensity drops toward zero. When $\bar{D}$ = 1000 Hz, with dipolar couplings ranging from 0 to 2000 Hz, the four-quantum line intensity is 6.5 times greater than the statistical-limit value.

Even greater enhancement occurs when the number of spins increases, as illustrated in Fig. V.12 for N=6. Again, random

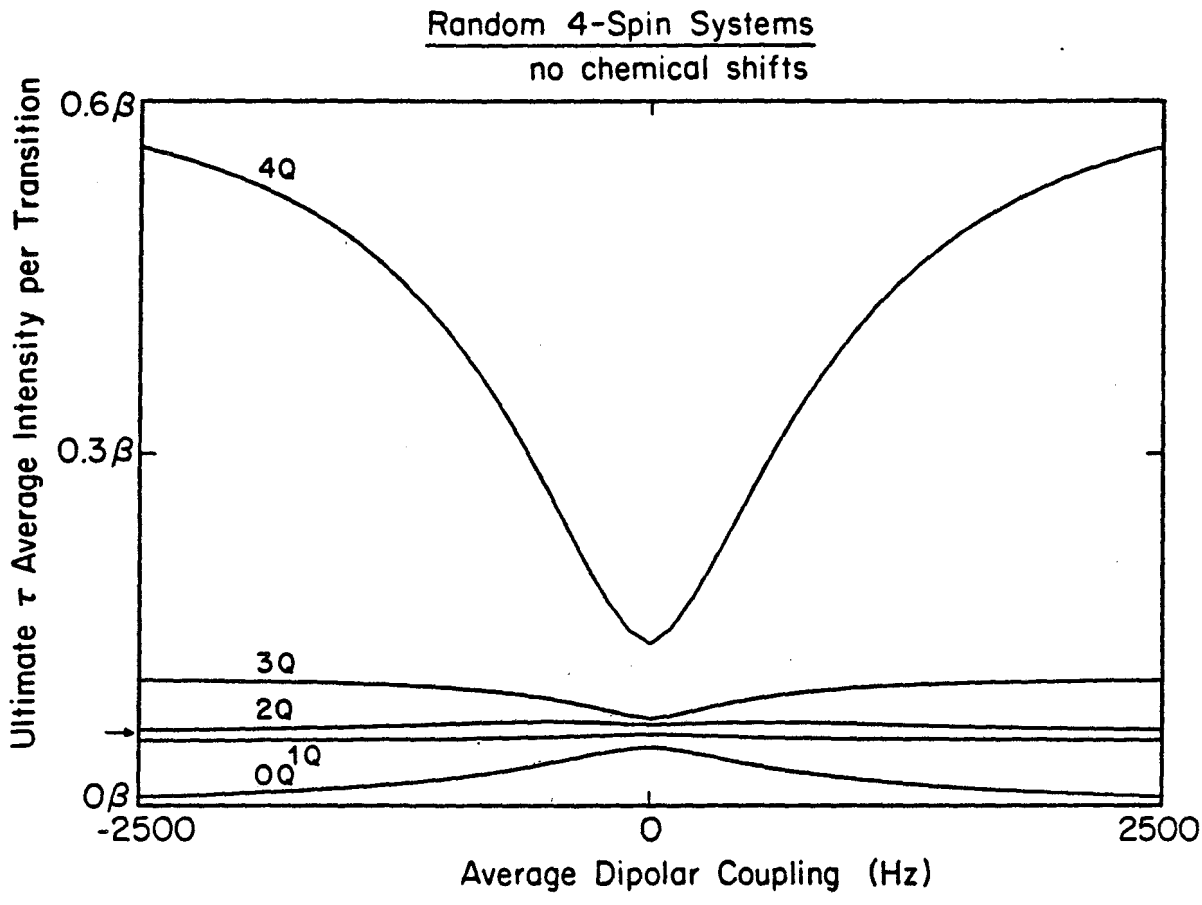

Figure V.11 Ultimate τ average intensity per transition for each MQ order as a function of the average dipolar coupling $\bar{D}$ in random four-spin systems. The arrow marks the statistical-limit intensity per transition (the same for all orders and all values of $\bar{D}$). Maximum range of D_{jk} values for each system: 2000 Hz.

dipolar couplings were generated between ± 1000 Hz and $\bar{D}$ then adjusted to the desired value. Small J-couplings were included but no chemical shifts, and intensities from 25 random "molecules" were averaged together for each $\bar{D}$ value. The ultimate τ average intensity of the six-quantum transition when $\bar{D}$ is comparable to the range of dipolar couplings is 27 times greater than the statistical-limit intensity per transition. The average five-quantum transition intensity is 3.9 times larger than the statistical value. For N=8, the comparable enhancements are 150 and 13.

The effect of chemical shifts is displayed for N=4 in Fig. V.13. For each line, dipolar and J-couplings were generated as described above. In addition, random chemical shifts within a specified range were included in the Hamiltonian. The four-quantum ultimate τ average intensities of 50 systems were averaged together for each point. The chemical shift range for curves a through g increases from ± 0 Hz to ± 3000 Hz; as the spread in chemical shift frequencies increases, the N-quantum enhancement is diluted, particularly for larger values of $\bar{D}$.

To summarize, nonselective excitation of high-quantum lines is, surprisingly, not so hopeless a procedure as the simple statistical-limit picture would imply, especially for systems with similar dipolar couplings. Even in completely general molecules, the residual selectivity of highly symmetric systems carries over and results in often sizeable improvement. This bodes well not only for ensemble-averaged MQ spectra but also for total spin

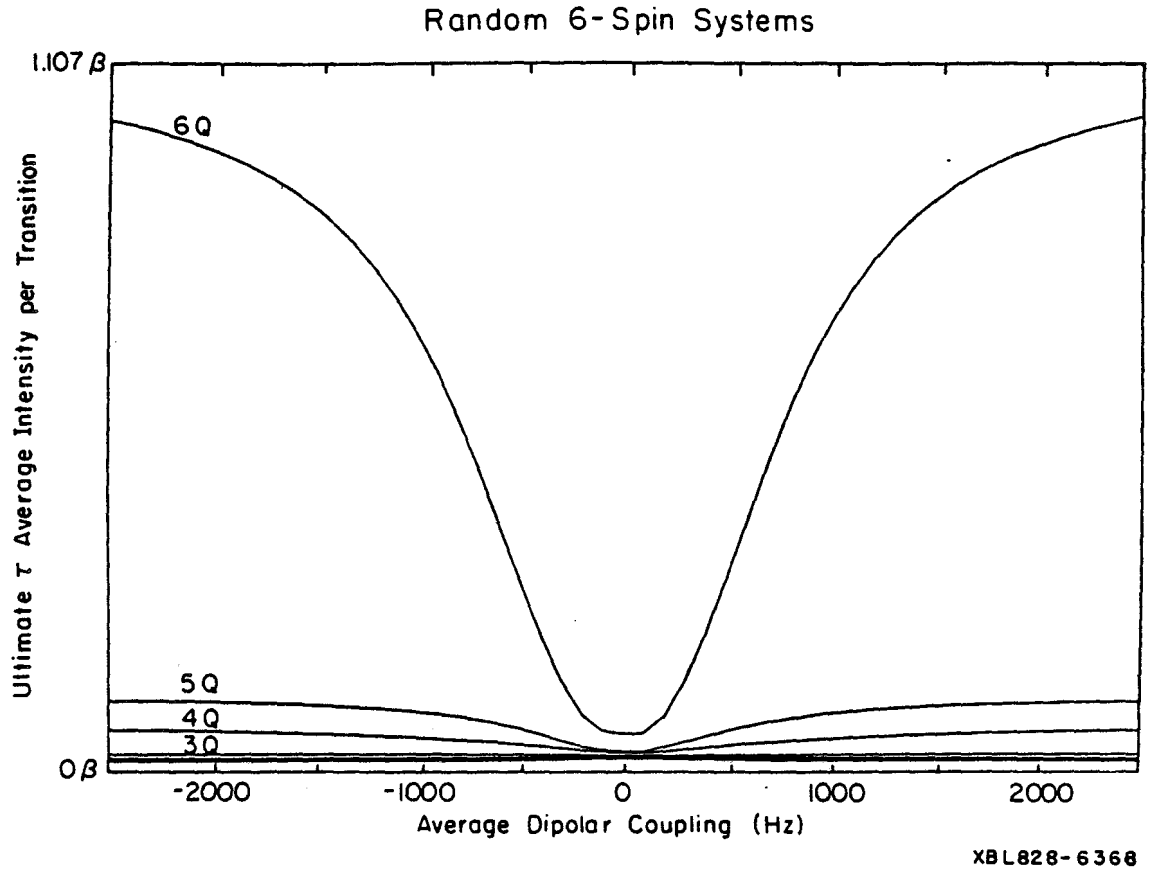

Figure V.12 Ultimate τ average intensity per transition for each MQ order as a function of the average dipolar coupling $\bar{D}$ in random six-spin systems with no chemical shifts. Zero-, one-, and two-quantum lines are bunched together at the bottom of the plot. Full vertical scale (1.107 β) marks the average six-quantum intensity in a system with all dipolar couplings equal. Maximum range of D_{jk} values for each system: 2000 Hz.

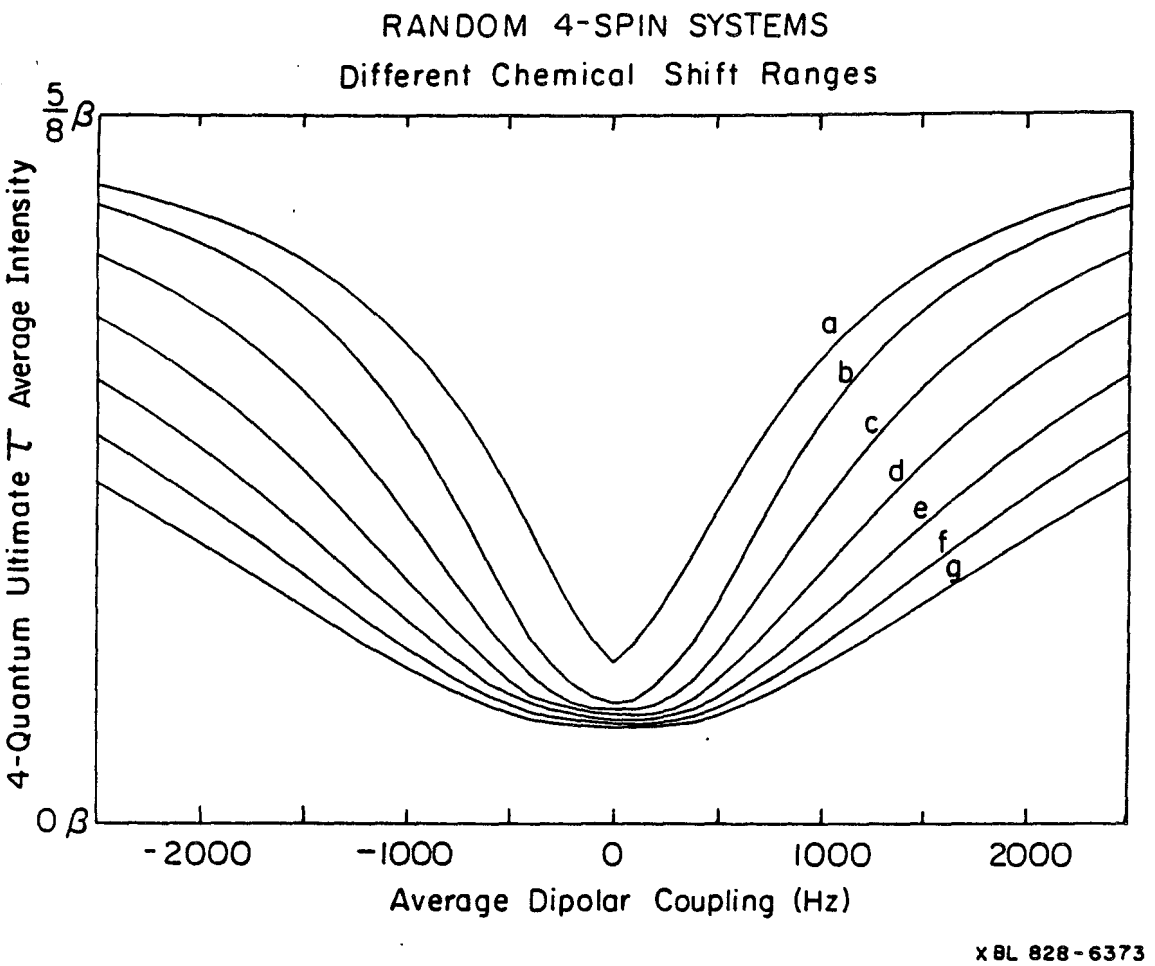

Figure V.13 Four-quantum ultimate τ average intensity as a function of the average dipolar coupling $\bar{D}$ in random 4-spin systems. Allowed ranges for random chemical shifts: (a) ±0 Hz, (b) ±500 Hz, (c) ±1000 Hz, (d) ±1500 Hz, (e) ±2000 Hz, (f) ±2500 Hz, (g) ±3000 Hz. Maximum range of D_{jk} values for each system: 2000 Hz.

coherence transfer echo experiments [119].

5.5.3 Residual Symmetry Effects When $\bar{D}$ Is Zero

It can be seen from Fig. V.11 that even when $\bar{D}$ equals zero, the four-quantum ultimate τ average intensity in a general four-spin system is still roughly twice as large as the statistical-limit value of 0.0625 β. This selectivity is due to residual effects from other symmetries. For example, the τ-averaged four-quantum intensity of a hypothetical four-spin C_{3v} system with no chemical shifts or J-couplings can be shown, after straightforward but lengthy evaluation of the appropriate matrices, to be given by the following formula:

$$<|\underline{S}_{4Q}|>_{\tau}(C_{3v}) = \frac{5}{64}\,\beta\,\frac{(29\,w^2 - 42\,vw + 45\,v^2)}{(7\,w^2 - 12\,vw + 9\,v^2)} \quad , \qquad (V.41)$$

where $v = D_{12} = D_{13} = D_{23}$ and $w = D_{14} = D_{24} = D_{34}$. The details of the derivation can be found in Appendix C. When $\bar{D} = 0$ ($v = -w$), the 4Q intensity is 0.324 β, or 5.18 times the statistical value. Some of this selectivity carries over to general four-spin systems with $\bar{D} = 0$.

Similarly, the average N-quantum intensity of a four-spin D_4 system with no J-couplings can also be calculated (back to Appendix C for the algebraic flourishes). In this molecule, we must be careful about degenerate single-quantum transitions--the simplified ultimate τ average formula $<|\underline{S}_{jk}|>_{\tau} = [A^{\dagger} X A]_{jk}$ is in fact incorrect for the D_4 case itself. Nonetheless, the

τ-averaged 4Q intensity of a distorted "quasi-D_4" molecule approaches the D_4 value:

$$<|S_{4Q}|>_\tau (D_4) = \frac{1}{8}\beta \frac{14 f^2 - 8 fg + 9 g^2}{4 f^2 - 4 fg + 3 g^2} , \qquad (V.42)$$

where $f = D_{12} = D_{23} = D_{34} = D_{14}$ and $g = D_{13} = D_{24}$. When $\bar{D} = 0$ ($g = -2f$), the ultimate τ average intensity is $11\beta/32 \approx 0.344\ \beta$.

The effect of general four-spin systems becoming more "D_4-like" is shown in Fig. V.14. For each system, six dipolar couplings were chosen randomly between ± 1000 Hz and adjusted such that $\bar{D} = 0$. Small J-couplings were also generated but no chemical shifts. An augmented coupling D' was then added to D_{12}, D_{23}, D_{34}, and D_{14}, while 2D' was subtracted from D_{13} and D_{24}, thereby keeping $\bar{D}$ constant but increasing the spread in coupling frequencies. D' was varied from -2500 Hz to 2500 Hz in increments of 100 Hz, and the 4Q intensities of 100 random systems were averaged together for each point. As $|D'|$ grows large compared to the range of dipolar couplings, the general spin systems more and more closely resemble the true D_4 system, and the 4Q intensities approach $11\beta/32$.

5.5.4 A Comparison of Two Eight-Spin Systems

To further illustrate the importance of $\bar{d}$ (the ratio of the average dipolar coupling to the r.m.s value) in its effect on the N-quantum signal, two eight-spin systems with random couplings but no chemical shifts are compared here. For system 1, dipolar

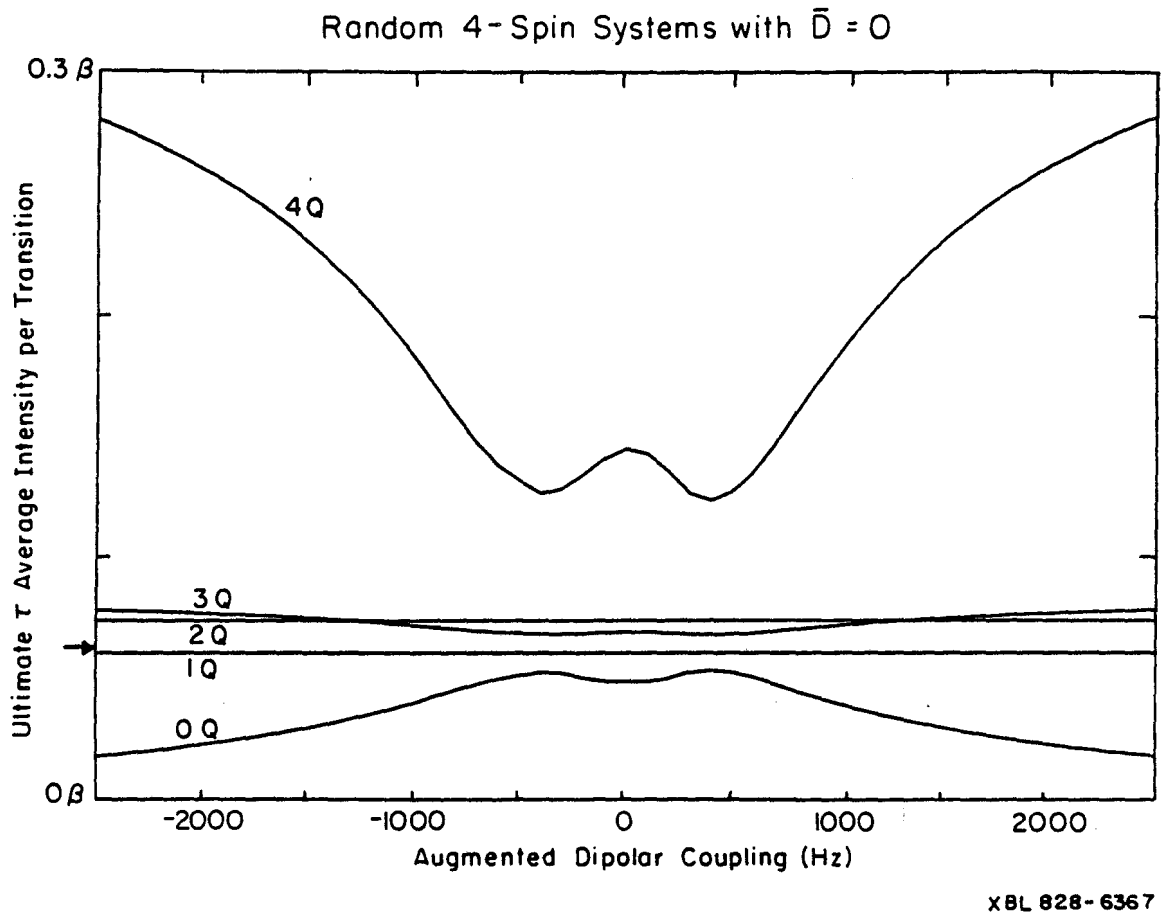

Figure V.14 Ultimate τ average intensity per transition for different MQ orders as a function of the "D_4-character" of random four-spin systems with $\bar{D} = 0$. Each point is an average over 100 such systems. D_{ij} values were chosen randomly between ±1000 Hz and adjusted so that $\bar{D} = 0$; a variable augmented dipolar coupling D' was then added to D_{12}, D_{23}, D_{34}, and D_{14} while 2D' was subtracted from D_{13} and D_{24}. As $|D'|$ increases, these random systems become more "D_4-like". The arrow marks the statistical limit intensity per transition.

couplings were generated between ± 500 Hz and then adjusted so that $\bar{D} = 0$. For system 2, 500 Hz was added to each of these D_{ij}'s. J-couplings, generated between ± 10 Hz, were the same in each case. Both sets of dipolar couplings are characterized by the same standard deviation, 297.4 Hz, but the value of d differs between the "molecules": d = 0 for system 1, while for system 2, d = 0.864. A comparison of various other parameters can be found in Table V.7. In addition, the prepared 8Q coherences and intensities as a function of τ are displayed in Figs. V.15 and V.16 (note the large difference in vertical scales). The eight-quantum intensity for system 2 varies far more periodically than that for system 1, and its ultimate τ average value is 67 times larger.

As stated earlier, the reason for this disparity lies in the similarity of system 2 to the case of eight fully equivalent spins. One eigenstate in each Zeeman manifold of system 2 approximates an equivalent-spin A_1 eigenstate. Recall the expression for N-quantum coherence:

$$P_{k\bar{k}} = 2i \sum_{a<b} B_{ab} \sin\omega_{ba} \tau \quad . \qquad (V.43)$$

The B_{ab} elements connecting the aforementioned eigenstates are far bigger than any other B_{ab} terms. These few large components give rise to both the size of the 8Q signal and its periodicity--effectively only a few sine terms contribute to its evolution.

Table V.7

A Comparison of Two Eight-Spin Systems

	System 1	System 2
$\bar{D}$	0.0 Hz	500 Hz
d	0.0	0.864
B_{ab} values for 8Q coherence:		
average	0.0	0.0
average deviation	2.72×10^{-4}	1.89×10^{-4}
standard deviation	8.49×10^{-4}	6.95×10^{-3}
largest value	0.0163	0.440
8Q ultimate τ average (even-selective sequence)	0.0330	2.209
8Q signal-results from 1001 τ values:		
$\langle\lvert P_{jk}\rvert\rangle$	0.1428	1.261
$\langle\lvert P_{jk}\rvert^2\rangle$	0.0324	2.249
$\langle\lvert P_{jk}\rvert^2\rangle/\langle\lvert P_{jk}\rvert\rangle^2$	1.587	1.415

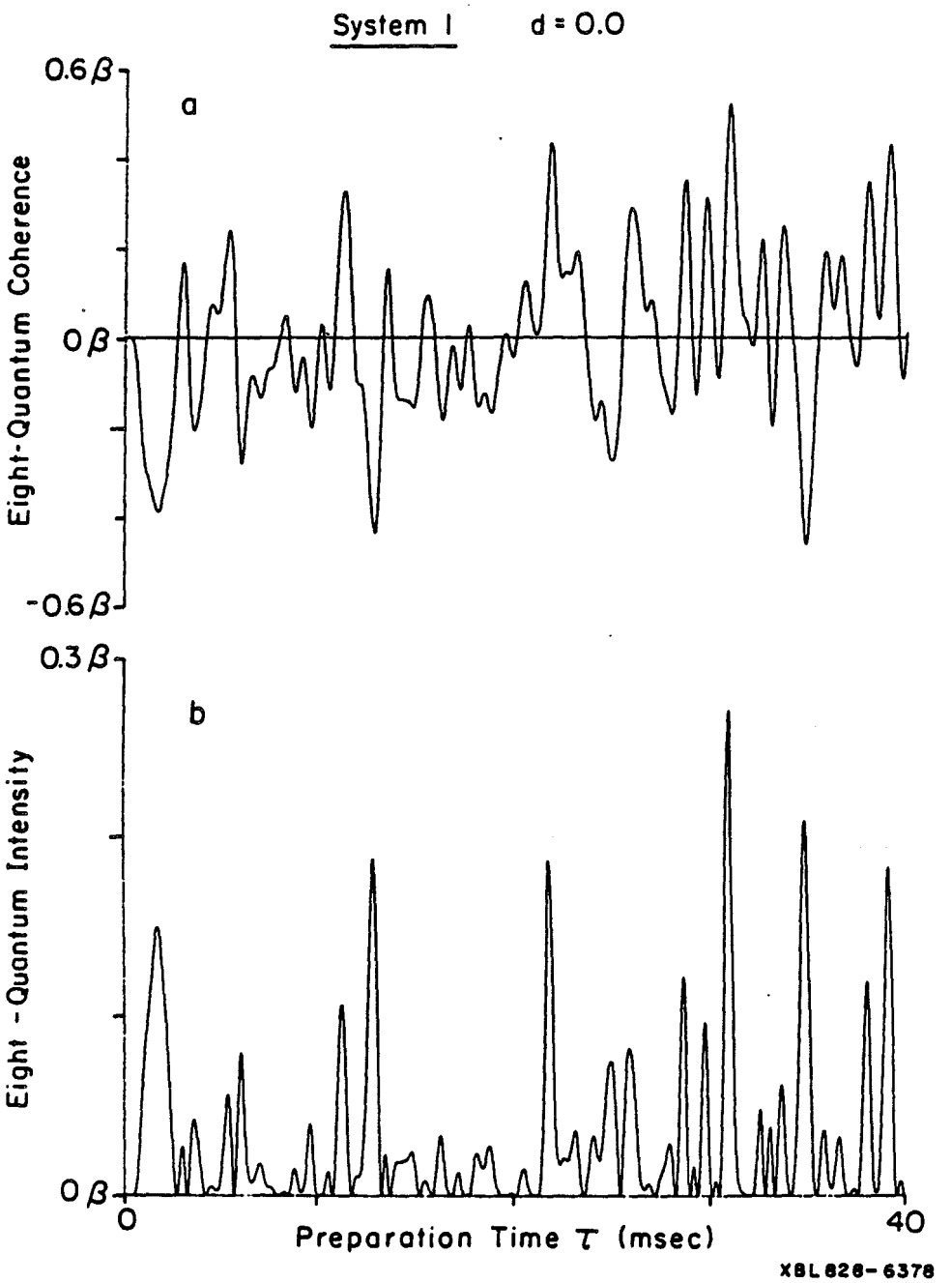

Figure V.15 Eight-quantum prepared coherence and intensity as a function of τ (= t_2) for a random eight-spin system with $-500\ \text{Hz} \leq D_{ij} \leq 500\ \text{Hz}$ and $\bar{D} = d = 0$.

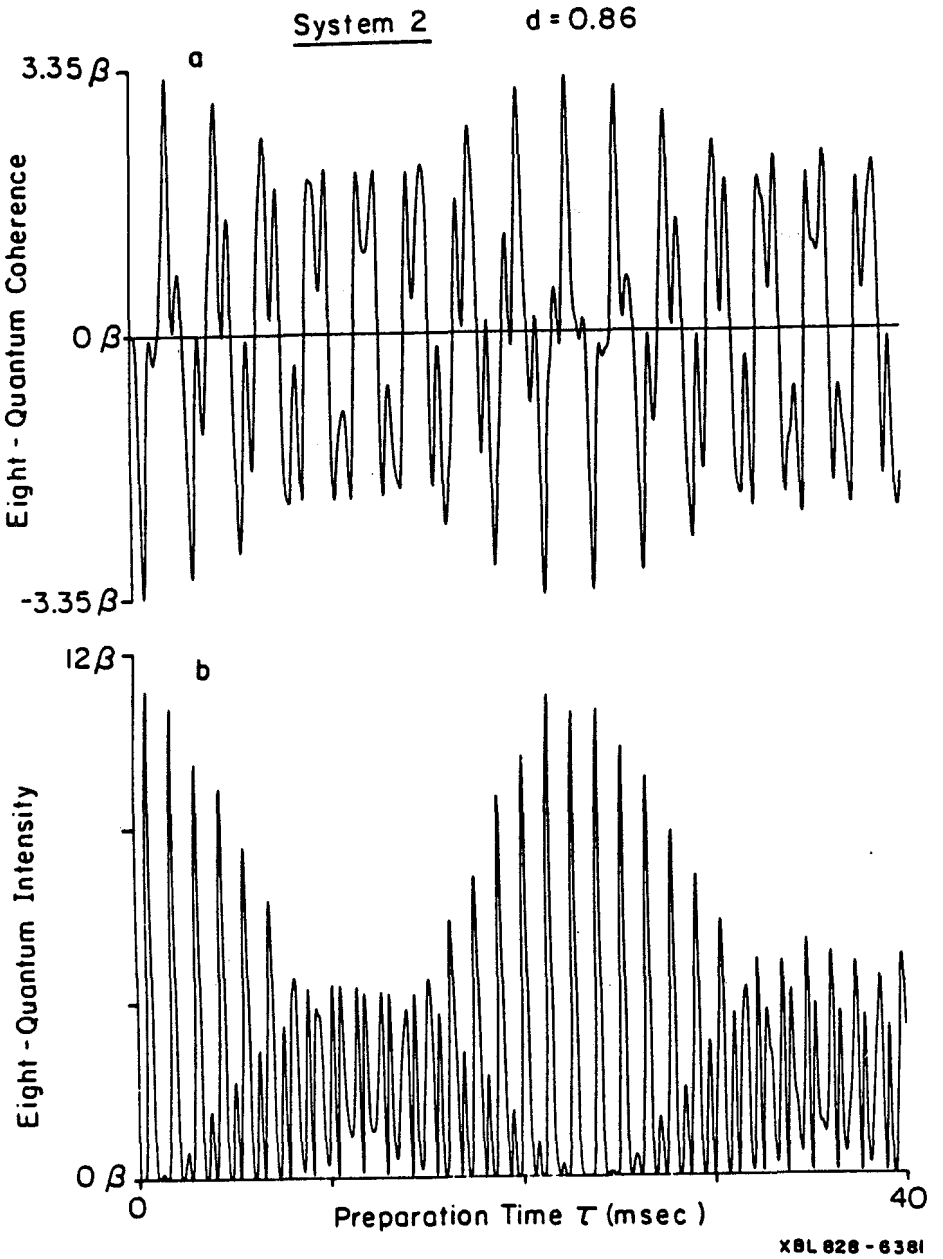

Figure V.16 Eight-quantum prepared coherence and intensity vs. τ for a second random eight-spin system with 0 Hz $\leq D_{ij} \leq$ 1000 Hz, $\bar{D}$ = 500 Hz, and $d = \bar{D}/D_{rms} = 0.864$. Note the near-periodicity of each function (a result of a few large B_{ab} values in the expansion of P_{jk}) and the greatly increased amplitude compared to system 1 in Fig. V.15.

In contrast, the B_{ab} terms which sum to give $P_{k\bar{k}}$ for system 1 are more nearly the same size; there are no "favored" eigenstates.

The prepared 8Q coherences of systems 1 and 2 also differ in their autocorrelation functions, as discussed in the next section.

5.6 The Autocorrelation Function of Prepared Coherence

The autocorrelation function of a function f(t) is defined as [113]

$$[f*f](\tau) = \int_{-\infty}^{\infty} f^*(t)\ f(t+\tau)dt \quad . \tag{V.44}$$

If f is not square-integrable, i.e., if

$$\int_{-\infty}^{\infty} |f|^2\ dt = \infty \quad , \tag{V.45}$$

then a modified definition can be used [128]:

$$[f*f](\tau) = \lim_{T\to\infty} \frac{1}{2T} \int_{-T}^{T} f^*(t)\ f(t+\tau)dt \quad . \tag{V.46}$$

With this definition, f*f at $\tau=0$ is just the average value of $|f|^2$. As τ increases, f*f is a measure of the overlap between f^* and f shifted by an amount τ, again averaged over time. If f(t) changes rapidly, f*f will quickly decay from its initial value. If f(t) is a truly random function of time, then f*f will go to zero as τ increases--that is to say, when averaged over

time there is a monotonic decrease in correlation between $f^*(t)$ and $f(t+\tau)$ as τ increases. For large enough τ, $f^*(t)$ and $f(t+\tau)$ become completely uncorrelated; a knowledge of $f(t)$ is then of no use in determining the value of $f(t+\tau)$. On the other hand, if $f(t)$ is a periodic function, then f^*f will also be periodic since the overlap of $f^*(t)$ and $f(t+\tau)$ will go through maxima and minima as τ is varied.

The autocorrelation function of prepared coherence P_{jk} can be calculated as follows:

$$
\begin{aligned}
[P_{jk}{*}P_{jk}](\tau) &= \lim_{T\to\infty} \frac{1}{2T} \int_{-T}^{T} P^*_{jk}(t)\, P_{jk}(t+\tau)\,dt \\
&= \lim_{T\to\infty} \frac{1}{2T} \int_{-T}^{T} \{\sum_{a,b} B_{ab} \exp(-i\omega_{ba}t)\} \\
&\qquad \cdot\{\sum_{a',b'} B_{a'b'} \exp[i\omega_{b'a'}(t+\tau)]\,dt \\
&= \sum_{a,b} \sum_{a',b'} B_{ab}\, B_{a'b'} \exp(i\omega_{b'a'}\tau) \\
&\qquad \cdot \lim_{T\to\infty} \frac{1}{2T} \int_{-T}^{T} \exp[i(\omega_{b'a'}-\omega_{ba})t]\,dt \,.
\end{aligned}
\tag{V.47}
$$

The limit expression equals one when $\omega_{b'a'} = \omega_{ba}$ but is zero otherwise. Ignoring for now the problem of degenerate single-quantum frequencies $\omega_{b'a'}$ and ω_{ba}, the quadruple sum thus simplifies to a double sum:

$$[P_{jk}{*}P_{jk}](\tau) = \sum_{a,b} B_{ab}^2 \exp(i\,\omega_{ba}\,\tau) \quad . \tag{V.48}$$

It can be seen that when $\tau=0$, the autocorrelation function of P_{jk} equals the ultimate τ average intensity. Overall, the expression for $P_{jk}{*}P_{jk}$ is very similar to that for P_{jk}--the only difference is the substitution of B_{ab}^2 for B_{ab}.

The two random eight-spin systems considered earlier have very different autocorrelation functions (Fig. V.17). For system 1 with its profusion of similar B_{ab} values, many frequencies ω_{ba} contribute to the expression for $P_{jk}{*}P_{jk}$. The result is similar to the autocorrelation function of a truly random process: a monotonic decay from an initial value to near zero with no appreciable recurrence. For system 2, in contrast, a few B_{ab}^2 $\exp(i\,\omega_{ba}\,\tau)$ terms dominate in Eq. V.48, making the autocorrelation function sinusoidal and periodic.

5.7 Average Intensities in Isotropic Systems

Ultimate τ average intensities in isotropic systems have also been briefly investigated. Here $\mathcal{H}_D = 0$ and thus J-couplings are the sole source of spin-spin interaction. If multiple-quantum coherence is to develop, there must be chemical shift differences as well; otherwise only single-quantum transitions can be prepared. (This can be seen by rewriting Eq. IV.33c with $\mathcal{H}_{xx}$ equal to $\mathcal{H}_J$:

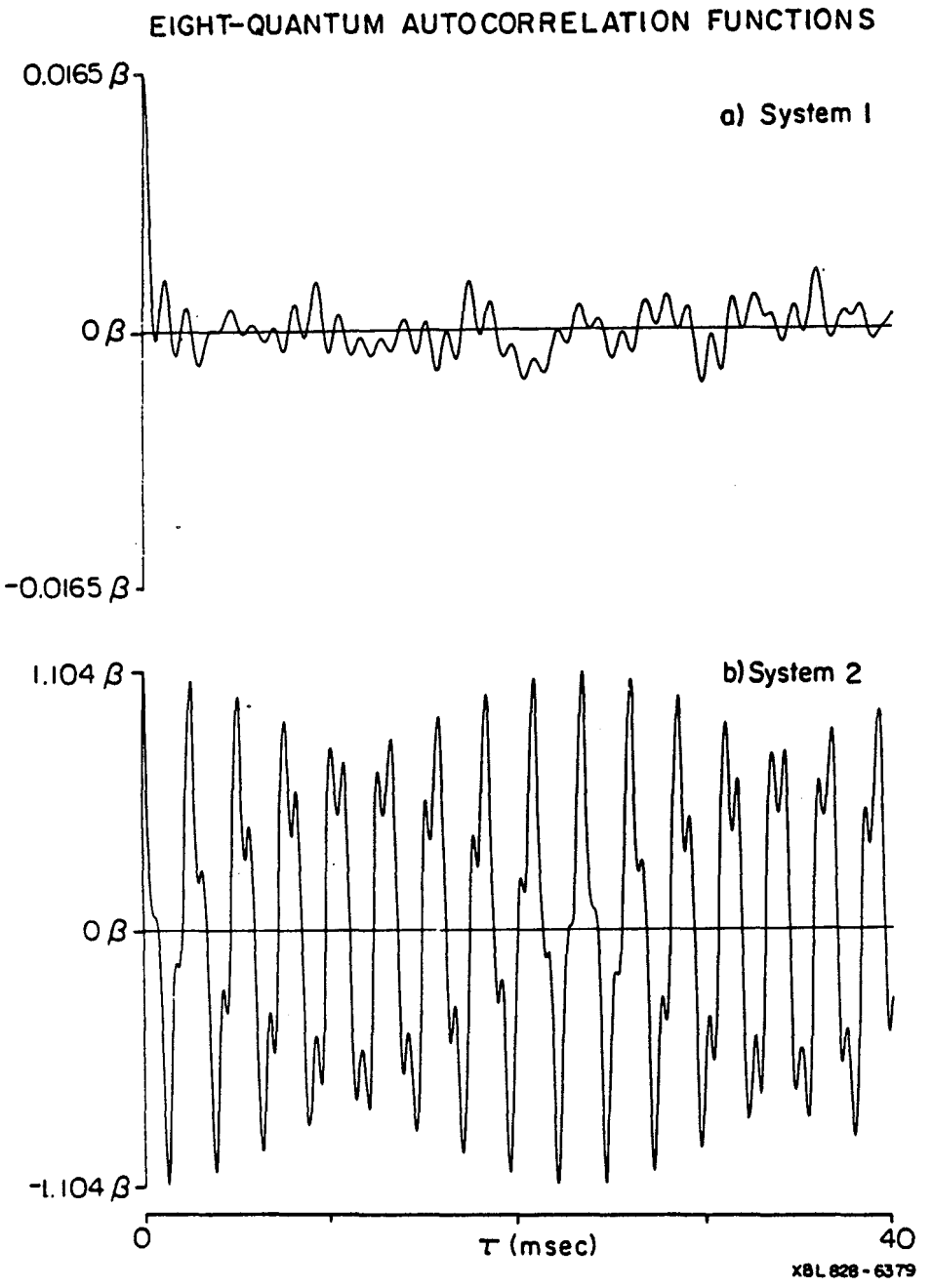

Figure V.17 Autocorrelation functions for eight-quantum prepared coherence in two random eight-spin systems. As could be predicted from the corresponding plots of 8Q coherence vs. preparation time (Figs. V.15 and V.16), the coherence autocorrelation function for system 2 has much greater periodicity and amplitude than that for system 1.

$$\beta P = \cos\Delta\omega\tau \; e^{-i\mathcal{H}_J\tau} \; \beta \; I_z \; e^{i\mathcal{H}_J\tau} - \sin\Delta\omega\tau \; e^{-i\mathcal{H}_J\tau} \; \beta \; I_y \; e^{i\mathcal{H}_J\tau} \tag{V.49a}$$

$$= \cos\Delta\omega\tau \; \beta \; I_z - \sin\Delta\omega\tau \; \beta \; I_y \tag{V.49b}$$

since

$$[\mathcal{H}_J, I_z] = [\mathcal{H}_J, I_y] = 0.)$$

The degree of higher-quantum excitation depends on the relative sizes of the J-coupling constants and the chemical shift differences. In the first-order limit ($|\sigma_j - \sigma_k| \gg J_{jk}$), the N-quantum coherence magnitude can be shown [55] to be given by the following:

$$\frac{1}{2}\beta \sum_j \cos(\Delta\omega - \sigma_j)\tau \prod_{k \neq j} \sin(J_{jk}\tau/2) \quad \text{for N even} \quad , \tag{V.50a}$$

$$\frac{1}{2}\beta \sum_j \sin(\Delta\omega - \sigma_j)\tau \prod_{k \neq j} \sin(J_{jk}\tau/2) \quad \text{for N odd.} \tag{V.50b}$$

The τ-averaged N-quantum intensity calculated from these expressions is exactly the statistical-limit value. Note, however, that for N-quantum coherence to develop after a reasonably short time τ, there must be at least one spin j with healthy couplings J_{jk} to all other spins. (This "cluster coupling" condition is not necessary for the creation of N-quantum coherence in anisotropic dipolar-coupled systems.) As for lower-

quantum lines, computer simulation of first-order systems has shown that all transitions are on the average excited equally, in complete accord with the statistical model.

In contrast, for the strong-coupling limit ($J_{jk} > |\sigma_j - \sigma_k|$), the same sort of higher-quantum enhancement occurs as in anisotropic systems. Again the effect is most pronounced when the bilinear coupling constants (here the J_{jk} values) are nearly equal.

5.8 Total Spectral Intensity When τ Does Not Equal t_2

Thus far, only the case of $t_2=\tau$ has been considered. We will now examine the effect on signal intensity of varying τ and t_2 independently. Figure V.18 is a calculation of the total intensity of the magnitude MQ spectrum of oriented benzene as a function of t_2 for two different values of τ. Figure V.19 displays the total magnitude spectrum intensity for benzene over a range of τ and t_2 values. Clearly, there is something special, but not spectacular, about $t_2=\tau$. A simple argument follows to explain why there is a maximum in total spectral intensity there and why this maximum is about 1.27 times the $t_2 \neq \tau$ "baseline."

Recall from Eq. V.6 that the magnitude of a given MQ line can be written as

$$|\underline{S}_{jk}| = \beta \, |P_{jk}(\tau) \, Q_{kj}(t_2)| \quad . \tag{V.51}$$

The ratio R of the total intensity at $t_2=\tau$ relative to the

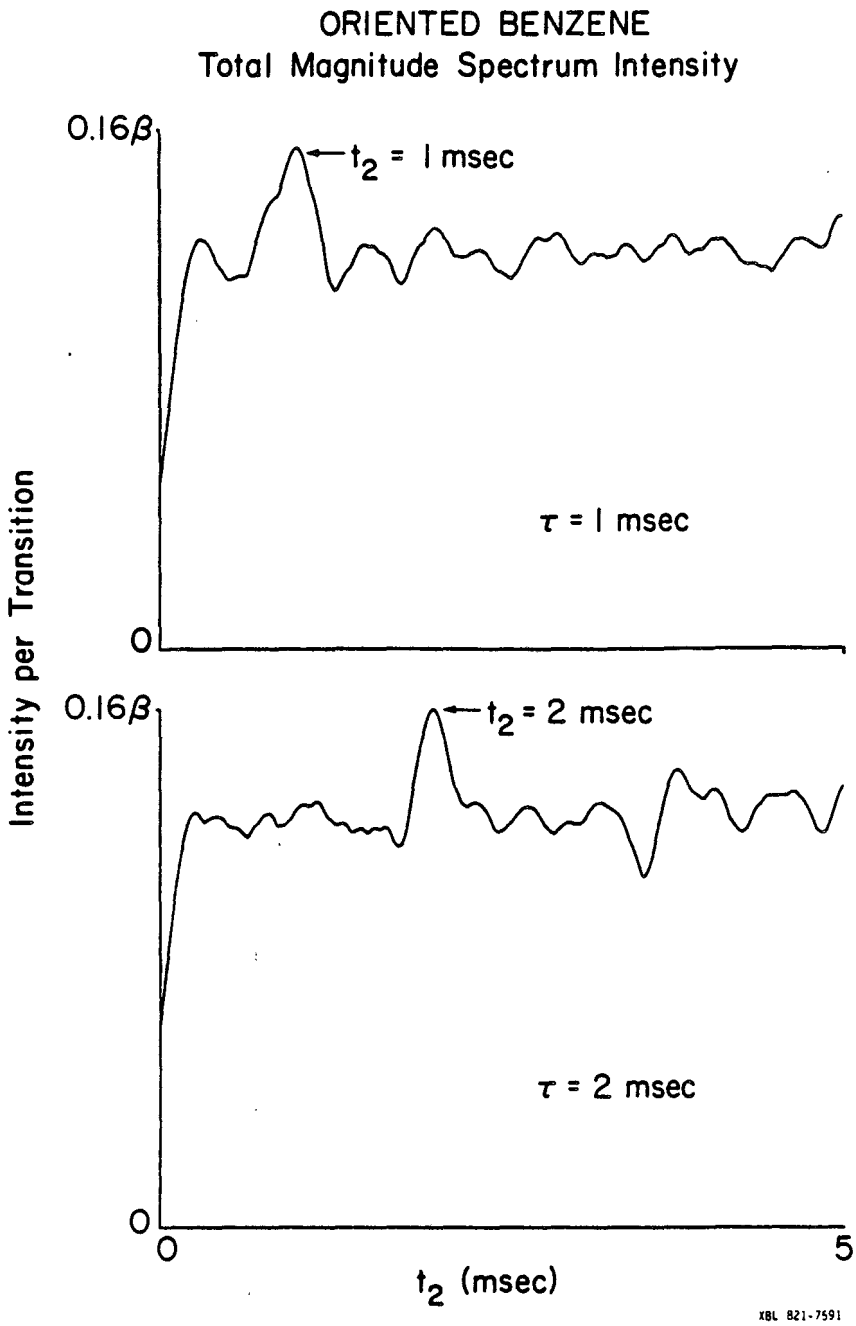

Figure V.18 Total magnitude spectrum intensity as a function of t_2 for oriented benzene, divided by the number of allowed transitions. In each plot there is a bulge when $t_2=\tau$.

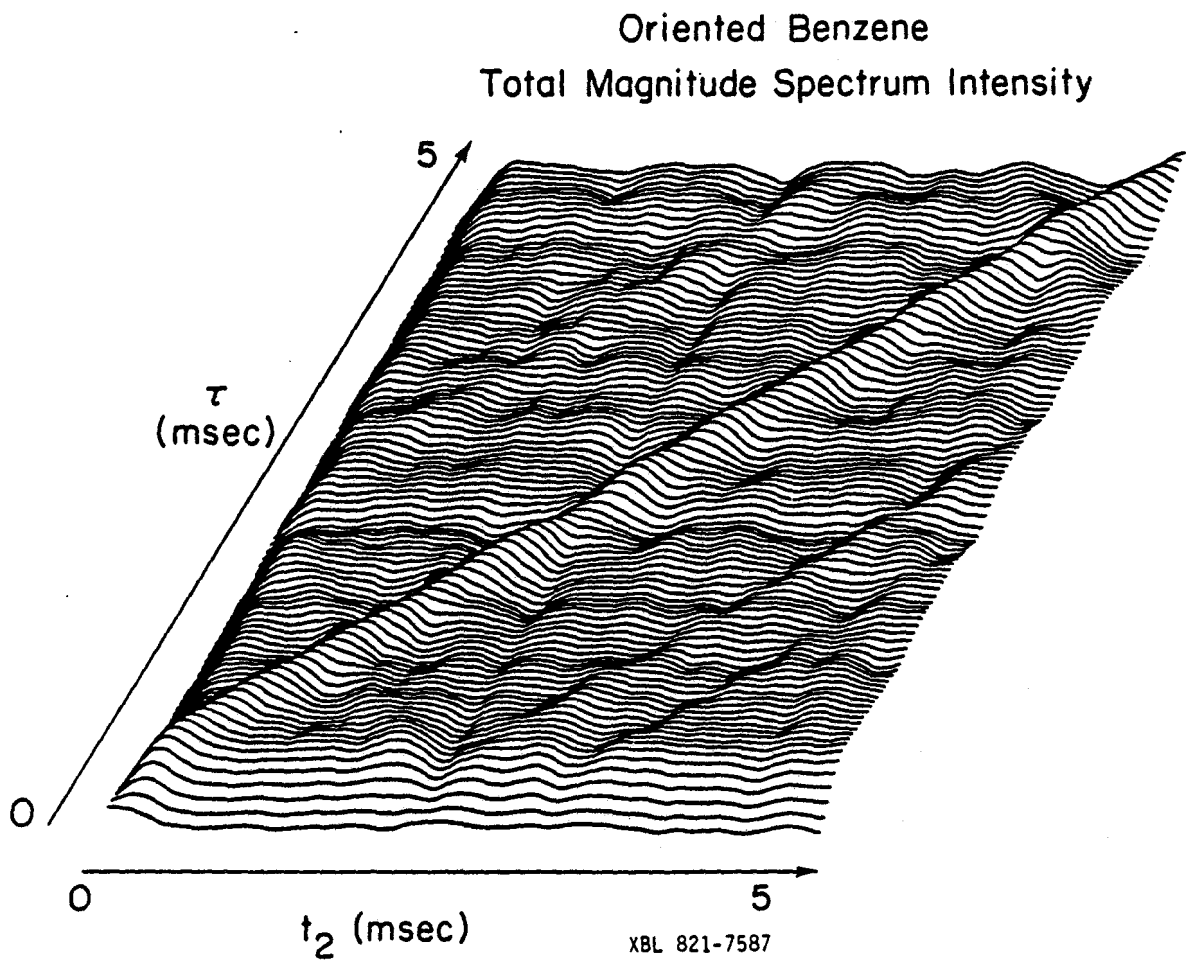

Figure V.19 Total magnitude spectrum intensity as a function of both τ and t_2 for oriented benzene.

"baseline" is

$$R = \frac{\sum_j \sum_k |P_{jk}^2(\tau)|}{<\sum_j \sum_k |P_{jk}(\tau)\ Q_{kj}(t_2)|>_{t_2}} \quad . \tag{V.52}$$

Both numerator and denominator involve the summation of many transition intensities for one value of τ. We will assume that the same ratio holds if we look at a single MQ transition but average over many values of τ, in a sense substituting a time average for an ensemble average. That is, we assert that

$$R \approx \frac{<|P_{jk}^2(\tau)|>_\tau}{<<|P_{jk}(\tau)\ Q_{kj}(t_2)|>t_2>_\tau} \tag{V.53}$$

and concentrate on just a single line. $<|P_{jk}^2|>_\tau$ is just the ultimate τ average intensity of the transition:

$$<|P_{jk}^2|>_\tau = \sum_a \sum_b B_{ab}^2 \quad . \tag{V.54}$$

On the other hand,

$$<<|P_{jk}(\tau)\ Q_{kj}(t_2)|>_{t_2}>_\tau = <|P_{jk}|>_\tau <|Q_{kj}|>_{t_2}$$

$$= <|P_{jk}|>_\tau^2 \tag{V.55}$$

and hence

$$R = \langle |P_{jk}|^2 \rangle_\tau / \langle |P_{jk}| \rangle_\tau^2 \tag{V.56a}$$

$$= \bar{\sigma}_{jk}^{\;2} + 1 \quad , \tag{V.56b}$$

where $\bar{\sigma}_{jk}$ is the relative standard deviation of $|P_{jk}|$.

For simplicity, rewrite P_{jk} as follows:

$$P_{jk} = \sum_a \sum_b B_{ab}\, e^{i\omega_{ba}\tau} \equiv \sum_\ell P_\ell\, e^{i\omega_\ell \tau} \quad . \tag{V.57}$$

$|P_{jk}|$ is the magnitude of the sum of complex numbers with fixed real lengths P_ℓ and varying phases $\phi_\ell = \omega_\ell \tau$. In general, the single-quantum frequencies ω_ℓ are unequal, so as τ varies these components fan out in the complex plane like different hands on a clock. The τ-averaged probability density associated with a given component is simply

$$\underline{P}_\ell(r) = \delta(r - P_\ell) \quad . \tag{V.58}$$

For a fixed value of τ, P_{jk} can be thought of as a complex plane random walk of q steps, where q is the number of components. The τ-averaged probability density of P_{jk} is difficult to compute exactly, but can be approximated using the central limit theorem [129] as a two-dimensional Gaussian:

$$\underline{P}(r) = \frac{1}{\pi\alpha^2}\, e^{-r^2/\alpha^2} \quad . \tag{V.59}$$

With this approximation,

$$<|P_{jk}|^2>_\tau = \overline{r^2} = \int_0^\infty \int_0^{2\pi} r^2 \, \underline{P}(r) r \, dr \, d\phi = \alpha^2 \quad , \qquad (V.60a)$$

$$<|P_{jk}|>_\tau = \bar{r} = \int_0^\infty \int_0^{2\pi} r \, \underline{P}(r) r \, dr \, d\phi = \frac{1}{2}\sqrt{\pi}\,\alpha \quad , \qquad (V.60b)$$

$$R = \frac{\overline{r^2}}{(\bar{r})^2} = \frac{4}{\pi} \approx 1.27 \quad . \qquad (V.60c)$$

Thus for a given line, the average over τ of the transition intensity for $t_2=\tau$ should be 1.27 times the average intensity when τ and t_2 are varied separately.

The averaging is somewhat different for $|k>$ to $|\bar{k}>$ transitions. It was shown previously that $P_{k\bar{k}}$ is always purely imaginary. For such transitions, $B_{ba} = -B_{ab}$, and

$$P_{k\bar{k}} = 2i \sum_{a} \sum_{<b} B_{ab} \sin\omega_{ba}\tau = i \sum_{\ell} c_\ell \sin\omega_\ell \tau \quad . \qquad (V.61)$$

Each component of $P_{k\bar{k}}$ now oscillates only along the complex axis with a τ-averaged probability density given by [129]

$$\underline{P}_\ell(y) = \frac{1}{\pi} [c_\ell^{\,2} - y^2]^{-1/2} \qquad (y^2 \le c_\ell^{\,2}) \qquad (V.62)$$

and displayed in Fig. V.20.

For a fixed value of τ, $P_{k\bar{k}}$ can be thought of as a one-dimensional random walk; averaged over τ its probability density will again be assumed to be a Gaussian:

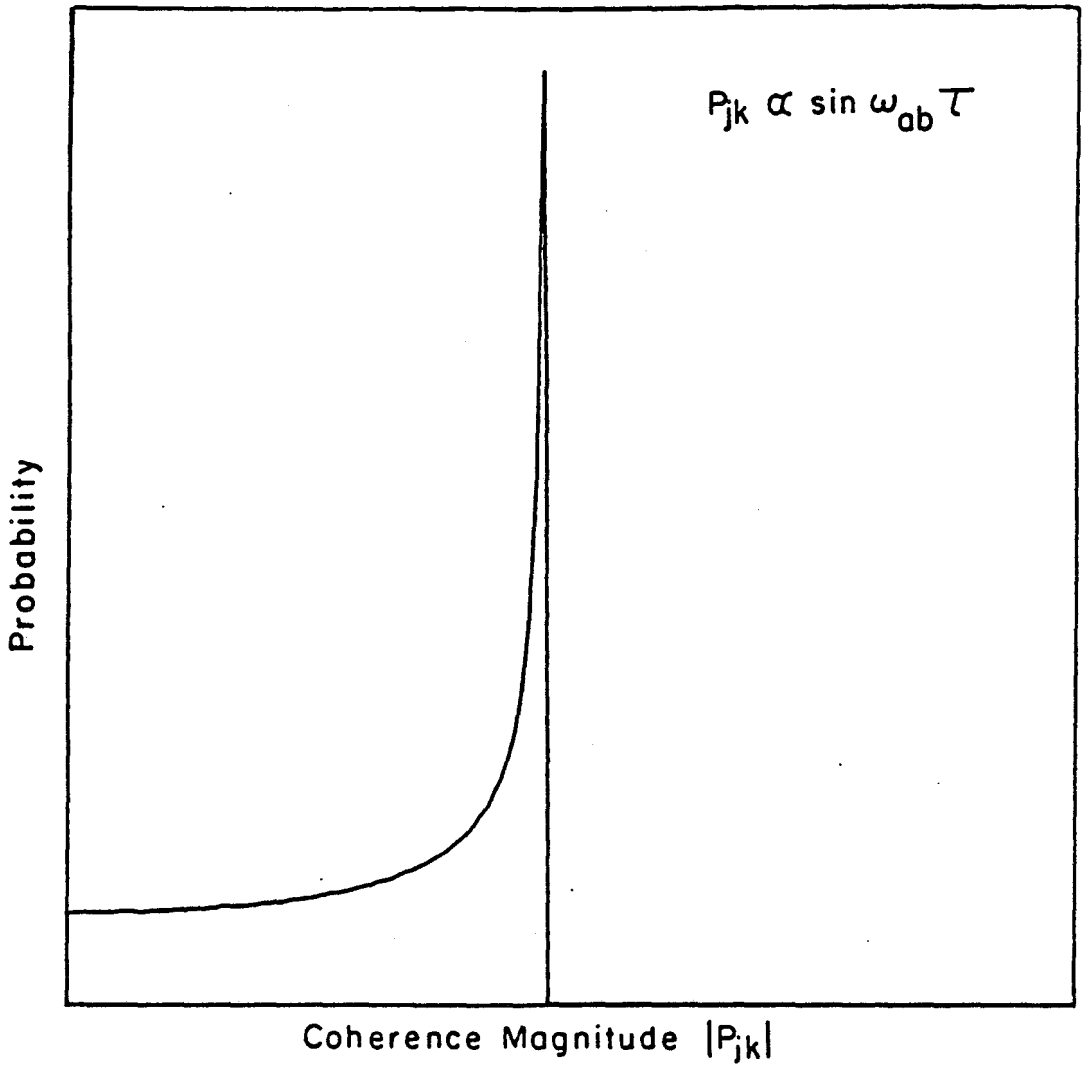

XBL828-6375

Figure V.20 A probability distribution for the prepared coherence magnitude of a spin-inversion transition when only one $B_{ab} \sin\omega_{ab} \tau$ term contributes to P_{jk} ($|k\rangle \equiv |\bar{j}\rangle$). Such is actually the case for the two-quantum B_2 transition in benzene. The functional form of this distribution is given by Eq. V.62, and the ratio $R = \pi^2/8 \approx 1.234$.

$$\underline{P}(y) = (2\pi)^{-1/2}\,\sigma^{-1}\,e^{-y^2/2\sigma^2} \quad . \qquad \text{(V.63)}$$

In this case,

$$R = \frac{\langle|P_{k\bar{k}}|^2\rangle_\tau}{\langle|P_{k\bar{k}}|\rangle_\tau^{\,2}} = \frac{\overline{y^2}}{(\overline{|y|})^2} = \frac{\sigma^2}{(\sqrt{2/\pi}\,\sigma)^2} = \frac{\pi}{2} \approx 1.57 \quad . \qquad \text{(V.64)}$$

Because spin-inversion transitions are at most a small percentage of the total number of transitions, they do not contribute much to the total magnitude spectrum intensity. Thus, as stated earlier, this total intensity at $t_2=\tau$ should be about 1.27 times larger than the intensity when $t_2\neq\tau$.

The ratio R was calculated for the totally symmetric A_1 transitions of oriented acetaldehyde by averaging over 200 000 values of τ; results are listed in Table V.8. For this molecule, the four quantum line is the only A_1 spin-inversion transition and R for it is 1.585. The average value of R for all other transitions is 1.271. Both numbers are very close to the random-walk values.

Also in Table V.8 are similar results for the A_1 transitions of oriented benzene, obtained by averaging over 20 000 τ values. The average ratio for odd-quantum orders (for which there can be no spin-inversion transitions) is 1.22, very close to the predicted ratio for two-dimensional random walks. The ratio for the spin-inversion six-quantum line is 1.44. Though smaller than the prediction of the simple 1-D random walk model, this value is, to think positively, closer to $\pi/2$ than $4/\pi$.

Table V.8

R as a Function of Multiple-Quantum Order (A_1 Transitions)

ΔM	Benzene	Acetaldehyde
0	1.290	1.298
1	1.218	1.256
2	1.223	1.277
3	1.225	1.283
4	1.253	1.585
5	1.239	
6	1.441	

Actually, the value of R relates back to the value of d, the ratio of the average dipolar coupling to the r.m.s. coupling. The last line of Table V.7 compares R for the N-quantum transitions of the two eight-spin systems considered in section 5.5.4. For system 1 with d=0, the B_{ab} elements which comprise $P_{k\bar{k}}$ and which constitute the step lengths of the random walk are roughly comparable in size. The central limit theorem with its prediction of a Gaussian probability density should be especially accurate and R should be close to $\pi/2$, as indeed it is for system 1 (R = 1.587). In contrast, when $d \approx 1$, as in system 2, a few B_{ab} elements are far larger than the rest, generating a few "giant strides" in the random walk. The central limit assumption is thus less valid, and R is expected to lie between $\pi/2$ and its value for the single-component probability density of Eq. V.62, namely $\pi^2/8 \approx 1.234$. For system 2 with d=0.864, R=1.415. As a comparison, d for benzene is 0.776 and R=1.44 as noted above.

In addition to the calculation of R values, the actual distribution of $|P_{jk}|$ for each multiple-quantum order was computed for both the benzene A_1 transitions and acetaldehyde A_1 transitions by again averaging over many values of τ. In Fig. V.21 $P(r)$ vs. r is plotted for benzene with $\Delta M=1$, $\Delta M=3$, and $\Delta M=6$. Figure V.22 displays $P(r)$ vs. r for acetaldehyde. In each case except the benzene six-quantum transition, the distribution indeed appears roughly Gaussian.

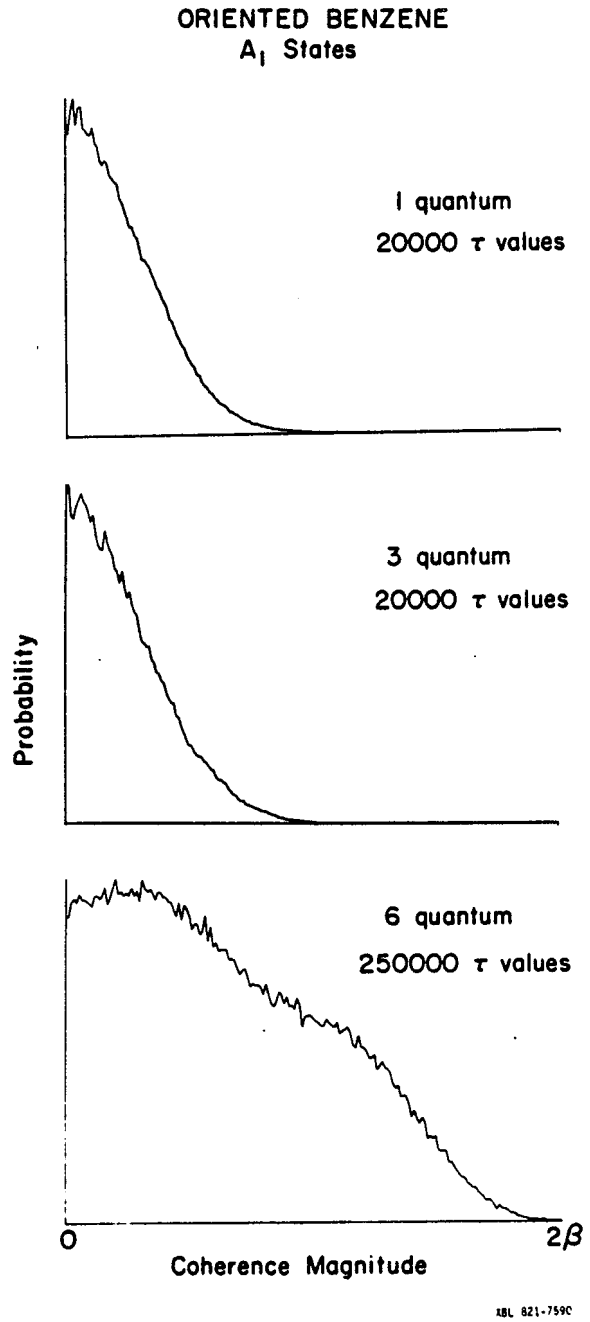

Figure V.21 Probability distribution for the average prepared coherence magnitude of A_1 transitions in oriented benzene, obtained by averaging over many values of τ. Ideally, curves (a) and (b) are profiles of two-dimensional Gaussians; curve (c) is ideally half of a one-dimensional Gaussian.

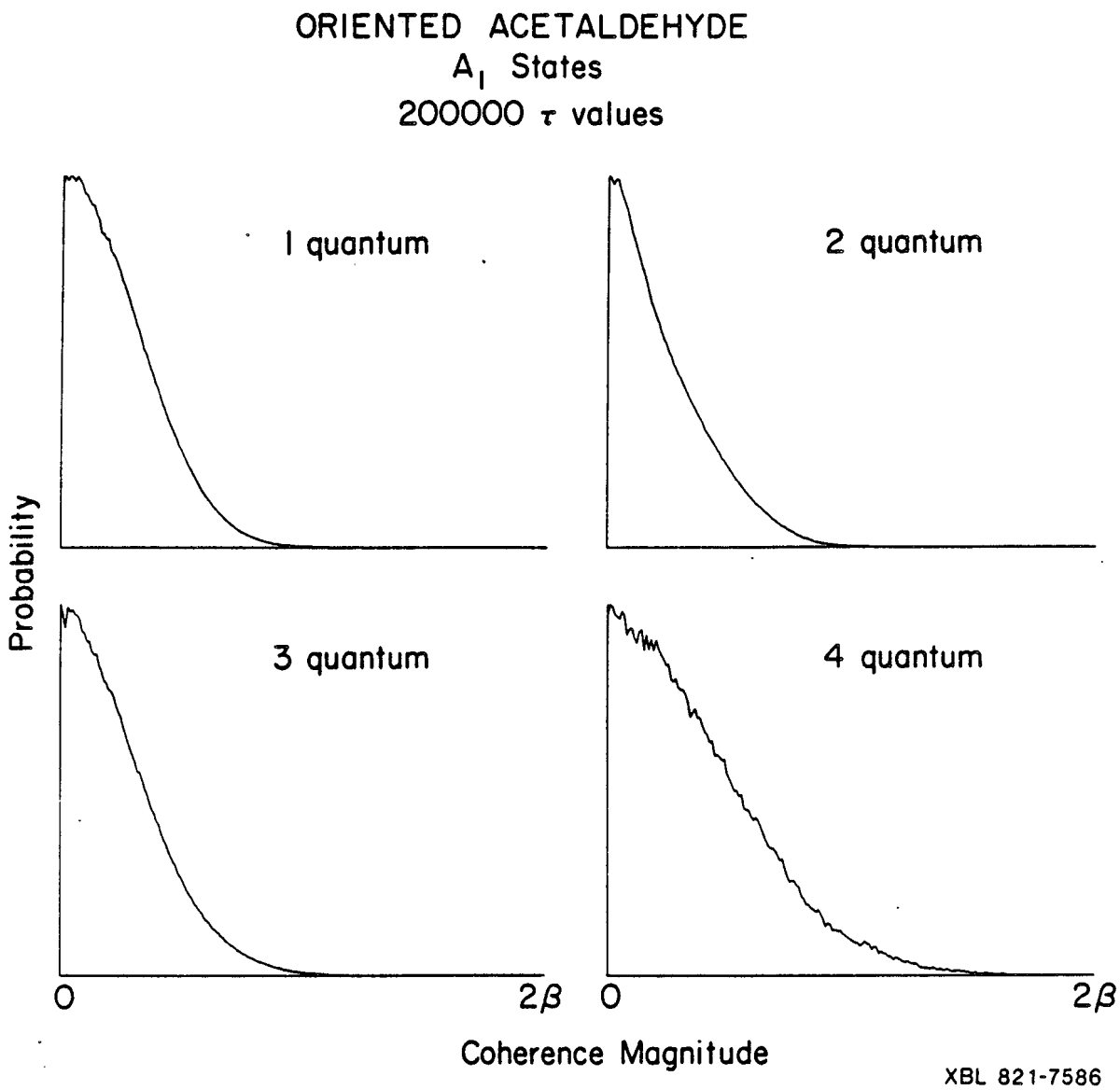

Figure V.22 Probability distribution for the average prepared coherence magnitude of A_1 transitions in oriented acetaldehyde.

To summarize, it can be seen that choosing t_2 equal to τ is advantageous but not crucial in the three-pulse multiple-quantum experiment. When magnet homogeneity is good, one may, for optimal signal-to-noise, sample the magnetization at many values of t_2. One can then average together the magnitude MQ spectra associated with each value of t_2 [55], or take the two-dimensional transform [100,108] and compress the resulting magnitude spectrum along the multiple-quantum axis. When magnet homogeneity is bad, however, echoing pulses [40,105,107] must be added to the pulse sequence at 1/2 τ and during the detection period. Under these circumstances, the magnetization can be measured at only a limited number of points in the detection period, and one might as well choose $t_2=\tau$ as one of them.

5.9 Further Tinkering with the Pulse Sequence

As the final act of this study in intensity, two variations in the basic three-pulse sequence will now be briefly investigated: a variable flip angle for the second and third pulses and the addition of a pi pulse moored in the midst of evolution.

5.9.1 Flip-Angle Frolics

Except for the gerade-ungerade selectivity experiment described at the end of Chapter IV, only 90° pulses for MQ preparation and detection have been considered thus far. Varying the flip angles, however, leads to different multiple-quantum intensities and, as we have seen, to different selection rules.

The first pulse is not very interesting. Assuming its phase is -90°, the density matrix after the first pulse is

$$\rho = \beta(\cos\theta\ I_z + \sin\theta\ I_x) \quad . \tag{V.65}$$

That portion of ρ which is proportional to I_z is unchanged during the preparation period and gives rise only to single-quantum coherence after the second preparation pulse. Hence we will keep the flip angle of the first pulse at 90°.

Playing with the second and third pulses is more entertaining. Figure V.23 displays the ultimate τ average intensity per transition for the A_1 representation of oriented benzene as a function of flip angle. (To keep $Q_{kj} = P_{jk}$, it is convenient to use matching flip angles for pulse 2 and pulse 3.) The most striking aspect of this figure is that the plots of intensity vs. θ become more narrowly centered about θ=90° as ΔM increases. As one would intuitively expect, the highest-quantum transition is the least tolerant of pulse misadjustment. The earlier observation that intensity per transition increases with the value of ΔM, especially for a molecule with similar dipolar couplings like benzene, is thus seen to be true only for $\theta \approx 90°$.

Figure V.24 features ultimate τ average intensities for the B_1 states of benzene, also as a function of flip angle. The zero-quantum plot is of interest here. When θ=90°, transitions between the three M=0 ungerade eigenstates are forbidden. Away

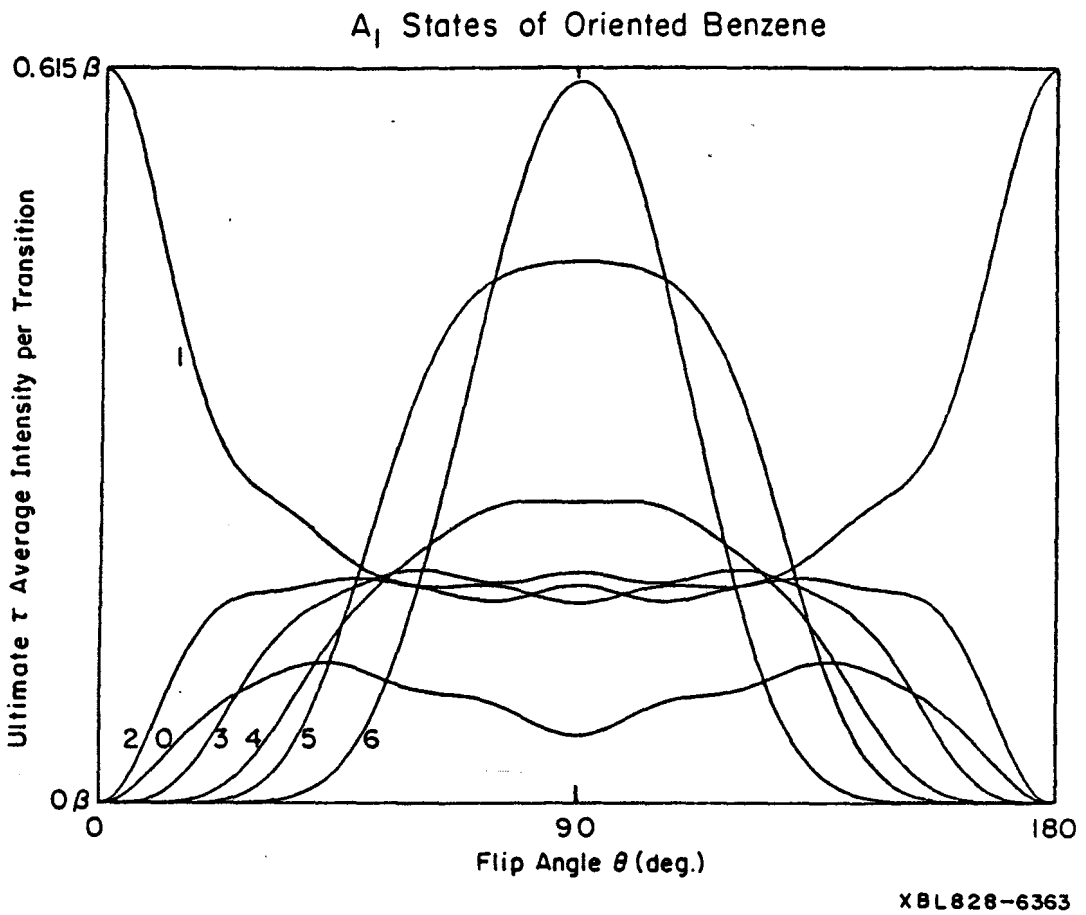

Figure V.23 Ultimate τ average intensity per transition for each MQ order of benzene A_1 states as a function of the flip angle of the second and third pulses in the standard three-pulse experiment. Note that high-quantum transitions are most sensitive to deviations from θ=90°.

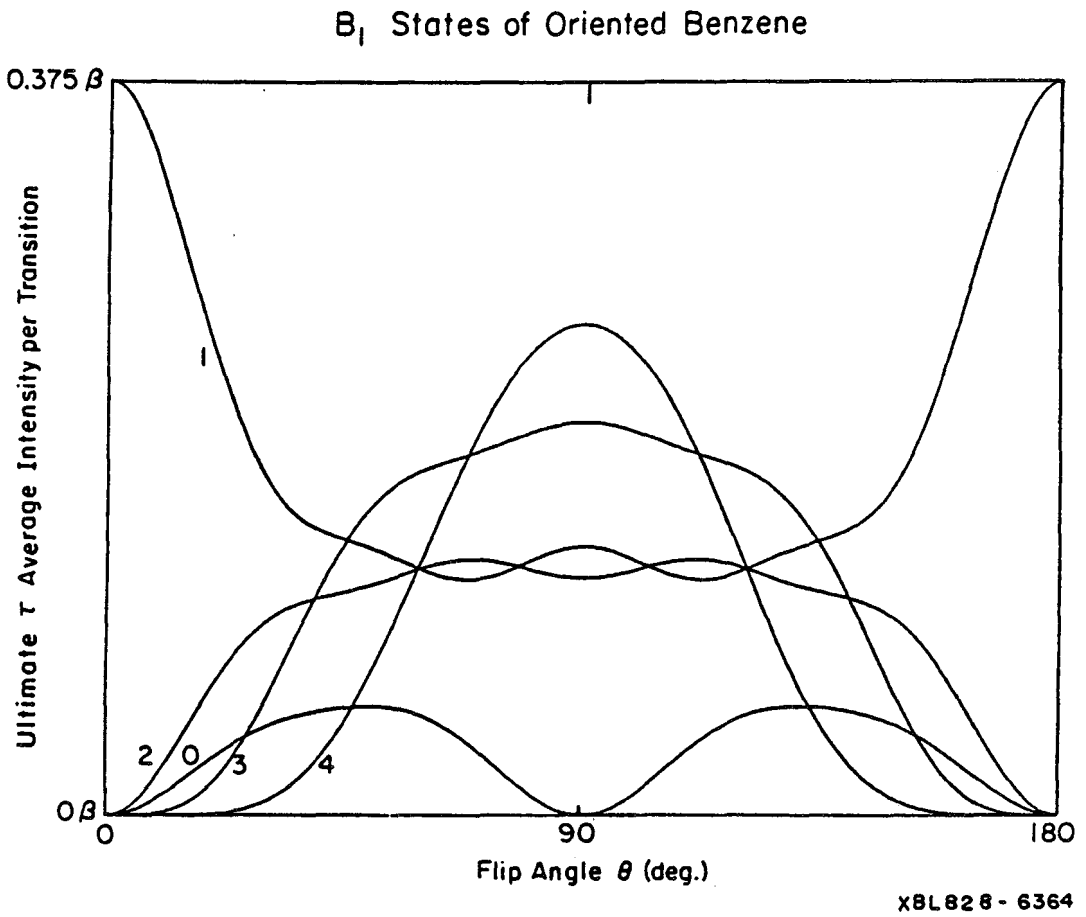

Figure V.24 A companion to Figure V.23--ultimate τ average intensities per transition as a function of flip angle for each MQ order of benzene B_1 states. The u↔u M=0 zero-quantum transitions forbidden at θ=90° appear for other flip angles.

from 90°, however, the selection rule is relaxed, in particular at θ=45° (as discussed in Chapter IV).

5.9.2 Effects of a Pi Pulse in Evolution

It was noted in section 4.7.1 that a pi pulse in the middle of the evolution period will remove inhomogeneous line broadening in the multiple-quantum spectrum. If all spins have the same chemical shift, then the spectrum of each MQ order is otherwise unaffected by the additional pulse. When chemical shift differences are present, however, spectral analysis is more complicated, as outlined below.

Let C be the propagator (in the basis set of the Hamiltonian) for whatever we choose to stick in the middle of the preparation period. The expression for multiple-quantum signal as a function of t_1 becomes

$$s(t_1) = \beta \, \mathrm{Tr}\{e^{-iEt_1/2} \, C \, e^{-iEt_1/2} \, P \, e^{iEt_1/2} \, C^{\dagger} \, e^{iEt_1/2} \, Q\}$$

$$= \beta \sum_{j,k} \sum_{\ell,m} C_{j\ell} \, P_{\ell m} \, (C^{\dagger})_{mk} \, Q_{kj} \, \exp[\tfrac{1}{2}(E_m+E_k-E_\ell-E_j)t_1] \tag{V.66}$$

(a variation on Eq. V.5). Fourier transforming yields

$$\underline{S} = \beta \sum_{j,k} \sum_{\ell,m} C_{j\ell} \, P_{\ell m} \, C^{*}_{km} \, Q_{kj} \, \delta\{\omega - \tfrac{1}{2}\,[(E_m-E_\ell)+(E_k-E_j)]\} \tag{V.67}$$

or with $\tau = t_2$,

$$\underline{S} = \beta \sum_{j,k} \sum_{\ell,m} C_{j\ell} P_{\ell m} C^*_{km} P_{jk} \delta[\omega - \frac{1}{2}(\omega_{m\ell} + \omega_{kj})] \quad . \qquad (V.68)$$

(Kumar [130], Turner [131], and Sinton [56] have derived much the same result.)

In the simplest case (all that will be considered here), C is just the propagator for a 180x pulse:

$$C = S^\dagger e^{-i\pi I_x} S \quad , \qquad (V.69)$$

where S is the eigenvector matrix for $\mathcal{H}$. In the spin-product basis, the only non-zero elements of $e^{-i\pi I_x}$ are those connecting spin-inversion pairs, and each of these elements equals i^N. (See Appendix D for details.) In the normal ordering of spin-product states, $e^{-i\pi I_x}$ is thus "mirror-image diagonal" with non-zero elements running from lower left to upper right. The elements of C are in turn given by

$$\begin{aligned} C_{ab} &= (S^\dagger e^{-i\pi I_x} S)_{ab} \\ &= \sum_{\mu,\nu} (S^\dagger)_{a\mu} S_{\nu b} \delta_{\nu,\bar{\mu}} \\ &= i^N \sum_{\mu} S_{\mu a} S_{\bar{\mu} b} \quad . \end{aligned} \qquad (V.70)$$

When the internal Hamiltonian is purely bilinear, these elements are zero except for the following:

$$\text{when } M_a \neq 0 \ , \ C_{a\bar{a}} = i^N \quad , \tag{V.71a}$$

$$\text{when } M_a = 0 \ , \ C_{a\bar{a}} = C_{aa} = \pm(i)^N \quad , \tag{V.71b}$$

where the plus sign is used for a gerade state and the minus sign for an ungerade state. As expected,the resulting multiple-quantum spectrum is exactly what was calculated earlier when no pi pulse was included:

$$\begin{aligned} \underline{S} &= \sum_{j,k} \sum_{\ell,m} C_{j\ell} \, P_{\ell m} \, C^*_{km} \, P_{jk} \, \delta[\omega - \tfrac{1}{2}(\omega_{m\ell}+\omega_{kj})] \\ &= \sum_{j,k} \sum_{\ell,m} \delta_{\ell,\bar{j}} \, P_{\ell m} \, \delta_{m,\bar{k}} \, P_{jk} \, \delta[\omega - \tfrac{1}{2}(\omega_{m\ell}+\omega_{kj})] \\ &= \sum_{j,k} P^2_{jk} \, \delta(\omega-\omega_{kj}) \quad . \end{aligned} \tag{V.72}$$

Now for the general case. Because S is block diagonal, partitioned according to the value of M, C is "mirror-image block diagonal"--elements C_{ab} are non-zero only when $M_a = -M_b$. As such, a pi pulse in the evolution period will not mix MQ orders; a given n-quantum coherence is transferred by the pulse only to other n-quantum coherences. To be more specific, a coherence between states with Zeeman quantum numbers M_1 and M_2

is transferred to coherences between states with Zeeman quantum numbers $-M_1$ and $-M_2$. Each transfer of coherence from $P_{\ell m}$ to $Q_{kj}=P_{jk}$ is manifested in the MQ spectrum by a line at the average of the two frequencies involved, namely $\omega_{m\ell}$ and ω_{kj}.

In Figs. V.25 and V.26, multiple-quantum spectra of a four-spin C_{3v} system are presented as a function of the chemical shift difference, with and without a pi pulse in the evolution period. The dipolar and J-couplings used for each simulation were those found for acetaldehyde (see section 4.8.3), but the methyl-aldehyde chemical shift was varied between 0 and 800 Hz. Ten equally-spaced values of $\tau=t_2$ from 2 to 20 msec were chosen in each case and the resulting magnitude spectra were averaged together. The effective offset frequency $\Delta\omega$ was 5000 Hz.

Consider first the spectra in Fig. V.25, for which no pi pulse was included in evolution. When $\Delta\sigma = 0$, each MQ order is symmetric about its center frequency $(\Delta M)(\Delta\omega)$ as expected. For small values of $\Delta\sigma$, a few lines are split and some small additional transitions appear. The intensity and spacing of most of the initial doublets remain virtually unchanged but they are no longer centered about $(\Delta M)(\Delta\omega)$. For larger values of $\Delta\sigma$, all traces of the initial spectral symmetry disappear.

Compare these results to those of Fig. V.26, for which a pi pulse was present in evolution. The most striking difference is that the pi pulse preserves the reflection symmetry of each MQ order independent of chemical shifts. When $\Delta\sigma$ is small, two

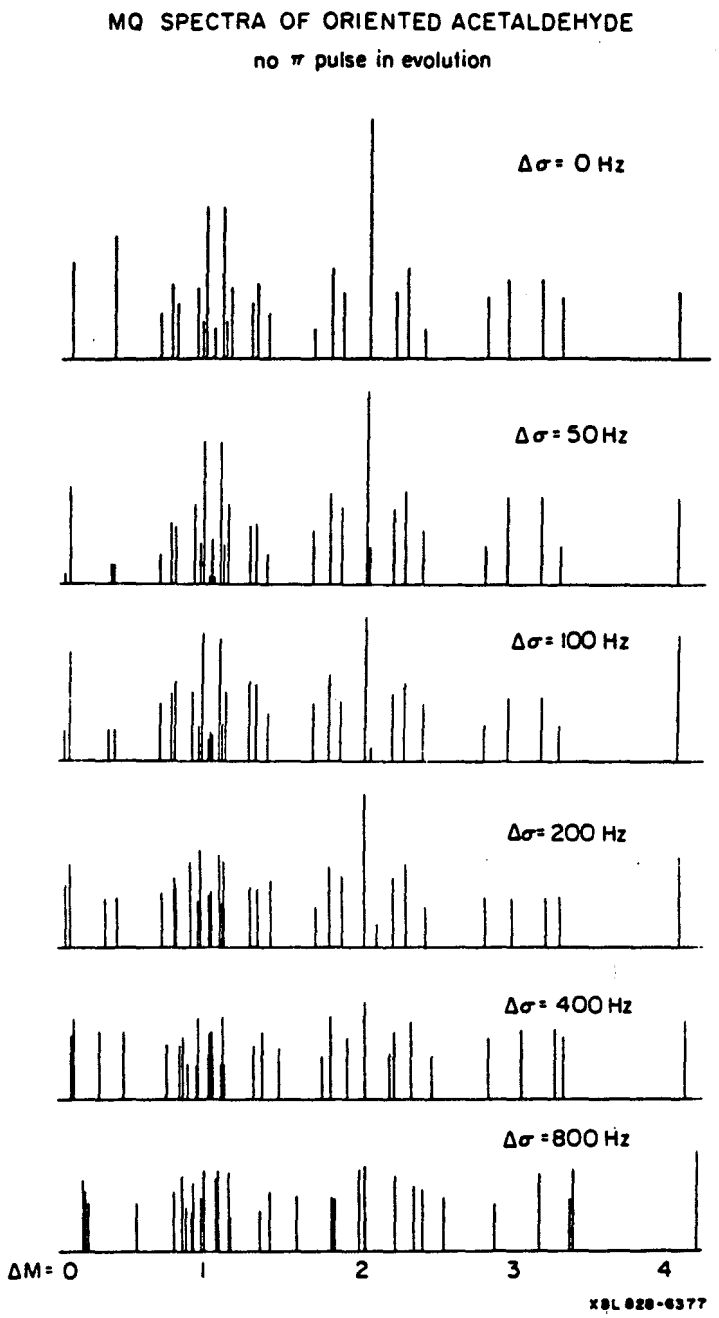

Figure V.25 Simulated three-pulse MQ spectra of oriented acetaldehyde with the dipolar and J-couplings used in section 4.8.3 but various methyl-aldehyde chemical shift differences. In each case, magnitude spectra for ten equally spaced values of $\tau = t_2$ from 2 msec to 20 msec were averaged together. The offset frequency is 5000 Hz, and all spectra are to the same scale.

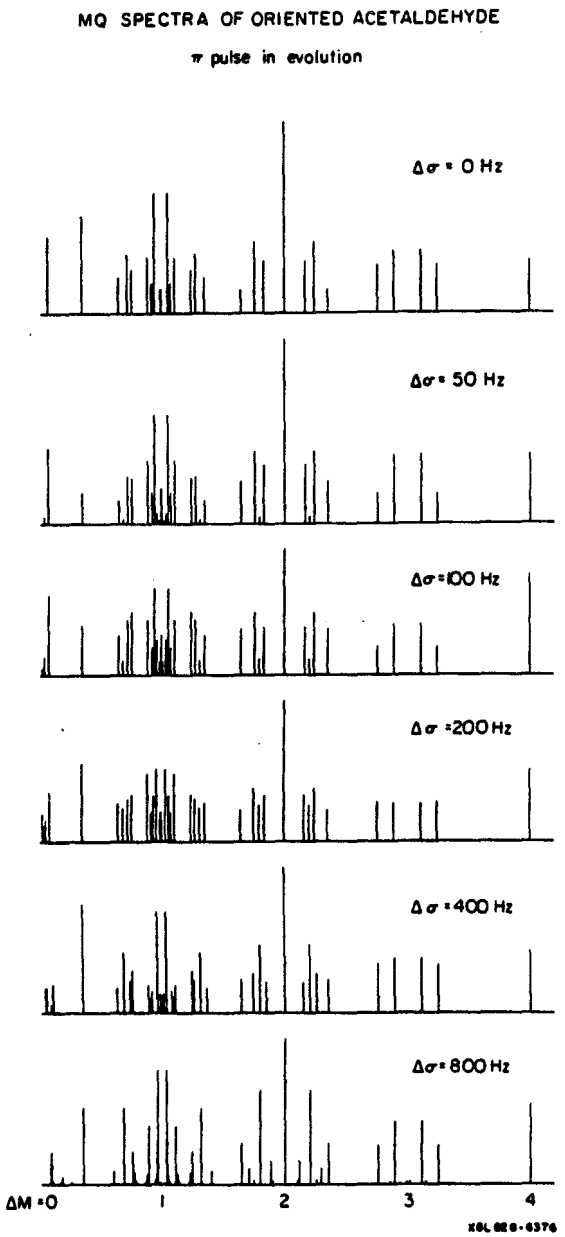

Figure V.26 Another set of simulated MQ spectra for oriented acetaldehyde. The coupling constants, chemical shift differences, and preparation times are as in Fig. V.25. For these spectra, however, a π pulse has been included in the middle of the evolution period. As a result, each spectral order is symmetric about $(\Delta M)(\Delta\omega)$, where $\Delta\omega$ is the effective TPPI offset frequency (5000 Hz in this case). All spectra are to the same scale.

effects occur: (1) The intensities of the initial lines change but not the frequencies. (2) Small additional transitions appear. For larger $\Delta\sigma$ values, this "first generation" of new lines grows up to become comparable in magnitude to the now-shifted initial transitions; furthermore, a second generation of additional transitions appears.

That the frequencies in an evolution-echo experiment are apparently unaffected to first order by a chemical shift is an important simplification in the analysis of TPPI spectra, as discussed by Drobny [57] and Sinton [56]. For example, in the case of our friend the 4,4'-disubstituted biphenyl, the relatively small chemical shift difference between "inner" and "outer" protons can be set to zero when fitting the dipolar couplings. (Indeed, unless the lineshape-fitting program is explicitly tailored to an evolution-echo sequence, the symmetry of each experimental MQ order would force the fitted chemical shift difference to be zero.) That the intensities are affected to first order by a chemical shift means that an accurate simulation of a TPPI spectrum should include the effects of a pi pulse. A knowledge of the actual chemical shifts is therefore required--these could be estimated from isotropic spectra.

5.10 Conclusions

A good many bits have been shuffled in obtaining the results of this chapter. Fortunately, the dozens of data files and mounds of computer paper have revealed at least a few details

concerning multiple-quantum intensities. First of all, the intuitive concept of an incubation period for preparation and detection of MQ coherence has been confirmed. For short values of $\tau = t_2$, the growth of n-quantum intensity in a dipolar-coupled system is in general proportional to τ^{2n-2} for $n > 0$. Beyond the incubation period (given roughly by the inverse of the average dipolar coupling), the average intensity per transition for lower-quantum orders is essentially constant and roughly equal to the symmetry-adjusted statistical-limit value. The average intensities per transition of higher-quantum orders are usually larger.

Simulations based on discrete τ values are naturally most accurate in matching experimental spectra, but when many τ values must be averaged over for large spin systems, a faster method for estimating intensities is desirable. The statistical-limit model provides a first approximation and is easy to calculate, but the ultimate τ average approach is much more realistic, especially for higher-quantum orders. Of course, the ultimate τ average does have its limitations: (1) The method assumes that every $\sin^2\omega_{ba}\tau$ and $\cos^2\omega_{ba}\tau$ term in the expression for $|P_{jk}^2|$ is averaged to 1/2 in a time less than T_2^*. This may not be true for small single-quantum frequencies ω_{ba}. (2) Overlapping transition intensities add coherently as a sum of magnitudes rather than incoherently as a sum of complex values. (3) The efficient algorithm for calculating ultimate τ average intensities $[\underline{S}_{jk} = (A^\dagger X A)_{jk}]$ is invalid for some highly-symmetric systems with vanishing

J-couplings. (4) The effect on intensities of a pi pulse in evolution for a system with chemical shifts cannot be included. Nonetheless, an ultimate τ average simulation can be used to estimate the intrinsic strength of transitions, eliminating variations due to "good" or "bad" τ values. Moreover, ultimate τ averages provide an efficient way of exploring intensity as a function of coupling parameters.

Such explorations have revealed that higher-quantum transitions are on the average more intense than lower-quantum transitions. This inherent selectivity for the simple three-pulse experiment is most pronounced in highly symmetric molecules but carries over as well to general systems with couplings reminiscent of the symmetric case. In particular, systems for which the average dipolar coupling is comparable to the r.m.s. coupling have much stronger high-quantum transitions than the statistical-limit model would predict. An example of such a system would be a planar molecule, for which all dipolar coupling constants have the same sign ... there is hope yet for the fabled seventeen- and eighteen-quantum transitions in hexamethylbenzene.

APPENDIX A

SOME PROPERTIES OF EXPONENTIAL OPERATORS

In the ever-evolving world of density matrix manipulation, exponential operators are constantly rotating into view. In this appendix, several useful properties of these beasts are presented; details can be found in books by Louisell [132] and Haeberlen [24] and in an article by Wilcox [133].

1. The exponential operator $e^{\pm iA}$ is defined as follows:

$$e^{\pm iA} \equiv \underset{\approx}{1} \pm iA - \frac{1}{2} A^2 \mp \frac{i}{6} A^3 + \frac{1}{24} A^4 + \ldots \tag{A.1}$$

If A is hermitian ($A^\dagger = A$), then $e^{\pm iA}$ is unitary $[(e^{\pm iA})^\dagger = (e^{\pm iA})^{-1} = e^{\mp iA}]$. Analogous to Eq. A.1, one also defines

$$\cos(cA) \equiv \underset{\approx}{1} - \frac{1}{2} c^2 A^2 + \frac{1}{24} c^4 A^4 - \ldots \quad , \tag{A.2}$$

$$\sin(cA) \equiv cA - \frac{1}{6} c^3 A^3 + \ldots \quad , \tag{A.3}$$

where c is a constant.

2. Simplifying an exponential operator requires a tad of caution:

$$e^{-i(A+B)} = e^{-iA} e^{-iB} = e^{-iB} e^{-iA} \tag{A.4}$$

<u>if</u> <u>and</u> <u>only</u> <u>if</u> $[A,B] = 0$.

3. If $[A,B] \neq 0$, then $e^{-iB}\, e^{-iA}$ can be expanded using the Baker-Campbell-Hausdorff formula:

$$e^{-iB}e^{-iA} = \exp\{-i(A+B) - \frac{1}{2}\,[B,A] + \frac{i}{12}\,[B,[B,A]] + \frac{i}{12}\,[[B,A],A] + \ldots\}\ . \quad (A.5)$$

This formula is equivalent to an average Hamiltonian expansion when the Hamiltonian makes one discrete change during a cycle.

There is also an expansion for $e^{-i(A+B)}$, the Zassenhaus formula:

$$e^{-i(A,B)} = e^{-iA}e^{-iB}\ \exp\{\tfrac{1}{2}[A,B]\}\exp\{\tfrac{i}{3}[B,[A,B]] + \tfrac{i}{6}[A,[A,B]]\}\cdot\ \ldots (A.6)$$

If $[A,[A,B]] = [B,[A,B]] = 0$, then both Eqs. A.5 and A.6 simplify to

$$e^{-i(A+B)} = e^{-iA}e^{-iB}e^{[A,B]/2} = e^{-iB}e^{-iA}e^{[B,A]/2} \quad , \qquad (A.7)$$

4. If U is a unitary matrix and

$$A = U\ D\ U^{\dagger} \quad , \qquad (A.8)$$

then

$$e^{-iA} = U\ e^{-iD}\ U^{\dagger} \quad . \qquad (A.9)$$

In particular, this relation is true when U is the transformation matrix of eigenvectors that diagonalizes A:

$$A = U\,D\,U^{\dagger} \quad , \quad D \text{ diagonal} \quad . \tag{A.10}$$

Eq. A.9 is then straightforward to evaluate since e^{-iD} is itself diagonal with

$$(e^{-iD})_{jj} = e^{-iD_{jj}} \quad . \tag{A.11}$$

5. Similarly, if

$$C = e^{-iA}\,B\,e^{iA} \quad , \tag{A.12}$$

then

$$e^{-iC} = e^{-iA}\,e^{-iB}\,e^{iA} \quad . \tag{A.13}$$

A transformation of this type is often used in calculating an effective Hamiltonian. The expansion of C is as follows:

$$C = B - i[A,B] - \frac{1}{2}[A,[A,B]] + \frac{i}{6}[A,[A,[A,B]]] + \ldots \quad . \tag{A.14}$$

APPENDIX B

VANISHING B_1 TRANSITIONS IN BENZENE

B.1 Introduction

A curious finding in the course of simulating the MQ spectrum of benzene was that one of the M=0 B_1 states is only slightly coupled to other states in its representation, as determined by calculating matrix elements of I_x. Moreover, when the small isotropic J-couplings are omitted from the calculation, this state is not coupled at all, as if some additional symmetry operation acts to isolate the state in its own representation. (In addition, its energy is zero when $\mathcal{H} = \mathcal{H}_D$.) The purpose of this appendix is to prove analytically what the computer has suggested numerically.

The B_1 representation of benzene contains seven states with M quantum numbers 2, 1, 0, 0, 0, -1, and -2. Of these, we are interested in the three M=0 states plus the M=1 state to which they couple via I_x. (States with $|M| > 0$ form spin-inversion pairs, so results for the M=1 eigenstate will hold also for M=-1.) Our plan of attack will be as follows: (1) Construct the appropriate symmetry-adapted functions for benzene. (2) Set up the 3x3 Hamiltonian for the M=0 B_1 states and prove that one energy eigenvalue equals zero. (3) Find the eigenfunction corresponding to this energy. (4) Show that matrix elements of I_x involving this state are zero.

B.2 Symmetry-Adapted Functions

The projection operator [96,97] for the B_1 representation of the D_6 point group can be constructed from its character table:

$$P^{(B_1)} = \sum_R [\chi^{B_1}(R)]^* \hat{O}_R$$

$$= \hat{E} - \hat{C}_6 - \hat{C}_6^{-1} + \hat{C}_3 + \hat{C}_3^{-1} - \hat{C}_2 + 3\,\hat{C}_2' - 3\,\hat{C}_2'' \quad . \qquad \text{(B.1)}$$

The effect of this operator on spin-product states is to generate symmetry-adapted functions ϕ for each Zeeman manifold of the B_1 representation. For M=1,

$$\phi_1 = \frac{1}{\sqrt{6}} \{ |- + - + + +\rangle + |- + + + - +\rangle + |+ + - + - +\rangle$$

$$- |+ - + - + +\rangle - |+ - + + + -\rangle - |+ + + - + -\rangle \} \,. \text{(B.2)}$$

For M = 0,

$$\phi_{0a} = \frac{1}{\sqrt{6}} \{ |- - - + + +\rangle + |- + + + - -\rangle + |+ + - - - +\rangle$$

$$- |+ - - - + +\rangle - |- - + + + -\rangle - |+ + + - - -\rangle \}, \text{(B.3)}$$

$$\phi_{0b} = \frac{1}{\sqrt{12}} \{ |- - + - + +\rangle + |+ + + + - -\rangle + |+ + - - + -\rangle$$

$$+ |+ - + - - +\rangle + |+ - - + + -\rangle + |- + + - + -\rangle$$

$$- |- + - + + -\rangle - |+ - - + - +\rangle - |- + + - - +\rangle$$

$$- |- - + + - +\rangle - |+ + - + - -\rangle - |- + - - + +\rangle \}, \text{(B.4)}$$

$$\phi_{0c} = \frac{1}{\sqrt{2}} \{|- + - + - +> - |+ - + - + ->\} \quad . \tag{B.5}$$

The single M=1 symmetry-adapted function is itself an eigenstate of the benzene spin Hamiltonian. For M=0, the 3x3 block of the Hamiltonian involving functions ϕ_{0a}, ϕ_{0b}, and ϕ_{0c} must be diagonalized to obtain all the energies and eigenstates.

B.3 Analyzing the Hamiltonian for M=0

Although the dipolar Hamiltonian is most easily constructed in the simple spin-product basis set, the resulting M=0 block is an unwieldly 20x20 matrix. Hence the utility of symmetry-adapted functions: for the B_1 representation only a 3x3 matrix need be considered. We must, however, use Eqs. B.3-B.5 to calculate matrix elements in the symmetry-adapted basis set as linear combinations of spin-product matrix elements. The result is as follows, where the basis set is $\{\phi_{0a}, \phi_{0b}, \phi_{0c}\}$ and D_o, D_m, and D_p are the ortho, meta, and para dipolar couplings:

$$\mathcal{H}_D = \frac{1}{4} \begin{pmatrix} -2D_o-2D_m-D_p & -\sqrt{2}(D_o-2D_m) & -\sqrt{3}\, D_p \\ -\sqrt{2}(D_o-2D_m) & -4\, D_m+2D_p & \sqrt{6}\, D_o \\ -\sqrt{3}\, D_p & \sqrt{6}\, D_o & -6\, D_o+6D_m-3D_p \end{pmatrix} \tag{B.6}$$

Were we interested in all of the eigenstates and eigenvalues of this matrix, we would first solve the secular equation

$$\mathrm{Det}(\mathcal{H}_D - \lambda \underset{\approx}{1}) = 0 \tag{B.7}$$

for the eigenvalues λ. However, the computer results indicate that

the eigenstate of interest has energy equal to zero. To check this analytically, we need only prove that the determinant of $\mathcal{H}_D$ itself is zero. The standard formula [134] and a page of algebra suffice to verify that this is indeed the case.

B.4 Constructing the Wayward Eigenstate

If ψ_0 is the eigenstate corresponding to $\lambda=0$, then

$$\mathcal{H}_D \psi_0 = 0 \quad . \tag{B.8}$$

Solving for ψ_0 as a linear combination of the symmetry-adapted functions is straightforward but paper-intensive; the result is

$$\psi_0 = \underline{N}\{[\sqrt{3}(D_o-2D_m+D_p)]\phi_{0a} + [\sqrt{6}(D_o-D_m)]\phi_{0b} + [D_o-D_p]\phi_{0c}\} \quad , \tag{B.9}$$

where $\underline{N}$ is the normalization constant. To prove that ψ_0 does not connect to other B_1 states, we must show that

$$\langle\phi_1|I_x|\psi_0\rangle = 0 \quad . \tag{B.10}$$

We first calculate the following matrix elements:

$$\langle\phi_1|I_x|\phi_{0a}\rangle = \frac{1}{2} \tag{B.11}$$

$$\langle\phi_1|I_x|\phi_{0b}\rangle = -\frac{\sqrt{2}}{2} \tag{B.12}$$

$$\langle\phi_1|I_x|\phi_{0c}\rangle = \frac{\sqrt{3}}{2} \quad . \tag{B.13}$$

Then at last,

$$\begin{aligned}\langle\phi_1|I_x|\psi_0\rangle = \frac{1}{2}\,\underline{N}\,\{&(\sqrt{3})(D_o-2D_m+D_p)\\ &+(-\sqrt{2})(\sqrt{6})(D_o-D_m)\\ &+(\sqrt{3})(D_o-D_p)\\ &= 0 \quad (!) \quad .\end{aligned} \tag{B.14}$$

Like the proverbial cheese, ψ_0 stands alone--an uncoupled state. It should be stressed that for this finding to hold, J-couplings must be absent, but there is no requirement as to the relative sizes of D_o, D_m, and D_p. In particular, no hexagon ratios were assumed in the proof.

As a final thought, I suspect that in the course of his benzene analysis, Saupe [112] made the same observations and performed the same manipulations.

APPENDIX C

AN ANALYSIS OF DIPOLAR-COUPLED FOUR-SPIN SYSTEMS

C.1 Introduction

In section 5.5, computed ultimate τ average MQ intensities are studied as a function of various dipolar coupling parameters, in particular the ratio of the average dipolar coupling to the r.m.s. value. The purpose of this appendix is to present a few analytical expressions to complement the numerical results. For simplicity, we focus on four-spin systems with no J-couplings and no chemical shift differences: $\mathcal{H} = \mathcal{H}_D$. Moreover, to obtain expressions for N-quantum intensity, we will invoke D_4 or C_{3v} symmetry. First, however, let us zero in on some general properties of the M=0 block of the dipolar Hamiltonian.

C.2 A Look at the M=0 Eigenstates of $\mathcal{H}_D$

$\mathcal{H}_D$ is a purely bilinear operator and as such, it commutes with the spin-inversion operator Π (see section 4.6.3). Eigenstates of $\mathcal{H}_D$ with $M \neq 0$ form spin-inversion pairs; we thus can skip an analysis of any state with $M < 0$ since its energy and its form in the spin-product basis can be determined from the corresponding $M > 0$ state. When M=0, eigenstates of $\mathcal{H}_D$ are either gerade or ungerade with respect to spin inversion:

$$\Pi \psi = \psi \quad \text{(gerade)} \quad , \tag{C.1a}$$

$$\Pi \psi = -\psi \quad \text{(ungerade)} \quad . \tag{C.1b}$$

If gerade and ungerade linear combinations of the spin-product states are chosen as basis functions, then the 6x6 M=0 block of $\mathcal{H}_D$ for a four-spin system can be decomposed into two 3x3 matrices. In the gerade basis set $\{(|- - + +\rangle + |+ + - -\rangle)/\sqrt{2},\ (|- + - +\rangle + |+ - + -\rangle)/\sqrt{2},\ (|- + + -\rangle + |+ - - +\rangle)/\sqrt{2}\}$,

$$\mathcal{H}_{Dg} = -\frac{1}{4}\begin{pmatrix} -p+q+r & r & q \\ r & p-q+r & p \\ q & p & p+q-r \end{pmatrix} , \qquad (C.2)$$

where $p = D_{12} + D_{34}$, $q = D_{13} + D_{24}$, and $r = D_{14} + D_{23}$. The corresponding ungerade basis set is $\{(|- - + +\rangle - |+ + - -\rangle)/\sqrt{2},\ (|- + - +\rangle - |+ - + -\rangle)/\sqrt{2},\ (|- + + -\rangle - |+ - - +\rangle)/\sqrt{2}$. Here

$$\mathcal{H}_{Du} = -\frac{1}{4}\begin{pmatrix} -p+q+r & c & b \\ c & p-q+r & a \\ b & a & p+q-r \end{pmatrix} , \qquad (C.3)$$

where p, q, and r are defined as above and $a = D_{12} - D_{34}$, $b = D_{13} - D_{24}$, and $c = D_{14} - D_{23}$. $\mathcal{H}_{Dg}$ and $\mathcal{H}_{Du}$ can be diagonalized analytically, unlike the original 6x6 matrix.

C.3 The Wayward State

Computer studies of general four-spin systems with $\mathcal{H} = \mathcal{H}_D$ indicate the presence of a "wayward" state ψ_w for which

$$\mathcal{H}_D\ \psi_w = 0 \quad , \qquad (C.4)$$

$$I_z\ \psi_w = 0 \quad , \qquad (C.5)$$

$$\langle\psi_i|I_x|\psi_w\rangle = 0 \quad , \tag{C.6}$$

where ψ_i is any eigenstate of $\mathcal{H}_D$ with $|M| = 1$. Furthermore, a look at the computed eigenvectors reveals that ψ_w is a gerade state. These results imply that $\lambda = 0$ is one solution of the secular equation

$$\mathrm{Det}(\mathcal{H}_{Dg} - \lambda \underset{\approx}{1}) = 0 \tag{C.7}$$

or that

$$\mathrm{Det}(\mathcal{H}_{Dg}) = 0 \quad . \tag{C.8}$$

A straightforward application of algebra confirms the numerical results: $\mathrm{Det}(\mathcal{H}_{Dg})$ <u>is</u> zero. The other two energy eigenvalues of $\mathcal{H}_{Dg}$ are then easy to find:

$$E_{0g+} = -\frac{1}{4}\left[\left(\frac{S}{2}\right) + R\right] \quad ,$$

$$E_{0g-} = -\frac{1}{4}\left[\left(\frac{S}{2}\right) - R\right] \quad , \tag{C.9}$$

where S, the sum of the six dipolar couplings, equals p+q+r and

$$R = \left[9\left(\frac{S}{2}\right)^2 - 6(pq + pr + qr)\right]^{1/2} \quad . \tag{C.10}$$

Elements x, y, and z describing ψ_w in the gerade basis set mentioned earlier are found by solving the equation

$$\mathcal{H}_{Dg}\begin{pmatrix} x \\ y \\ z \end{pmatrix} = 0 \quad , \tag{C.11}$$

After a healthy dose of algebra one finds

$$\begin{pmatrix} x \\ y \\ z \end{pmatrix} = N\begin{pmatrix} r-q \\ p-r \\ q-p \end{pmatrix} \quad , \tag{C.12}$$

where N is the (uninteresting) normalization factor. Note that $x+y+z = 0$.

To prove that ψ_w is uncoupled from other states is to prove that Eq. C.6 is true. Assume ψ_i is an M=1 state of the general form

$$\psi_i = a|- + + +> + b|+ - + +> + c|+ + - +> + d|+ + + -> \quad , \tag{C.13}$$

(Choosing an M=-1 state would yield the same result.) A little manipulation reveals that

$$<\psi_i|I_x|\psi_{0g}> = \frac{1}{2}\,(x+y+z)(a+b+c+d) \quad , \tag{C.14}$$

where ψ_{0g} is any gerade M=0 state. Clearly this matrix element is always zero when $x+y+z = 0$, so ψ_w is indeed an uncoupled state for <u>any</u> set of dipolar couplings. When J-couplings or chemical shifts are introduced into the Hamiltonian, however, $x+y+z \neq 0$ and ψ_w rejoins its peers.

I have not been able to determine if the phenomenon of an uncoupled M=0 state occurs in general for larger spin systems when

$\mathcal{H} = \mathcal{H}_D$. Computer results for N=6 and N=8 do not predict such a state, although round-off errors may cloud the true situation. As discussed in Appendix B, one of the M=0 B_1 states of benzene is uncoupled when J-couplings are removed from the Hamiltonian.

C.4 Four-Quantum Intensity for D_4 Symmetry

We now wish to derive an expression for N-quantum τ-averaged intensity in a four-spin, purely dipolar-coupled system. The general case of six random couplings would involve considerable manipulation; instead we will focus on two special cases: D_4 symmetry in this section, C_{3v} symmetry in the next.

The relevant A_1 representation for a four-spin D_4 system contains six states with Zeeman quantum numbers 2, 1, 0, 0, -1, and -2. For couplings, we will choose

$$f = \frac{1}{2} p = \frac{1}{2} r = D_{12} = D_{23} = D_{34} = D_{14} \quad , \tag{C.15}$$

$$q = \frac{1}{2} q = D_{13} = D_{24} \quad . \tag{C.16}$$

The sum of the couplings is then

$$S = 4f + 2g \quad , \tag{C.17}$$

and the resulting energies and eigenfunctions for the A_1 states with $M \neq 0$ are as follows:

$$M = 2 \qquad E_2 = \frac{1}{4} S \qquad \psi_2 = |+ + + +\rangle$$

$$M = 1 \qquad E_1 = -\frac{1}{8} S \qquad \psi_1 = \frac{1}{2}\{|- + + +\rangle + |+ - + +\rangle + |+ + - +\rangle + |+ + + -\rangle\}$$

$$M = -1 \qquad E_{-1} = -\frac{1}{8} S \qquad \psi_{-1} = \frac{1}{2}\{|- - - +\rangle + |- - + -\rangle + |- + - -\rangle + |+ - - -\rangle\}$$

$$M = -2 \qquad E_{-2} = \frac{1}{4} S \qquad \psi_{-2} = |- - - -\rangle \quad .$$

Group-theoretic arguments as well as computer results assign the two M=0 states as gerade. From Eq. C.9, the energies for states ψ_{0g+} and ψ_{0g-} are $(-\frac{1}{4})[(\frac{S}{2}) \pm R]$, with

$$R^2 = 3p^2 - 3pq + \frac{9}{4} q^2 = 12 f^2 - 12 fg + 9 g^2 \quad . \tag{C.18}$$

It is not necessary to determine each of the coefficients x, y, and z in the expansions of ψ_{0g+} and ψ_{0g-}; as could be guessed from Eq. C.14, a knowledge of (x+y+z) is sufficient to obtain the four-quantum intensity. Let s_+ and s_- be the respective sums. The appropriate symbol shuffling then yields the following:

$$s_+^{\,2} = \frac{3}{4} (1 + \frac{S}{2R}) \quad , \tag{C.19a}$$

$$s_-^{\,2} = \frac{3}{4} (1 - \frac{S}{2R}) \quad . \tag{C.19b}$$

Now for the heart of the calculation. The four-quantum coherence as a function of τ is given by

$$\beta\, P_{4Q}(\tau) = \beta\langle\psi_{-2}|P(\tau)|\psi_2\rangle = \beta\sum_{a,b} \langle\psi_{-2}|A|\psi_a\rangle\langle\psi_a|X|\psi_b\rangle\langle\psi_b|A|\psi_2\rangle \cdot e^{i\omega_{ba}\tau} \quad . \tag{C.20}$$

After evaluating and multiplying the various matrix elements and frequencies ω_{ba}, one finds

$$\beta\, P_{4Q}(\tau) = -\frac{i}{2}\beta\,[2(s_+^2 - s_-^2)\sin(\frac{R\tau}{4}) - \sin(\frac{3S\tau}{8})]$$

$$= -\frac{i}{2}\beta\,[\frac{3S}{2R}\sin(\frac{R\tau}{4}) - \sin(\frac{3S\tau}{8})] \quad . \tag{C.21}$$

As a check on this formula, we note that when all couplings are equal (f=g), we have

$$R = \frac{i}{2}S \tag{C.22}$$

$$S = 6\,\bar{D} \tag{C.23}$$

and

$$\beta\, P_{4Q}(\tau) = -\frac{i}{2}\beta\,[3\sin(\frac{3\bar{D}\tau}{4}) - \sin(\frac{9\bar{D}\tau}{4})]$$

$$= -2i\sin^3(\frac{3\bar{D}\tau}{4}) \quad , \tag{C.24}$$

exactly as in the previously derived Eq. V.38a with $\Delta\omega = 0$.

The magnitude of the four-quantum transition intensity in a $t_2 = \tau$ experiment is given by

$$|\underline{S}_{4Q}| = \frac{\beta}{4} \left[\frac{3S}{2R} \sin\left(\frac{R\tau}{4}\right) - \sin\left(\frac{3S\tau}{8}\right)\right]^2 \tag{C.25}$$

for an even-selective sequence and half as much for a sequence in which the phase of the second and third pulses is shifted by 45° to permit excitation and detection of all MQ orders. Averaging the intensity over τ for this latter case yields

$$\begin{aligned} \langle|\underline{S}_{4Q}|\rangle_\tau &= \frac{\beta}{16} \left[\frac{9S^2}{4R^2} + 1\right] \\ &= \frac{\beta}{8} \; \frac{8f^2 + 4fg + 3g^2}{4f^2 - 4fg + 3g^2} \quad . \end{aligned} \tag{C.26}$$

The intensity is greatest ($5\beta/8$) when f=g and approaches the non-selective statistical-limit value of $\beta/16$ when $S \approx 0$ ($g \approx -2f$). When S is exactly zero, the averaging that preceded Eq. C.26 is invalid and $\underline{S}_{4Q} = 0$ for all τ values.

The ultimate τ average four-quantum intensity can also be calculated using the simplified formula of section 5.4.3.1:

$$\langle|\underline{S}_{4Q}|\rangle_\tau = \beta \sum_{a,b} \langle\psi_{-2}|A|\psi_a\rangle^2 \langle\psi_a|X|\psi_b\rangle^2 \langle\psi_b|A|\psi_2\rangle^2 \tag{C.27a}$$

$$= \frac{\beta}{16} \left[1 + 4\left(s_+^{\,4} + s_-^{\,4}\right)\right]$$

$$= \frac{\beta}{16} \left[\frac{11}{2} + \frac{9S^2}{8R^2}\right]$$

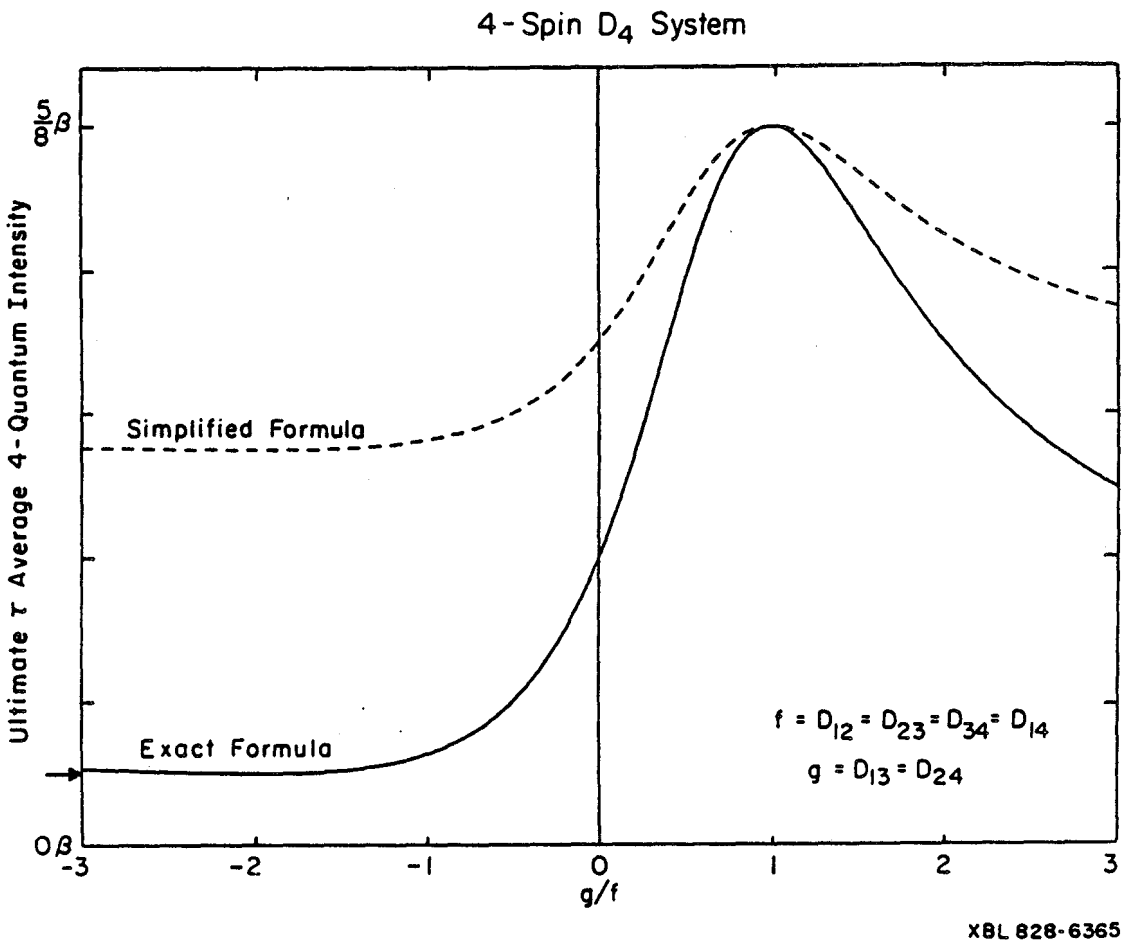

Figure C.1 The ultimate τ average 4Q intensity of a four-spin D_4 system as a function of the ratio of the two unique dipolar coupling constants. In using the "exact" formula, the effect of degenerate single-quantum transition frequencies is specifically included in the calculation of intensities; this complication is ignored when using the "simplified" formula. Both curves have the same maximum value (5β/8) for the equivalent-spin case (g = f), and both have a minimum at $\bar{D} = 0$ (g = -2f). (Actually, the exact formula predicts zero 4Q intensity at precisely $\bar{D} = 0$, but this dip is not included here.) The arrow marks the statistical-limit intensity per transition (β/16).

$$= \frac{\beta}{8} \frac{14f^2 - 8fg + 9g^2}{4f^2 - 4fg + 3g^2} \tag{C.27b}$$

When f=g, the ultimate τ average intensity is $5\beta/8$, coinciding with the exact τ average intensity given by Eq. C.26. For other ratios of f and g, however, the two formulas give different results, as illustrated in Fig. C.1. The discrepancy is due to the neglect of overlapping single-quantum frequencies in the simplified "ultimate" expression, in particular $E_{0g-} - E_1 = E_{-1} - E_{0g+} = R/4$ and $E_{0g+} - E_1 = E_{-1} - E_{0g-} = -R/4$. For this highly symmetric system, the unsimplified ultimate τ average expression, Eq. V.22, should therefore be used.

Nonetheless, Eq. C.27b does provide the limiting N-quantum intensity for general four-spin "shiftless" systems with quasi-D_4 character. (A general system would not have the degenerate single-quantum transitions that reduce the four-quantum intensity in the true D_4 case.) The minimum value of the "ultimate" intensity occurs when $\mathcal{S}=0$. This value, $11\beta/32$, is still 5.5 times greater than the statistical-limit intensity for a general four-spin system.

C.5 Four-Quantum Intensity for C_{3v} Symmetry

As a second example of N-quantum selectivity in a four-spin system, consider the C_{3v} case with $\mathcal{H} = \mathcal{H}_D$. As recorded in Table IV.3, there are two representations, A_1 and E. Let $v = D_{12} = D_{13} = D_{23}$ be one unique dipolar coupling and $w = D_{14} = D_{24} = D_{34}$ be the other. The eight resulting A_1 energies and eigenvectors are displayed in Table C.1. Note that one of the M=0 states is gerade and the other ungerade.

Table C.1

A_1 Energies and Eigenvectors for a Four-Spin C_{3v} System with $\mathcal{H} = \mathcal{H}_D$

M	Energy	Eigenvector
2	$\frac{3}{4}(v+w)$	$\psi_2 = \lvert + + + +\rangle$
1	$-\frac{1}{4}(w+F)$	$\psi_{1+} = c_+\{\lvert + + + -\rangle\}$ $+ d_+\{\lvert - + + +\rangle + \lvert + - + +\rangle + \lvert + + - +\rangle\}$
1	$-\frac{1}{4}(w-F)$	$\psi_{1-} = c_-\{\lvert + + + -\rangle\}$ $+ d_-\{\lvert - + + +\rangle + \lvert + - + +\rangle + \lvert + + - +\rangle\}$
0	$-\frac{3}{4}(v+w)$	$\psi_{0g} = \frac{1}{\sqrt{6}}\{\lvert - - + +\rangle + \lvert - + - +\rangle + \lvert - + + -\rangle$ $+ \lvert + - - +\rangle + \lvert + - + -\rangle + \lvert + + - -\rangle\}$
0	$-\frac{1}{4}(3v-w)$	$\psi_{0u} = \frac{1}{\sqrt{6}}\{\lvert - - + +\rangle + \lvert - + - +\rangle + \lvert - + + -\rangle$ $- \lvert + - - +\rangle - \lvert + - + -\rangle - \lvert + + - -\rangle\}$
-1	$-\frac{1}{4}(w+F)$	$\psi_{-1+} = c_+\{\lvert - - - +\rangle\}$ $+ d_+\{\lvert + - - -\rangle + \lvert - + - -\rangle + \lvert - - + -\rangle\}$
-1	$-\frac{1}{4}(w-F)$	$\psi_{-1-} = c_-\{\lvert - - - +\rangle\}$ $+ d_-\{\lvert + - - -\rangle + \lvert - + - -\rangle + \lvert - - + -\rangle\}$
-2	$\frac{3}{4}(v+w)$	$\psi_{-2} = \lvert - - - -\rangle$

$v = D_{12} = D_{13} = D_{23} \qquad w = D_{14} = D_{24} = D_{34}$

$F = [7w^2 - 12vw + 9v^2]^{1/2}$

$d_\pm = w[2F^2 \pm 2F(2w-3v)]^{-1/2} \qquad c_\pm = \frac{2w-3v\pm F}{w}\, d_\pm$

Equation C.27a can be used to calculate the ultimate τ average four-quantum intensity--unlike the D_4 case, there is no problem with overlap of single-quantum frequencies. The result, after heinous algebraic thrashing, is given by

$$<|\underline{S}_{4Q}|>_\tau = \frac{5}{128}\beta\ [(c_+ + 3\ d_+)^4 + (c_- + 3\ d_-)^4]$$

$$= \frac{5}{64}\ \beta\ \frac{29w^2 - 42vw + 45v^2}{7w^2 - 12vw + 9v^2}\quad , \qquad \text{(C.28)}$$

where $c_\pm$ and $d_\pm$ are defined in Table C.1. The averaged four-quantum intensity is plotted as a function of v/w in Fig. C.2. When all couplings are equal (v = w), the intensity is $5\beta/8$ as before. When the sum of the couplings is zero (v = -w), the intensity is 0.324β, or 5.18 times the statistical-limit value of $\beta/16$.

A final curious fact--no matrix elements involving the ungerade M=0 state contribute to the four-quantum intensity. This is a consequence of a more general rule: in a system without chemical shifts, all B_{ab} terms involving ungerade M=0 states are zero in the expression for N-quantum prepared coherence,

$$P_{k\bar{k}} = 2i \sum_{a<b} B_{ab}\ \sin\omega_{ba}\tau \quad . \qquad \text{(C.29)}$$

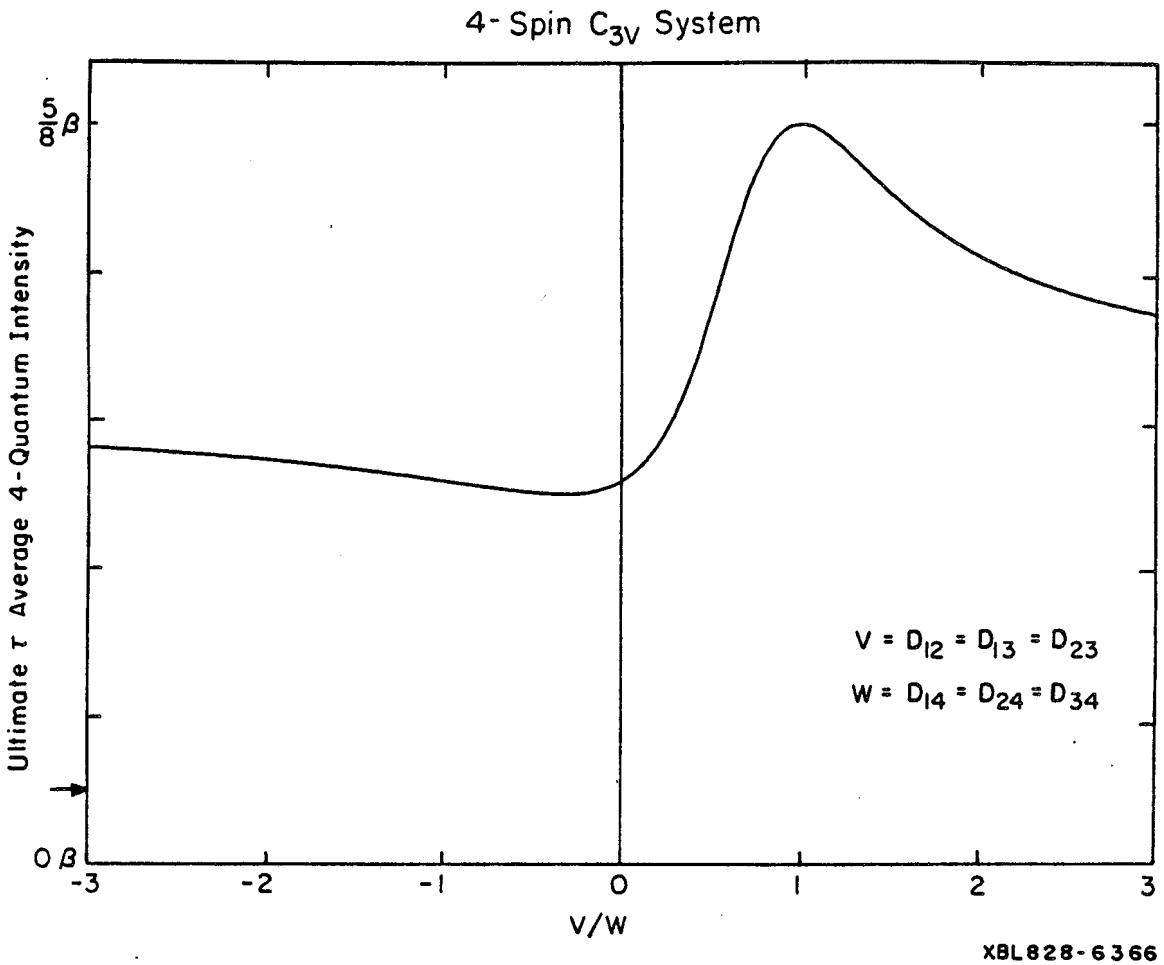

Figure C.2 The ultimate τ average 4Q intensity of a four-spin C_{3v} system as a function of the ratio of the two unique dipolar coupling constants. The maximum intensity of 5β/8 occurs for the equivalent-spin case (v = w). When $\bar{D}$ = 0 (v = -w), the intensity is 0.324β . The arrow marks the statistical-limit intensity per transition (β/16).

APPENDIX D

A LOOK AT THREE-PULSE MULTIPLE-QUANTUM PROGRAMS

A number of programs have been written to analyze the ever-timely three-pulse sequence for systems with up to eight coupled spin-$\frac{1}{2}$ nuclei, among them SPEC, SPECHO, EVOKNEVO, ULTAV, and ENSAVE. In each, it is assumed that hard pulses are used ($\omega_1 >> D_{ij}, J_{ij}, \sigma_j$), so that $\mathcal{H}_{internal}$ and $\mathcal{H}_{rf}$ can be diagonalized separately. Computation begins by setting up the internal Hamiltonian in the spin-product basis set. Because the Hamiltonian commutes with I_z, it is block-diagonal with respect to the value of M, and each block is created and diagonalized separately. For convenience, the spin-product states are represented as numbers; the six-spin state |+-++-->, for example, corresponds to 101100 (base 2) or 44. Off-diagonal matrix elements are computed by comparing two such numbers bit by bit in search of a two-spin flip-flop. After every element of a given Hamiltonian block has been calculated, a standard Jacobi transformation algorithm is used for diagonalization. The energies and the eigenvector matrix are stored for later use.

When the entire Hamiltonian has been diagonalized, the process of symmetry labeling and sorting begins. (Naturally, a more efficient and accurate procedure would be to establish the permutation symmetry and irreducible representations of $\mathcal{H}_{int}$ prior to diagonalization, but the following somewhat "quick and dirty" technique works well except in the case of accidental degeneracies.) Central to the method is the evaluation of matrix elements of I_x involving eigenstates of $\mathcal{H}_{int}$. These elements are straightforward to compute: the

eigenstates as expanded in the spin-product basis were obtained during diagonalization, and appropriate portions of I_x in the spin-product basis are easily constructed.

Because I_x belongs to the totally symmetric A_1 representation, it only connects states of the same irreducible representation. As an example, any eigenstate ψ_i with $M = N/2 - 1$ for which the matrix element

$$\langle\psi_{N/2}|I_x|\psi_i\rangle$$

is non-zero must be an A_1 state since $\psi_{N/2} = |+++\ldots+\rangle$ is always an A_1 state. In general, if ψ_a and ψ_b are two eigenstates differing in M value by ±1 and if $|\langle\psi_a|I_x|\psi_b\rangle|$ is greater than some small cut-off number q (non-zero to allow for round-off errors), then ψ_a and ψ_b belong to the same irreducible representation. A smaller value of this matrix element magnitude is not interpreted immediately as proof of differing representations, however. Instead, only if no string of eigenstates $\psi_c, \psi_d, \psi_e, \ldots \psi_j$ is found such that $|\langle\psi_a|I_x|\psi_c\rangle| > q$, $|\langle\psi_c|I_x|\psi_d\rangle| > q$, $|\langle\psi_d|I_x|\psi_e\rangle| > q$, ..., $|\langle\psi_j|I_x|\psi_b\rangle| > q$ are ψ_a and ψ_b assigned to different representations. In this manner, eventually every eigenstate gets labeled.

Of the various irreducible representations obtained by this procedure, only the totally symmetric one (A_1) is immediately identifiable in general. For the others, an analysis of the permutation properties of the relevant eigenstates yields the proper designation (B_1, E_{2g}, etc.).

Attention then shifts to the construction of I_x and the pulse propagator $\exp(i\omega_1 t I_y)$ in the spin-product basis. The latter matrix is calculated directly with no need for exponentiation. Generalizing to pulses of a given rf phase ϕ, we can write

$$\exp\{i\omega_1 t\ (\cos\phi\ I_x + \sin\phi\ I_y)\} = \prod_{j=1}^{N} \exp(i\theta I_{\phi j}) \quad , \tag{D.1}$$

where N is the number of spins, $\theta = \omega_1 t$ is the pulse flip angle, and $I_{\phi j}$ is a single-spin operator:

$$I_{\phi j} = \cos\phi\ I_{xj} + \sin\phi\ I_{yj} \quad . \tag{D.2}$$

Making use of the fact that for a single spin,

$$I_{xj}^2 = I_{yj}^2 = I_{\phi j}^2 = \frac{1}{4}\,\underset{\approx}{1} \quad , \tag{D.3}$$

we obtain

$$\prod_{j=1}^{N} \exp(i\theta I_{\phi j}) = \prod_{j=1}^{N} \{(\cos\tfrac{\theta}{2})\ \underset{\approx}{1} + (2i\ \sin\tfrac{\theta}{2})\ I_{\phi j}\} \quad . \tag{D.4}$$

(Kumar [130] and Turner [131] have used this expression analytically.) For a 90° pulse,

$$\prod_{j=1}^{N} \exp(i\ \tfrac{\pi}{2}\ I_{\phi j}) = 2^{-N/2} \prod_{j=1}^{N} (\underset{\approx}{1} + 2i\ I_{\phi j}) \quad . \tag{D.5}$$

A given matrix element is obtained by comparing the two direct-product states involved spin by spin. If among the N spins, there are k cases of $\langle +_j | I_{\phi j} | -_j \rangle$ and n cases of $\langle -_j | I_{\phi j} | +_j \rangle$, then the matrix element equals

$$(\cos \frac{\theta}{2})^{N-(n+k)} \; (i \sin \frac{\theta}{2})^{n+k} \; e^{i(n-k)\phi} \quad . \tag{D.6}$$

For a y-pulse ($\phi = \pi/2$) this becomes

$$(\cos \frac{\theta}{2})^{N-(n+k)} \; (\sin \frac{\theta}{2})^{n+k} \; (-1)^n \quad , \tag{D.7}$$

and for a 90° y-pulse we get

$$2^{-N/2} \; (-1)^n \quad . \tag{D.8}$$

Using simple expressions like these, the entire $2^N \times 2^N$ pulse propagator matrix can be easily set up in the spin-product basis.

Once I_x and the pulse propagator have been calculated, they are transformed into the basis set of the internal Hamiltonian, becoming the matrices X and A defined in section V.2. The block-diagonal form of the overall eigenvector matrix S is made use of to minimize the number of multiplications. Matrices X and A are then sorted according to irreducible representation; the result is a direct sum of smaller matrices $X^{(\mu)}$ and $A^{(\mu)}$.

At this point, the various programs diverge according to which spectral quantities are desired. In those programs that deal with specific values of $\tau = t_2$, the prepared density matrix for

representation μ is calculated:

$$P_{jk}^{(\mu)} = \sum_{a,b} A_{aj}^{(\mu)} X_{ab}^{(\mu)} A_{bk}^{(\mu)} e^{i\omega_{ba}\tau} \quad . \tag{D.9}$$

The intensity of the j→k transition is $|\{P_{jk}^{(\mu)}(\tau)\}^2|$. In some programs (such as EVOKNEVO), a loop over τ values lies within a loop over the different representations, in other programs (such as SPEC) this arrangement is reversed.

When ultimate τ average intensities are of interest, matrices $A^{(\mu)}$ and $X^{(\mu)}$ are calculated:

$$A_{jk}^{(\mu)} = [A_{jk}^{(\mu)}]^2 \quad , \tag{D.10a}$$

$$X_{jk}^{(\mu)} = [X_{jk}^{(\mu)}]^2 \quad . \tag{D.10b}$$

The elements of $[A^{(\mu)\dagger} X^{(\mu)} A^{(\mu)}]$ are the ultimate τ average intensities for irreducible representation μ.

APPENDIX E

PROGRAM NOTES

The following is a brief description of some of the computer programs developed for double-quantum and multiple-quantum simulation. All are written in Fortran, and most are currently VAX compatible and stored on tape.

Spin-1 Systems

DQC. A general program for computing the exact response of a three-level system to any sort of pulse sequence. Quadrupole frequencies, offset frequencies, pulse parameters, or time can be varied.

DQCW6. Calculates the effect of both phase-cycled cw excitation and relaxation on a three-level system. $I_{p,i}$ operator coefficients can be followed as a function of the number of cycles or studied in steady state as a function of pulse strength or frequency. Used to generate Figs. 3.5 through 3.14.

DQTWO. Similar to DQC, but treats a system of two dipolar-coupled deuterons.

DQUICK. Uses the analytical expressions in Tables II.6 and II.7 for the evolution of a deuteron under a two-term Hamiltonian and a user-specified range of times and ν_1 values to quickly obtain the best double-quantum pulse or quadrupole echo sequence for a powder.

GARY. A variant of DQUICK specialized for the quadrupole echo sequence. Used to obtain the pulse parameters in Fig. II.28.

SOS2. Generates the double-quantum powder lineshape of an axially symmetric chemical shielding tensor, broadened by second-order quadrupole shifts and (optionally) distorted by a DQ transfer function (previously calculated using DQC). Used for Figs. II.39-II.41.

TENSE. Computes pulse-sequence-distorted chemical shielding powder lineshapes when the chemical shielding tensor and the EFG tensor are non-axial or non-aligned--see Figs. II.34-II.36.

TENSORS1. Calculates two-dimensional powder spectra (single-quantum frequencies along one axis, double-quantum frequencies along the other), with or without pulse sequence distortion. The chemical shielding and EFG tensors are assumed to be axial and aligned. Used for Figs. II.37 and II.38.

Coupled Spin-$\frac{1}{2}$ Systems

[In most of these programs, the form of the pulse sequence is fixed: two hard pulses in the preparation period and one in the detection period. The exceptions are DINKPULSE and DINK2D (one weak preparation pulse); EDSEL, MQC3, and MQC3D (user-designed sequences); and UVIEW (no pulses involved).]

ANGLE1. Calculates the ultimate τ average intensity per transition for each MQ order as a function of rf pulse flip angle. Used to create Figs. V.23 and V.24. Input data from program MOLEC.

AUTOCORR. Generates the autocorrelation function of prepared coherence (averaged over each MQ order). Input from program EVOQUE.

CARBOY. Very much like EDSEL, except that one of the spins is a heteronucleus (e.g., ^{13}C instead of ^{1}H). Both "carbon" and "proton" pulses can be applied. Input is via program CARQUE.

DINKPULSE. Considers the use of a weak pulse for MQ preparation. The average coherence magnitude for each MQ order is calculated as a function of either the pulse strength or pulse length. Input from program DINKQUE.

DINK2D. A two-dimensional analog of DINKPULSE--pulse length and ν_1 values can be varied simultaneously.

EDSEL. Displays the density matrix of a system with four spins or less after a general preparation sequence of hard pulses and delays. Input from program EDQUE.

ENSAVE. Calculates an ultimate τ average by the slow and careful method of considering all the $B_{ab}B_{a'b'}$ cross-terms (Eq. V.22). Input from program MOLEC.

ENSAVE2. A variant of ENSAVE that skips the $B_{ab}B_{a'b'}$ terms which give rise solely to even-odd selection in systems without chemical shift differences.

EVOKNEVO. Calculates the average prepared coherence magnitude per transition and the average intensity per transition for each MQ order as a function of $\tau = t_2$. Used for Figs. V.4, V.7, and V.8. Input from program EVOQUE.

EXFUNK. For each MQ order, this program compares the average prepared coherence magnitude and the PPPI excitation function (see ref. 126), both as a function of τ. Input from EVOQUE.

MOMENTS4. Starting with a randomly chosen $\mathcal{H}_D$, this program computes the ultimate τ average and statistical-limit second moments and fourth moments for each MQ order. Input from program MOM4QUE.

MQC3. Computes the time evolution of three methyl protons for a general pulse sequence.

MQC3D. Displays the density matrix for three methyl protons after a general pulse sequence.

NQEVO. Calculates the prepared coherence and intensity of the N-quantum transition as a function of $\tau = t_2$, plus its autocorrelation function and various averaged quantities. Used to generate Figs. V.5 and V.15-V.17. Input from program EVOQUE.

PROBDO. This program generates a probability distribution for the average prepared coherence magnitude of each MQ order and was used to creates Figs. V.21 and V.22. Input from program TAUQUE.

SNAPSHOT. Displays prepared density matrices for different representations and τ values. Input from program EVOQUE.

SPEC. Generates MQ spectra with a choice of intensities: exact values for a particular τ or set of τ's, ultimate τ average values, statistical-limit values, or symmetry-adjusted statistical-limit values. Used frequently in Chapter V. Input data supplied by program SPEQUE.

SPECHO. A variant of SPEC with a pi pulse in the middle of evolution--an example appears in Fig. V.26. Ultimate τ average intensities are not obtainable.

SPIFFY. Generates MQ spectra as a function of some molecular parameter--a dipolar coupling, for example, or a chemical shift. Figs. IV.10-IV.12 are three examples. Input via program SPIFFQUE.

SQSPEC. Calculates a standard single-quantum spectrum, as in Fig. IV.2. Input data from program MOLEC.

TAUPOWER. For each MQ order, this program displays the average coefficient associated with different powers of τ in the expansion of the prepared density matrix (Eqs. V.15a, V.15b). Such information

was used in constructing Table V.1. Input data from program TAUPOWQUE.

T2BER. Calculates the total spectral intensity as a function of detection time t_2 for a fixed value of the preparation time τ. Used for Fig. V.18. Input from program T2QUE.

ULTAV. Calculates ultimate τ average intensities the fast way: $\langle \underline{S}_{jk} \rangle = (A \; X \; A)_{jk}$, where $A_{\ell m} = A^2_{\ell m}$ and $X_{\ell m} = X^2_{\ell m}$. Input data provided by program MOLEC.

UVIEW. Displays eigenvectors expanded in the spin-product basis.

WIMP76. A variant of SPEC for use with eight-spin systems when the normal symmetry-sorting algorithm doesn't work well. This program skips symmetry sorting altogether but then to save time computes only the N-quantum, (N-1)-quantum and (N-2)- quantum ultimate τ average intensities.

YS. Computes second moments and ultimate τ average intensities for each MQ order. Input data from MOLEC.

General Programs and Subroutines

CATPAC. A collection of manipulation and multiplication subroutines for complex matrices. The corresponding collection for real matrices is entitled RATPAC.

FILEOP. This program performs various arithmetic operations on the elements of a data file or two such files. Specifically, it can be used for element-by-element addition or multiplication of data files.

HEIGEN. Diagonalizes a complex hermitian matrix using the Jacobi transformation method. It is derived from program EIGEN of the IBM Scientific Subroutine Package [52].

REIGEN. Another offspring of EIGEN for diagonalizing a real symmetric matrix.

In addition, a number of plotting programs have been written for the Tektronix 4014 display terminal and 4662 plotter connected to the Biodynamics VAX. These make use of various Tektronix Plot-10 subroutines and include programs for displaying equally spaced data points (PLOT1, PLOT16), MQ spectra (PLOTTO, WAZOO, HUNKPLOT), a series of related MQ spectra (SPIFFPLOT), two-dimensional data arrays (PLOT2D, PLOT2DS), spin-vector projections (JCP2), and transfer functions (JCPTF).

APPENDIX F

POSTSCRIPT

Lord, carry me back to the rotating frame,
Where spins fear my pulses and cringe at my name;
I'll bully them into unnatural states,
Then ponder the patterns coherence creates.

References

1. E. M. Purcell, H. C. Torrey, and R. V. Pound, Phys. Rev. 69, 37 (1946).
2. F. Bloch, W. W. Hansen, and M. Packard, Phys. Rev. 70, 474 (1946).
3. M. Goeppert-Meyer, Ann. Physik 9, 273 (1931).
4. W. A. Anderson, Phys. Rev. 104, 850 (1956).
5. J. I. Kaplan and S. Meiboom, Phys. Rev. 106, 499 (1957).
6. W. A. Anderson, R. Freeman, and C. A. Reilly, J. Chem. Phys. 39, 1518 (1963).
7. J. I. Musher, J. Chem. Phys. 40, 983 (1964).
8. K. A. McLauchlan and D. H. Whiffen, Proc. Chem. Soc., 144 (1962); A. D. Cohen and K. A. McLauchlan, Disc. Faraday Soc. 34, 132 (1962).
9. A. D. Cohen and D. H. Whiffen, Mol. Phys. 7, 449 (1964).
10. G. Bodenhausen, "Multiple-Quantum NMR", Progress in NMR Spectroscopy, Ed. J. W. Emsley, J. Feeney, and L. H. Sutcliffe (Pergamon, Oxford, 1981), Vol. 14, pp. 137-173.
11. T. C. Farrar and E. D. Becker, Pulse and Fourier Transform NMR (Academic, New York, 1971).
12. E. Fukushima and S. B. W. Roeder, Experimental Pulse NMR: A Nuts and Bolts Approach (Addison-Wesley, Reading, Massachusetts, 1981).
13. A. Wokaun and R. R. Ernst, Mol. Phys. 36, 317 (1978).
14. M. E. Stoll, A. J. Vega, and R. W. Vaughan, J. Chem. Phys. 67

2029 (1977).

15. R. Poupko, R. L. Vold, and R. R. Vold, J. Magn. Reson. 34, 67 (1979).

16. G. Bodenhausen, R. L. Vold, and R. R. Vold, J. Magn. Reson. 37, 93 (1980).

17. J. Tang and A. Pines, J. Chem. Phys. 72, 3290 (1980).

18. J. Tang, Ph.D. Thesis, University of California, Berkeley, 1981 (published as Lawrence Berkeley Laboratory report LBL-13605).

19. J. Tang and A. Pines, J. Chem. Phys. 73, 2512 (1980).

20. A. Abragam, The Principles of Nuclear Magnetism (Oxford University Press, London, 1961).

21. C. P. Slichter, Principles of Magnetic Resonance (Harper and Row, New York, 1963; Springer-Verlag, Berlin, 1978).

22. A. Carrington and A. C. McLachlan, Introduction to Magnetic Resonance (Harper and Row, New York, 1967).

23. M. Mehring, "High Resolution NMR Spectroscopy in Solids", NMR: Basic Principles and Progress, Ed. P. Diehl, E. Fluck, and R. Kosfeld (Springer-Verlag, Berlin, 1976), Vol. 11.

24. U. Haeberlen, "High Resolution NMR in Solids: Selective Averaging", Advances in Magnetic Resonance, Supplement 1 (Academic, New York, 1976).

25. J. W. Emsley and J. C. Lindon, NMR Spectroscopy Using Liquid Crystal Solvents (Pergamon, Oxford, 1975).

26. Reference 21, Chapter 1.

27. I. N. Levine, Quantum Chemistry (Allyn and Bacon, Boston, 1970),

Vol. I, Chapter 5.

28. Reference 23, Chapter 2.

29. Reference 24, Chapter 2.

30. J. F. Nye, Physical Properties of Crystals (Oxford University Press, London, 1972).

31. M. E. Rose, Elementary Theory of Angular Momentum (Wiley, New York, 1957).

32. B. L. Silver, Irreducible Tensor Methods (Academic, New York, 1976).

33. N. Davidson, Statistical Mechanics (McGraw-Hill, New York, 1962), Chapter 12,

34. M. Sargent, M. O. Scully, and W. E. Lamb, Laser Physics, (Addison-Wesley, Reading, Massachusetts, 1974), Chapter 2.

35. Reference 21, Chapter 2.

36. Reference 20, Chapter 2.

37. Reference 21, Chapter 5.

38. L. M. Jackman and S. Sternhell, Applications of Nuclear Magnetic Resonance Spectroscopy in Organic Chemistry (Pergamon, Oxford, 1969).

39. Reference 23, Chapter 5.

40. D. E. Wemmer, Ph.D. Thesis, University of California, Berkeley, 1978 (published as Lawrence Berkeley Laboratory report LBL-8042).

41. Reference 20, Chapters 6 and 7.

42. R. G. Barnes and J. W. Bloom, J. Chem. Phys. 57, 3082 (1972).

43. Reference 22, Chapter 3.

44. Reference 21, Chapter 3.

45. S. Meiboom and L. C. Snyder, Acc. Chem. Res. 4, 81 (1971).

46. P. Diehl and C. L. Khetrapal, "NMR Studies of Molecules Oriented in the Nematic Phase of Liquid Crystals", NMR: Basic Principles and Progress, Ed. P. Diehl, E. Fluck, and R. Kosfeld (Springer-Verlag, Berlin, 1969), Vol. 1, pp. 1-96.

47. Reference 25, Chapter 2.

48. Reference 25, Chapter 7.

49. P. D. Buckley, K. W. Jolley, and D. N. Pinder, "Application of Density Matrix Theory to NMR Line-Shape Calculations", Progress in NMR Spectroscopy, Ed. J. W. Emsley, J. Feeney, and L. H. Sutcliffe (Pergamon, Oxford, 1975), Vol. 10, pp. 1-26.

50. J. H. Wilkinson, The Algebraic Eigenvalue Problem (Oxford University Press, London, 1965).

51. P. Diehl, H. Kellerhals, and E. Lustig, "Computer Assistance in the Analysis of High-Resolution NMR Spectra", NMR: Basic Principles and Progress, Ed. P. Diehl, E. Fluck, and R. Kosfeld (Springer-Verlag, Berlin, 1972), Vol. 6.

52. IBM System/360 Scientific Subroutine Package, Programmer's Manual (IBM Technical Publications Dept., New York, 1967).

53. U. Haeberlen and J. S. Waugh, Phys. Rev, 175, 453 (1968).

54. J. S. Waugh, "Coherent Averaging and Double Resonance in Solids", NMR: Basic Principles and Progress, Ed. P. Diehl, E. Fluck, and R. Kosfeld (Springer-Verlag, Berlin, 1976), Vol. 13, pp. 23-30.

55. W. S. Warren, Ph.D. Thesis, University of California, Berkeley, 1980 (published as Lawrence Berkeley Laboratory report LBL-11885).

56. S. W. Sinton, Ph.D. Thesis, University of California, Berkeley, 1981 (published as Lawrence Berkeley Laboratory report LBL-13604).

57. G. P. Drobny, Ph.D. Thesis, University of California, Berkeley (1982).

58. D. P. Weitekamp, Ph.D. Thesis, University of California, Berkeley (1982).

59. R. E. Eckman, Ph.D. Thesis, University of California, Berkeley (1982).

60. D. R. Hofstadter, Scientific American 245(5), 22 (Nov., 1981).

61. R. P. Feynman, F. L. Vernon, and R. W. Hellwarth, J. Appl. Phys. 28, 49 (1957).

62. H. Hatanaka, T. Terao, and T. Hashi, J. Phys. Soc. Japan 39, 835 (1975); H. Hatanaka and T. Hashi, J. Phys. Soc. Japan 39, 1139 (1975); H. Hatanaka, T. Ozawa, and T. Hashi, J. Phys. Soc. Japan 42, 2069 (1977); H. Hatanaka and T. Hashi, Physics Letters 67A, 183 (1978); H. Hatanaka and T. Hashi, Phys. Rev. B 21, 2677 (1980); H. Hatanaka and T. Hashi, J. Phys. Soc. Japan 50, 3629 (1981).

63a. S. Vega, T. W. Shattuck, and A. Pines, Phys. Rev. Lett. 37, 43 (1976).

63b. T. W. Shattuck, Ph.D. Thesis, University of California, Berkeley, 1976 (published as Lawrence Berkeley Laboratory report LBL-5458).

64. A. Pines, S. Vega, D. J. Ruben, T. W. Shattuck, and D. E. Wemmer, Proc. IV Ampere Int. Summer School, Pula, Yugoslavia (1976).

65. S. Vega and A. Pines, J. Chem. Phys. 66, 5624 (1977).

66. S. Vega, J. Chem. Phys. 68, 5518 (1978).

67. A. Wokaun and R. R. Ernst, J. Chem. Phys. 67, 1752 (1977).

68. D. G. Gold and E. L. Hahn, Phys. Rev. A 16, 324 (1977); D. G. Gold, Ph.D. Thesis, University of California, Berkeley (1978).

69. R. G. Brewer and E. L. Hahn, Phys. Rev. A 11, 1641 (1975).

70. S. Hsi, H. Zimmermann, and Z. Luz, J. Chem. Phys. 69, 4126 (1978).

71. G. L. Hoatson and K. J. Packer, Mol. Phys. 40, 1153 (1980).

72. M. E. Stoll, E. K. Wolff, and M. Mehring, Phys. Rev. A 17, 1561 (1978); E. K. Wolff and M. Mehring, Phys. Lett. 70A, 125 (1979); M. Mehring, E. K. Wolff, and M. E. Stoll, J. Magn. Reson. 37, 475 (1980).

73. P. L. Corio, Structure of High-Resolution NMR Spectra (Academic, New York, 1966).

74. S. Vega, J. Chem. Phys. 63, 3769 (1975).

75. J. Jeener and P. Broekaert, Phys. Rev. 157, 232 (1967).

76. G. Drobny, private communication.

77. M. Bloom, J. H. Davis, and M. I. Valic, Can. J. Phys. 58, 1510 (1980).

78. E. O. Brigham, The Fast Fourier Transform (Prentice-Hall, Englewood Cliffs, New Jersey, 1974).

79. H. W. Spiess, H. Zimmermann, and U. Haeberlen, Chem. Phys. 12, 123 (1976).

80. T. Chiba, J. Chem. Phys. 39, 947 (1963).

81. M. Linder, A. Hoehener, and R. R. Ernst, J. Chem. Phys. 73, 4959 (1980).

82. S. Yatsiv, Phys. Rev. 113, 1522 (1959).

83. Reference 25, Chapter 1.

84. A. Saupe, Z. Naturforsch. 19a, 161 (1964).

85. Reference 25, Chapter 4.

86. L. C. Snyder and S. Meiboom, J. Chem. Phys. 44, 4057 (1966).

87. J. W. Emsley and G. R. Luckhurst, Mol. Phys. 41, 19 (1980).

88. E. E. Burnell and C. A. deLange, J. Magn. Reson. 39, 461 (1980).

89. E. E. Burnell and C. A. deLange, Chem. Phys. Lett. 76, 268 (1980).

90. A. Saupe and G. Englert, Phys. Rev. Lett. 11, 462 (1963); G. Englert and A. Saupe, Z. Naturforsch. 19a, 172 (1964).

91. Reference 25, Chapter 8.

92. C. L. Khetrapal and A. C. Kunwar, "NMR Studies of Molecules Oriented in Thermotropic Liquid Crystals," Advances in Magnetic Resonance, Ed. J. S. Waugh (Academic, New York, 1977), Vol. 9, pp. 302-422.

93. S. Sinton and A. Pines, Chem. Phys. Lett. 76, 263 (1980).

94. W. Niederberger, P. Diehl, and L. Lunazzi, Mol. Phys. 26, 571 (1973).

95. W. S. Warren and A. Pines, J. Am. Chem. Soc. 103, 1613 (1981).

96. M. Tinkham, Group Theory and Quantum Mechanics (McGraw-Hill, New York, 1964).

97. D. S. Schonland, Molecular Symmetry: An Introduction to Group Theory and its Uses in Chemistry (Van Nostrand, London, 1965).

98. E. B. Wilson, J. Chem. Phys. 27, 60 (1957).

99. R. G. Jones, "The Use of Symmetry in Nuclear Magnetic Resonance," NMR: Basic Principles and Progress, Ed. P. Diehl, E. Fluck, and R. Kosfeld (Springer-Verlag, Berlin, 1969), Vol. 1, pp. 97-174.

100. W. P. Aue, E. Bartholdi, and R. R. Ernst, J. Chem. Phys. 64, 2229 (1976).

101. A. Pines, D. Wemmer, J. Tang, and S. Sinton, Bull. Am. Phys. Soc. 23, 21 (1978).

102. W. S. Warren, S. Sinton, D. P. Weitekamp, and A. Pines, Phys. Rev. Lett. 43, 1791 (1979).

103. W. S. Warren, D. P. Weitekamp, and A. Pines, J. Chem. Phys. 73, 2084 (1980); W. S. Warren, D. P. Weitekamp, and A. Pines, J. Magn. Reson. 40, 581 (1980); W. S. Warren and A. Pines, J. Chem. Phys. 74, 2808 (1981).

104. G. Drobny, A. Pines, S. Sinton, W. S. Warren, and D. P. Weitekamp, Phil. Trans. R. Soc. Lond. A 299, 585 (1981).

105. E. L. Hahn, Phys. Rev. 80, 580 (1950).

106. D. P. Weitekamp, private communication.

107. H. Y. Carr and E. M. Purcell, Phys. Rev. 94, 630 (1954).

108. A. Wokaun and R. R. Ernst, Chem. Phys. Lett. 52, 407 (1977).

109. G. Drobny, A. Pines, S. Sinton, D. P. Weitekamp, and D. Wemmer, Faraday Symp. Chem. Soc. 13, 49 (1979).

110. P. L. Corio, Structure of High-Resolution NMR Spectra (Academic, New York, 1966).

111. J. R. Garbow, private communication.

112. A. Saupe, Z. Naturforsch. 20a, 572 (1965).

113. R. N. Bracewell, The Fourier Transform and its Applications 2nd Ed., (McGraw-Hill, New York, 1978).

114. A. A. Maudsley, A. Wokaun, and R. R. Ernst, Chem. Phys. Lett. 55, 9 (1978).

115. A. Bax, P. G. deLong, A. F. Mehlkopf, and J. Smidt, Chem. Phys. Lett. 69, 567 (1980).

116. J. B. Murdoch, W. S. Warren, D. P. Weitekamp, and A. Pines, J. Magn. Reson. (submitted).

117. H. S. Gutowsky, D. W. McCall, and C. P. Slichter, J. Chem. Phys. 21, 279 (1953).

118. P. Diehl, H. Bösiger, and H. Zimmermann, J. Magn. Reson. 33, 113 (1979).

119. D. P. Weitekamp, J. R. Garbow, J. B. Murdoch, and A. Pines, J. Am. Chem. Soc. 103, 3578 (1981).

120. Reference 25, Chapter 3.

121. J. W. Emsley, J. C. Lindon, and J. Tabony, J. Chem. Soc., Faraday II 71, 586 (1975).

122. W. S. Warren, J. B. Murdoch, and A. Pines, J. Magn. Reson. (submitted).

123. W. K. Rhim, A. Pines, and J. S. Waugh, Phys. Rev. B 3, 684 (1971).

124. Y. S. Yen, private communication.

125. Y. S. Yen, J. Tang, J. B. Murdoch, and A. Pines, to be published.

126. D. P. Weitekamp, J. R. Garbow, and A. Pines, J. Magn. Reson. 46, 529 (1982).

127. C. S. Yannoni, J. Am. Chem. Soc. 92, 5237 (1970).

128. D. Middleton, An Introduction to Statistical Communication Theory, (McGraw-Hill, New York, 1960).

129. F. Reif, Fundamentals of Statistical and Thermal Physics, (McGraw-Hill, New York, 1965).

130. A. Kumar, J. Mag. Reson. 30, 227 (1978).

131. D. L. Turner, J. Magn. Reson. 46, 213 (1982).

132. W. H. Louisell, Quantum Statistical Properties of Radiation, (Wiley, New York, 1973).

133. R. M. Wilcox, J. Math. Phys. 8, 962 (1967).

134. R. S. Burington, Handbook of Mathematical Tables and Formulas, (Handbook Publishers, Sandusky, Ohio, 1949).

"Better down the road without that load."

Neil Young